Investigation of Protective Mechanisms of Organic Coatings by Thermal Testing and Electrochemical Techniques

A Thesis Submitted for the Degree of Doctor of Philosophy
at the University of Oxford,
Hilary Term 2011

Zalilah Sharer Sahir
Wolfson College
April 11, 2011

Abstract

Zalilah Sharer Sahir
Wolfson College

DPhil in Materials
Hilary Term 2011

Investigation of Protective Mechanisms of Organic Coatings by Thermal Testing and Electrochemical Techniques

This work investigated the protection of mechanism of organic coatings on steel exposed to 3% sodium chloride solution at 50°C, coupled with the use of electrochemical impedance spectroscopy (EIS) to monitor progress of corrosion and degradation of coating. Unlike Walter[1], EIS measurement was conducted at 50°C as well as after cooling, and measurements at intermediate temperatures have been used to characterize the dependence of the process involved.

The proposition that corrosion rate is controlled by the ionic resistance of an organic coating has been tested. EIS results were fitted to a model circuit and changes in the film resistance and charge-transfer resistance with temperature were analyzed to deduce activation energies for the processes involved. Surprisingly, the calculated activation energy for coating resistance is significantly lower than the activation energy for the charge transfer resistance. This suggests that ion conduction in the coating, as apparent in an AC measurement, cannot be controlling the corrosion rate.

Potentiostatic pulse tests on coated metal enable iR-corrected polarization curves to be plotted at different temperatures. From this, the activation energy determined from the corrosion currents also higher matches the higher activation energy value calculated from the charge transfer resistance. However, measurements of coating resistance on free films of the same coating also generate higher activation energy values, leaving two possible models that can account for the results.

[1] G.W. Walter, Corrosion Science, 32, 10, 1085

Acknowledgements

I am extremely indebted to my supervisor, **Professor John Sykes** for his endless guidance, encouragement, generosity and patience throughout my PhD journey - this thesis would not have been possible without his help. For most of my PhD, I thought no one cared about corrosion and coating but within the last three years, I have met several people who do especially **Bi Huichao**, **David Lee**, **Jesus Manuel Vega** and **Yan Xu**. You guys rock and made the day in the lab more enjoyable. Special thanks also go to **David Le**e who proof-read this thesis.

I want to thank **Gabrielle Chapman** for her help on SEM and Lyn Richmond for her kindness and always welcoming to extend her help in anything. I would also like to extend my sincere thanks to **Noor Azlin** and **Zamri** for our friendship that has made my last years in Oxford extremely pleasurable.

Malaysian Ministry of Higher Education, MOHE is gratefully acknowledged for awarding the PhD scholarship and **University of Technology Malaysia** for allowing me to take study leave to pursue my PhD study. Conference funding from MOHE, also made the Moscow trip possible. Thanks to **International Paint** for providing the samples and **Shell Global Solution** for providing financial support for this study.

And finally, I offer my heartfelt thanks to my sibling; **Sarimah, Ahadah, Shadan, Ajidah, Arbain** and **Hairuddin** for their encouragement and moral support during the period of this work.

Zalilah Sharer Sahir
Wolfson College, April 2011

Preface

The work described in this thesis was carried out by the author in the Department of Materials at the University of Oxford, between November 2007 and November 2010, under the supervision of Prof. John Sykes. No part of this thesis has been submitted for a degree at this or any other university. Where the work of other authors has been included in the text, this has been duly acknowledged and a full list of references is given at the end of the thesis.

Extracts from this work have been presented at the following meetings:

- Poster presentation at 'NACE Corrosion 2010', San Antonio, Texas, USA, March 2010
- Oral presentation at '51st Corrosion Science Symposium', Southampton, UK, September 2010
- Oral presentation at 'EUROCORR 2010', Moscow, RUSSIA, September 2010
- Oral presentation at 'AETOC 2011', Mons, BELGIUM, April 2011

Dedications

This thesis is dedicated to the memory of my late parent, ***Sharer*** *(1931-2010) and* ***Aishah*** *(1941-2006). Both of you were a great dad and mom, and I really miss you both. Mom often told me when I was a young girl how important it was that I get a good education. I have never forgotten your wise words.*

Contents

CHAPTER 1

INTRODUCTION

The main focus of this thesis is testing organic coatings on steel exposed to 3% sodium chloride solution at 50°C, coupled with the use of electrochemical impedance spectroscopy (EIS) to monitor the progress of corrosion and degradation of coatings. Unlike Walter [1], EIS measurements were conducted at 50°C as well as after cooling, and measurements at intermediate temperatures have been used to characterize the dependence of the processes involved.

1.1 Organic Coatings and Corrosion

Organic coatings have been widely used to protect metals from corrosion by acting as a barrier between the substrate and the corrosive environment [2]. Despite great advances in organic coating technology in recent years, organic coatings eventually lose their protective properties whereupon corrosion of metals will occur under the coating. A lot of research concerning corrosion and corrosion protection of metal has been performed because of its critical importance in engineering structure applications. Several different types and mechanisms for failure of a protective organic coating have been proposed; however there are still conflicting evidence and ideas within the literature. It is still unclear how to completely explain coating degradation of a real coating system that contains inhibitive or sacrificial pigments.

1.2 Costs of Corrosion

The annual cost of corrosion in the United States of America has been estimated between $8 and $126 billion per year [3]. However, a recent study shows this amount has doubled to $276 billion per year which is equivalent to 3.1% of the US GDP (gross domestic product) [4]. **Figure 1.1** shows a breakdown of five major sector categories for analysis in the corrosion cost study and the total direct cost is $137.9 billion. This figure was then extrapolated to the total US economy ($8.79 trillion) for an annual cost of corrosion of $276 billion. Fortunately, corrosion is controllable but at a cost which has been estimated by US National Bureau of standards at a total direct cost of $121 billion. Thus corrosion prevention has some importance because it has been estimated that 25 to 30% of annual corrosion cost can be saved by application of corrosion control techniques. Many corrosion control techniques have been developed, but the biggest portion (88.3%) was attributed to organic coatings [4].

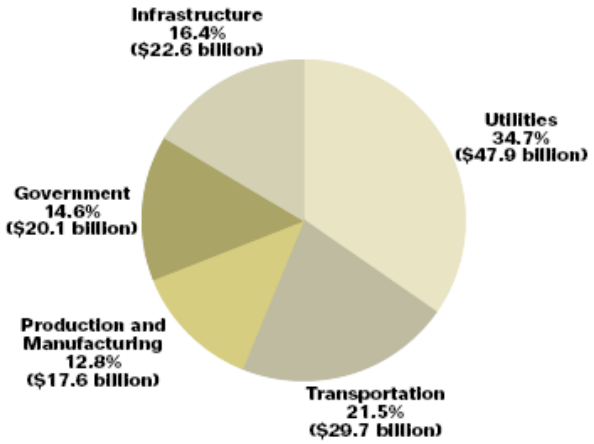

Figure 1.1 – Cost of corrosion in sector categories in a US study in 2001 [4]

1.3 Research Objective and Thesis Outline

The overall objective of this thesis combines two approaches. The first approach involves the use of an accelerated test. Since corrosion through exposure to the natural environment is extremely slow, an accelerated test is employed with the aim to speed up the coating failure without changing the degradation mechanism. The second approach is to use electrochemical impedance spectroscopy (EIS) to allow early detection of coating degradation.

The aim of this thesis is to study the protective mechanism of organic coatings (attached and free film) by exposing the sample to a more aggressive environment; salt solution at 50^{o}C. EIS testing of exposed samples were conducted across a range of temperatures to find whether there is a link between the temperature dependence of coating resistance and that of the corrosion process underneath the coating.

This section provides an overview of the research presented over the following nine chapters. **Figure 1.2** provides a diagrammatic overview of the thesis structure. **Chapter 2** provides a literature review concerning corrosion and corrosion control through organic coatings. This chapter discussed four basic mechanisms by which organic coatings provide protection. Major coating failure mechanisms such as corrosion initiation and blistering underneath the coating are discussed. Differences between exposure test at natural and accelerated environment have also been addressed.

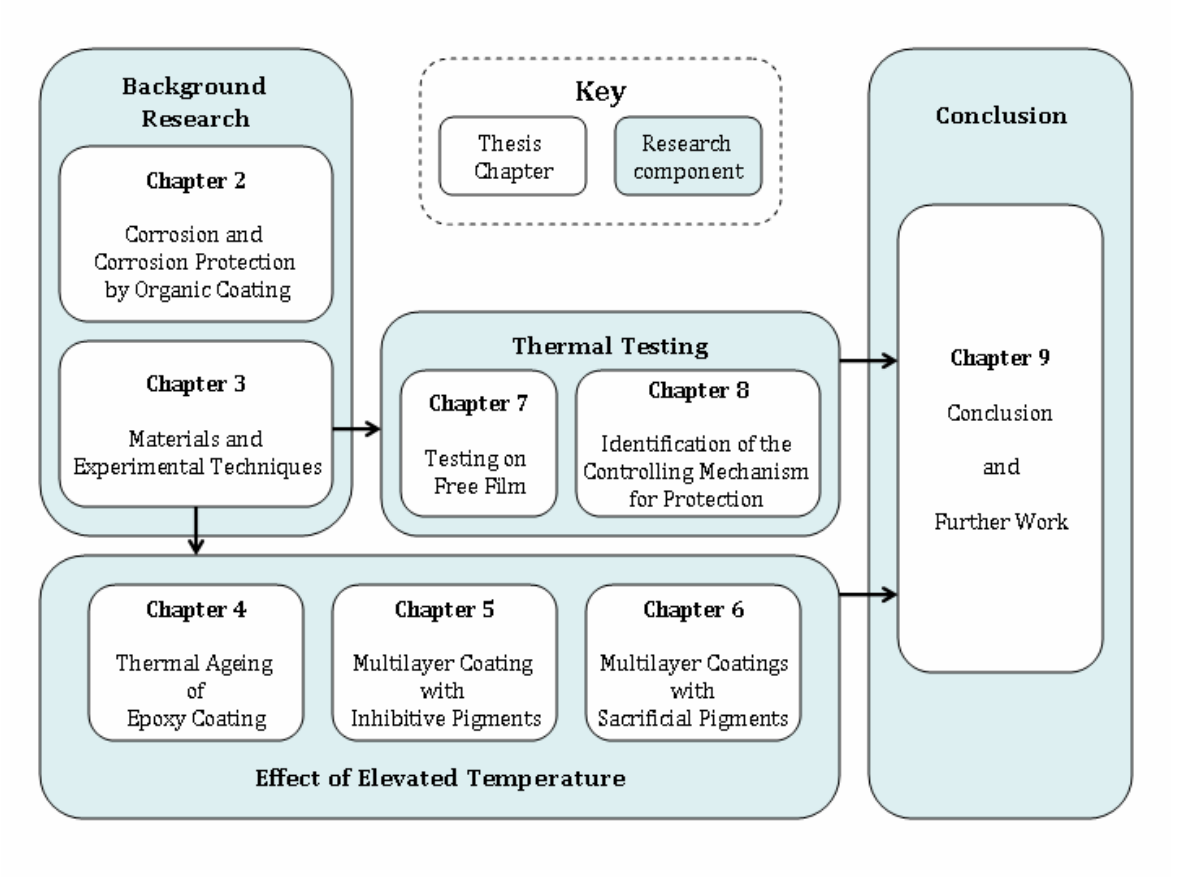

Figure 1.2 - Overview of thesis structure

Chapter 3 describes the experimental techniques adopted in this study. A brief description of coating materials is given at the beginning of this chapter. Electrochemical characterization using AC impedance measurement and Kelvin probe is described in detail.

Chapter 4 presents the results of high temperature exposure of several epoxy coatings, periodically measured with AC impedance. The results have been analyzed and the link between temperature dependence of the coating and charge transfer resistance was established. The variation of temperature dependence between the cooling and heating

regime was also established. This chapter ends with the application of the scanning Kelvin probe which generates a potential map for an area underneath a blistering coated panel.

Whilst some link on the temperature dependence between coating properties and charge transfer has been established for several epoxy coatings, it is interesting to see whether the same conclusion holds for a real system used in the field. Thus, **Chapters 5** and **6** report the results of high temperature exposure of two real systems used in the field i.e. zinc phosphate pigmented and zinc rich paint primer with top coatings.

Chapter 7 discusses the results of free film when the surrounding temperature is altered to above and below the ambient temperature. Effect of ion mobility on the free film performance has also been described. **Chapter 8** reports the findings on temperature dependence of polarization curves measured using a potentiostatic pulse test (PPT). Finally, **Chapter 9** concludes the thesis by summarizing the main findings and suggestions for further work are presented.

CHAPTER 2

CORROSION AND CORROSION PROTECTION OF ORGANIC COATING

2.1 Corrosion Principles and Mechanism

Corrosion is the natural process of deterioration or destruction of a material due to a chemical or electrochemical reaction with its environment. With a few exceptions, all metals corrode when in contact with corrosive environments, air and moisture; pure and salt water; gases such as sulphur dioxide, chlorine and hydrogen sulphide [3]. The most common corrosion process is the destruction of metals through electrochemical reactions taking place on the metal surface, either in a liquid or gaseous environment. The majority of objects that protective coatings are applied to are made of steel.

Taking iron as an example, the corrosion process is illustrated in the following paragraphs. Corrosion of iron can be explained as an electrochemical process. The following reaction describes the corrosion process of iron in the presence of water and oxygen [3];

$2Fe \rightarrow 2Fe^{2+} + 4e^-$ anodic reaction (2.1)

$O_2 + 2\,H_2O + 4\,e^- \rightarrow 4\,OH^-$ cathodic reaction (2.2)

The overall reaction (when Fe^{2+} and OH^- react together in solution);

$$2\,Fe + O_2 + 2\,H_2O \rightarrow 2\,Fe^{2+} + 4\,OH^- \rightarrow 2\,Fe(OH)_2 \qquad (2.3)$$

However, $Fe(OH)_2$ is unstable in oxygenated solution thus it is usually oxidized to a ferric salt compound also known as rust;

$$2Fe(OH)_2 + H_2O + 0.5O_2 \rightarrow 2Fe(OH)_3 \qquad (2.4)$$

For corrosion to occur, apart from a thermodynamically unstable metallic material, three other components must also be present: an electron acceptor, an electrolyte and an electrical path between the anode and the cathode. The anode is the region of the metal surface that deteriorates where the oxidation reaction (anodic reaction) occurs to release electrons. The cathode is the region of the metal that does not corrode as the reduction process (cathodic reaction) takes place by consuming electrons produced at the anode. These two regions, connected electronically by the metal and ionically by the electrolyte, are referred to as the corrosion cell as shown in **Figure 2.1**.

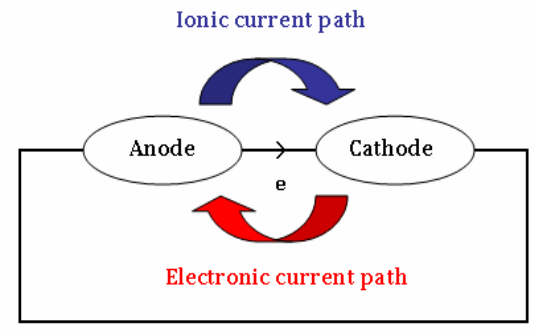

Figure 2.1 - Schematic diagram of corrosion cell

An electrochemical cell forms with the occurrence of metal corrosion, in which electrons, resulting from the anodic reaction, flow from the anode to the cathode in the metal, simultaneously ions in the electrolyte also flow to complete the corrosion circuit. The driving force for such current flow is a potential difference between the two sites and the current passing is known as the corrosion current. The rate at which a metal corrodes depends on the magnitude of the corrosion current therefore any corrosion protection method will aim to limit this corrosion current.

2.2 Organic Coatings for Corrosion Protection on Metal

An organic coating is an important component of a corrosion protection system. It is usually applied to a pre-treated clean metal surface in the liquid state by brushing, spraying or rolling [5, 6]. Organic coatings used for corrosion protection usually serve three functions [6].

Firstly, they serve as a physical barrier between the metal substrate and the corrosive environment. They reduce the permeability of water, oxygen and other aggressive species, which may promote corrosion [5]. Secondly, they can serve as reservoirs for corrosion inhibiting pigments. Coatings containing inhibiting pigments provide protection to the substrate after corrosion processes begin at defects or inhomogeneities [6, 7]. However, it is widely accepted that, in general, coatings act mostly through their interference with the ionic charge flow such that the overall corrosion rate is reduced.

2.2.1 Components of Organic Coating

Organic coatings usually consist of four basic constituents [8]; resin binders, pigments, additives and solvents.

Binders: They are responsible for film formation of an organic coating by forming a continuous polymeric phase that adheres to the metal substrate [5, 6, 9]. The binder usually acts as a physical barrier against aggressive species, thus coatings are usually classified according to the type of binder [10]. Typical binders are organic polymers e.g. epoxy, acrylic, polyurethane, polyester, alkyd and chlorinated rubber.

Pigments: They are used to strengthen the coating structure, but also serve other functions [5, 9]. Pigments are usually in the form of powder that is colloidally suspended and remain dispersed in the binder after film formation. They act as colouring agent, opacifier, anti-corrosion agent and extender. Extender pigments such as talc and mica are sometimes added to reduce permeability to aggressive species such as water and oxygen. Their flaky structure when orientated parallel to the substrate, forces aggressive species to take longer, complex diffusion paths before reaching the metal substrate [6, 11, 12]. They may also be added to reduce cost.

Additives: They are usually added in small quantities to modify some properties of coatings, for example drying time of the coating mixture, coating film hardness, coating mixture stability, pigment dispersion, sedimentation prevention and surface activation [13].

Solvents: They are volatile organic compounds (VOC) which are added to reduce coating viscosity for easy application on a metal substrate [5, 9]. They evaporate during the curing process of the coating. Problems arise with these organic solvents that have resulted in legislation aiming at reducing the VOC emissions. This has brought the attention to alternative environmentally friendly water-borne coatings which have low VOC content.

2.3 Protection Mechanisms of Organic Coatings

As mentioned before, all of the following are necessary for corrosion to occur on metal surface;

- A medium in which the ions can move, e.g. water
- A reduction process at the cathode
- A dissolution process at the anode
- An electrolytic path between the anode and cathode

Any of the above items could be the rate-controlling step. The elimination of any one of those four can reduce or slow down the corrosion process. This can be achieved by the application of an organic coating on the metal surface. Organic coatings can provide corrosion protection of metallic substrates through a variety of mechanisms as illustrated in **Figure 2.2** depending on the service environment [8, 14].

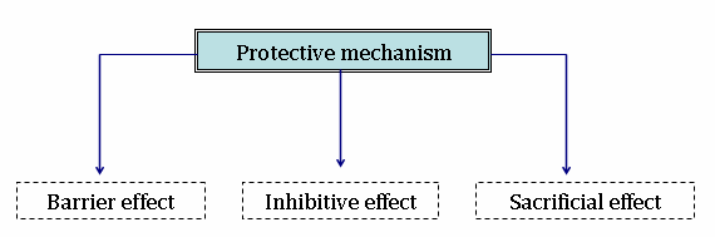

Figure 2.2 - Protective mechanisms of organic coatings

The main protection mechanisms by organic coatings are:

- Creating a **physical barrier** that keeps out charged ions and retards the penetration of water or oxygen
- Creating a path of extremely **high electrical resistance**, thus inhibiting anode-cathode reaction
- Serving as a reservoir for corrosion **inhibiting pigment**, thus passivating the metal surface
- Providing a **sacrificial anode** for the dissolution process

It is impossible to employ all these protective mechanisms in one coating. However, one or two particular protection mechanisms may dominate in an individual coating system. In addition, the effectiveness of each mechanism will depend upon its specific corrosion process and coating environment.

2.3.1 Physical Barrier Properties

Although organic coatings are said to offer protection to the metal by acting as a barrier to water, oxygen and ions, in actual practice these barrier properties are

limited because all organic coatings are permeable to water and oxygen to a significant extent [15]. There is a common agreement that water permeability is faster than that required for corrosion to occur on the bare metal [16-18]. Mayne [19] estimated that the permeation rate of water is about 100 times larger than the amount needed for the free corrosion of the steel substrate, thus concluded that water permeability is not the rate-limiting factor in the corrosion process. Haagen and Funke [20] did a comparison of water permeability for several coatings with the amount of water needed for corrosion of bare steel. They agreed with the previous work by Mayne [19] and concluded that more water can be supplied by permeation than is needed for the corrosion process to proceed. Therefore, water permeability cannot be the rate-limiting factor in the corrosion process. **Table 2.1** shows the permeability of 100µm thick free film to water vapour through several coatings.

Table 2.1 - Water vapour permeability of paint films at 23-25^{o}C

	Water vapour permeability for 100µm coating (mgcm^{-2}d^{-1})
Alkyd resin	2.3
Chlorinated rubber	1.0
Polyurethane	1.4
Polyester resin	1.3
Epoxy-coal tar	1.1
Phenolic resin	1.1
Nitrocellulose	4.8
Water necessary for corrosion of unpainted steel	0.003-0.06

Source: Haagen, H. and Funke, W., *J.O.C.C.A.,* 58, 10, 359, 1975

Despite that, the role of water permeation through the coating cannot be completely ignored. Haagen and Funke [20] have pointed out that although water permeability is not the rate-limiting factor in the corrosion process, it may be the rate-limiting factor in adhesion loss.

There is some disagreement whether oxygen permeation through organic coatings is controlling the rate of corrosion. Stratmann et al. [21] reported that oxygen permeability for a defect free coating is sufficient for the corrosion reaction to occur. Guruviah [22] studied corrosion of coated panels under various accelerated test methods and found that in the presence of salt, electrolytic resistance of the coating was the dominant factor in predicting performance. However, in the absence of salt, oxygen permeation was the rate-controlling factor for the same method and coating. For coated panels above a critical level of contamination, oxygen permeation is said to be the controlling factor in determining the corrosion rate [23].

In his previous work, Mayne argued that oxygen permeation is not the rate-controlling factor in the corrosion process. He measured corrosion rates beneath the paint and found that the corrosion rate is very much smaller than the rates of available oxygen at the metal surface [19]. This is supported by Haagen and Funke [20] who studied oxygen permeation rates for several types of coatings as illustrated in **Table 2.2**. In general, water and oxygen are necessary for the corrosion process; however, their permeation through the coating is not a rate-determining step [19, 20, 22, 24].

Table 2.2 - Oxygen permeability of paint films at 20°C

	Oxygen permeability for 100 μm coating ($mgcm^{-2}d^{-1}$)
Alkyd resin	0.0103
Chlorinated rubber	0.0022
Epoxy-polyamide	0.0073
VC-VA copolymer	0.0075
Nitrocellulose	0.106
Oxygen necessary for corrosion of unpainted steel	0.008 - 0.150

Source: Haagen, H. and Funke, W., *J.O.C.C.A.,* 58, 10, 359, 1975

There are different theories concerning ion penetration into the coating. Generally the permeation of ions is much slower than the permeation of water [17]. A study by Ruggeri and Beck [25] on ion diffusion through polyurethane paint showed that the permeability of polyurethane to sodium and chloride ions is low. They found that ionic conduction in polyurethane changes as the external electrolyte concentration changes. Kittleberger and Elm [26] measured ion transport rates using sodium chloride and found that the rate of ion diffusion was very much smaller than the diffusion rates for oxygen and water. They also observed a linear relationship between diffusion rate and the reciprocal of film resistance, suggesting that the transport of sodium chloride through the coating is as ions, rather than ion pairs or undissociated molecules.

So, it has been established in the literature that in most cases water and oxygen permeability through coatings is sufficient to facilitate corrosion on the metal surface [19, 20, 22, 24]. This suggests that physical barrier properties alone are not sufficient

for coatings to protect metals from corrosion. This is when resistance inhibition, which is also part of the barrier mechanism, may supply additional corrosion protection to the metal substrate.

2.3.2 Electrolytic Resistance/Resistance Inhibition/Ionic Resistance

One of the main corrosion protection mechanisms of organic coatings is due to their high electrical resistance that limits the current flow from the anode and cathode [27]. This mechanism is normally known as electrolytic resistance, resistance inhibition and ionic resistance. The terms 'electrolytic resistance' and 'ionic resistance' are frequently used because Kittleberger and Elm have shown a linear relationship between the diffusion of ions and the reciprocal of the film resistance [28]. However, Mayne frequently used the term 'resistance inhibition' when dealing with the protection mechanism on metal by organic coatings. **Figure 2.3**, is based upon the work of Mayne [19, 27, 29, 30].

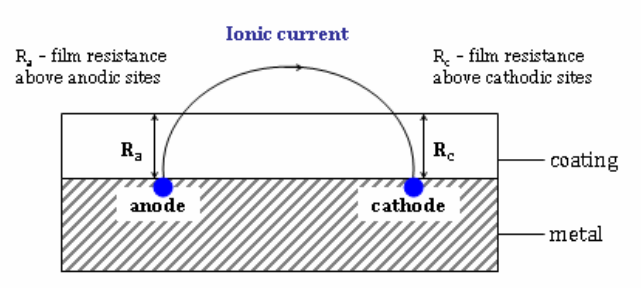

Figure 2.3 - Diagram illustrating Mayne's mechanism of 'resistance inhibition'

This diagram shows how a coating protects a metal from corrosion by having a high ionic resistance that limits the ionic current flow of ions between the anode and

cathode. Mayne found a good correlation between a high resistance coating and a greater protection for the metal from corrosion.

It was in the late 1940's, Bacon, Smith and Rugg [24] examined over 300 coating systems that were exposed to sodium chloride solution. They measured the DC resistance on steels to obtain a correlation between the coating performance and resistance. They suggested that coatings which maintain resistance values above 10^8 ohm.cm^2 are good, while those that fall below 10^6 ohm.cm^2 are poor and those in between as fair. They showed that high resistance values of the coated steel correlate with good outdoor performance.

Much work has been carried out largely on free films by Mayne and co-workers in the early years (1952-1965), and they deduced that the resistance of immersed coatings can change over time [19, 27, 31, 32] . Their work indicated that at least two processes control the ionic resistance of immersed coatings:

- A fast change, which is associated with water uptake (takes place within minutes of immersion)
- A slow change, which is associated with ion exchange (takes place after weeks or months)

Maitland and Mayne [31] found that the electrolytic resistance of an immersed coating depends on the concentration of the immersed solution. Their study on alkyd resin immersed in different electrolyte solution concentrations resulted in two different

findings. They observed for some samples that the resistance of the alkyd resin coating decreased with increasing solution concentration. This type of behaviour they called 'D' type. On the other hand, they also observed a different behaviour for the same coating where the resistance increased with increasing solution concentration. This type of behaviour they called 'I' type. Mayne [30] postulated that water activity[2] was responsible for controlling conduction in I-type films whereas ion activity was responsible for controlling conduction in D-type films.

The first (I-type) films refer to coating areas that have a high resistance (good coating areas) as there are presumed to be no continuous pathways through the coating. Water ingress or egress is controlled largely by the relative thermodynamic activities of water within the coating and the electrolyte. A study by Kinsella has shown that the resistance of I-type films depends on the water activity of the external solution and is controlled by the water concentration changes in the coating [33].

The second (D-type) films are considered as areas with reduced cross linking and with pathways that exist allowing equilibration with the electrolyte [33-37]. Mayne and Scantlebury performed micro hardness tests and found that D-type areas were significantly softer than I-type areas. They attributed this behaviour to inhomogeneities in cross-link density [38]. Later studies by Mayne and Mills showed that a low resistance of the coating correlates to the presence of corrosion underneath the coating [35]. As a result, the same coating can have certain areas with either I-type

[2] The term water activity describes the amount of water available for hydration of materials.

or D-type regions. Thus, in reality coatings are heterogeneous [39] and certain areas are more susceptible to degradation than others [35, 38].

Amongst the weakness of organic coatings is that they are easily mechanically damaged. This may accelerate the corrosion underneath the coating at or near the damaged area. Thus, barrier properties and resistance inhibition are no longer sufficient to give protection to the metal substrate. Inhibitive or sacrificial pigments are then often incorporated in the coating primer formulation to give protection at the defect.

2.3.3 Inhibitive Pigments

Chemical inhibition can be provided by inhibitive pigments in the primer coating. In the presence of water, inhibitive pigments release soluble species that migrate to the defects on the metal surface and suppress corrosion reactions. Alternatively a passive oxide layer may form on the metal surface that slows down the rate of iron dissolution and reduces the oxygen diffusion [40, 41]. Inhibitive pigments can be classified according to their actions towards the anodic and cathodic reactions. Anodic inhibitors are also known as passivating pigments e.g. chromates and phosphates form a protective oxide film on the metal surface. A mechanism of these inhibitive pigments involves blocking the diffusion of corrosive species to the metal surface and reduces the corrosion rate by increasing the anodic polarization [42]. Cathodic inhibitors decrease the rate of cathodic reaction for example by forming insoluble deposits on the metal surface that reduce oxygen diffusion to the metal [40, 41].

The most effective inhibitor is one that works well in a wide range of environments. Pigment solubility as well as pH is important factors in the corrosion inhibiting process. In addition, the amount of soluble inhibiting species should be in sufficient concentrations to inhibit the corrosion process [43]. Turgoose [44] suggested that three important factors should be taken into consideration when dealing with coatings containing inhibitive pigments. These include pigment solubility and end product composition, electrolyte immersion concentration and alkalinity or acidic conditions at the metal surface.

Among the different kinds of pigment, red lead and zinc chromate were historically the best for steel due to their excellent anti-corrosion resistance. However, both of them are highly toxic and not environmentally-friendly. Thus, ongoing research is still being carried out globally to find non-toxic and environmentally-friendly pigments which are as good as chromate pigments. At present, of the available non toxic and environmentally friendly pigments, zinc phosphate is the most frequently used anti-corrosive pigment for steel [45-47].

Protection Mechanism by Zinc Phosphate

Zinc ions are known as a cathodic corrosion inhibitor and can precipitate in the form of zinc hydroxide in the presence of hydroxyl ions. In the presence of chloride ions, the hydroxide forms a soluble complex compound. As an inhibitor, normally zinc is combined with other anions such as phosphates to provide more effective performance than individual components [48]. Regarding its mechanism of inhibition, Sinko [43]

suggested that phosphate helps to stabilize the protective oxides on metal substrates and provides protection via a "pore-plugging" mechanism. In this mechanism, he postulated the theory that the defective sites on the substrate are repaired or plugged by insoluble precipitates formed by the inhibiting ions.

Generally, zinc phosphate gives good protective performance in industrial environments due to its high solubility in acidic media [49]. The protection offered by zinc phosphate on steel is said to rely on the formation of an iron oxyhydroxides film that passivates the steel surface [50, 51]. The mechanism of protection would also involve polarization of the cathodic areas due to precipitation of basic insoluble salts on the steel surface [50, 52, 53].

Turgoose and co-workers [54] suggested that the inhibitive action of zinc is more effective if zinc is combined with anion mixtures; e.g. zinc phosphate, zinc chromate and zinc molybdate. They act as a cathodic inhibitor by forming precipitates on the steel surface of zinc compounds thus resisting oxygen diffusion which reduces the corrosion reaction on the metal surface.

Performance of Zinc Phosphate Coating Exposed to Accelerated Tests

Contradictory results were reported regarding the performance of zinc phosphate as an anticorrosion pigment when exposed to accelerated tests [46, 55]. Samples in an accelerated test show a very much lower corrosion protection than in field tests. Some

suggested that this is due to the low solubility and a coarse crystallinity of the zinc phosphate [56, 57]. Romagnoli and Vetere observed that the penetration rate of aggressive ions is increased in an accelerated test, but not the solubility of zinc phosphate. This resulted in unbalanced protection as more ions penetrate into the coating but the protective capacity of both the phosphate anion and the iron oxide layer on the metal substrate remained unchanged [58]. Some authors maintain that zinc phosphate increases barrier properties of organic coatings [56], while others disagreed [59]. More research is still needed to understand the inhibitive mechanism of zinc phosphate pigment, as its mechanism is not well understood.

2.3.4 Sacrificial Protection / Cathodic Protection

Cathodic protection by organic coatings offers a different method of corrosion protection to the metal. Rather than relying on the barrier properties of the coating, the coating employs metallic pigments such as zinc, which are more anodic than the metal substrate. When zinc is in contact with steel, it produces an anodic dissolution current at a more negative potential. The addition of zinc particles as sacrificial anodes to steel shifts the potential lower where steel is protected from being corroded. Thus corrosion is prevented by the preferential dissolution of the anodic zinc pigments, until metallic zinc becomes depleted [14].

Figure 2.4 illustrates the schematic diagram of cathodic protection by a sacrifical anode (zinc). Without the presence of zinc, the corrosion potential, E_{corr} and the corrosion current, i_{corr} are given by the intersection of the anodic and cathodic curves

i.e. where anodic and cathodic reactions rates are equal. If impressed cathodic current, i_1 is applied then the potential of the specimen is lowered to E_1, where the specimen is fully protected. When zinc is coupled with iron, the potential of the specimen is lowered to a more negative potential, E_{couple} whereby the anodic current, i_a is balanced with the cathodic current, i_c.

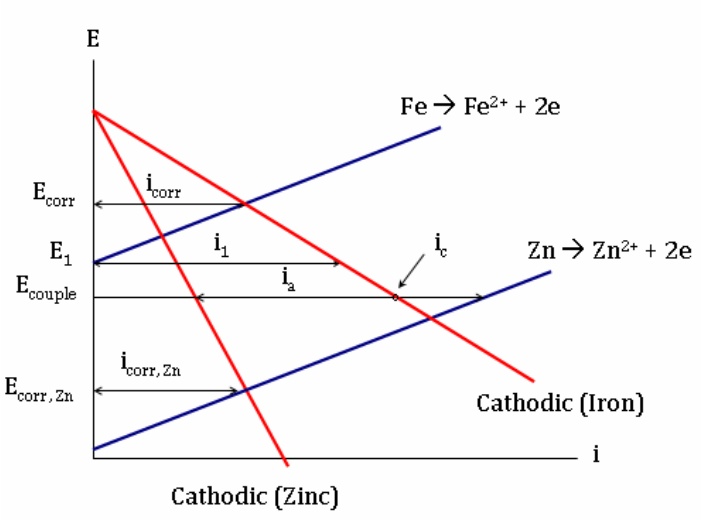

Figure 2.4 – Schematic diagram of cathodic protection by a sacrificial anode

Morcillo and co-workers have demonstrated that zinc rich paints are more anodic than steel and hence will protect the steel substrate from being corroded [60-62]. Generally, zinc rich paints provide both galvanic protection and a barrier effect [63, 64]. The first mechanism depends on having a high zinc content in the primer formulation [14].

Galvanic Stage (1st stage of protection) (active protection)

It is necessary that zinc particles have electrical contact with the steel substrate and each other for the sacrificial action to proceed. Once water is available between those contacts, zinc preferentially dissolves (zinc acts as a sacrificial anode) allowing cathodic protection of the steel substrate. The resistance to corrosion is dependent on the galvanic current transfer by the zinc particles but as long as there is sufficient zinc to act as the anode the steel is galvanically protected. The electrochemical process [65] corresponding to the oxidation of zinc particles;

$Zn \rightarrow Zn^{2+} + 2e$ (anodic process) (2.5)

and the reduction of the dissolved oxygen on the steel according to reaction;

$O_2 + 2H_2O + 4e \rightarrow 4OH^-$ (cathodic process) (2.6)

This stage normally occurs at the beginning of the coating's lifetime and gradually disappears with time [14]. Earlier work by Feliu et al. reported that this mechanism becomes inactive after a relatively short time and suggested that other mechanisms must be present for the coating to continue providing corrosion protection [66]. Ross and Wolstenholme [67] stated that the subsequent loss of cathodic protection has been associated with either a loss of the zinc-steel contact or with the zinc corrosion product build up on the zinc particle surfaces.

Barrier Stage (2nd stage of protection) (passive protection)

As zinc particles are actively corroding, less area for the electrical contact to the steel becomes available and this gradually decreases with time. Thus, after a certain time the potential of the steel exceeds the protection potential. According to Abreu et al., the cathodic protection effect disappears when the corrosion potential of the steel shifts to a more positive value than -0.85 V_{SCE} [68]. Several researchers have suggested other mechanisms are available to allow the coating to continue giving protection towards the steel substrate. Their investigation showed that zinc corrosion product is blocking the pores in the coating thus improving the barrier properties [69, 70]. However, Ross and Wolstenholme [67] suggested that protection may be also due to the deposition of inhibitive zinc compounds on steel rather than sealing of the pores by zinc corrosion product. Their study indicates that any reduction in active zinc pigment was not by restricting cathodic protection by polarization of the zinc but rather by reducing the production of inhibitive zinc compounds.

Figure 2.5 is a schematic diagram showing the protective mechanism of zinc rich paint on steel substrate upon immersion in salt solution. Initially an electrolyte penetrates through the conductive pathways or pores. As soon as it makes contact with zinc and steel, zinc starts to corrode and thus provide cathodic protection to steel (**Figure 2.5a**). Dissolution of zinc around the pores and corrosion products are building up as seen in **Figure 2.5b**. As the exposure time increases, the deposition of corrosion products at the base of the pores followed by pore plugging (**Figure 2.5c**) probably occurs. This suggests that the coating continues to give protection to the metal via a barrier effect.

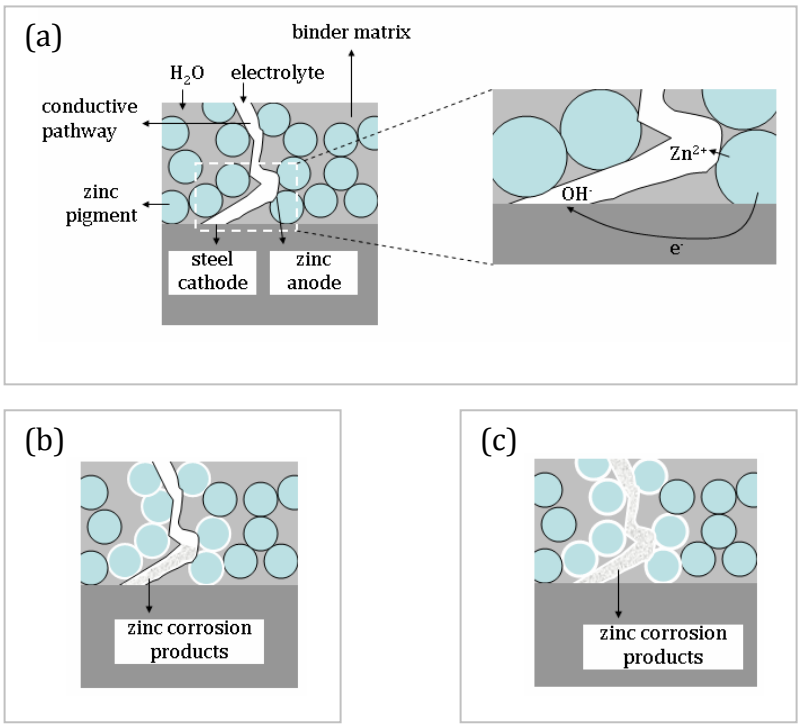

Figure 2.5 – Representation of sacrificial action of zinc rich paint coating upon immersion in salt solution [71]

Despite its widespread use in the marine and petrochemical industry, there is little information in the literature describing the corrosion mechanism of zinc rich paint when exposed at 50°C. The coating is reported to provide excellent cathodic protection to the steel when exposed at ambient temperature [60, 62]. Undrum [72] stated in his review paper regarding the limitation of zinc rich paint in contact with hot water that exposing the coating to high temperatures significantly decreases the galvanic activity.

2.4 Coating Degradation and Corrosion Mechanisms

This section presents a brief overview on the major mechanisms that cause failure of an intact organic coating. Among the most severe and common forms of visible failure in immersed organic coating systems are adhesion loss which leads to corrosion initiation and blistering.

2.4.1 Adhesion and Corrosion Initiation

The first sign of degradation of intact coatings that have been exposed to immersion in electrolyte is often reduced adhesion between the coating and the metal substrate. The mechanism responsible for the reduced adhesion has been proposed by Leidheiser and Funke [73] and is referred to as chemical-mechanical disbonding due to the presence of water at the coating/metal interface. They also defined the degree to which the adhesion properties of a coated system are retained after permeation of water as 'wet adhesion'. Funke [74] argues that reduced adhesion is a requisite but not sufficient to initiate corrosion process underneath the coating. Others have stated that reduced adhesion is only relevant to corrosion protection when the coating barrier's properties are compromised [75-78].

It is well known that corrosion initiation underneath an intact coating system involves two stages; (i) formation of conductive pathways and (ii) migration of corrosive species to the metal surface through pathways.

Formation of conductive pathways

The first stage of coating degradation can be defined by the formation of conductive pathways within the coating that allow the transport of water, oxygen and ions from the environment to the metal surface. Nguyen and Hubbard [79] assume that the formation of conductive pathways in an intact coating is due to water attack at the hydrophilic, weak regions of the coating followed by the interconnection of these regions.

Transport of corrosive species to the metal surface

Following the formation of conductive pathways, corrosive species such as water, salt and oxygen travel from the electrolyte environment and reach the metal surface. This will form the corrosion environment which leads to corrosion process at the coating/metal interface. As the corrosion reactions at the anodic area are progressing, the cathodic process is following as well at the periphery of the conductive pathways [79]. As both reactions continue, blisters form at separate anode sites and at cathode sites which can develop into cathodic delamination. One common mechanism for loss of coating adhesion on mild steel substrates is cathodic delamination which is due to the cathodic activity which generates alkali and is affected by the rate of cathodic reaction underneath the coating [80]. Reduction of adhesion due to water absorption at the coating/metal interface will be hindered by corrosion product formation suggesting that blisters will occur rather than delamination [73].

2.4.2 Blistering underneath Intact Coatings

Blistering is one of the first signs of the breakdown in the protective nature of the coating. The definition of blistering (**Figure 2.6**) is given as the failure of a coating by the development of large or small round spherical pimples on the metal surface [81]. This blister can be either dry or filled with liquid. Blisters arise when the coating loses adherence due to penetration of water through the film. The accumulation of water at the coating/metal interface in sufficient quantity will force the film up from the metal substrate. Under different circumstances, blister formation can follow different mechanisms [82].

Figure 2.6 - Blistering on coated panel

Osmotic Blistering

The osmotic mechanism is probably the most common mechanism by which blisters form. It was Mayne [83] who first reported in 1959 that when there is a presence of soluble salt concentration beneath the coating at a certain threshold value it was

common to observe premature coating deterioration in the form of fine blisters and an increase in the corrosion rate of the metallic substrate under the coating. Koehler [84] identified that contaminants such as soluble salts at the coating/metal interface to be destructive due to their ability to draw water through the coating by osmosis. This explanation was further established by Morcillo [85] and is illustrated in **Figure 2.7**. This figure shows that coating degradation induced by the presence of soluble salts at the coating/substrate interface depends upon osmotic water migration through the coatings that can lead to osmotic blistering and under-film corrosion of the coating.

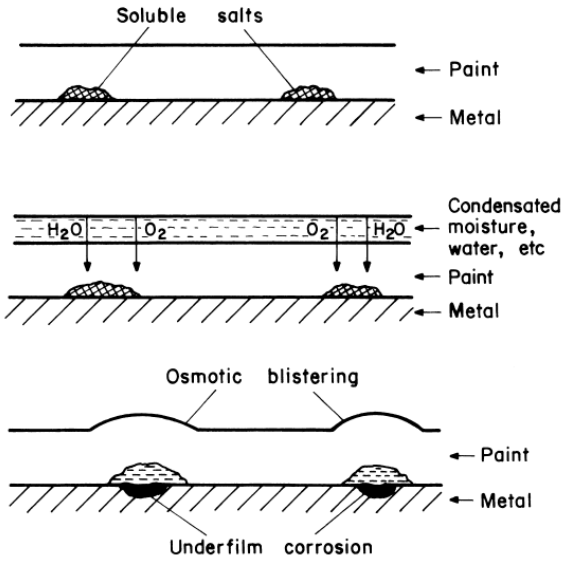

Figure 2.7 - Model for osmotic blistering formation [85]

Blisters due to Swelling

The mechanism of blistering by volume expansion of the coating states that water absorbed by the film causes swelling, which eventually leads to blister formation. This

mechanism seemed dubious to Funke [82] as he suggested that if swelling produced a large enough stress in the film to cause a blister, it is more likely that this stress would result in complete delamination of the film. Crossen [86], using scanning acoustic microscopy (SAM), observed that re-wetting coated steel occasionally led to immediate re-appearance of blisters that did not contain water and he attributed this finding to stresses from coating swelling.

Anodic/Neutral/Cathodic Blistering

Neutral blisters contain solution that is weakly acid to neutral and without alkali cation involvement. Anodic blisters require a low pH to proceed [80]. Reduction of adhesion due to water adsorption at the coating/metal interface suggests that differential aeration is responsible for neutral blistering [87]. **Figure 2.8** presents a model for the degradation of an intact coating on steel in a neutral electrolyte by Nguyen and Hubbard [79].

Following the formation of conductive pathways due to the attack of water in hydrophilic regions (1), ions migrate to the coating/metal interface through the conductive pathways (2). Anodes develop at the base of the pathways (3) and cathodes develop at the periphery of the pathways (4). Na^+ ions migrate along the coating/metal interface to the cathodic sites for charge neutralization (5) and form NaOH, whereby the alkalinity causes cathodic delamination (6). Water is drawn into the coating and corrosion products formation may plug the pores, after which blisters are formed.

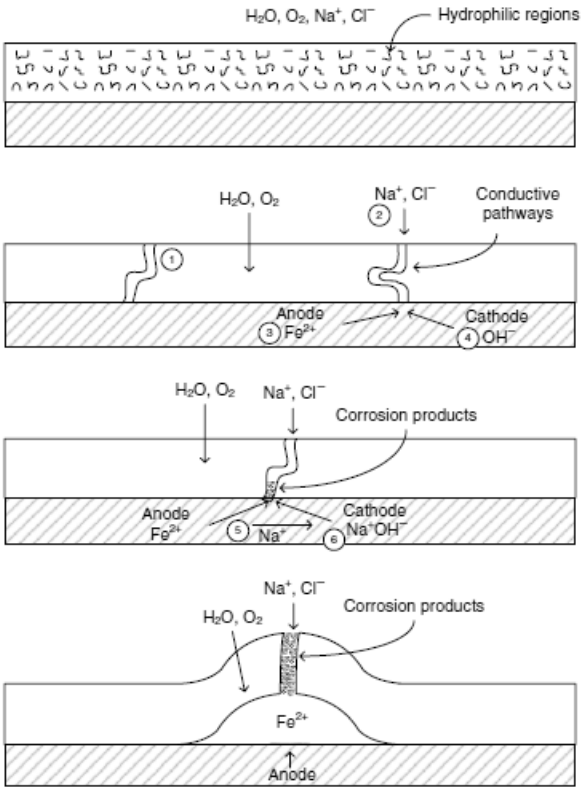

Figure 2.8- Model for the degradation of an intact coating on steel in a neutral electrolyte by Nguyen and Hubbard [79]

de Wit and co-workers [88] say that in the presence of pores or defects in a coating, corrosion cells can establish by differential aeration at the base of the defect and the surrounding area. The degradation will depend on the nature of the corrosion products. If the corrosion products are soluble or contain no species which can be further oxidised, the rate of oxygen transport via the defect or pores is much greater than the rate of oxygen through the coating (**Figure 2.9a**). In this case the base of the blister will be cathodic and local anodes will reside at the periphery. If the corrosion products can be further oxidised, as with steel, the pore can become 'plugged', oxygen transport is blocked and may result in cathodic delamination.

This can occur at the edge of the blister (**Figure 2.9b**) or in separate blisters near the defect (**Figure 2.9c**) [88].

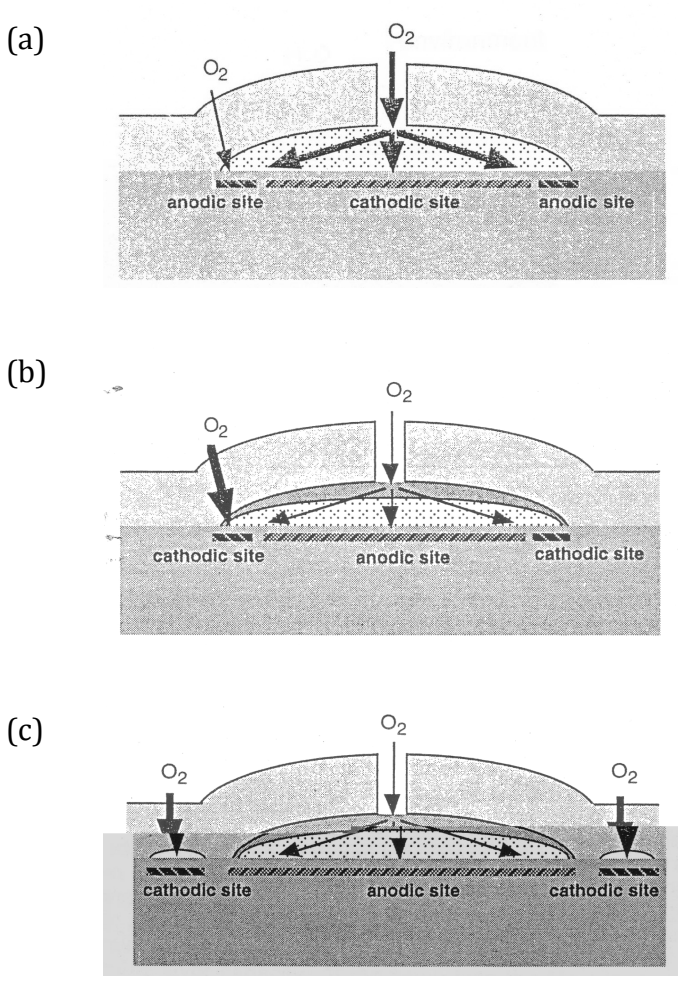

Figure 2.9 – (a) anodic undermining, (b) cathodic disbondment, (c) cathodic blistering a distance from the defect [88]

2.5 Performance Testing of Protective Coating

2.5.1 Outdoor Exposure

The performance of organic coatings have been evaluated using a variety of outdoor and laboratory tests for more than 100 years [89, 90]. The most reliable test to study the performance of a coating is to expose the coated panels to the real environment in which the coating will be used for [91]. The normal practice of this kind of test is by mounting the coated panels on exposure racks as in **Figure 2.10**.

Figure 2.10 - Typical setup for outdoor exposure of coated panels [71]

Although this test offers a good representation of the actual service life, the time taken in gathering the results is generally too long because they often require 10 to 20 years [92, 93]. Another drawback of actual outdoor exposure is the variability of the natural environment where no location or time period is the same. This greatly affects the way a coating degrades.

2.5.2 Accelerated Exposure Test

The aim of accelerated testing is to duplicate the test in the laboratory, as closely as possible to the test conducted at its natural environment but the result is drawn in a much shorter time. Many researchers have attempted to speed up the coating degradation by increasing the physical and chemical stresses. These include UV radiation, water and moisture, temperature and exposure to salt solution. The first stress is solely for organic coatings whereas the latter three are major causes of corrosion of bare metals [14]. Ideally this form of accelerated test only causes the coated panel to fail faster than it normally would in its natural environment and does not introduce different degradation mechanisms from those that occur at ambient temperatures [91, 94, 95].

Generally the salt solution used for exposure tests is NaCl solution. However, in the 1960's, Harrison and Tickle [96] argued that ammonium sulphate with a small amount of sodium chloride solution gives a better prediction of outdoor performance over sodium chloride solution. Thus Harrison's solution (3.25% ammonium sulphate, 0.25% sodium chloride in distilled water) [97] is said to be best for typical industry while sodium chloride solution is mainly for marine applications. Timmins [98] employed a diluted solution based on Harrison's formula (0.4% $(NH_4)_2SO_4$ + 0.05% NaCl) in a Prohesion test that provided improved prediction over the salt spray test.

2.6 Thermal Property of Coating

Temperature changes impose a direct impact on the corrosive protective performance of coatings; especially in an environment where the value of temperature keeps changing. For example, a natural gas pipeline network often has continuous changes in temperature, with a possible range as high as 135^{o}C in the vicinity of a natural gas well to an ambient temperature at a pumping station.

The glass transition temperature, T_g is a very important parameter for organic coating films whereby at temperatures higher than T_g, the polymer chain will have sufficient energy to overcome attractive forces to move vibrationally, so that it become soft and flexible. At temperatures lower than T_g, the polymer becomes harder and brittle due to the great reduction in its flexibility. The expansion rate of the polymer is also increased with increasing temperature due to the enhanced segmental chain motion movement.

2.6.1 Arrhenius Equation

In 1889, Arrhenius noted that the reaction rate versus temperature data for many reactions fitted the equation below;

$$K = Ae^{\frac{-E_A}{RT}} \qquad (2.7)$$

where A and E_A are constants characteristic of the reaction. A is the pre-exponential factor (linked to the collision factor), E_A is the Arrhenius activation energy in Jmol^{-1}, R

is the universal gas constant (8.314 $Jmol^{-1}K^{-1}$) and T is the absolute temperature in Kelvin. The Arrhenius equation can be explained by the molecular collision theory, which relates to the fraction of collisions that results in a reaction event. For example two colliding gas molecules require a certain minimum kinetic energy to initiate the breaking of the appropriate bonds and to allow the formation of a new compound. The required minimum energy is known as the activation energy and may be supplied by collisions in bimolecular reactions. As the temperature increases, more molecules will possess the required activation energy and the reaction rate will increase, by a factor of $e^{-\frac{E_A}{RT}}$ as shown by the Maxwell distribution law [99]. Taking the logarithm of equation (2.7), gives

$$\ln K = \ln A - \frac{E_A}{RT} \qquad (2.8)$$

or

$$\log_{10} K = \log_{10} A - \frac{E_A}{2.3RT} \qquad (2.9)$$

If conduction in the paint film is an activated process, the conductance, κ should obey the Arrhenius equation;

$$\log_{10} \kappa = \log_{10} \kappa_o - \frac{E_A}{2.3RT} \qquad (2.10)$$

The conductance, κ = 1/R, thus

$$\log_{10} \kappa = -\log_{10} R \qquad (2.11)$$

$$\log_{10} R = \log_{10} \frac{1}{\kappa_o} + \frac{E_A}{2.3RT} \qquad (2.12)$$

If the Arrhenius equation is obeyed, a plot of $\log_{10}$ R versus 1/T would generate a straight line with a positive slope of $E_A/2.3R$. Activation energy, E_A, can be found by multiplying the slope with 2.3R where R is the gas constant (8.314 $Jmol^{-1}K^{-1}$).

2.6.2 Thermal Effects on Corrosion Protection of Organic Coating

Thermal effects on coating properties as well as the reaction involved at the coating/metal interface must be taken into account when considering the performance of the organic coating. Bierwagen et al. investigated the acceleration of coating failure by high temperature and suggested that an increase in temperature increases the rate of diffusion of the electrolyte into the coating. This reduced the barrier properties of the coating and enhanced the chemical and physical ageing effect from attack by the electrolyte [94]. Recent work by Rezaei et al. on polyurethane coatings exposed at two different temperatures showed that the higher temperature without the presence of ions has a considerable impact on the reduction of coating performance. The impact on coating resistance is more severe, as their test results show that the presence of ions reduces the service life of the coating and higher temperature accelerates the degradation process [100].

It has been reported by Oliveira and Ferreira that high temperature testing only affects the transport phenomena of active species through the paint coating and does not introduce forms and mechanisms of degradation different from those that occur at

room temperature [101]. Li et al. [102] have shown that the barrier properties of the organic coatings are remarkably affected by high temperatures or thermal cycling. Coatings become more permeable and less protective which facilitates the transportation of the permeating species through the coating films. In return this initiates corrosion at the coating/metal interface.

Previous work on the relationships between activation energy, polymer thermal transition and corrosion process is reviewed in the following paragraph. Li et al. [103] proposed that penetration of the chemical species into the polymers at temperatures around the polymer T_g could be characterized by the activation energy. The possibility of the measurement of activation energy to provide information about the electrochemical parameters under various physicochemical conditions in corrosion mechanism research has been suggested by Santarini [104]. However no further explanation was given on any possible effect of thermal transition on a corroding system.

Cappadonia and co-workers [105] measured the conductance of a polymer membrane (Nafion 117) using EIS to determine its activation energy. Two activation energies were observed; 51.1–64.6kJmol^{-1} below and 10.6–34.7kJmol^{-1} above the transition temperature. They suggested that the transition of the polymer's electrochemical properties might be explained in terms of the changes in activation energy due to the influence of various water contents in the membrane above and below T_g.

Mayne and Mills [106] were the first to observe the effects of film thermal transitions in electrical measurements. They observed sharp changes in paint film activation energies with increasing temperature while examining the DC resistance of paint films exposed to KCl solutions of various ionic strengths. They attributed these changes to the structural transitions in the paint film. They conducted more extensive work [107] to study the influence of the transition temperature on coating resistance and water uptake when structural changes occur in the paint films. A similar conclusion was made as before, where the abrupt changes in DC resistance take place at the transition temperatures. However this time they noted that the sharp changes in DC resistance at thermal transitions were significantly noticeable only in I-type films for which conductance varied inversely with that of the electrolyte in which they were immersed.

Bierwagen et al. [102] studied the effect of temperature on fusion-bonded epoxy coating and found that the coating performance depends on whether the temperature is above or below the coating T_g. Coating failure was distinctly accelerated when the coatings were exposed above T_g versus exposure below T_g, and the authors warned that one should not use data from above the coating T_g to predict a lower-temperature performance of that coating. So higher temperatures are expected to speed up failure, but care is needed to avoid crossing a transition that fundamentally affects behaviour.

2.7 Overview of the Literature

Based upon this literature review, the following summary can be drawn. The protection mechanisms of organic coatings are highly complex because they depend

upon simultaneous action of different factors. Some researchers suggest that the importance of barrier coating properties are the permeability to oxygen, water and maintaining a strong adhesion to the metal substrate when exposed to water [20, 73] while others believe that the protection offered by organic coatings is due to its high electrical resistance above the interface thus preventing the external flow between anodic and cathodic areas underneath the coating [19, 24, 108]. As a result, the question of the exact mechanism that is responsible to protect the metal surface from corrosion or the relative contributions of different mechanisms remains open.

Accelerated testing in the form of high temperature exposure are chosen for this study as strong evidence from the literature indicate that high temperature stress does not introduce different degradation mechanisms from those that occur at ambient temperature [91, 94, 95]. It has been suggested that this form of accelerated test only affects the transport phenomena of active species through the paint coating [101].

CHAPTER 3

MATERIALS AND EXPERIMENTAL TECHNIQUES

3.1 Introduction

The major aim of this study is to investigate the protective mechanisms of an organic coating on steel when exposed to a more aggressive environment. Corrosion in nature is an electrochemical process, so it is logical to use electrochemical techniques to measure corrosion that occurs at the coating/metal interface. In general, the performance testing of a coated metal is carried out by an exposure method, where the samples are exposed to a corrosive environment. In this work, the corrosive environment will be a salt solution (usually NaCl, but also KCl, LiCl and NH_4Cl). Unless described otherwise, the coated panels were exposed in 3% NaCl solution (by weight). The coated panels were typically exposed at a surrounding temperature maintained at 50^oC. Coating durability is then assessed by periodic inspection and AC impedance. This technique is able to provide results on the corrosion protection capability within hours, days, and weeks instead of months and years compared to exposure studies under real atmospheric conditions. It also reflects the faster failure expected in marine environments. In this chapter, the main techniques, electrochemical impedance spectroscopy (EIS) and scanning Kelvin probe (SKP), along with the coating property measurement will be discussed in detail.

3.2 Coating Details

Six different kinds of epoxy coating were tested and their brief descriptions are presented in **Table 3.1**. All coatings were applied on the grit-blasted mild steel by airless spray. The Q coated panels come as a finished product from the supplier, International Paint Ltd. with dimensions of 150mm x 75mm and all the edges were painted with high solid modified epoxy barrier coating that can withstand high temperature.

Table 3.1 – Coating system information

System	Thickness	Layer	Coating details
PCE	75µm	1-layer	Polyamide cured epoxy (PCE)
2-CE	75µm	1-layer	2 component epoxy (2-CE)
1L-EP	150µm	1-layer	Epoxy phenolic (1L-EP)
2L-EP	250µm	2-layer	Epoxy phenolic (2L-EP)
ZR-FS[1]	290µm	3-layer	Zinc rich epoxy primer + middle[2] + top coat[3] (ZR-FS)
ZP-FS[1]	290µm	3-layer	Zinc phosphate epoxy primer + middle[2] + top coat[3] (ZR-FS)

[1]Full system
[2]A low VOC, high solids, high build, two-component epoxy coating, pigmented with micaceous iron oxide
[3]A two-component acrylic polyurethane finish

3.3 Electrochemical Impedance Spectroscopy

Electrochemical Impedance Spectroscopy (EIS) is a well-established method for determining information regarding the performance of the protective properties of an organic coating on metals and their changes during exposure to corrosive environment [37, 109, 110]. A survey done by Murray showed that publications dealing with EIS for

the testing of coatings are the largest portion of the coating literature [111]. In his subsequent paper, Murray has proven that EIS is particularly useful in the study of protective coatings, providing a minimally destructive technique to obtain specific information about coating and corrosion properties [112].

3.3.1 Principles

In this technique, impedance is determined by applying an alternating potential of widely varying frequency and the corresponding current response is recorded [6]. The alternating voltage applied can be represented by the following equation:

$$V(t) = V_o \sin\omega t \qquad (3.1)$$

and the current response to this alternating voltage will be at a phase difference of ϕ with respect to the applied potential that depends upon frequency:

$$I(t) = I_o \sin\left(\omega t + \phi\right) \qquad (3.2)$$

According to Ohm's law, the ratio between the potential, V(t) and current, I(t) is called the impedance, Z (ω), at the chosen angular frequency, ω.

$$Z(\omega) = \frac{V(t)}{I(t)} = \frac{V_o \sin(\omega)}{I_o \sin\left(\omega t + \phi\right)} = Z'(\omega) + jZ''(\omega) \qquad (3.3)$$

The angle, ϕ accounts for the shift of the peak current value with respect to that of the potential. As shown in equation (3.3), the impedance is given in terms of real, Z'(ω)

and imaginary, jZ''(ω) components. A spectrum can be obtained by varying the frequency of the applied signal.

3.3.2 Equipment Setup

The electrochemical measurements were taken with an ACM instruments Gill AC potentiostat operating with a high-impedance paint buffer system. Tests were carried out at the free corrosion potential with 20mV amplitude peak-to-peak excitation waveforms, an amplitude that gives only minimal perturbation to the electrochemical test system. The frequency range used is from 0.1 to 30 kHz. These settings usually took about 5 to 6 minutes for completion which is deemed reasonable for the system not to change significantly during the test. It was noted that the smaller the lower frequency range used (up to 0.001 Hz), the more information would be recorded. However the time taken to record the data points is longer which can lead to changes of the electrochemical processes of the electrode.

The equipment setup is shown in **Figure 3.1** and ACM analysis software 4.4 was used to analyze the data generated by this equipment. **Figure 3.2** represents the test cell used in taking the electrochemical measurements on protective coatings on a metal substrate. The coated panel was immersed in a beaker filled with the salt solution. To complete the electrochemical cell, a platinum mesh parallel to the coating surface is used as the counter electrode (CE); the metal substrate is used as the working electrode (WE) and a saturated calomel electrode, SCE as the reference electrode (RE).

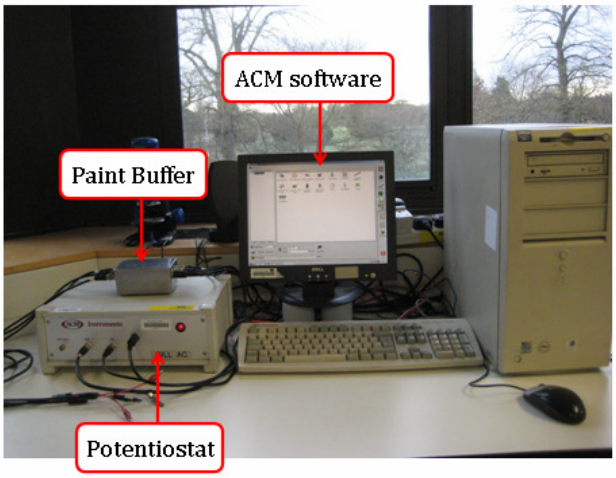

Figure 3.1 - Electrochemical equipment setup

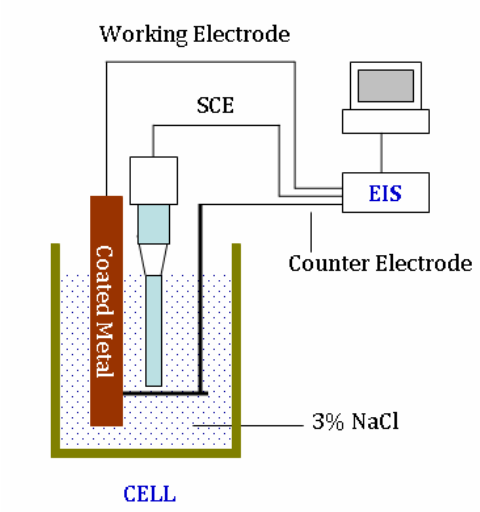

Figure 3.2 - Electrochemical cell

3.3.3 Impedance Spectra of Protective Coatings

The impedance of a coating system may be described graphically by means of two common types of diagram, Nyquist plots (Z'(ω) versus Z''(ω)) or Bode plots (log |Z| and phase angle, ϕ versus log frequency, f) an example for each is shown in **Figure 3.3**. In **Figure 3.3b**, the impedance modulus, |Z| drops as the frequency rises, and thus low frequency data is on the left side of the plot while higher frequencies on the right. The impedance spectra can be analyzed by fitting it to the response of an equivalent circuit composed of resistors and capacitors, thereby determining various characteristic properties of the coating.

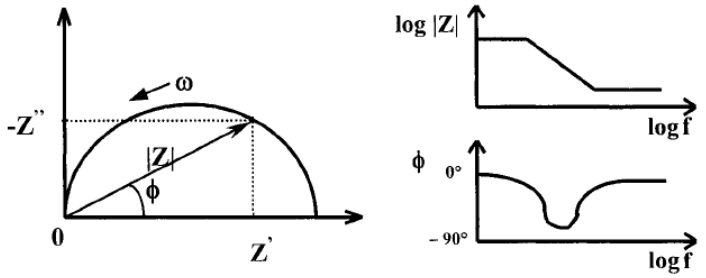

(a) (b)

Figure 3.3 - Nyquist plot (a) and Bode plot (b)

Figures 3.4 to **3.6** show schematic electrochemical characteristics of a coated metal under immersed conditions comprising an intact film, a permeable film and a permeable film with the corrosion process occurring at the interface [37, 113]. The equivalent circuit in **Figure 3.4c** corresponds to a defect-free coated metal, which consists of an electrolyte resistance, R_e, and coating capacitance, C_c. As immersion time increases, the coating becomes permeable to the electrolyte and the circuit becomes

more complicated (**Figure 3.5c**) with the addition of a coating resistance, R_p. **Figure 3.6c** displays the equivalent circuit of a permeable film with the presence of the corrosion process at the interface, which can be represented by the double layer capacitance, C_{dl} and charge transfer resistance, R_{ct}.

The impedance spectra change considerably over the lifetime of a coated metal being tested. Initially, the coated metal behaves like a capacitor and is shown as an almost straight line in the Nyquist plot (**Figure 3.4b**). After longer immersion, when the electrolyte starts to penetrate into the coating, the arc becomes a semicircle (**Figure 3.5b**).

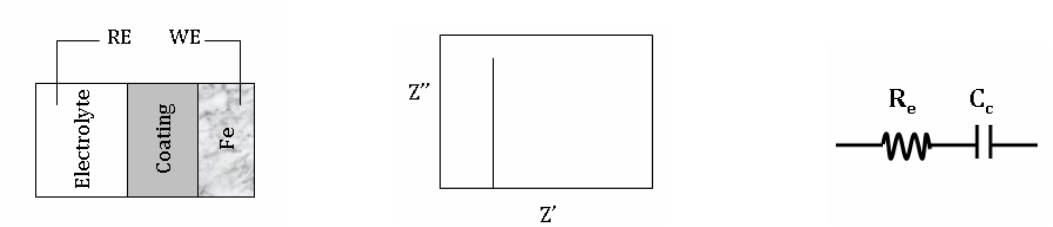

(a) system tested (b) Nyquist plot (c) equivalent circuit

Figure 3.4-Schematic electrochemical characteristics of defect-free coating [113]

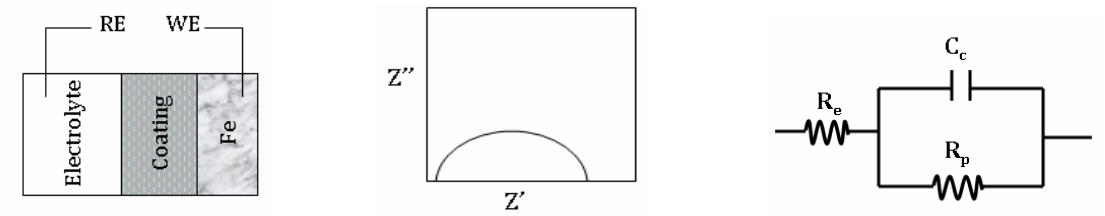

(a) system tested (b) Nyquist plot (c) equivalent circuit

Figure 3.5-Schematic electrochemical characteristics of a permeable coating [113]

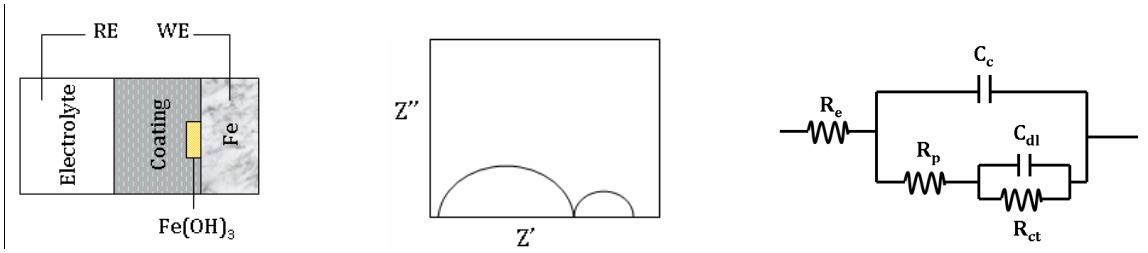

(a) system tested (b) Nyquist plot (c) equivalent circuit

Figure 3.6-Schematic electrochemical characteristics of coating systems with corrosion processes at the interface [113]

The diameter of the semicircle generally becomes smaller with increasing time, which corresponds to a decrease in the impedance modulus at the lowest frequency of the Bode plot (**Figure 3.7**). This signifies a decrease in the coating resistance. Due to continuing degradation, a second semicircle will appear in the Nyquist plot (**Figure 3.6b**). This may indicate a separation between the coating film and the metal substrate, which provides information concerning the corrosion reaction at the interface.

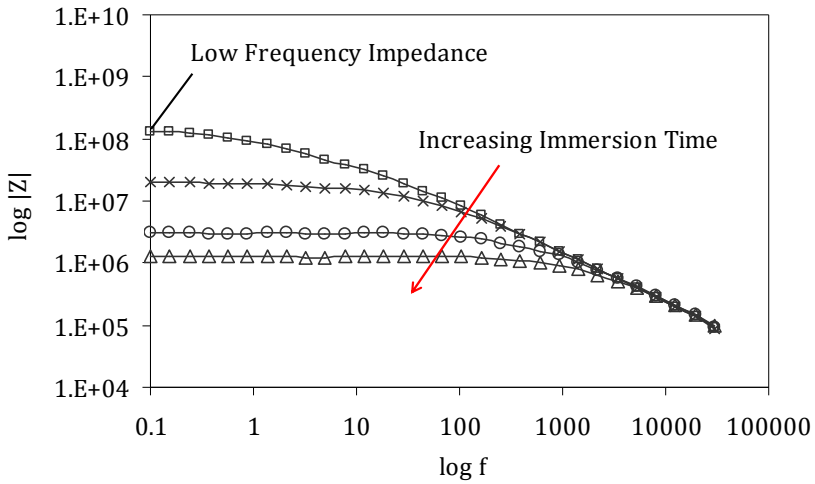

Figure 3.7 - Impedance modulus versus frequency for coated metal

Generally, the impedance of a coating decreases with time depending upon the corrosiveness of the environment and the coating formulation. Gradually the impedance will drop to the point where coating permeability to ions is very high and corrosion protection is lost. The low frequency impedance modulus has been considered as almost equivalent to the DC coating resistance in the stages of exposure of a coating system prior to any significant damage [95].

3.3.4 Equivalent Circuit for Coated Metal

Several equivalent circuits consisting of electrical elements i.e. resistors and capacitors have been used throughout this study to characterise the coating properties according to its real electrochemical properties. These elements are normally arranged in **Figure 3.8** to represent the electrochemical properties of a coated panel. In **Figure 3.8a,** it is assumed that the coating behaves homogeneously where coating and the interface can each be represented by a single resistor and capacitor in parallel. Meanwhile in **Figure 3.8b** the behaviour of the coating is assumed to be dominated by a local defect and **Figure 3.8c** shows the coating system with the presence of a Warburg diffusion impedance linked to the corrosion reaction. In **Figure 3.8b** and **3.8c** C_{dl} and R_{ct} represent the double layer capacitance and charge transfer resistance at a site (or sites) of corrosion activity.

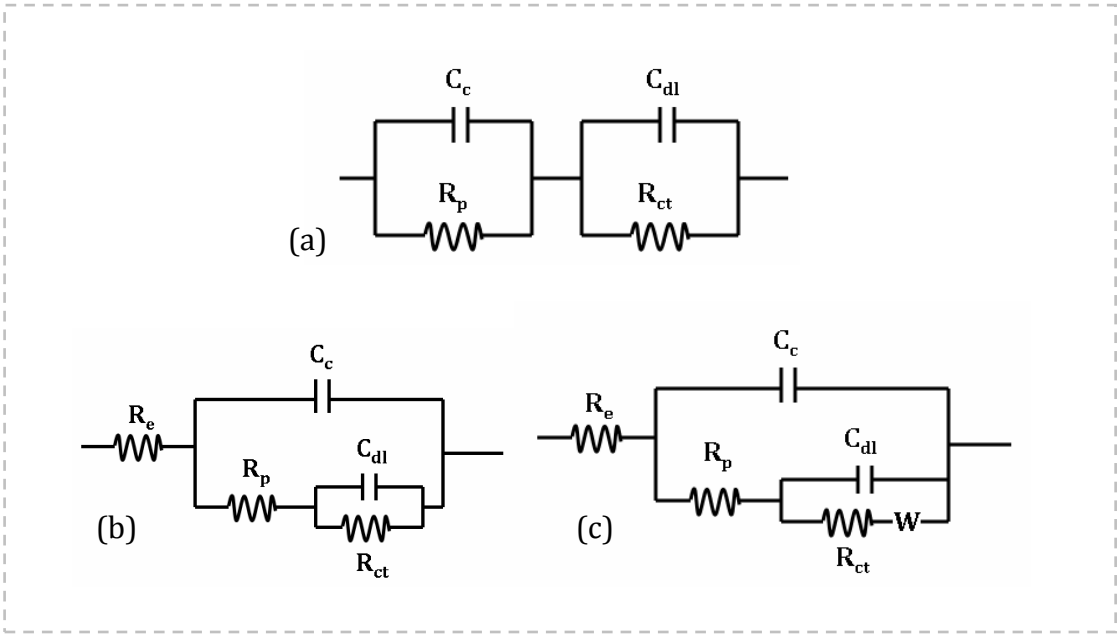

Figure 3.8 – Equivalent circuit used for a coated metal [37]

In some cases the model circuit in **Figure 3.8b** is a more realistic representation of a coated metal, where the coating resistance is considered to be short circuited by the lower resistance, R_p e.g. pore. The combination of R_{ct} and C_{dl} represents the behaviour at the base of the pore. At the early stages of exposure, only local areas of the surface are active when the pore model seems most appropriate. However, after long exposure it is possible that the active surface area becomes larger and corrosion activity is present across the metal surface. Under these circumstances, the two time constant series (**Figure 3.8a**) is considered more suitable.

The values for the equivalent circuit elements can be obtained by fitting the EIS impedance spectra using non-linear least-squares fitting software (ZSimpWin). The respective electrical symbols in the circuit are discussed in detail in the following section.

3.3.5 Physical Meaning of Equivalent Circuit

Equivalent circuits are usually used to represent specific physical phenomena where the user is able to investigate the electrochemical properties of each element and find out what is happening to the coated metal. In this section, it is of interest to discuss the significance of the elements of the equivalent circuit as illustrated in **Figure 3.9** from the point of view of the behaviour of a failed protective coating.

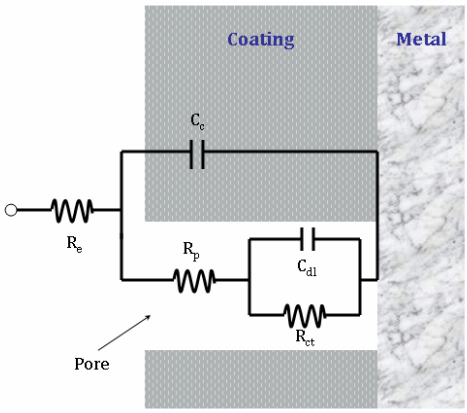

R_e = electrolyte resistance

R_p = coating resistance

C_c = coating capacitance

R_{ct} = charge transfer resistance

C_{dl} = double layer capacitance

Figure 3.9 - Equivalent circuit and schematic plan of a failed coating

R_e: R_e is the *electrolyte resistance* between the coating and the reference electrode, however its value is usually very small (1-50 ohm) and hence is negligible.

C_c: The value of *coating capacitance* generally depends on the amount of water absorbed by the coating. A significant increase in C_c value indicates higher water absorption into the coating and the coating capacitance is given by:

$$C_c = \frac{\varepsilon \varepsilon_o A}{d} \qquad (3.4)$$

where ε_o is the permittivity of free space (8.845 x 10^{-14} F/cm)

ε is the relative permittivity of the polymer

d is the coating thickness

A is the exposed area of the electrode.

The relative permittivity (dielectric constant) of an organic coating is usually much less than 10 (roughly 3 to 8) whereas for water is approximately 80 when measured at

20°C [114]. As the relative permittivity of coatings are lower compared to that water water uptake by coatings results in a significant increase of the C_c. The increase in C_c during immersion in electrolyte is associated with the increase of dielectric constant of the coating due to the absorption of water into the coating [110]. The amount of water uptake in the coating can be extracted from the coating capacitance according to the Brasher-Kingsbury [115] empirical formula:

$$X_v = \frac{\log {}^{C_t}\!/_{C_o}}{\log \varepsilon_t} \qquad (3.5)$$

where X_v is the volume fraction of water in a coating film; C_t and C_o are coating capacitances measured at the beginning and at time t of the experiment, respectively, and ε_t is the dielectric constant of absorbed water at time t. Indeed, many researchers have used coating capacitance data for the calculation of water uptake by the coating [116-119].

R_p: *Coating resistance* is directly related to the barrier effect of the coating. The R_p value changes over time due to electrolyte penetration through microscopic pores of the coating. Thus, the magnitude of R_p can be used as an indicative level of protection given by the coating to the substrate. The commonly quoted threshold values for R_p are displayed in **Figure 3.10**.

Figure 3.10 - Correlation between coating resistance and level of protection [24, 30]

C_{dl} and **R_{ct}**: The values of the *double layer capacitance* and *charge transfer resistance* have often been associated with the exposed area at the coating/metal interface. Walter stated that C_{dl} is proportional to the area over which the coating has disbonded [120]. However, Amiruddin and Thierry mentioned that C_{dl} is more a measure of the electroactive area than the delaminated area. This implies that C_{dl} also depends on the electrochemical state of the surface (i.e. active or passive) [34]. The accumulation of corrosion products at the interface reduces the area of the double layer capacitor, which will lead to a decrease in the C_{dl} value. In theory, R_{ct} is inversely proportional to the corrosion rate at the coating/metal interface, thus is used in monitoring the protective properties of the applied coating.

R_{ct} is related to the rate of the anodic and cathodic reactions, allowing the calculation of corrosion rates using the Stern-Geary equation [121];

$$i_{corr} = -\frac{b_a b_c}{2.303 R_p \left(b_a + b_c\right)} \tag{3.6}$$

$$i_{corr} = -\frac{\mathrm{B}}{R_p} = B\frac{\Delta I}{\Delta V} \tag{3.7}$$

where i_{corr} is the corrosion current, b_a the anodic Tafel slope, b_c the cathodic Tafel slope and B is Stern-Geary constant. I/V for an electrode is non-linear, so R_p is small perturbations, i.e. 5-20mV. R_p here represents the polarisation resistance, which we can usually regard as identical with R_{ct}.

In many cases, constant phase elements (CPE) are used instead of capacitors for the selected equivalent circuit used in the fitting software. This is due to the depressed semicircles often seen in practice and CPE facilitates good data fitting for a non-ideal behaviour of the coating system [122]. CPE can be expressed as:

$$Z = \left(\frac{1}{j\omega C} \right)^{n} \qquad (3.8)$$

The value of n is from 0 to 1. An ideal capacitor can be described by a CPE with n =1 while n = 0.5 describes a Warburg which corresponds to a semi-infinite linear diffusion. CPE is denoted as 'Q' throughout the thesis.

Several explanations have been proposed for using CPE instead of capacitors [34, 123] but no general consensus has been reached and is still a matter of discussion in the literature. However, different physical interpretations regarding CPE are available [71].

3.3.6 Determination of Coating Performance by EIS

One of the major applications of EIS in coating study is the evaluation of the barrier properties of organic coatings on metal. Apart from that, it has also been used to obtain mechanistic information related to the corrosion process taking place at the coating/metal interface [8, 110, 116, 124-127]. As the coating degrades, the real part of the high frequency impedance decreases as a result of the formation of conductive pathways due to the penetration of corrosive species as well as water uptake into the

coating [18, 37, 128]. In addition, Walter and Deflorian et al. showed that the capacitance changes as the coating degrades [1, 117, 129].

3.4 Open Circuit Potential Monitoring

3.4.1 Principles

Open Circuit Potential (OCP), also known as the corrosion potential, is the potential of a working electrode when no external current is applied to the circuit. Monitoring the OCP values over a period can provide important information about the system under investigation. For example, the OCP value stays constant when the system has reached a steady state. The principle of OCP is that a shift towards more negative potentials shows a sign of active corrosion development, whereas potentials that are more positive indicate formation of a film, or passivation [130]. Nevertheless, care is needed in such interpretation, as potential will also fall if the cathodic process becomes inhibited.

3.4.2 Open Circuit Potential Measurement for Organic Coating

OCP measurement has been used by several researchers to confirm their results obtained by EIS to evaluate the corrosion protection performance [57, 131]. However, Mayne [132] has suggested that the potential for uncoated steel immersed in sea water is a compromise potential.

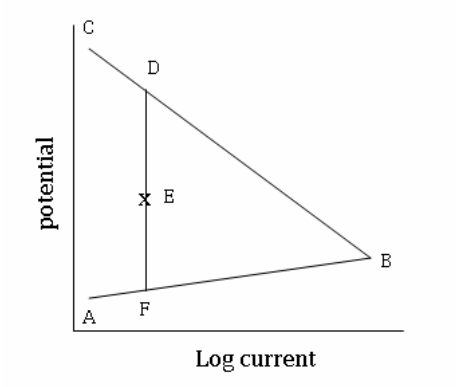

Figure 3.11 – Schematic Evans diagrams for a coated metal [132]

He explained further using the graphical method of representation developed by Evans (**Figure 3.11**), where the potential is given by the point B where CB and AB represent the cathodic and anodic polarization curves. On a coated panel, current must pass between anode and cathode thus; coating imposes a high electrolytic resistance at both anodic and cathodic areas. If the total resistance is R and *i* is the current represented by the abscissa of F, the intercept DF represent *i*R, and the lengths EF and ED should be in the ratio of the resistances of the anodic and cathodic pathways. If the resistance at the anodic and cathodic areas happen to be equal, the compromise potential will be given by the point E, which lies halfway between D and F. In general, in the early stages of immersion, it appears that resistance is lower above cathode so that point E will lie nearer to D than F (OCP value is more positive) [133].

Deyá and co-workers showed that the OCP of alkyd coatings changed toward less negative values when the coatings have high ionic resistance [134]. However, the OCP became more negative as sites that were more anodic developed over time. Marchebois et al. measured the OCP values of zinc rich epoxy coatings and concluded that as the

potential became more positive over time the protection mechanism changed from sacrificial to barrier inhibition during immersion [135]. In this study, OCP is used to monitor zinc-rich primer coatings.

3.5 Potentiostatic Pulse Technique (PPT)

In the potentiostatic pulse technique (PPT), potentials are applied in a series of steps (anodic or cathodic step) on top of the free corrosion potential. Correction of the potential is necessary to compensate for ohmic potential drop due to the presence of the coating film. PPT can be used to measure responses of current under a transient state, but in this work it is used to determine the steady current after a fixed time of polarization (**Figure 3.12**) and to minimize interference from charging of the coating capacitance. The resulted currents at different potentials were then used to plot polarization curves.

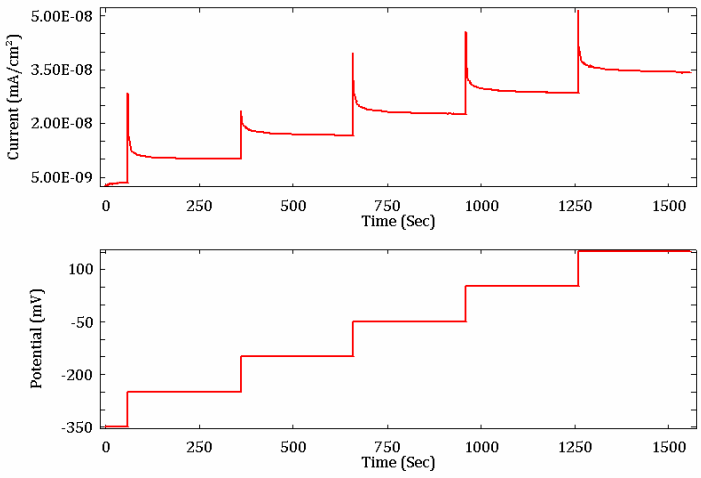

Figure 3.12 - Results of current transient (top) compared to potential pulse measurement (bottom)

The rest potentials of the coated panels were measured at the beginning of the test. Then a series of potential steps (typically 100–600mV) were applied from the rest potential. The resulting current was measured every 1 second until a fixed delay of 300s to allow the current to stabilise, before applying another potential step. Before each PPT measurement, EIS tests were conducted to gather coating resistance which is necessary for determination of iR-correction.

3.6 Experimental Details for Free Film Study

3.6.1 Preparation of Silver/Silver Chloride Electrode

A silver/silver chloride (Ag/AgCl) electrode was used as both the reference and counter electrode in the electrochemical tests during free film studies. The silver wire used here was 0.5mm diameter and approximately 5cm in length. The silver wire was cleaned with acetone and distilled water before coiling one end lead into a spiral. The spiral was covered with silver chloride by electrolyzing it for about 5 to 15 minutes in HCl (1 part concentrated HCl and 3 part deionized water) at about 1.5V, using a piece of platinised platinum as a cathode. The schematic cell for Ag/AgCl electrode preparation is illustrated in **Figure 3.13**. The silver chloride coating over the silver wire was dark grey or brownish in colour. The Ag/AgCl electrode was washed with acetone and distilled water before keeping it in a dark container filled with deionised water.

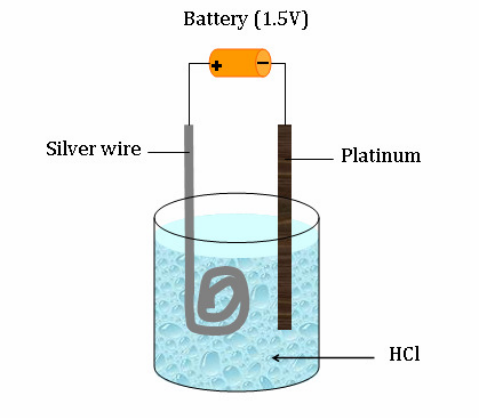

Figure 3.13 – Schematic cell for preparation of Ag/AgCl electrode

3.6.2 Mounting Free Film into the Test Cells

Free films were prepared by casting the epoxy-phenolic paint onto a sheet of thick silicone rubber using a draw-down bar. When the paint was dry, the silicon rubber could be peeled away from the paint film. The free film was left on the rubber at ambient condition for curing. Once the curing process was complete, the films were cut from sheets of thickness 150μm using a very sharp scalpel blade. The pieces of film were rinsed with distilled water and then blotted dry with a paper towel. Each film was sandwiched between two compartments of a permeation cell coupled with two silicone rubber gaskets (**Figure 3.14**).

An area of 7.06cm^2 of the film was exposed to the test solutions in the cell. This arrangement meant that the current leakage path between the two halves of the cell was very long. Two Ag/AgCl electrodes were inserted either side of the film to provide connection with the measuring equipment. The potential difference between these two

electrodes was small (0-5mV), which indicated that the electrodes were working well.

Figure 3.15 shows the front and side view of the cell.

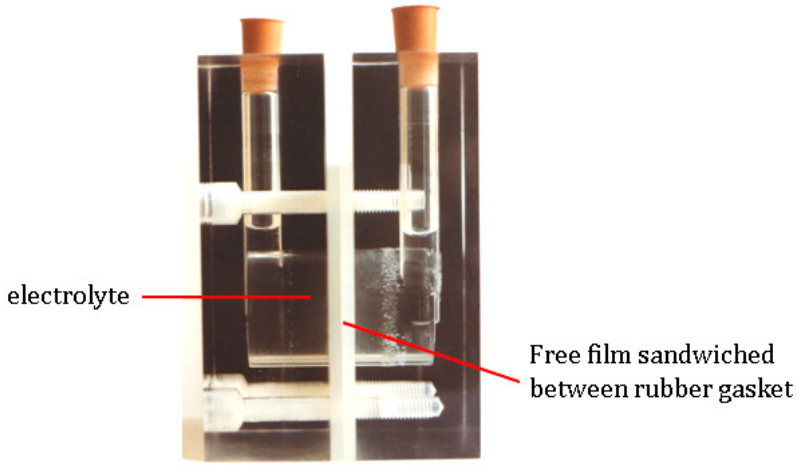

Figure 3.14 – Image of the cell used for holding the free film

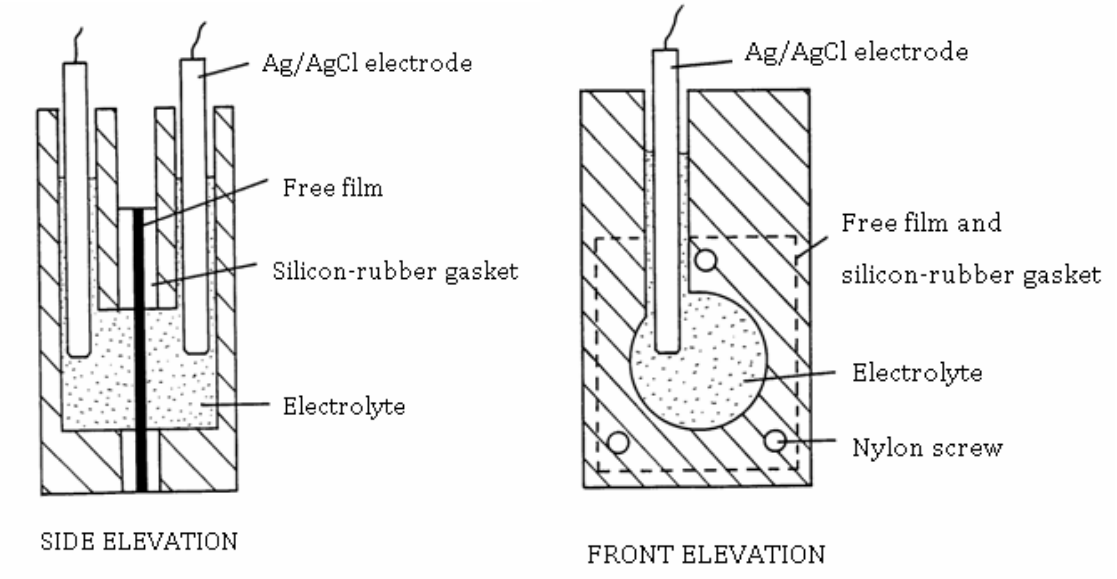

Figure 3.15 – Front and side elevation views of the cell used to hold the free film [136]

3.7 Scanning Kelvin Probe (SKP)

3.7.1 Principle

Scanning Kelvin probe (SKP) is a technique allowing a non-contact measurement of the surface of a metal giving values of corrosion potentials that can be calibrated to a standard scale [137]. The SKP uses a scanning vibrating gold tip as a quasi-reference electrode that enables it to map electrochemical potentials, even beneath a coating, thus allowing potential measurements of corrosion processes occurring in blisters and delaminated areas as well as at defects. SKP allows an image to be constructed that shows the potential distribution on the sample and identifies anodic and cathodic regions at defects and beneath the organic coating. This technique is very useful in corrosion studies around defects as a function of time as it produces results that can be related to the mechanistic description of the process [138].

The scanning Kelvin probe is a vibrating capacitor device used to measure the work function difference between a conducting specimen and a vibrating tip. If an external electrical contact is made between the specimen and the probe, their Fermi levels equalise and the resulting flow of charge produces a potential gradient between the plates, which is equal to the difference in the electronic work function. A variable 'backing potential' applied to the circuit is recorded at the unique point where the (average) electric field between the plates vanishes, resulting in a null output signal. For corrosion studies, the scanning Kelvin probe gives the potential of the specimen at that point that can then be calibrated to a standard scale.

3.7.2 Experimental Details

The KP Technology SKP system is shown in **Figure 3.16**. The SKP was operated using a circular silver tip with a 0.5mm flat end. Typically, the probe was set to vibrate at frequency of 60Hz with amplitude of 32μm and a gradient of 300, which gave a tip-sample separation of 64μm at closest approach. Measurements were taken using a sample backing voltage, V_b, in the range of $\pm$ 5000mV. This instrument uses a non-null technique that calculates the null point from the AC current at two bias values. This also allows automatic height control. For an area scan, the tip starts back left and then moves in a meander pattern, whereas for a line scan the tip start back left and moves in a line until the scan is complete. The SKP data was plotted using Origin 7.0. The area maps are based on 625 measurements and are presented in terms of relative potentials (arbitrary scale).

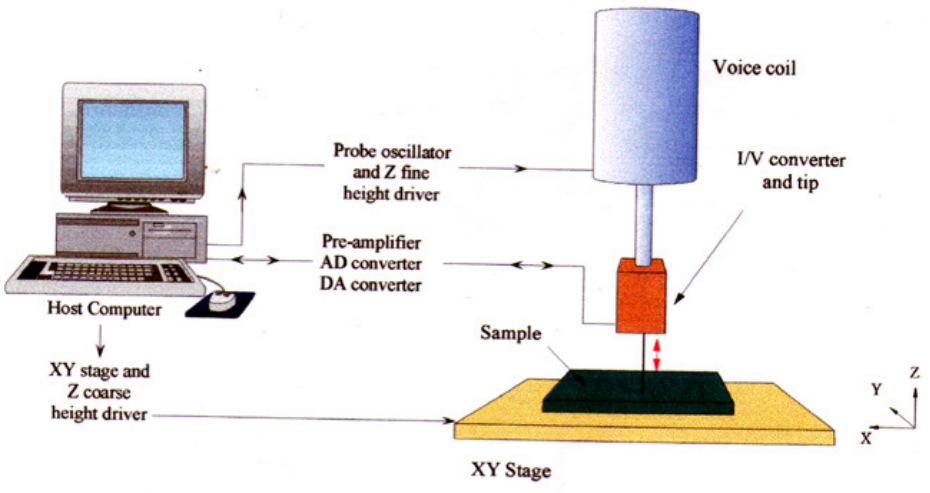

Figure 3.16 – Schematic of SKP set up (after SKP Technology Ltd)

3.7.3 Electrochemical Calibration

Calibration of the SKP was carried out by using several cylindrical metal samples (zinc, iron and copper) containing a reservoir of solution. The saturated solutions ($ZnSO_4$ for zinc, NaCl for iron and copper) were poured in the reservoir and connected to a saturated calomel electrode, SCE. The SCE was connected to a voltmeter so the potential reading of the respective metal sample can be recorded. The SKP was then used to take potential measurements at the surface of the solution. Both potentials measured using a voltmeter and SKP were then plotted together to determine the calibration factor. The calibration graph (**Figure 3.17**) has a gradient of 1.0434, thus confirming a 1:1 relationship between the electrochemical potential of the corroding metal and work function measured by SKP. The measured offset of 12.932mV can be used to convert the SKP raw data into electrochemical potential vs. SCE.

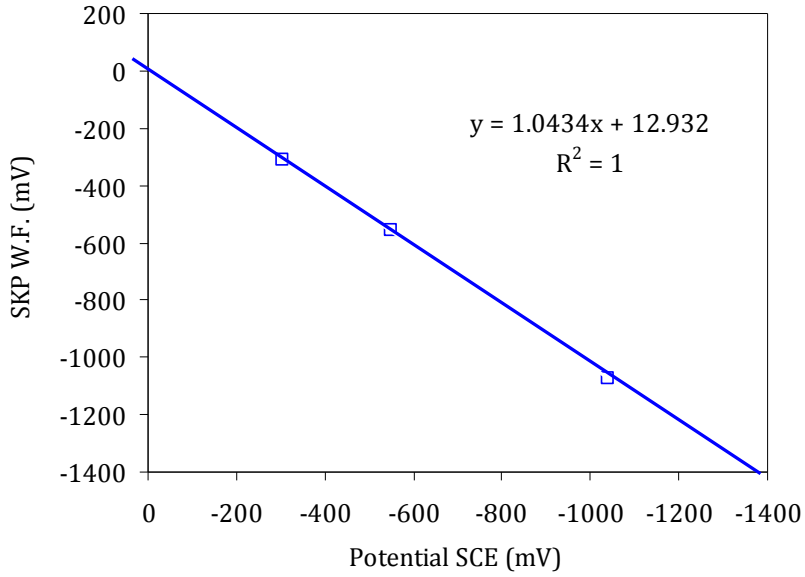

Figure 3.17 – SKP calibration graph for Zn, Fe and Cu metal standard vs. Ag probe tip

3.7.4 Determination of Coating Performance by SKP

One of the main significant advances of using SKP in coating studies is to better understand corrosion mechanisms under paint as well as the capability to produce maps illustrating potential and current distribution at a defect area. The mechanisms of the delamination process of organic coatings on steel have been investigated using local electrochemical and physical techniques. Stratmann et al. [18, 21, 139-147] employed a scanning Kelvin probe to measure potential distributions at a buried coating/substrate interface. Their studies were done under accelerated corrosive conditions and minimal surface treatments, therefore the prediction of delamination rate measured was far bigger than the value from commercial technical samples [148]. Reddy, Doherty and Sykes [149] have studied the mechanism of corrosion on a steel panel with a circular scribe defect painted with pigmented coating. They used SKP to examine the corrosion propagation at the defect and its periphery and discovered a reversal of anodes and cathodes at the scribe, beneath the coating. They have suggested that the reversal is due to the accumulation of the corrosion product at the defect. Potential mapping of electrochemical behaviour underneath the coating can lead to better understanding of the mechanism involved in coating breakdown. Later work by the same authors introduced an interpretation of the potential maps in terms of corrosion cells beneath the coating through generation of current maps, as they experienced difficulty from the former in identifying the correct region of electrochemical activity [150]. They concluded that current mapping could reveal patterns of anodic and cathodic activity at a defect and the area surrounding it. As

indicated in **Figure 3.18** by the shaded scale next to each map, the lightest areas on the map represents anodic sites, whereas the darker areas represent cathodic sites.

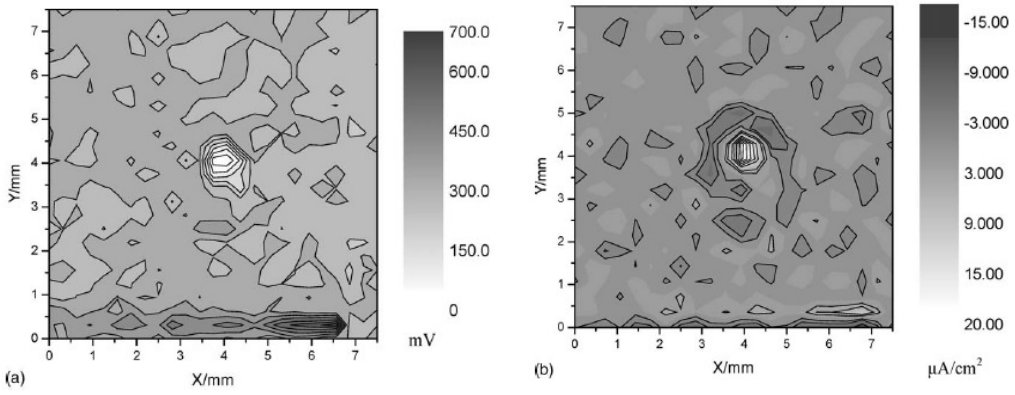

(a) potential map (b) current map

Figure 3.18 - SKP map for an 60 µm epoxy/talc coating on steel substrate exposed to 3% NaCl solution after 12 hours immersion [150]

3.8 Surface Characterization by Scanning Electron Microscopy (SEM)

A Scanning Electron Microscope (JEOL JSM-6300) was used to obtain SEM images of zinc rich primer surface before and after the exposure tests. The sample was placed on a conductive carbon tape that was stuck to a SEM stub. A gold coating was sputtered onto the sample in order to make it conductive during the imaging process. A secondary electron (SE) detector was used in order to image the coating layer particulates. All the SEM images presented in this thesis were taken at an accelerating voltage of 15 kV and at a working distance of 25 mm from the detector.

CHAPTER 4

THERMAL AGEING OF EPOXY COATING

4.1 Introduction

In this chapter investigations were carried out to assess the effect of temperature on the protective properties of several epoxy coatings. Firstly, exposure tests were conducted at ambient temperature and at 50^{o}C. Furthermore EIS impedance measurements were taken across a range of temperatures and used to determine the activation energies for ion conduction and the corrosion process. The temperature dependence test is conducted to explore the correlation between the coating resistances with the corrosion rate underneath the coating. Coated panels were also exposed to different alkali metal salts to further examine the effect of temperature on ion mobility through the coating. In addition SKP was used to map electrochemical potentials beneath the coating thus allowing potential measurements of the corrosion process occurring in a degradation of a coating by formation of blisters.

4.2 Experimental Details

4.2.1 Materials and Equipment

In this work, three different kinds of epoxy coating are being tested. They are polyamide cured epoxy (PCE), 2-component epoxy (2-CE) and epoxy-phenolic (EP) coatings. Further information on the coatings has been described in **Table 3.1**. For the EP coating, one or two-coat systems were tested, referred to as 1L-EP or 2L-EP respectively. EIS measurements were conducted using a 3-electrode cell as described in **Section 3.3.2**.

A Kelvin probe was used to map electrochemical potentials beneath the coating thus allowing potential measurements of corrosion processes occurring in blisters and delaminated areas. Further information on SKP can be found in **Section 3.7**.

4.2.2 Exposure Test

Exposure tests were conducted by immersion in 3% (by weight) sodium chloride solution at two different ambient temperatures, 21°C and 50°C for a period of time. For tests at 50°C, besides keeping the coated panels at 50°C in a controlled water bath, some panels were removed from the water bath and the EIS measurements were conducted at intermediate temperatures (50–21°C). After the panels had been tested, the cell was put back into the hot water bath and kept constant at 50°C until the time for the next measurement. The coated panels were typically assessed by EIS at

intervals of 3 days, 1 week, 2 weeks, 4 weeks and 8 weeks (unless failure occurred sooner). For each test, duplicate panels were tested but the EIS results presented here were based on one typical data. However, for activation energies, data from both duplicate experiments is included.

4.3 Results and Discussion

4.3.1 The Effect of Temperature on Coating Degradation

Exposure at Ambient Temperature, 21°C

Figures 4.1 to **4.4** show typical Bode and Nyquist plots of the coating after different periods of exposure at ambient temperature. The plots show the same general trend with a steady decrease in the impedance modulus, |Z| at low frequency; the 2L-EP coating sustains a higher |Z| than the other systems in line with its greater thickness.

In **Figure 4.1c** for the PCE coating, 2 distinct semicircles are seen by 14 days. The high frequency semicircle (near origin) gives the coating resistance, R_p and the low frequency semicircle characterizes the electrochemical process beneath the coating. By 21 days both semicircles have shrunk in size.

In **Figure 4.2c**, the 2-CE coating shows similar trends with two semicircles clearly evident by 7 days; shrinking over time.

In **Figure 4.3c**, degradation of the 1L-EP coating is slower, with indication of a second semicircle emerging at 14 days, becoming quite distinct by 30 days. During the 70 days of measurements, a small increase in the size of the first semicircle is observed, which could be indicative of the plugging of pores by corrosion products.

In **Figure 4.4c**, for the 2L-EP coating (where the coatings are in two layers with total thickness of 250 μm) it took 168 days before a complete semicircle became apparent.

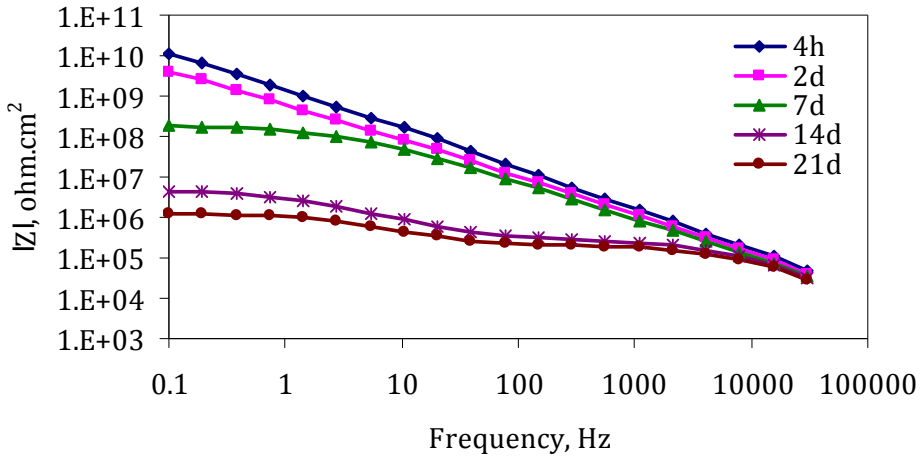

(a)

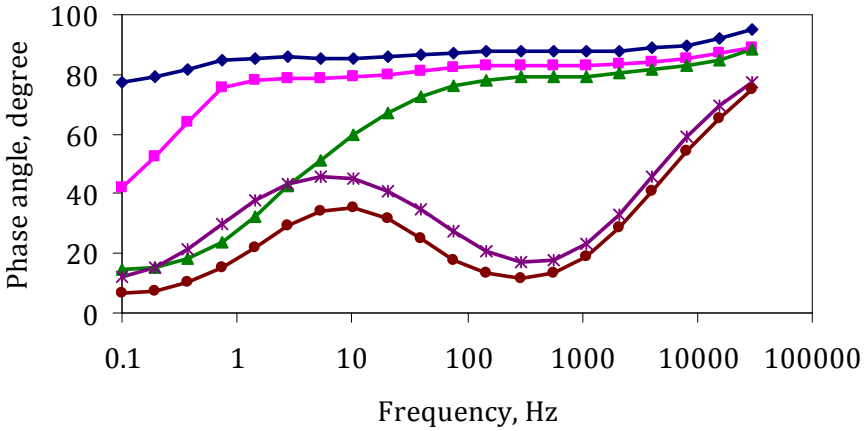

(b)

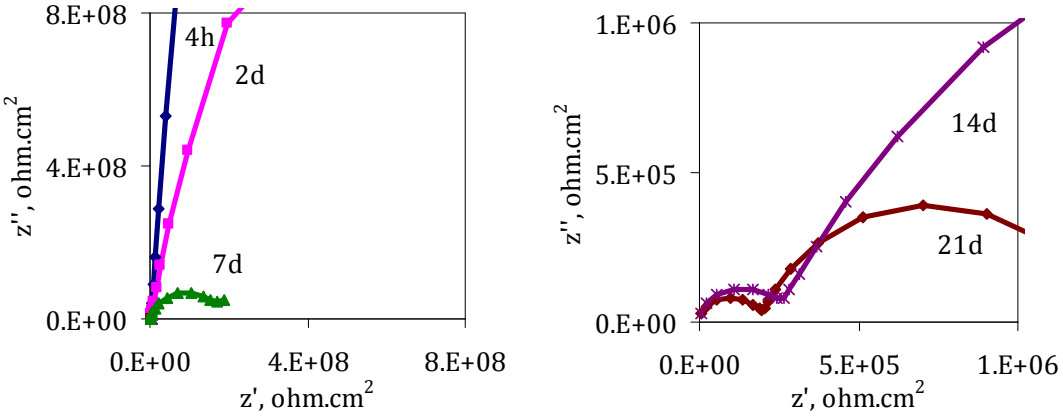

(c)

Figure 4.1 – Bode and Nyquist plots for PCE coating tested at 21°C

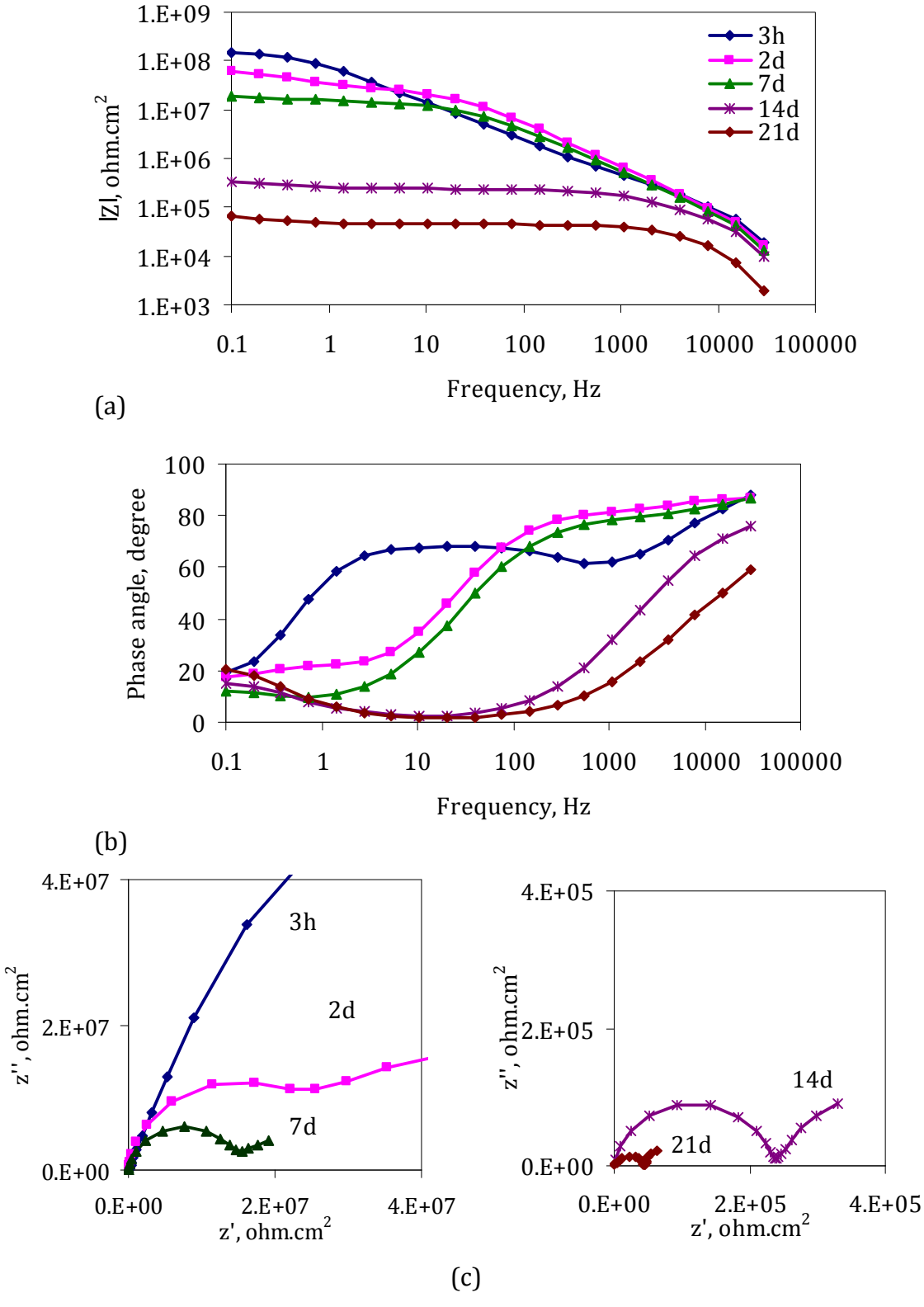

Figure 4.2 – Bode and Nyquist plots for 2-CE coating tested at 21°C

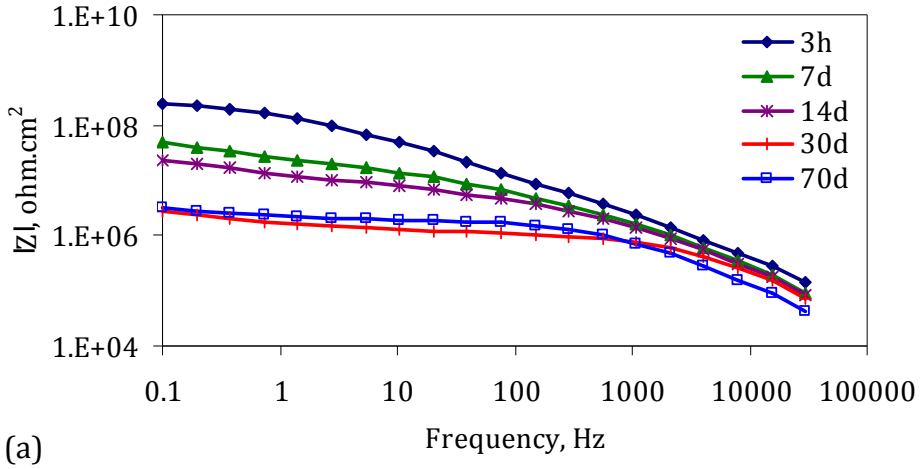

(a)

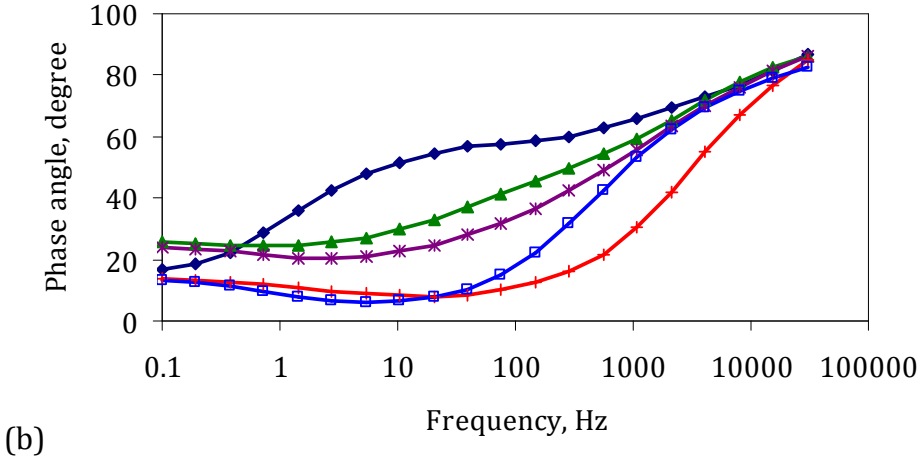

(b)

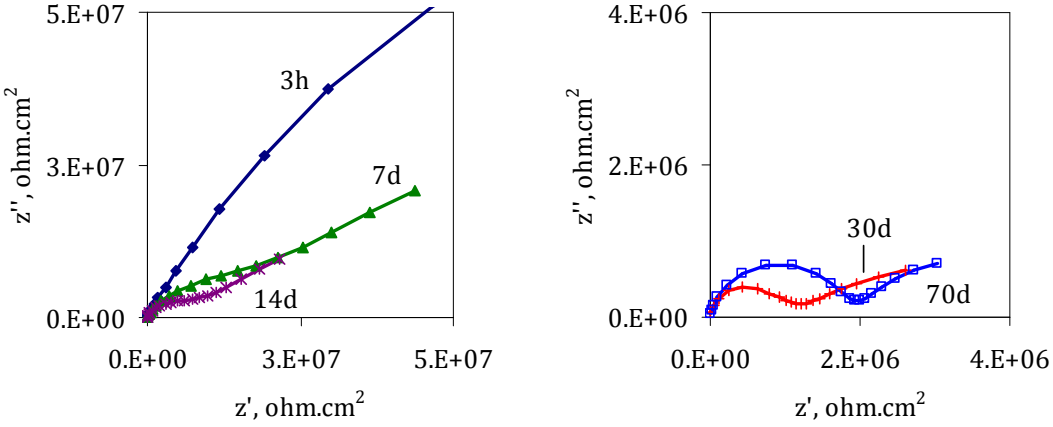

(c)

Figure 4.3– Bode plots for 1L-EP coating tested at 21°C

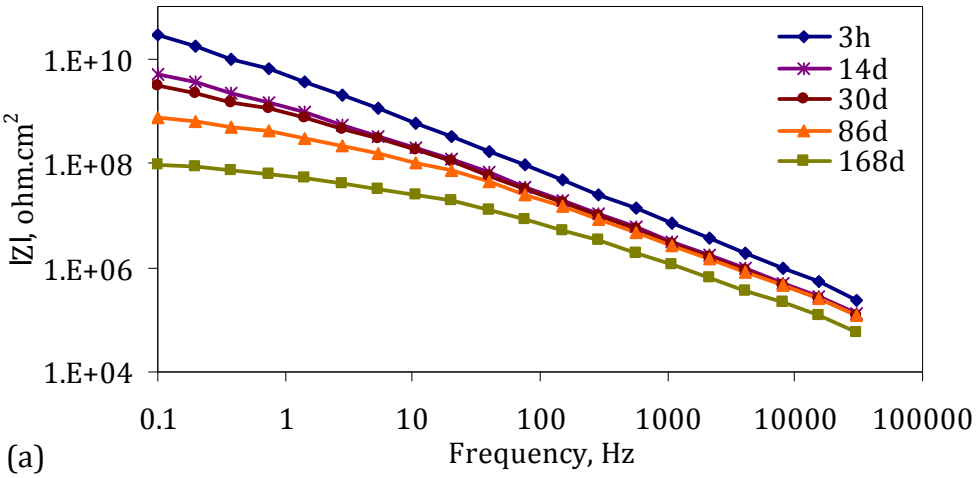

(a)

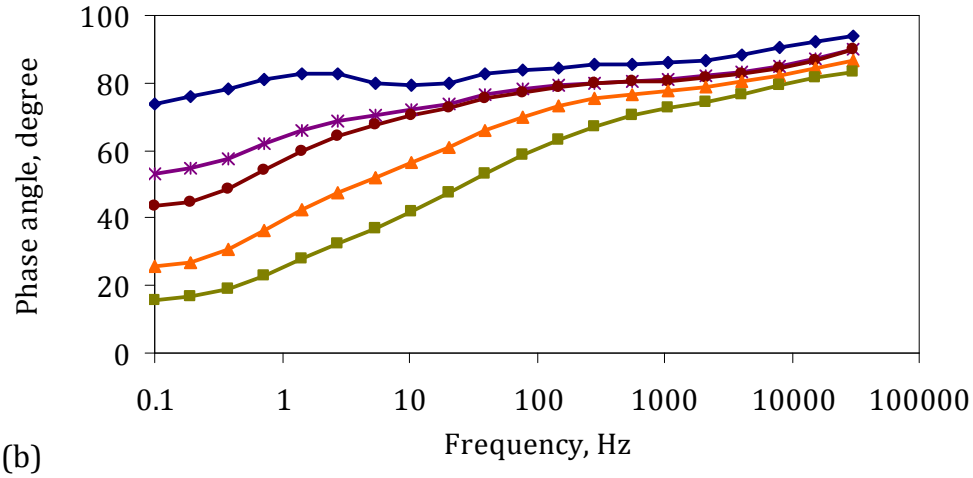

(b)

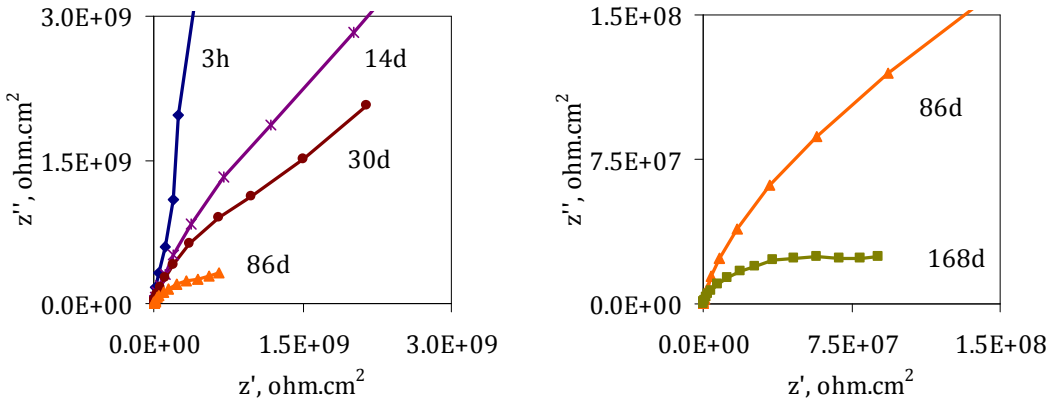

(c)

Figure 4.4– Bode plots for 2L-EP coating tested at 21°C

Exposure at 50°C

Figures 4.5 to **4.8** show typical EIS responses for the coated metals after different periods of exposure at 50°C. Degradation of PCE (**Figure 4.5**) and 2-CE (**Figure 4.6**) coatings are faster at 50°C compared to ambient temperature exposure (**Figure 4.1c** and **4.2c**), with indication of a second semicircle by 4 days.

In **Figure 4.7**, for the 1L-EP coating, the high frequency semicircle is seen to shrink much more quickly at 50°C compared to ambient temperature (**Figure 4.3c**). The second semicircle is also poorly defined. In **Figure 4.8**, 2L-EP (thicker coating: 2 layers) also degrades much more quickly than at 21°C (**Figure 4.4**). This result indicates that the use of high temperature does shorten the time of coating failure, as expected.

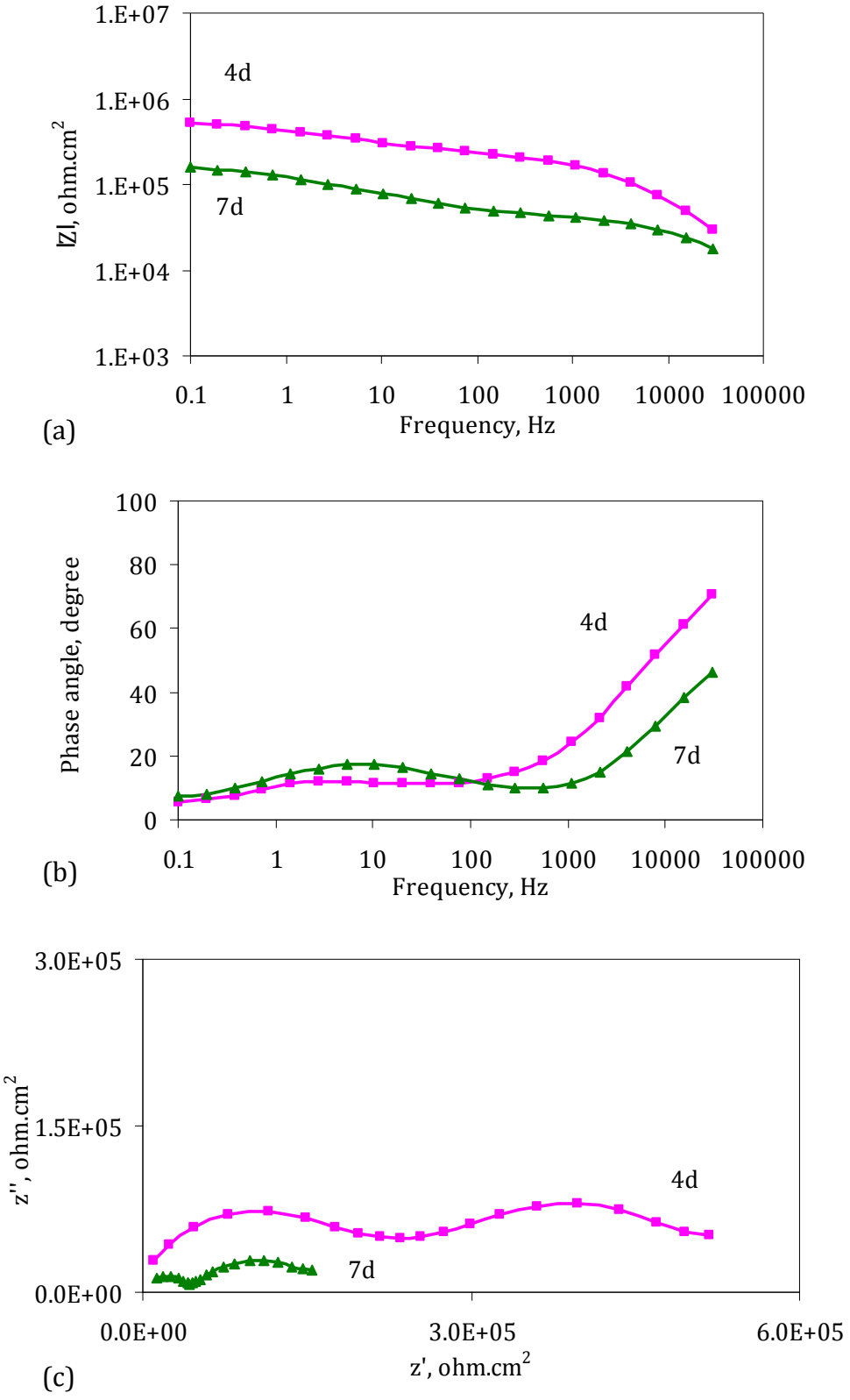

Figure 4.5 – Nyquist and Bode plot for PCE coating tested at 50°C

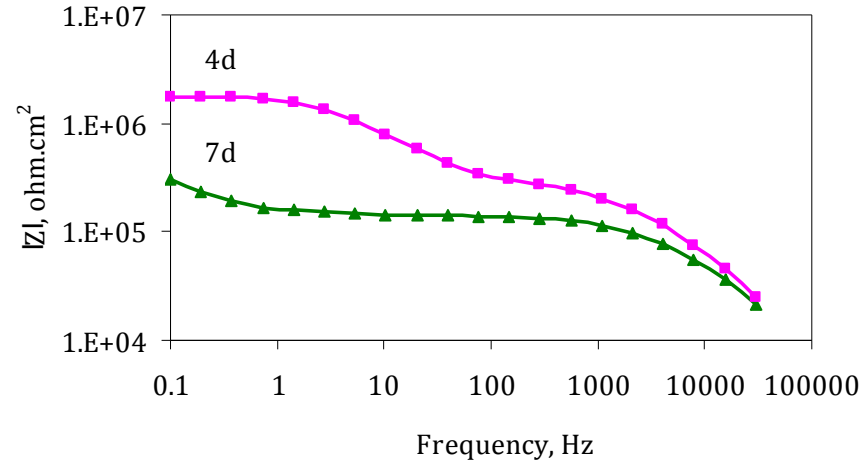

(a)

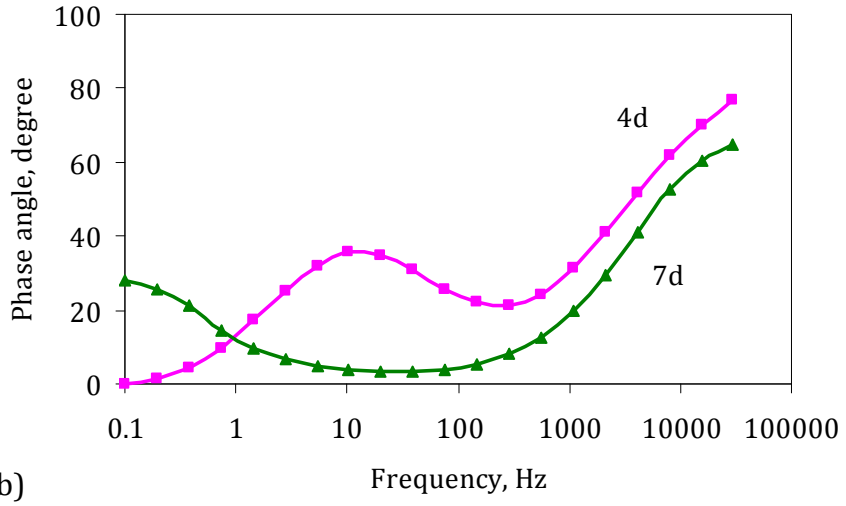

(b)

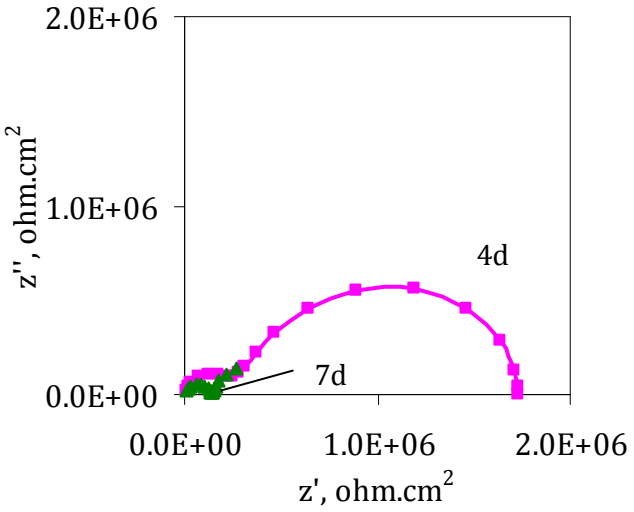

(c)

Figure 4.6 – Nyquist and Bode plot for 2-CE coating tested at 50°C

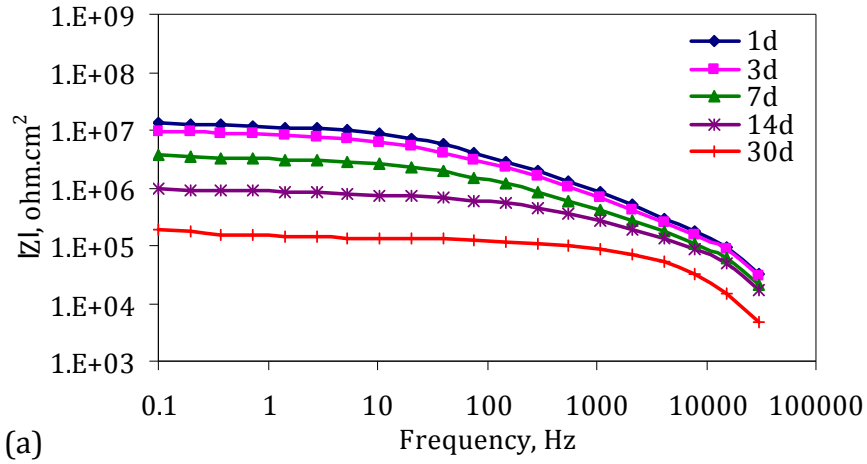

(a)

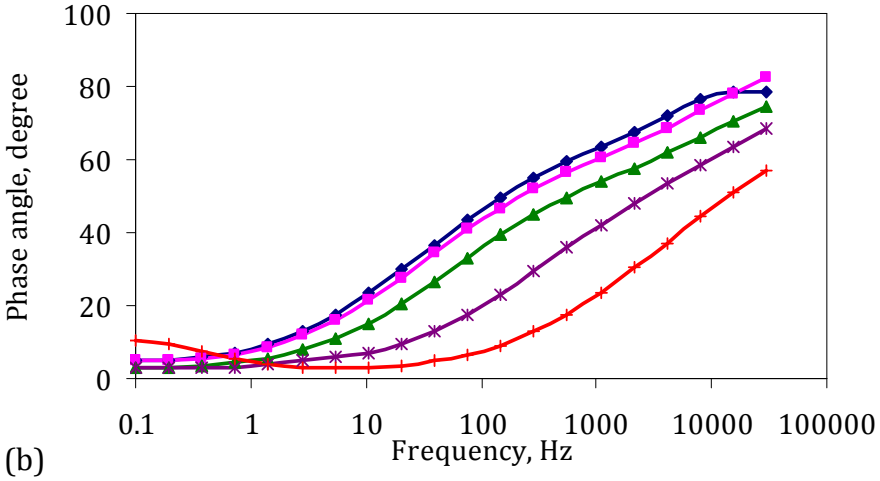

(b)

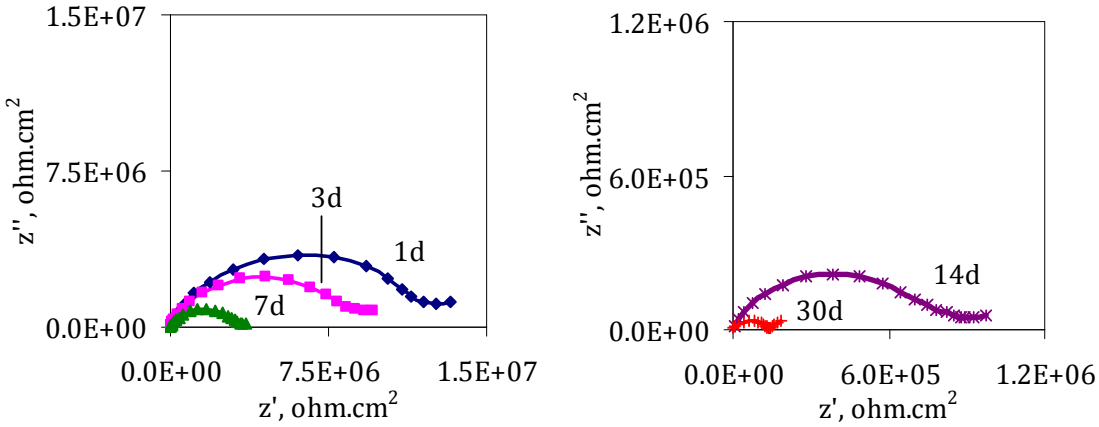

(c)

Figure 4.7– Nyquist and Bode plot for 1L-EP coating tested at 50°C

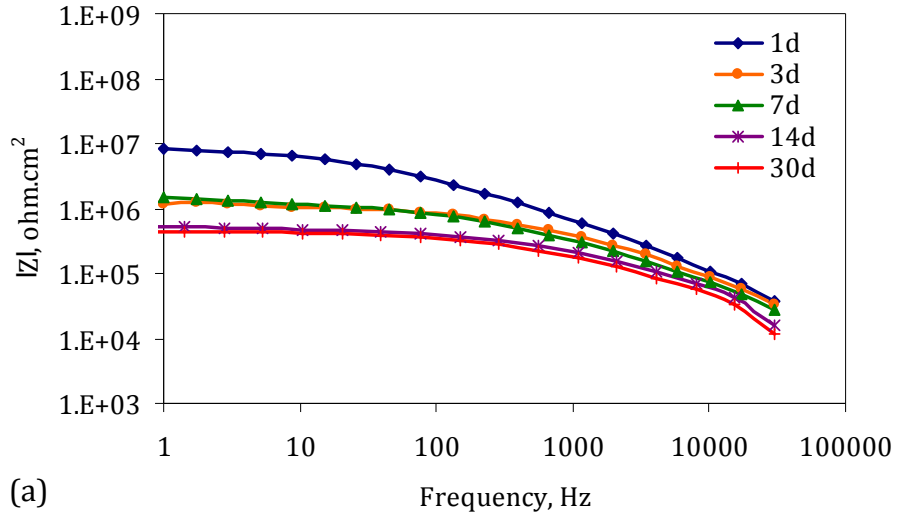

(a)

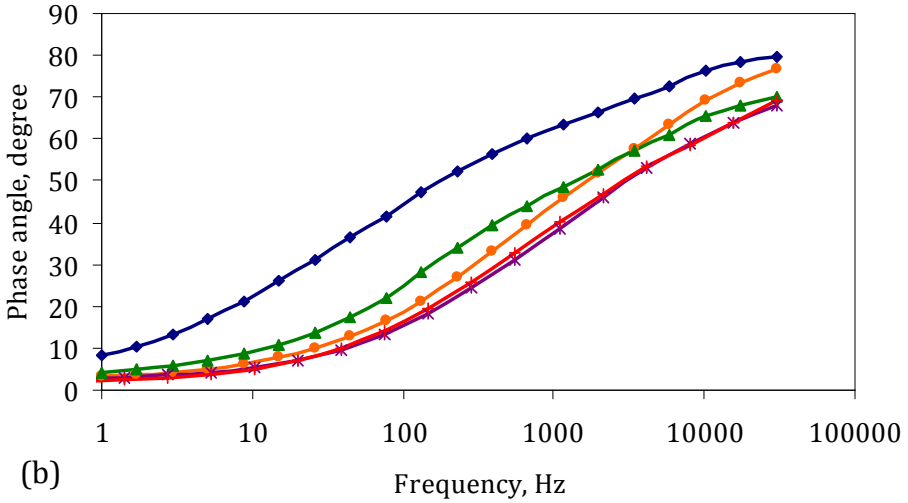

(b)

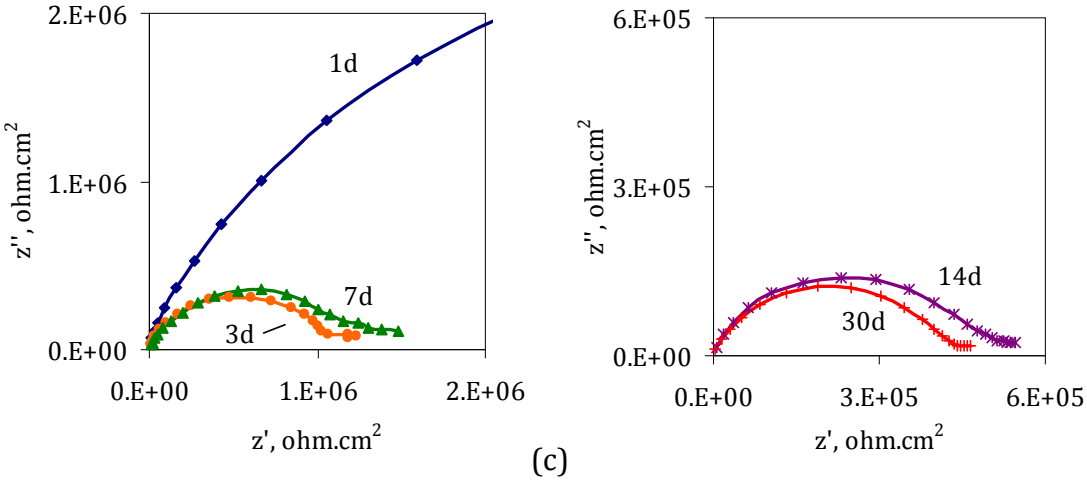

(c)

Figure 4.8– Nyquist and Bode plot for 2L-EP coating tested at 50°C

Visual Inspection

Figures 4.9 and **4.10** show the images of PCE and 1L-EP coated panels after exposure at 50°C. These images reveal the appearance of blisters after just a short immersion period. It was observed that the presence of blisters was noticed by 4 days on PCE coated panels and by 14 days on a 1L-EP coated panels. In **Figures 4.9b** and **4.10b**, the panels showed that the blisters grew over time, with increasing size and numbers. Further investigation using a scanning Kelvin probe on the electrochemical activity underneath the blister formed on PCE coated panels is discussed in **Section 4.3.9**.

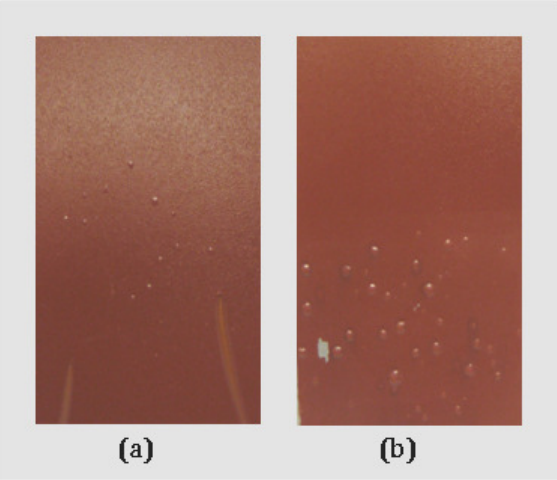

Figure 4.9 – Images of PCE coating tested at 50°C after (a) 4 days and (b) 12 days of exposure in 3% NaCl solution

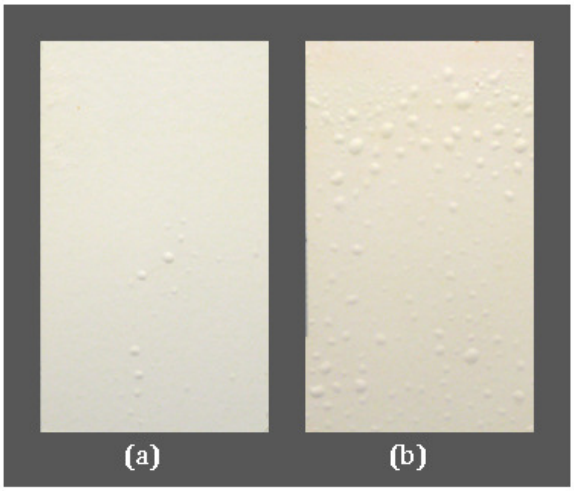

Figure 4.10 – Images of 1L-EP coating tested at 50°C after (a) 14 days and (b) 30 days of exposure in 3% NaCl solution

4.3.2 Assessment of Coating Behaviour Exposed at 50°C vs. (50°C-E_A[3])

As mentioned in **Section 4.2.2**, for exposure tests at 50°C, besides keeping the coated panels at a constant 50°C, for some exposure some panels were removed from the water bath and EIS measurement was conducted at intermediate temperatures from 50°C down to 21°C. This test enabled a further study on the temperature dependence of the coating and the charge transfer resistances over a period. After the panels had been tested, the cell was put back into the hot water bath and kept constant at 50°C until the time for the next measurement. This test is referred as '(50°C-E_A)' when describing the result. The main purpose of (50°C-E_A) test is not to make a more rigorous test condition, but to evaluate the activation energy for ion conduction in the coating and for the corrosion reaction. This test is compared with EIS data measured at constant 50°C.

Analysis of Bode Plot

EIS data for coated panels exposed at constant 50°C and (50°C-E_A) are plotted together to observe any significant difference that arises. This is to check whether imposing a short period of test where the panel is left to cool down has any effect when compared with the tests at constant 50°C. **Figures 4.11** to **4.13** show the Bode impedance spectrum for PCE, 2-CE and 1L-EP coated panel exposed at 50°C and (50°C-E_A). These figures show hardly any significant difference between coated panels exposed at constant 50°C and (50°C-E_A).

[3] Coated panel is exposed at 50°C but slowly cooled to ambient temperature to determine activation energy, E_A

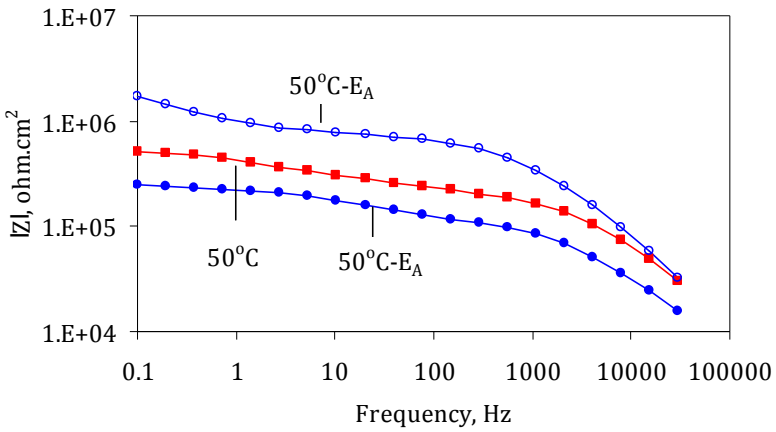

Figure 4.11 – Bode plot for PCE coating system after 4 days of exposure

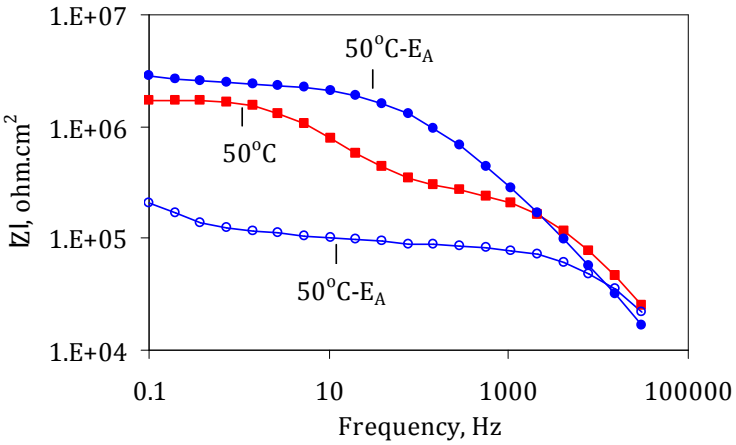

Figure 4.12 – Bode plot for 2-CE coating system after 4 days of exposure

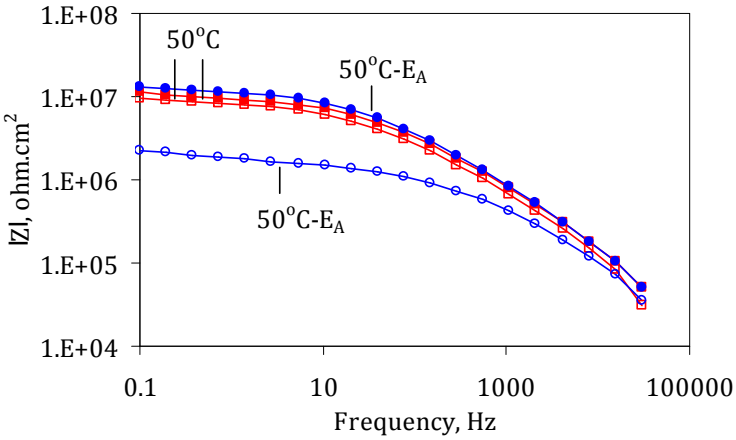

Figure 4.13 – Bode plot for 1L-EP coating system after 4 days of exposure

Effect of Temperature on EIS Response

In order to clearly show the effect of temperature, impedance spectra were plotted for tests conducted at 5°C intervals as the sample cooled down from 50 to 25°C (**Figures 4.14** and **4.15**). These plots show the influence of temperature on the impedance spectra of the coated panel. The Nyquist plot at high temperature shows a smaller semi-circle and the size becomes larger as the temperature drops. Similarly, the Bode plot shows the impedance modulus at low frequency, |Z| which increases as the temperature drops. When the temperature is increased, ions will migrate through the film more easily, the free volume in the polymer will increase and the solubility of water in the polymer increases so more water diffuses into the paint film.

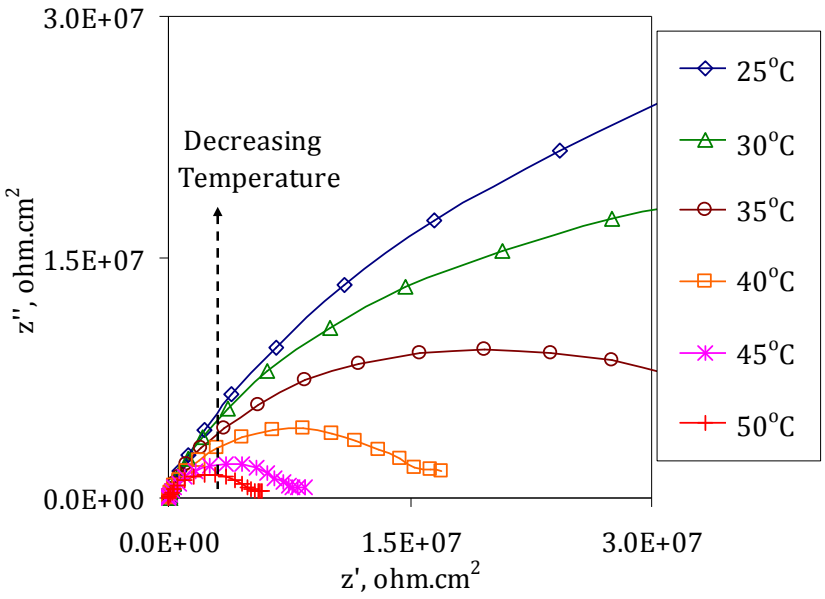

Figure 4.14 – Nyquist plots at various temperatures for 2L-EP coating after 1 day exposure at 50°C

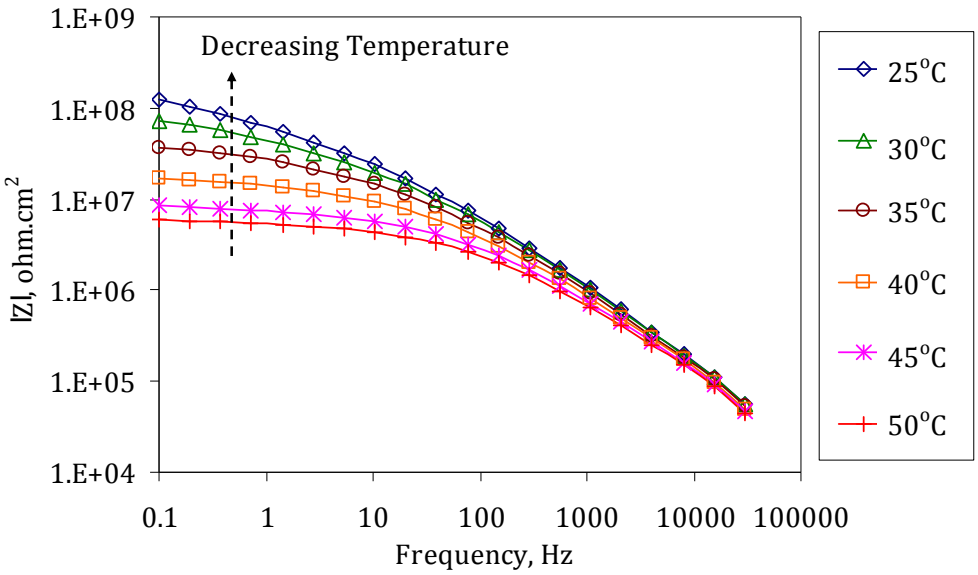

Figure 4.15 - Bode plots at various temperatures for 2L-EP coating after 1 day exposure at 50°C

Analysis of EIS

Initially the Nyquist plot shows only one semicircle but after longer periods of exposure two semicircles could clearly be seen. The impedance of the paint and the electrode will always be added but cannot always be distinguished from each other. EIS spectra were usually analyzed using non-linear least squares fitting (with ZSimpWin) to a R[Q[R[QR]]] model circuit (**Figure 4.16a**) or [RQ][RQ] (**Figure 4.16b**). R_p is the film resistance, here taken to be due to local weak spots where the coating is deteriorating or has broken down. Q is the constant phase element and the value of Q_c, coating capacitance, can be used to estimate the amount of water absorbed by the coating. The amount of water absorbed by the coating can be determined using the Brasher and Kingsbury equation [115]. R_{ct} is the charge transfer resistance and is an

indication of the corrosion rate to which it is related to the Stern-Geary equation [121]. Q_{dl} is the double layer capacitance which directly depends on the area of steel that is electrochemically active.

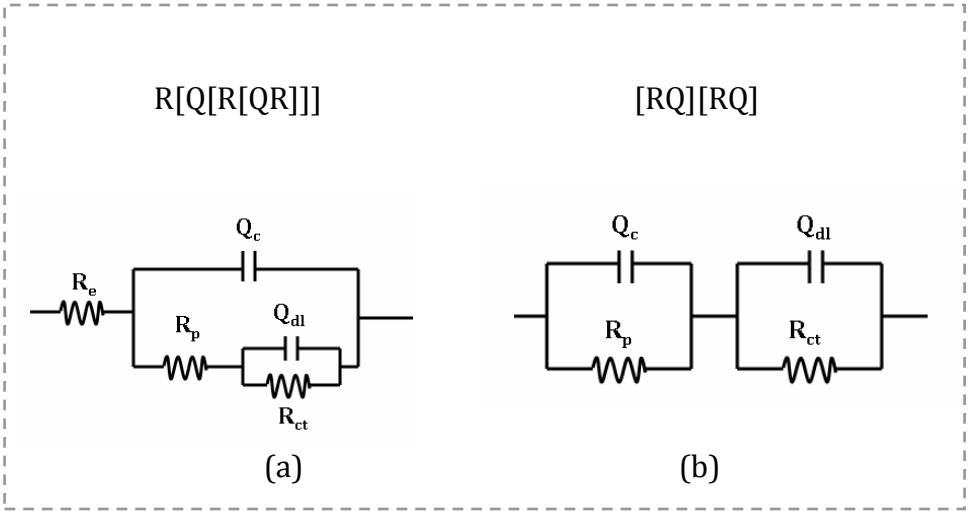

Figure 4.16 – Two time constant equivalent circuits, used for fitting EIS data

4.3.3 Temperature Dependence of PCE Coating

Figure 4.17 shows the effect of changing temperature on the EIS response of the PCE coating after 3 days exposure at 50°C. The semicircle decreases in size as temperature rises. The impedance spectrum is fitted with an equivalent circuit and the measured data and the fit is shown in **Figure 4.19**. There is a possibility that a third small semicircle exist for Nyquist plots after 7 days of exposure as shown in **Figure 4.18** so ideally a three time-constants equivalent circuit might be needed for a full analysis. However the curve could be fitted with two time constants with quite a good fit versus the measured data (**Figure 4.20**). The fitted parameters are summarized in **Tables 4.1**

and **4.2** which show the values of R_p and R_{ct} drop as the temperature rises. The '%error' and 'X^2' in the tables were derived from the fitting software. Notice that '%error' for R_{ct} (**Table 4.1**) is large which is probably due to the difficulty in fitting the incomplete second semicircle. Referring to equation (2.12), Arrhenius plots of log R versus 1/T were made to investigate whether log R obeyed the Arrhenius equation and if it did, enabling the activation energy, E_A to be calculated. The Arrhenius plots (**Figures 4.21**, **4.21a**, **4.22** and **4.22a**) display a reasonably good straight line so E_A can be calculated.

The typical T_g of epoxy resin is in the range of 70 to 170°C [151-153]. However, it is to be expected that the T_g for a water-saturated polymer would be significantly lower than this value. Bierwagen et al. [95] measured dry and wet[4] epoxy powder films and found that the T_g dropped from 100°C to 82°C. A study on T_g for epoxy resins by Liu et al. resulted in a very high T_g (170–267°C) which they associated with the highly cross-linked nature of the polymers [154]. Thus, the coating film used in this experiment will not be affected by immersion exposure at 50°C. In particular, the Arrhenius plots produced from this experiment are not expected to show any artefact due to passing through a transition and do not shows any obvious transition temperature. Mills and Mayne observed sharp changes in paint film activation energies upon reaching the transition temperature [106, 107].

[4] Film has been immersed in 3% NaCl solution for 8 months at 25°C and 1h at 90°C

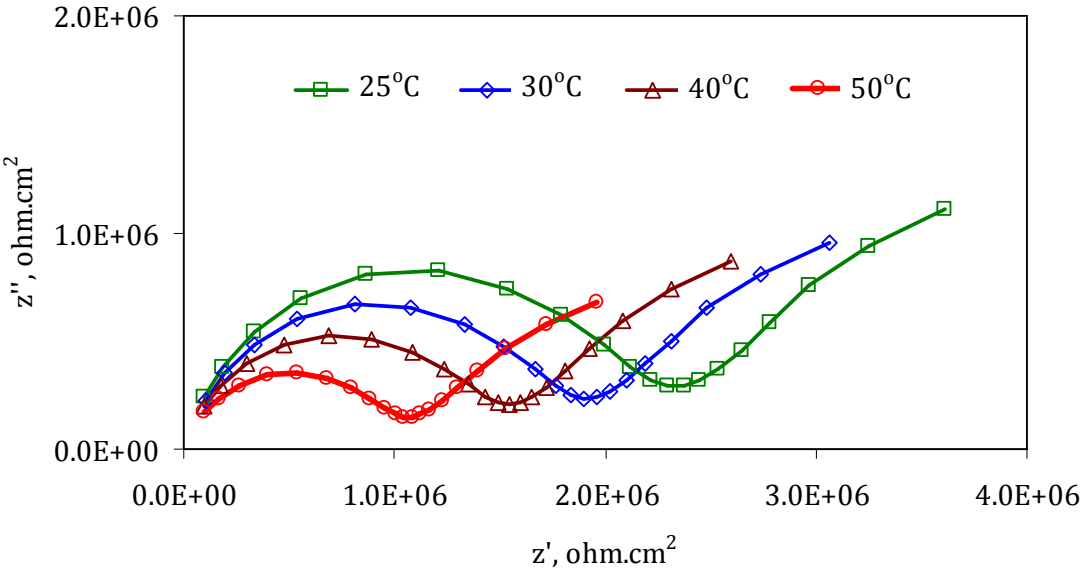

Figure 4.17 - Nyquist plots at various temperatures for PCE coating after 3 days of exposure at 50°C

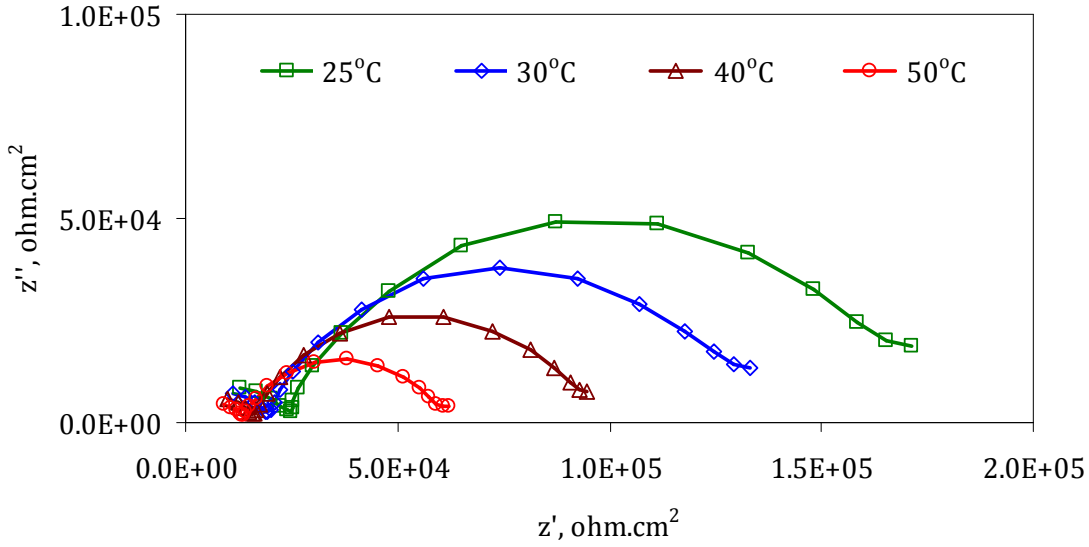

Figure 4.18- Nyquist plots at various temperatures for PCE coating after 7 days of exposure at 50°C

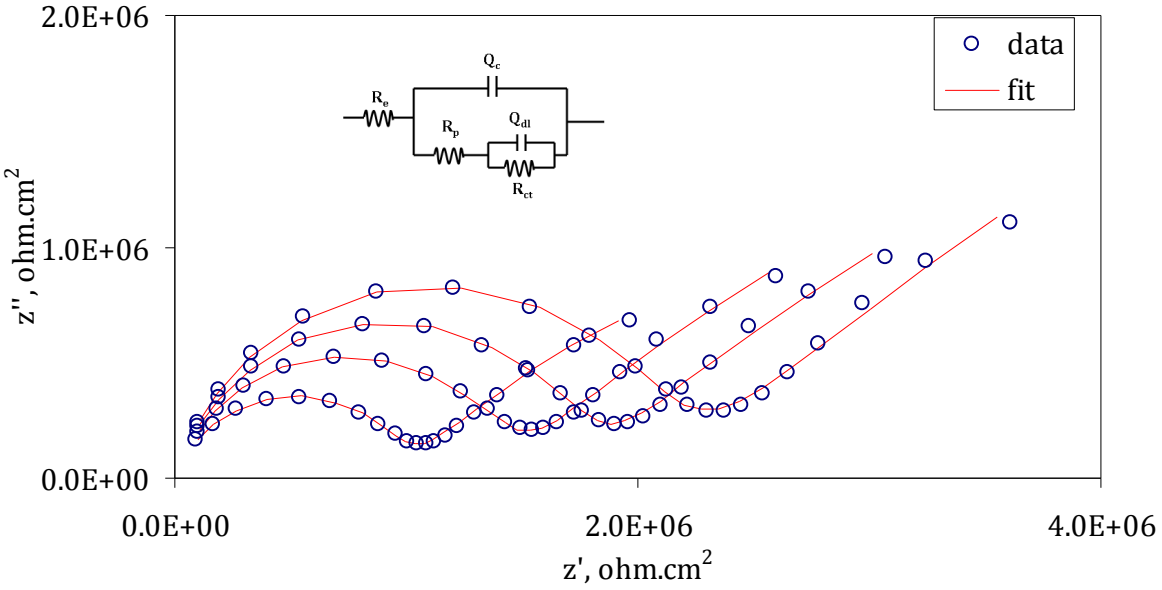

Figure 4.19 - Experimental (o) and simulated (-) Nyquist plot of PCE coating exposed at various temperatures after 3 days of exposure at 50°C

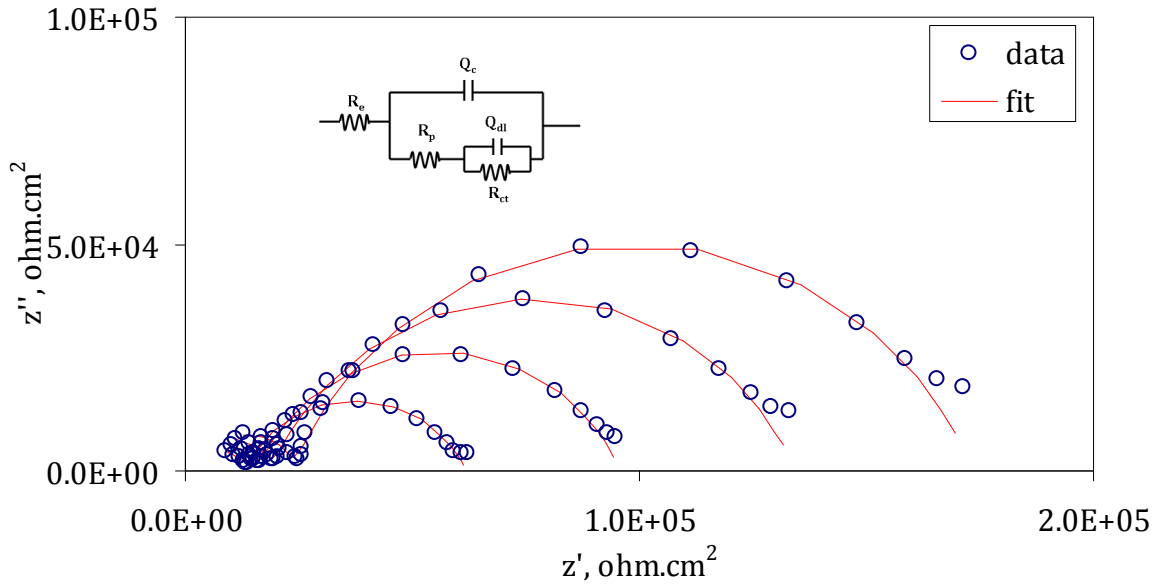

Figure 4.20 - Experimental (o) and simulated (-) Nyquist plot of PCE coating exposed at various temperatures after 7 days of exposure at 50°C

Table 4.1 – Parameters for PCE coating from fitting of EIS result after 3 days exposure at 50°C

Fitted circuit: R[Q[R[QR]]]

T (°C)	Q_c $(Fcm^{-2})^n$	Q_c (%error)	n	R_p (ohm.cm²)	R_p (%error)	Q_{dl} $(Fcm^{-2})^n$	Q_{dl} (%error)	n	R_{ct} (ohm.cm²)	R_{ct} (%error)	X^2
25	1.05E-09	12.60	0.82	2.14E+06	3.59	6.44E-07	10.72	0.46	2.53E+07	259.5	5.99E-04
30	1.22E-09	12.73	0.81	1.78E+06	3.13	7.05E-07	9.03	0.49	1.02E+07	96.72	5.60E-04
40	1.67E-09	12.75	0.79	1.44E+06	3.10	7.74E-07	11.35	0.49	9.07E+06	81.42	4.82E-04
50	2.35E-09	13.22	0.77	1.00E+06	2.91	9.07E-07	6.16	0.52	4.64E+06	39.23	4.07E-04

Table 4.2 – Parameters for PCE coating from fitting of EIS result after 7 days exposure at 50°C

Fitted circuit: R[Q[R[QR]]]

T (°C)	Q_c $(Fcm^{-2})^n$	Q_c (%error)	n	R_p (ohm.cm²)	R_p (%error)	Q_{dl} $(Fcm^{-2})^n$	Q_{dl} (%error)	n	R_{ct} (ohm.cm²)	R_{ct} (%error)	X^2
25	1.29E-09	84.38	0.88	1.96E+04	15.93	6.06E-07	8.59	0.75	1.50E+05	2.72	1.54E-03
30	2.20E-09	76.22	0.81	1.89E+04	20.91	6.77E-07	7.72	0.74	1.15E+05	2.27	1.08E-03
40	2.27E-09	69.20	0.82	1.55E+04	20.70	7.76E-07	7.11	0.74	8.01E+04	1.88	7.18E-04
50	3.68E-09	69.22	0.79	1.28E+04	22.38	9.59E-07	7.62	0.72	4.84E+04	1.81	5.33E-04

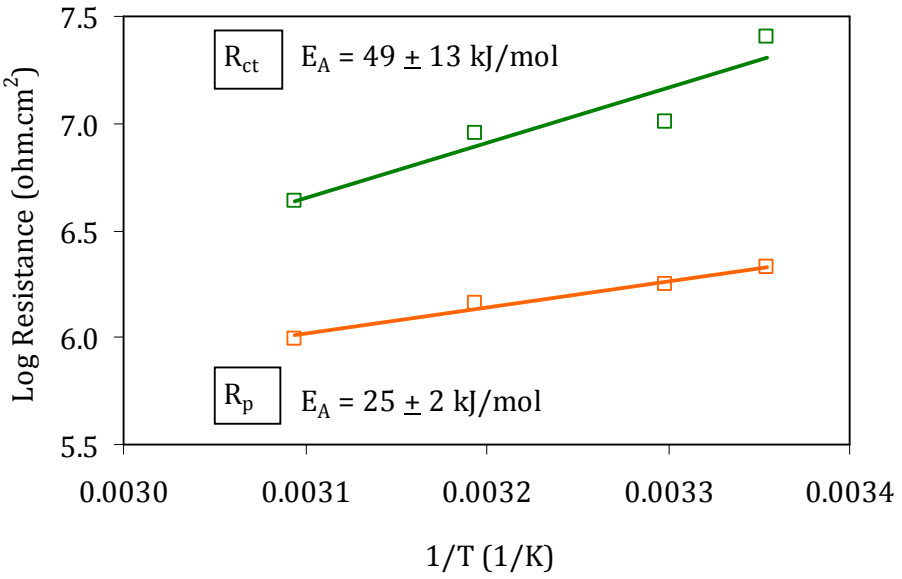

Figure 4.21 - Arrhenius plots of R_p and R_{ct} for PCE coating after 3 days of exposure at 50°C

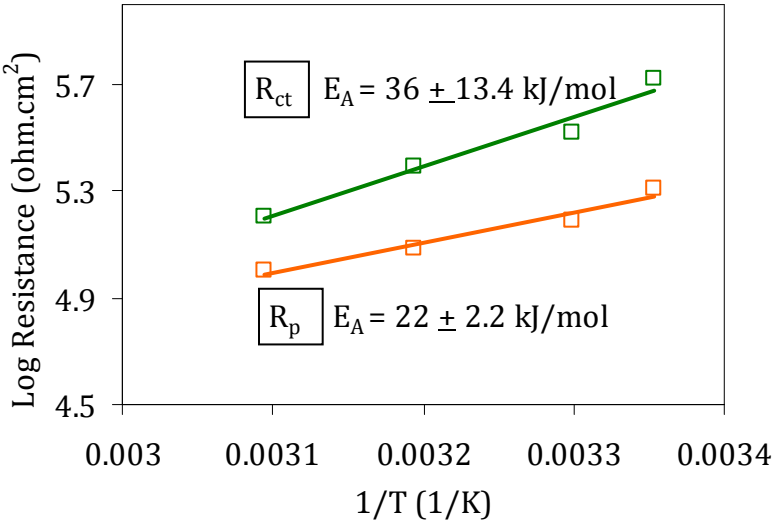

Figure 4.21a - Arrhenius plots of R_p and R_{ct} for PCE coating (other panel) after 3 days of exposure at 50°C

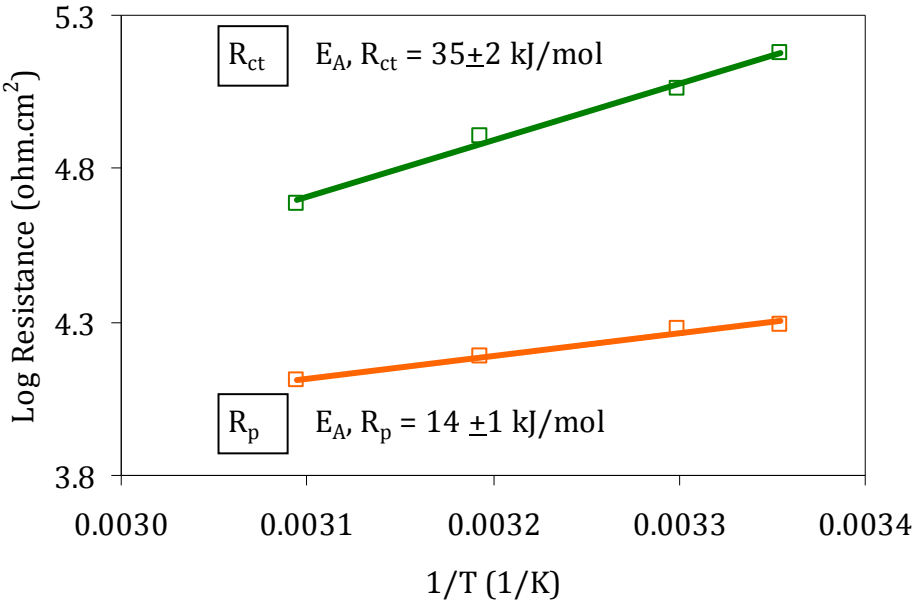

Figure 4.22 - Arrhenius plots of R_p and R_{ct} for PCE coating after 7 days of exposure at 50°C

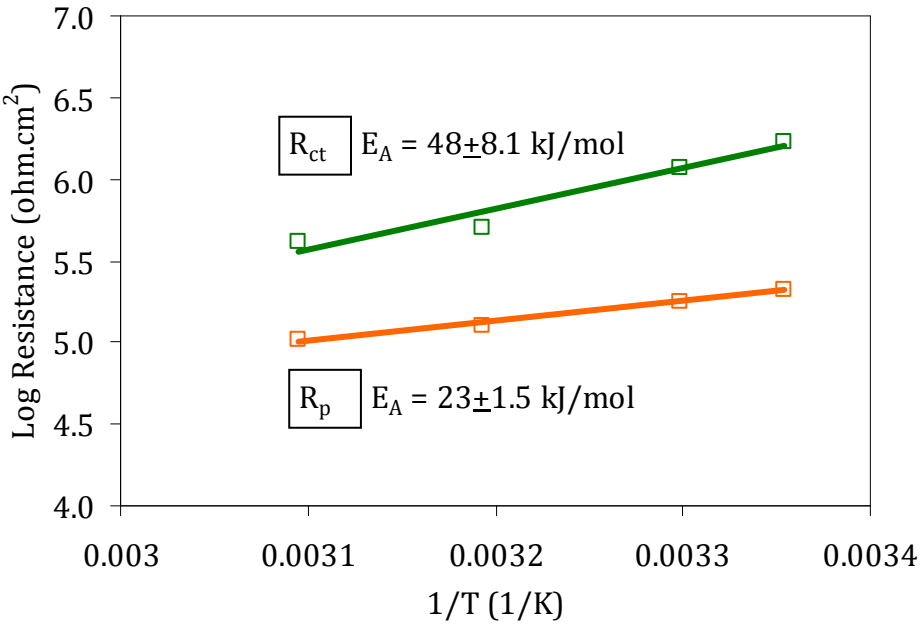

Figure 4.22a - Arrhenius plots of R_p and R_{ct} for PCE coating (other panel) after 7 days of exposure at 50°C

4.3.4 Temperature Dependence of 1L-EP Coating

Figures 4.23 and **4.24** shows the impedance spectra obtained for the 1L-EP coating at different temperatures after 3 and 7 days exposure. From these spectra the strong influence of temperature on the impedance of the coating is evident. The second semicircle at low frequency is not clearly seen for impedance spectra for day 3 and 7 measurements, thus the results are not really suitable for temperature influence analysis on the ion conduction and corrosion process. However, by 14 days of exposure (**Figure 4.25**) two distinct semicircles are seen. It is noticeable that the low frequency semicircles show a larger change with temperature than the high frequency semi circles.

To assess the influence of temperature on the ion conduction and corrosion process, the semicircles from **Figures 4.25** and **4.26** are fitted to an appropriate equivalent circuit and the measurement data seems to be a good match with the fitted spectra (**Figures 4.27** and **4.28**). The summary of the fitted parameters are listed in **Tables 4.3** and **4.4**. Coating resistance, R_p and charge transfer resistance, R_{ct} at different temperatures were then utilized to calculate the activation energy for ion conduction in the film and the corrosion process. Using equation (2.12), log resistance against the reciprocal of temperatures were plotted and a straight line indicates the Arrhenius equation is obeyed and enables activation energy, E_A to be found.

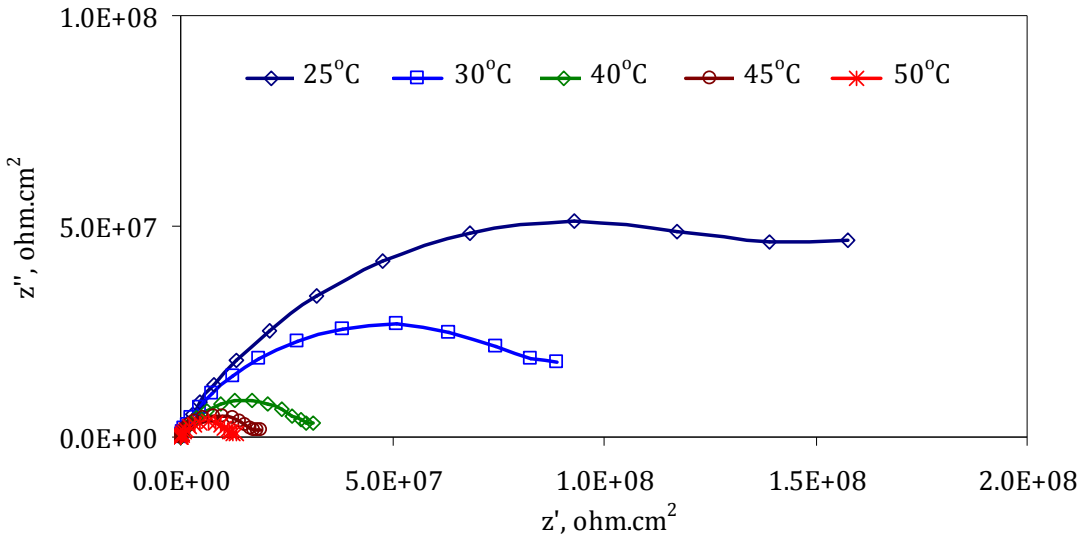

Figure 4.23 - Nyquist plots at various temperatures for 1L-EP coating after 3 days of exposure at 50°C

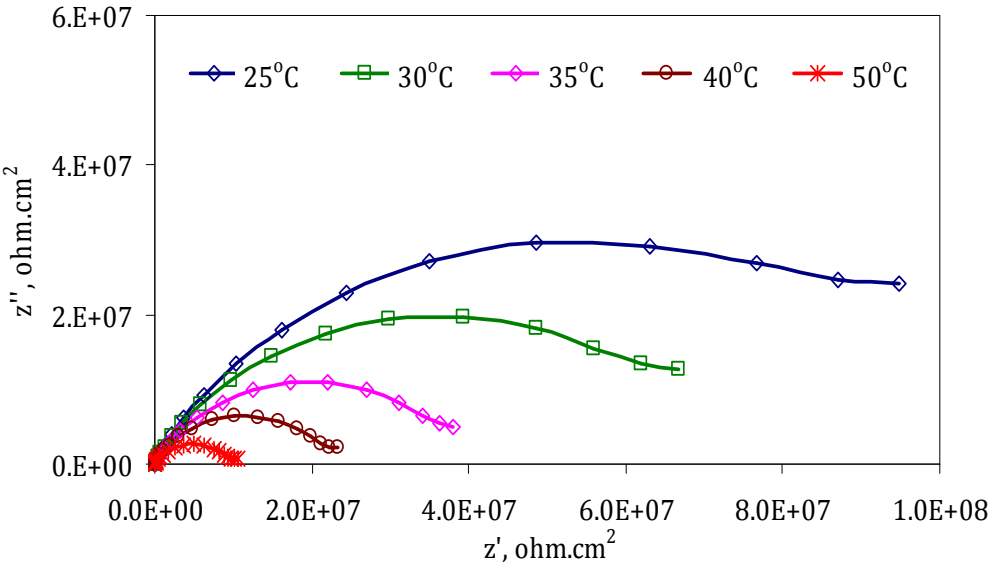

Figure 4.24 - Nyquist plots at various temperatures for 1L-EP coating after 7 days of exposure at 50°C

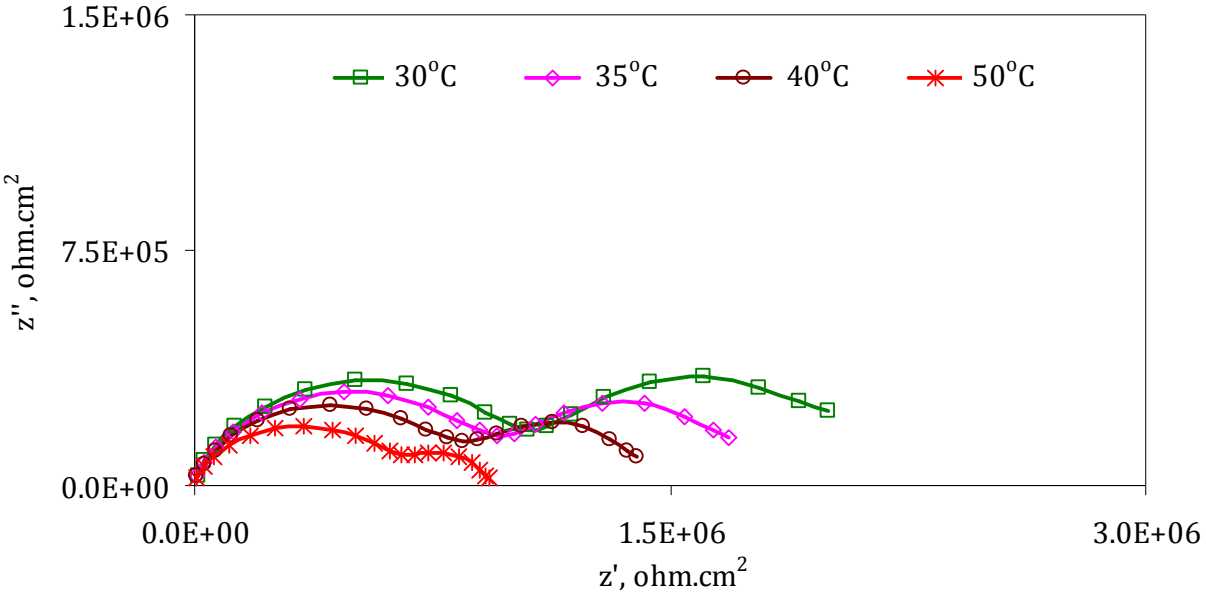

Figure 4.25 - Nyquist plots at various temperatures for 1L-EP coating after 14 days of exposure at 50°C

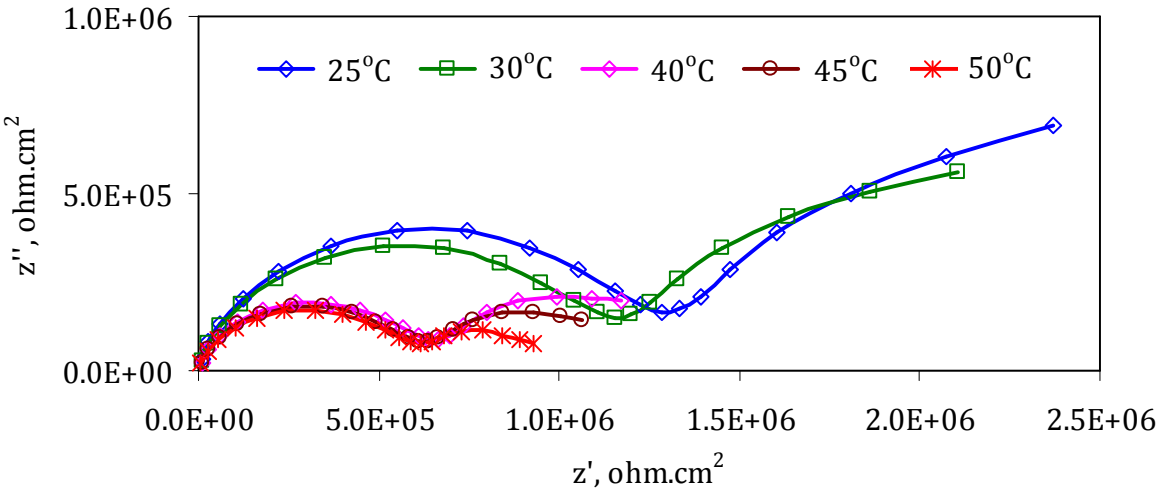

Figure 4.26 - Nyquist plots at various temperatures for 1L-EP coating after 30 days of exposure at 50°C

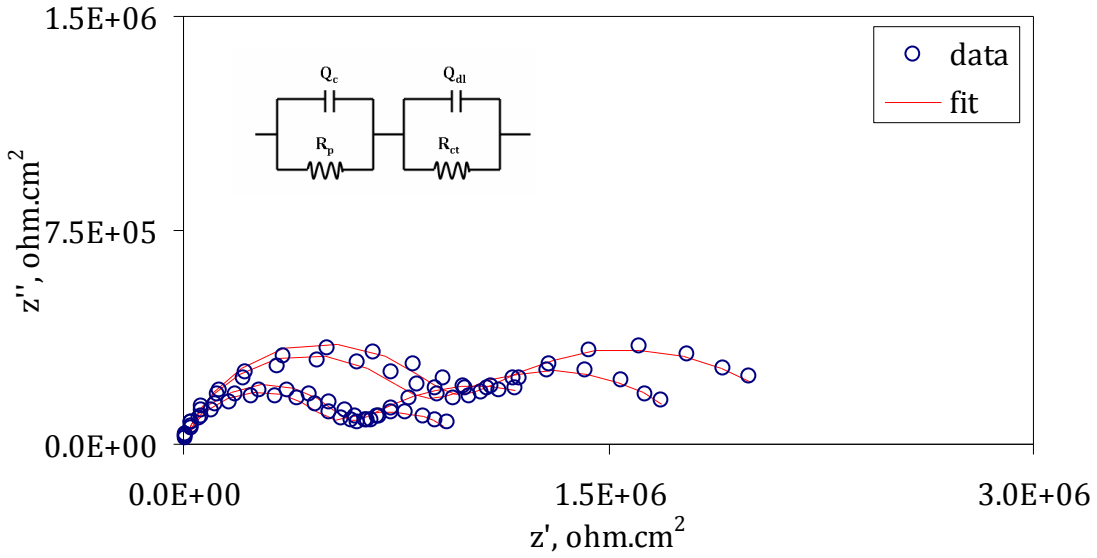

Figure 4.27 - Experimental (o) and simulated (-) Nyquist plot of 1L-EP coating exposed at various temperatures after 14 days of exposure at 50°C

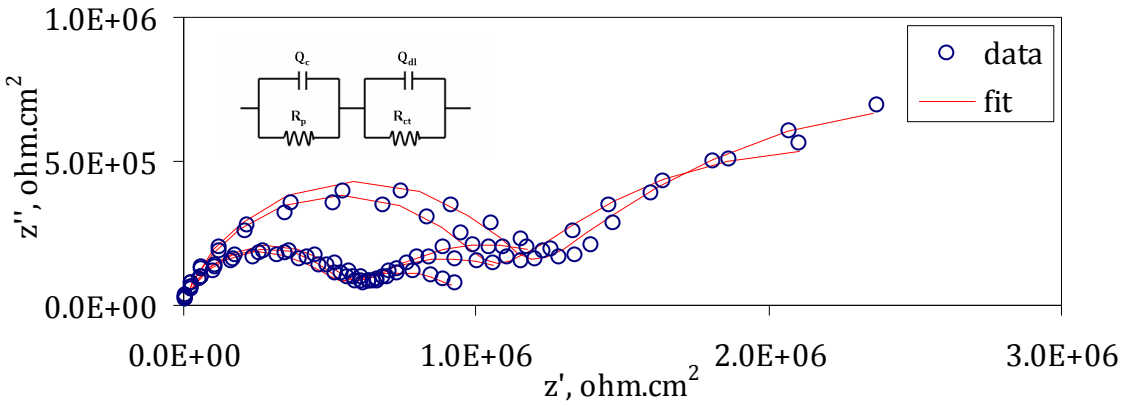

Figure 4.28 - Experimental (o) and simulated (-) Nyquist plot of 1L-EP coating exposed at various temperatures after 30 days of exposure at 50°C

Table 4.3 – Parameters for 1L-EP coating from fitting of EIS after 14 days exposure at 50°C

Fitted circuit: [RQ][RQ]

T (°C)	Q_c $(Fcm^{-2})^n$	Q_c (%error)	n	R_p (ohm.cm²)	R_p (%error)	Q_{dl} $(Fcm^{-2})^n$	Q_{dl} (%error)	n	R_{ct} (ohm.cm²)	R_{ct} (%error)	X^2
30	1.27E-09	40.95	0.80	9.04E+05	15.26	2.82E-07	37.65	0.57	2.25E+06	35.20	1.09E-02
35	1.38E-09	41.82	0.80	8.03E+05	17.73	2.86E-07	47.48	0.57	1.84E+06	37.16	1.16E-02
40	1.51E-09	47.77	0.79	6.94E+05	21.48	2.82E-07	53.52	0.57	1.48E+06	39.89	1.17E-02
50	1.83E-09	70.26	0.79	4.90E+05	37.47	2.20E-07	65.99	0.57	9.39E+05	54.64	1.16E-02

Table 4.4 – Parameters for 1L-EP coating from fitting of EIS after 30 days exposure at 50°C

Fitted circuit: [RQ][RQ]

T (°C)	Q_c $(Fcm^{-2})^n$	Q_c (%error)	n	R_p (ohm.cm²)	R_p (%error)	Q_{dl} $(Fcm^{-2})^n$	Q_{dl} (%error)	n	R_{ct} (ohm.cm²)	R_{ct} (%error)	X^2
25	1.26E-09	34.90	0.80	1.14E+06	12.02	5.87E-07	35.32	0.55	4.14E+06	96.70	1.29E-02
30	1.38E-09	37.41	0.79	1.02E+06	13.01	6.28E-07	37.69	0.54	3.43E+06	90.63	1.33E-02
40	1.69E-09	45.93	0.79	5.54E+05	15.44	8.01E-07	43.42	0.51	1.52E+06	60.15	1.25E-02
45	1.84E-09	51.16	0.79	5.23E+05	18.18	7.72E-07	49.36	0.51	1.28E+06	58.03	1.33E-02
50	2.05E-09	61.26	0.79	4.88E+05	24.62	6.18E-07	59.15	0.52	1.00E+06	55.36	1.34E-02

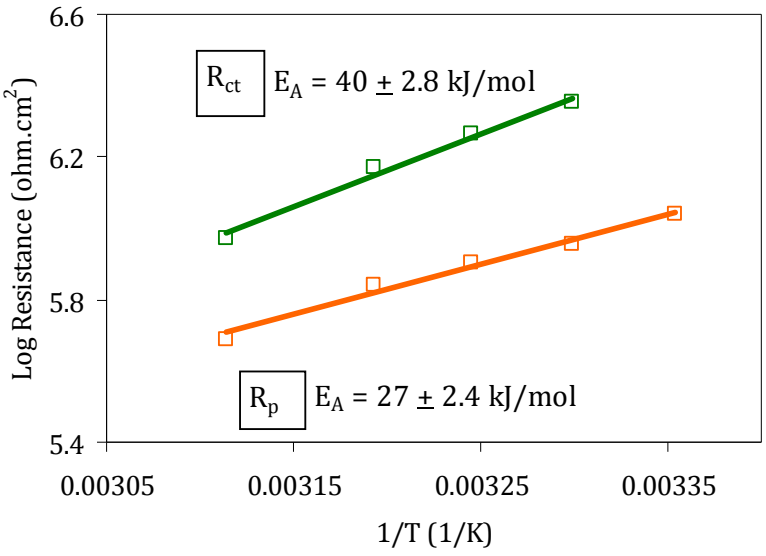

Figure 4.29 - Arrhenius plot of R_p and R_{ct} for 1L-EP coating after 14 days of exposure at 50°C

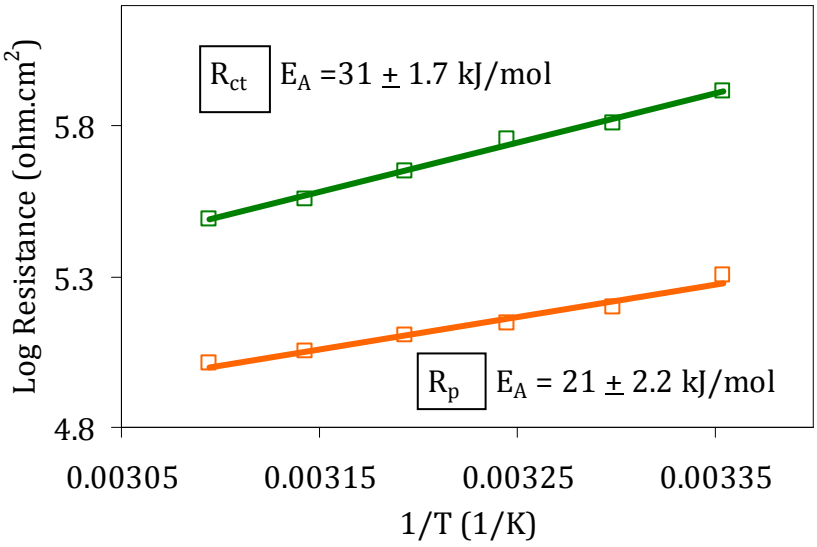

Figure 4.29a - Arrhenius plot of R_p and R_{ct} for 1L-EP coating (other panel) after 14 days of exposure at 50°C

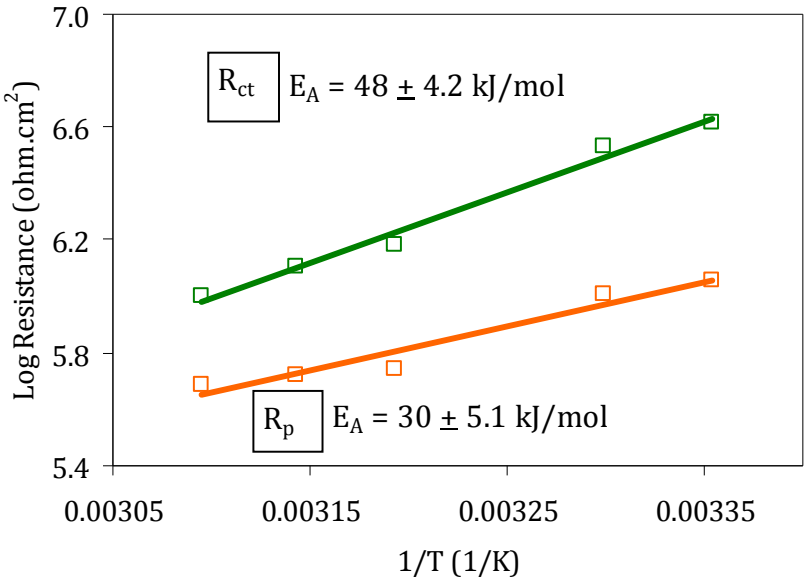

Figure 4.30- Arrhenius plot of R_p and R_{ct} for 1L-EP coating after 30 days of exposure at 50°C

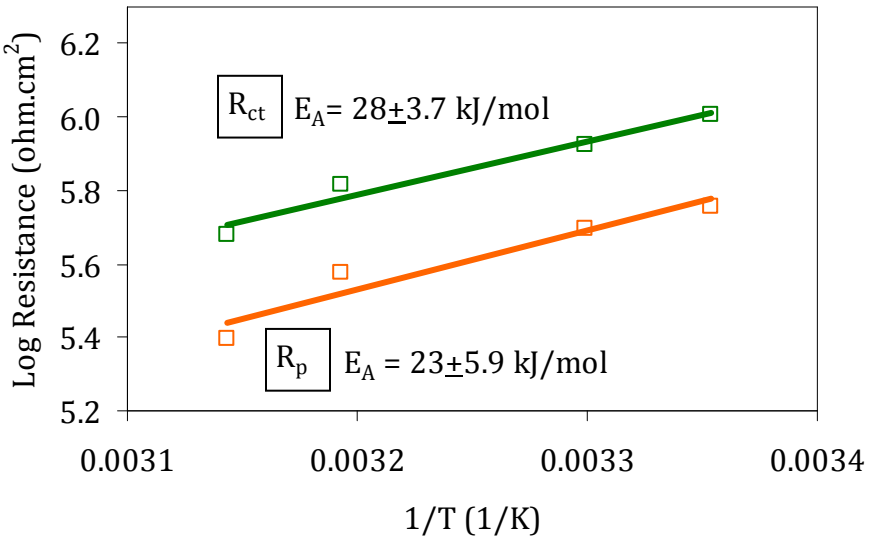

Figure 4.30a- Arrhenius plot of R_p and R_{ct} for 1L-EP coating (other panel) after 30 days of exposure at 50°C

A Review on Activation Energy from Some other Workers

Leidheiser and Wang [155] conducted a study on the effect of temperature on cathodic delamination of polybutadiene on galvanized steel. Their result yielded an activation energy for the delamination process of the order of 39.8kJmol^{-1}, a reasonable value for a diffusion process. Leidheiser and Catino [156] extended this study on the effect of temperature on cathodic delamination of polybutadiene on low carbon steel substrates in different alkali metal chloride solution. Their Arrhenius plots based on the delamination rate yielded activation energies of 50.64, 56.49, 48.96, 45.19 and 45.19 kJmol^{-1} for LiCl, NaCl, KCl, RbCl and CsCl respectively. They concluded that these activation energies are consistent with a rate-controlling process based on diffusion through the coating. Kellner [157] reported that the temperature dependence of cathodic disbondment of polyethylene tape with butyl rubber adhesive on blasted steel pipeline exposed to soil solution is 21.1 kJmol^{-1}. He also determined the temperature dependence for water diffusion in the coating using AC impedance and the value is 21.8 kJmol^{-1}.

Mill and Mayne [106, 107] determined the activation energy for charge transport for some paint films by measuring the resistance of free film as a function of temperature, the plotting of log (resistance) versus 1/T. The activation energies were found to vary from about 25–40 kJmol^{-1} for D-type films to 160 kJmol^{-1} for I-type films. Leidheiser et al. [158] obtained much lower activation energy values for I-type films of around 80–120 kJmol^{-1}. Steinsmo and co-workers [159] found a much wider range for the activation energy for charge transport through paint films between 51 and 227 kJmol^{-1}.

More recent work by Ochs and Vogelsang [160] showed that thicker coatings generated higher activation energies and their values range from 125 to 240 $kJmol^{-1}$.

4.3.5 Activation Energy for Ion Conduction and Corrosion Process

The effect of temperature on ion transport through the film and corrosion process can now be compared. For the PCE coating, the activation energy for ion transport (calculated from R_p) varies between 14 and 25 $kJmol^{-1}$ whereas for the 1L-EP coating it varies between 27 and 30 $kJmol^{-1}$. It is interesting to note that activation energies determined for the corrosion process (calculated from R_{ct}) for both coatings are significantly higher than the activation energies determined for ion transport through the film from the same EIS measurement. Activation energies determined from this work are summarized together with values from the literature (**Table 4.5**). The values obtained from this work are sensible as they lie within the range of values found in the literature [106, 107, 155-157, 159, 161].

From this work, it is quite clear that the activation energy for the corrosion reaction is significantly higher than that for ion conduction through the coating, thus ion conduction at defects determined from R_p cannot be controlling the corrosion rate. This is an important new observation that questions the value of coating resistance, as determined from AC impedance, as an indicator of the ability of a coating to protect the underlying metal. The possibility that corrosion is limited by higher resistance regions of the coating that form part of the corrosion current circuit, but cannot be measured because they are in parallel with low-resistance defects cannot be ruled out. However,

previous work on steel-zinc bi-electrodes has shown that polarization of the zinc limits the corrosion rate, rather than ionic resistance of the coating [162].

Table 4.5 - Activation energies for ion conduction or cathodic disbonding in paint film

Coating	Activation energy, E_A kJmol^{-1}		Reference
	R_p	R_{ct}	
Polyamide cured epoxy[3]	14–25	35–49	This work[1]
Epoxy phenolic[3]	27–30	28–48	This work[1]
Epoxy polyamide[3]	33	-	Skar [161][2]
Polybutadiene[3]	40	-	Skar [161][2]
Epoxy polyamide[4]	25–40	-	Mills and Mayne [107][1]
Polybutadiene[3]	39–69	-	Leidheiser and Catino [156][2]

[1] E_A for ion conduction
[2] E_A for cathodic disbonding
[3] Coated panel
[4] Free film

4.3.6 Activation Energy for Heating up and Cooling down Process

The results reported in **Section 4.3.5** were obtained in the cooling regime, thus it is desired to check whether they are reproducible in heating-cooling cycles on the same coated panel. The heating-cooling cycle started with heating of the coated panel in a controlled water bath from 21^{o}C to 50^{o}C while taking the EIS measurement at 25^{o}C, 35^{o}C, 45^{o}C and 50^{o}C. Then the coated metal was removed from the water bath and left to cool to room temperature in an insulated box while taking the EIS measurement at similar temperature intervals.

Figure 4.31 shows the change in the impedance modulus, |Z| at low frequency value (0.1Hz) during heating up and cooling down. All three coatings show a similar trend where |Z| drops as the temperature is raised. The impedance modulus increased again during cooling over a period of 5 hours but did not return to its initial value.

However in another extended test on a different heating-cooling regime (**Section 4.3.7**), if the coated panel was left for adequate time over a longer time scale, the impedance values did eventually return to the original value. This suggests that in addition to the direct affect of temperature on activated processes there is a slower change in the system; for instance equilibration with water. In addition, although the effect of heating is partially reversible, the coatings do show a degree of irreversible behaviour. Similar results were observed by Valentinelli et al. where they attributed this situation to absorption-desorption of water due to polymer shrinkage during exposure to elevated temperatures [163]. Miszcyk and Darowicki have found that the

increased water uptake at elevated temperatures is partially irreversible as the absorbed water was not fully desorbed during the subsequent cooling process. They claimed that the excess water may be permanently locked in micro-crack, micro-voids and local delamination sites [164].

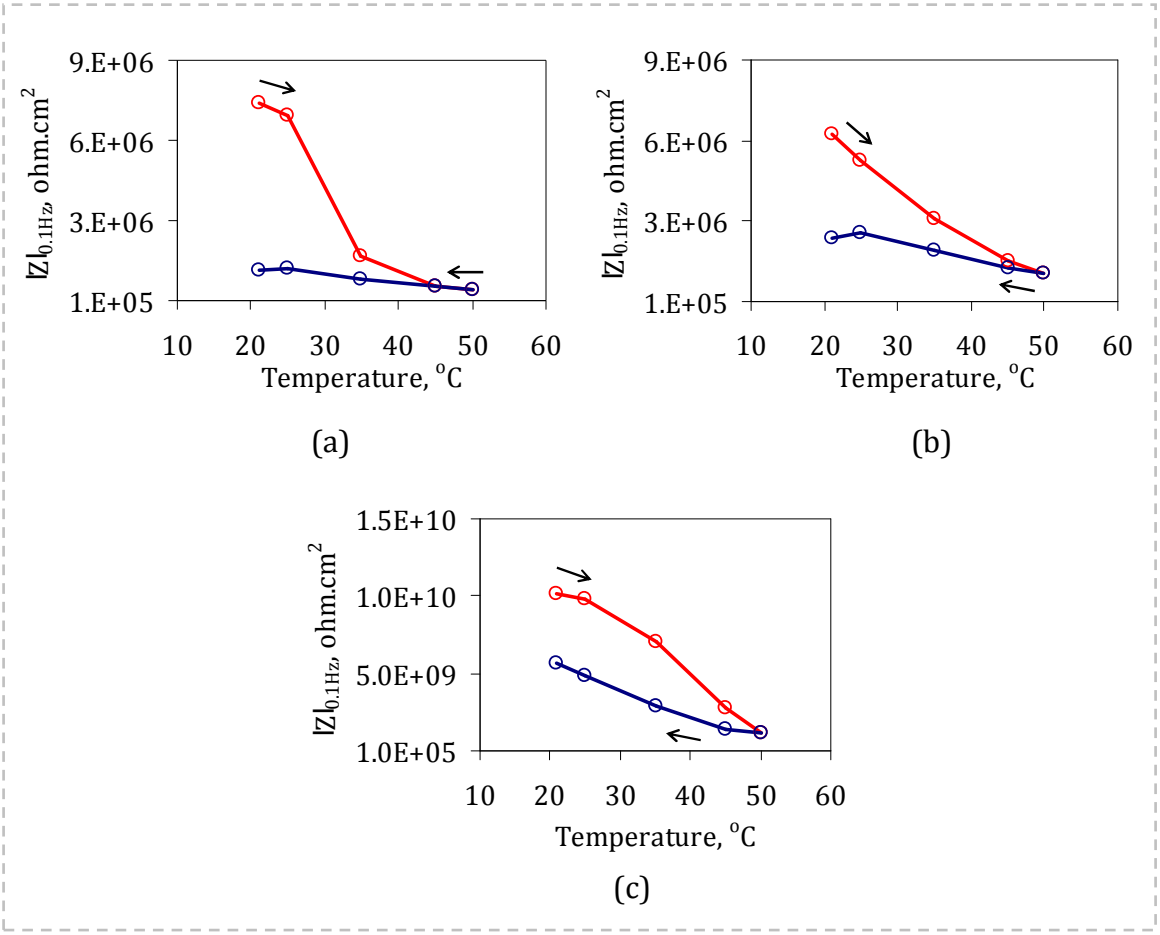

Figure 4.31 - Impedance modulus vs. temperature during heating (red line) and cooling (blue line) regimes for (a) PCE, (b) 2-CE and (c) 2L-EP coating

The impedance spectra from both tests were further analyzed with non-linear least squares fitting software (ZSimpWin). Then the logarithms of coating resistances were plotted against the reciprocal of temperature to construct the Arrhenius plots

illustrated in **Figure 4.32**. It was observed that the PCE and 2-CE coating have comparable activation energies from the cooling and heating regimes but not the 2L-EP coating. For the 2L-EP coating, the activation energy from the heating regime is almost double the activation energy from the cooling regime. The high activation energy for the heating regime may be due to water that is not totally removed during cooling. In addition, 2L-EP is a thicker coating which provides evidence that transport of species into and out of the film is limited.

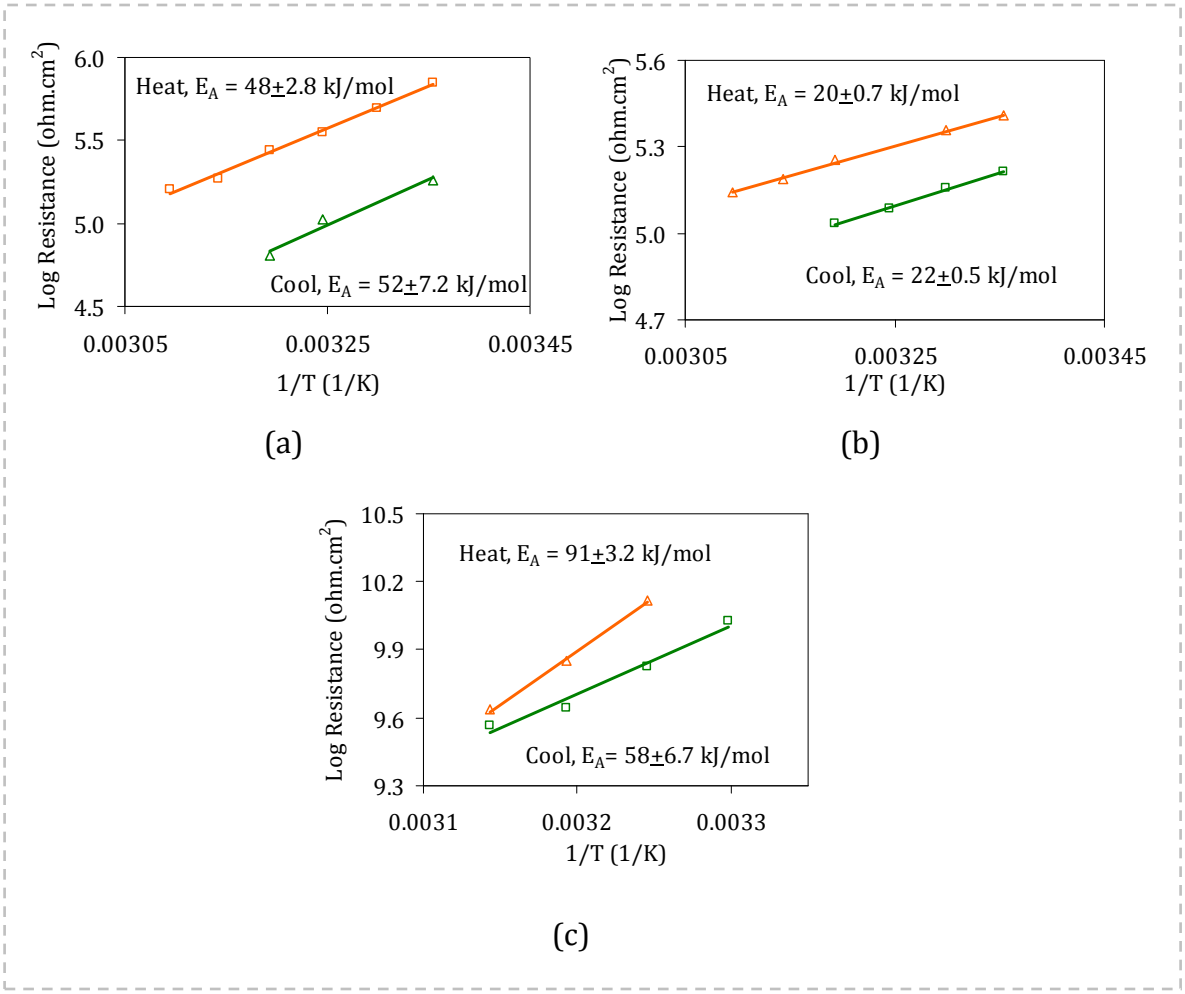

Figure 4.32 Arrhenius plots for heating up and cooling down regimes for (a) PCE; (b) 2-CE and (c) 2L-EP coating

4.3.7 Effect of Fast Heating and Cooling Test

This test uses more extreme temperature changes to investigate the recovery process of coating properties when the coated panel is exposed to hot solution for a short time. Initially the coated panel is immersed at 25°C until the EIS measurements are able to be recorded (roughly after 2 hours). The coated panel is then transferred into a 50°C NaCl solution and left to equilibrate for half an hour. The EIS measurements were subsequently recorded then the hot coated panel is transferred back into a 25°C NaCl solution. The hot coated panel is left to cool in the 25°C solution while EIS measurements are recorded over the cooling period.

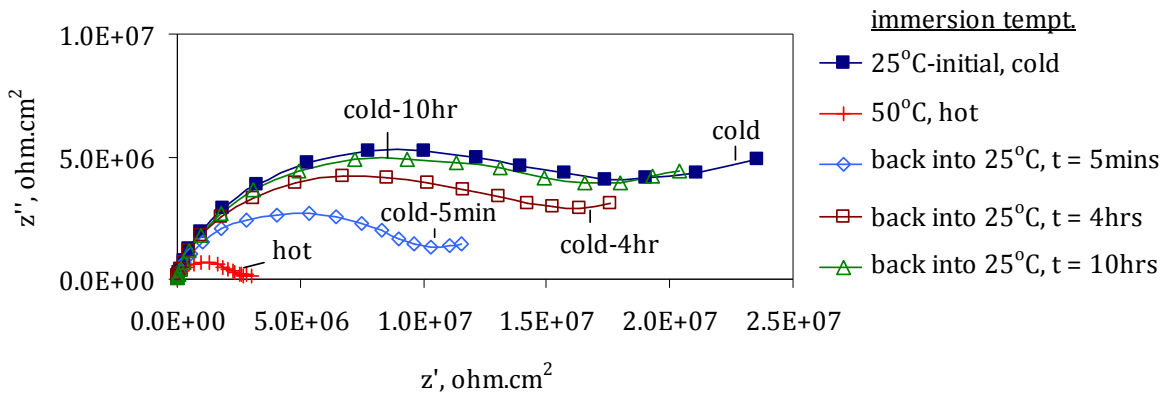

Figure 4.33 – Nyquist plots for 1L-EP coating showing changing response after moving the sample from cold to hot and back to cold solution

Figure 4.33 shows the Nyquist plot which represents the impedance spectra at stages before and during exposure at 50°C and when the coated metal is left to cool in solution at 25°C. Notice the drastic reduction in semicircle diameter when the coated panel is transferred from the cold solution to the hot solution. However, when the

coated panel is transferred back into the cold solution, the impedance spectra recovers back to the original shape but only after sufficient time; to allow for the water content to return to the equilibrium value.

To get more of an idea on what is happening during cooling; some of the impedance spectra in this test are fitted with the equivalent circuit R[Q[R[QR]]] to determine the resistance of the coating. Then the logarithm of the coating resistance versus the reciprocal of temperature is plotted based on impedance spectra recorded while the coated panel was placed in the hot solution and during cooling in the cold solution. This can give an estimate based on two temperature points for the Arrhenius plots. Using the slope of the lines, the calculated activation energies are 62, 45 and 60 $kJmol^{-1}$ for initial immersion, 5 minutes cooling and 10 hours cooling respectively.

This test indicated that if the coated panel was left for adequate time over a longer time scale, in this case after 10 hours, the impedance values did return to the original value. The activation energy taken using the resistance after 10 hours equilibration is comparable to that value at initial immersion. This is probably associated to the effect of water which usually related to faster charge-transport mechanisms. This water effect seems to be the most relevant in this case which shows a change in activation energy during cooling. At $50^{o}C$, equilibrium water content in the coating is achieved very quickly. However, the water content in the coating seems to equilibrate more slowly at $25^{o}C$.

4.3.8 The Effect of Cation Mobility on Coating Behaviour

In this work, the influence of the cation mobility on the electrochemical behaviour of coating was studied when immersed in high temperature solution. The aim is to explore the link between conduction in the coating through cations and the corrosion process beneath the coating. For that purpose, the coated metals were immersed in 0.5M chloride solution with different cations (Na^+, K^+ and Li^+). It is expected that a bigger cation will have bigger activation energy for ion transport through the coating. Two different coatings; 2-component epoxy (2-CE) and epoxy-phenolic (1L-EP) have been tested to find the link between the effects of cation mobility on the electrochemical behaviour when being exposed at high temperature immersion.

Observations and Comments of Some Workers

Work carried out by Leidheiser and co-workers [165] concluded that the rate of cathodic delamination in alkaline chloride solution increases when the hydrated cation radius decreases. Stratman et al. [144] concluded that the rate-determining step for delamination is given by the transport of cations along the metal/polymer interface. More recently it was shown by Deflorian and Rossi [166] that hydrated cations with a larger radius (Li^+ and Na^+) migrate mainly through the coating defects, while hydrated cations with a smaller radius (K^+ and Cs^+) diffuse through the intact coating. Mcleod [167] reported the same order of increasing rate of cathodic disbonding with cation type for vinyl coating and chlorinated rubber where Na^+ and Li^+ generate the smallest disbond area while K^+ generates the largest. He also measured the mobility of alkali-

metal ions in the coatings used; the ranking in mobility was $Li^+ < Na^+ < K^+$ which is in agreement with the size of its hydrated ion.

Evolution with Time of EIS Plots for 2-CE Coating

Figures 4.34 and **4.35** show the Nyquist and Bode plots for the 2-CE coating immersed in the respective 0.5M chloride solutions at 50°C. The presence of two semicircles is seen after 1 day for coatings immersed in K^+ solution (**Figure 4.34a**) and Na^+ solution (**Figure 4.34b**). In **Figure 4.34c**, the degradation is slower for the coating in Li^+ solution, with indication of a second semicircle emerging at 7 days and becoming quite distinct by 14 days.

The dependency of the impedance results on the cation present is evident from the beginning of immersion. It can be seen clearly from **Figure 4.35** that after 1 day of immersion, the drop in the impedance modulus at low frequency is dependent on the cation mobility, with K^+ and Na^+ solutions inducing more rapid decreases compared to the Li^+ solution.

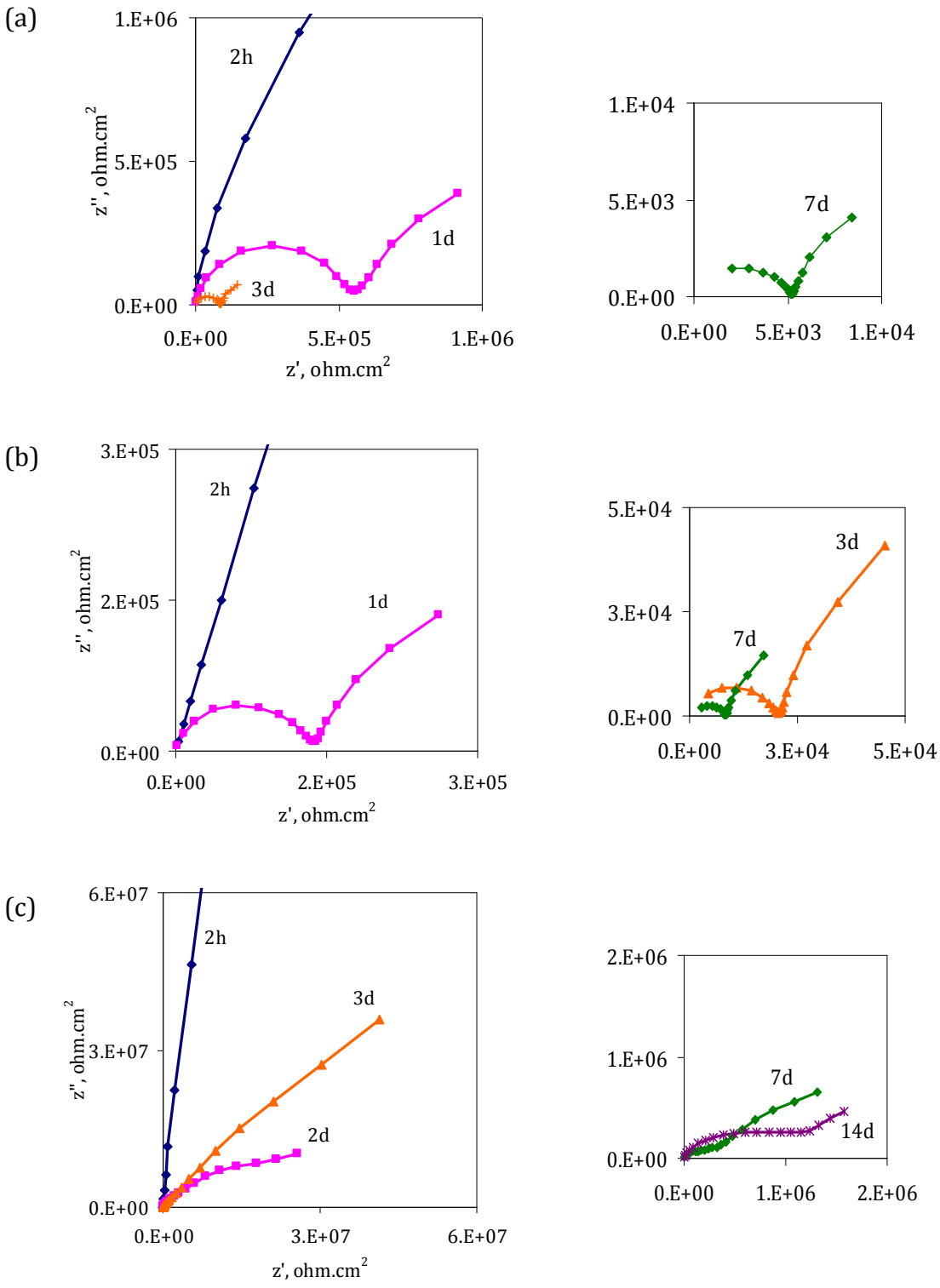

Figure 4.34 – Nyquist plots for 2-CE coating measured at 21°C and exposed at 50°C and immersed in (a) 0.5MKCl; (b) 0.5MNaCl and (c) 0.5MLiCl solution

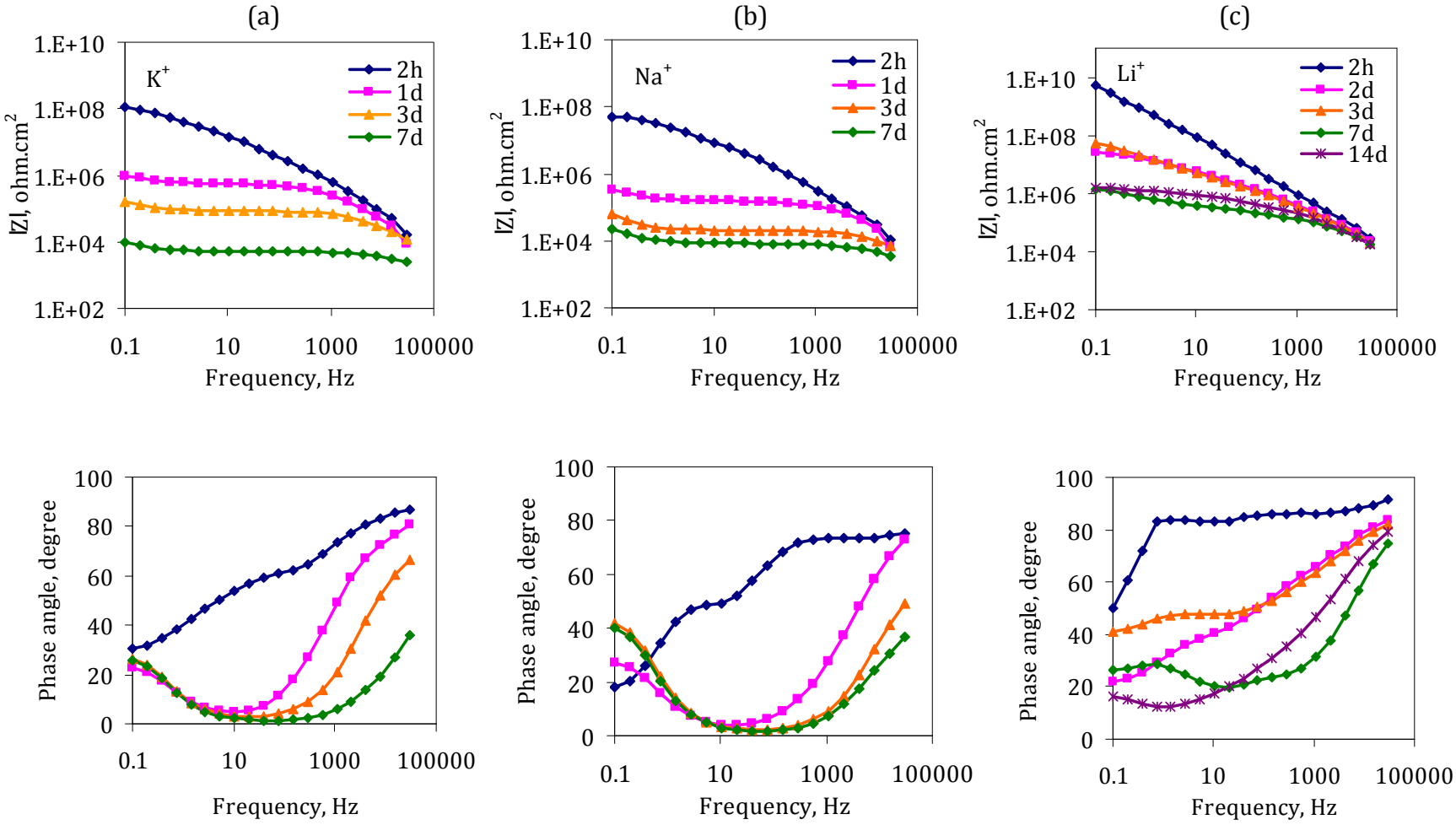

Figure 4.35 - Bode plots for 2-CE coating measured at 21°C and exposed at 50°C and immersed in

(a) 0.5MKCl; (b) 0.5MNaCl and (c) 0.5MLiCl solution

Greater severity of blistering is observed for coated panels exposed in K^+ and Na^+ solutions by 3 days of exposure. Subsequently, the coated metals in Na^+ and K^+ solutions show total failure after 7 days of immersion. It was observed that the coatings on both panels were covered in blisters (**Figure 4.36**). It can be seen that the size of blisters on coated panel exposed in the Na^+ solution is bigger than blisters on coated metal exposed in the K^+ solution, contrary to what might be expected. In contrast, the coated metal in the Li^+ solution is still fairly good which can probably attributed to the low mobility of the Li^+ ion.

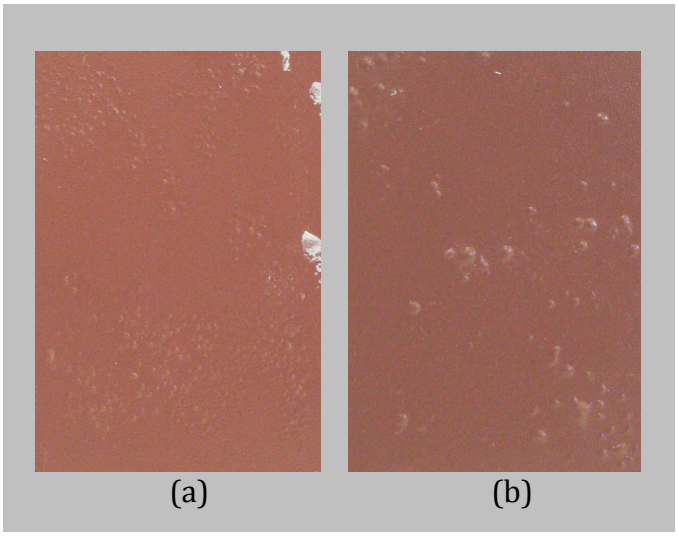

Figure 4.36 Images of 2-CE coated metal covered with blisters after 7 days exposure at 50^{o}C in (a) KCl and (b) NaCl solution

Evolution of 2-CE Coating Parameter with Time

The impedance spectra were fitted to an equivalent circuit R[Q[R[QR]]] and the value of each component in the circuit model is obtained and plotted as a function of the

immersion time (**Figures 4.37** and **4.38**). The resistance of the coated panels exposed to Na^+ and K^+ solutions dropped over time, however not for panels in the Li^+ solution. At early immersion its value rose and then one of the duplicates dropped rapidly while the other stayed constant. The coating capacitance rose over time for coatings exposed to all three cation solutions. These results suggest that 2-CE coatings in K^+ and Na^+ solutions do not provide long-term corrosion protection compared with coatings immersed in Li^+ solution. The inferior corrosion resistance behavior of coatings in Na^+ and K^+ solutions may be attributed to the large hydration ion size of Li^+ leading to a slower penetration of ion into the coating thus giving a slower rate of coating degradation. Cations will migrate into the coating at cathodic sites, suggesting this is where degradation occurs which leads to blisters. Notice that a sudden drop in resistance value for the coated panel exposed to the Li^+ solution (Li-1) is accompanied by a drop in capacitance as well. The presence of blisters and pinhole corrosion were observed on that panel surface (**Figure 4.39**).

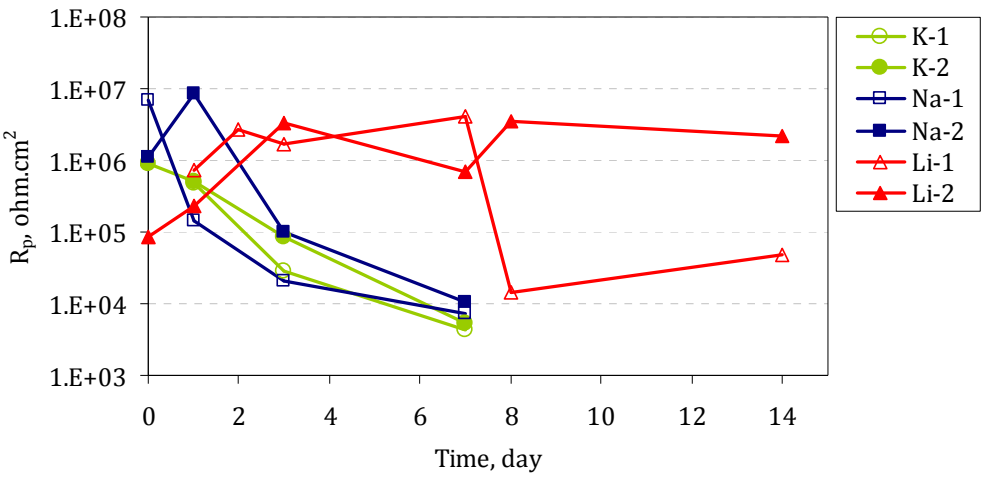

Figure 4.37 - Evolution of coating resistance with time for 2-CE coating (duplicate panels) immersed in K^+, Na^+ and Li^+ solution

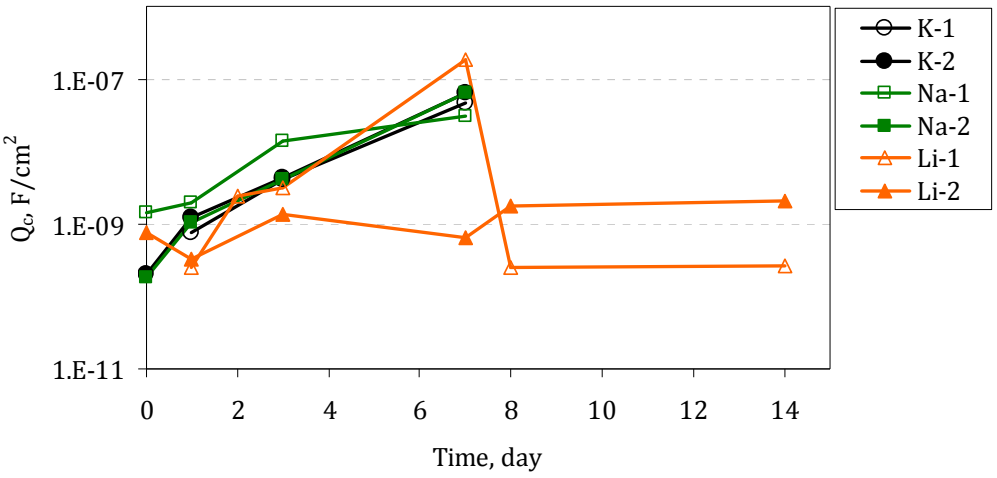

Figure 4.38 - Evolution of coating capacitance with time for 2-CE coating (duplicate panels) immersed in K^+, Na^+ and Li^+ solution

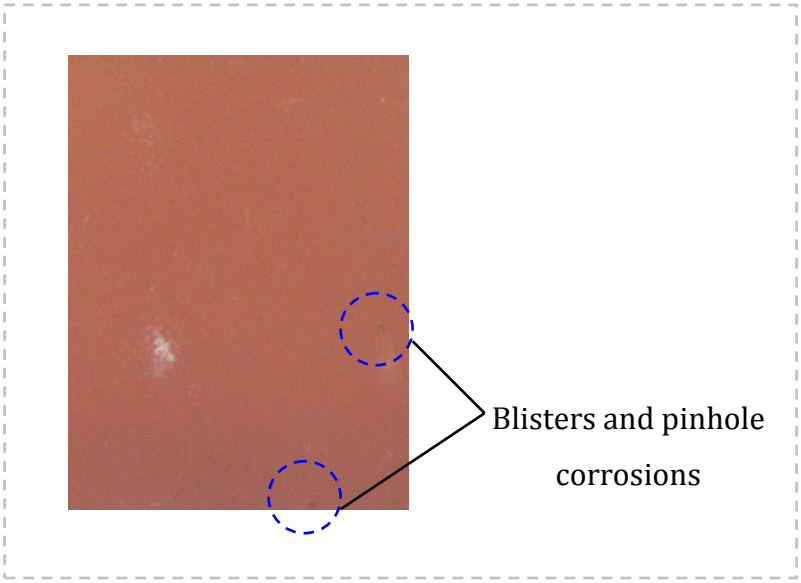

Figure 4.39 - Images of 2-CE coated metal (Li-1) with blisters and pinhole corrosions after 8 days exposure at 50°C in LiCl solution

Temperature Dependence of 2-CE Coating in Alkali Metal Chloride Solution

Figure 4.40 shows the Nyquist plot at various temperatures for the 2-CE coating after 3 days of immersion in K^+, Na^+ or Li^+ solutions. Two obvious time constants were observed for coatings in K^+ and Na^+ but not in Li^+. To evaluate the effect of temperature on the cation conduction, **Figure 4.40** was fitted with the equivalent circuit R[Q[R[QR]]] and good agreement was observed between the measured data and the fit (**Figure 4.41**). Notice two time constants with a Warburg equivalent circuit were used for Li^+ despite no obvious appearance of two semicircles in the spectra as it gave the best fit (**Figure 4.41c**).

Coating resistance, R_p and charge transfer resistance R_{ct} are then plotted against the reciprocal of temperature to give the activation energies for ion conduction in the film and the corrosion process (**Figure 4.42**). Arrhenius plots for alkali metal halide solutions based on ion conduction yielded activation energies of 9, 18 and 15 $kJmol^{-1}$ whereas for the corrosion process, activation energies of 10, 5 and 100 $kJmol^{-1}$ for KCl, NaCl and LiCl respectively were yielded.

(a) K^+

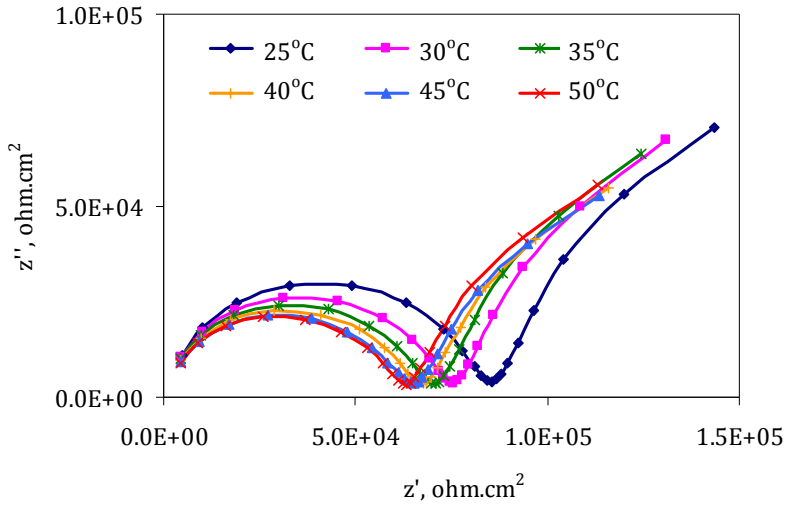

(b) Na^+

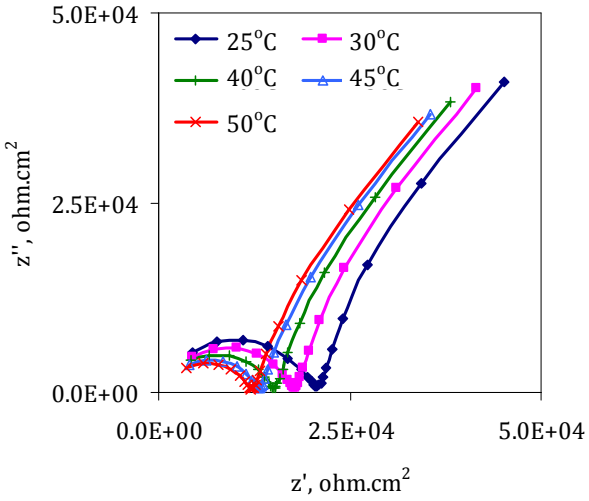

(c) Li^+

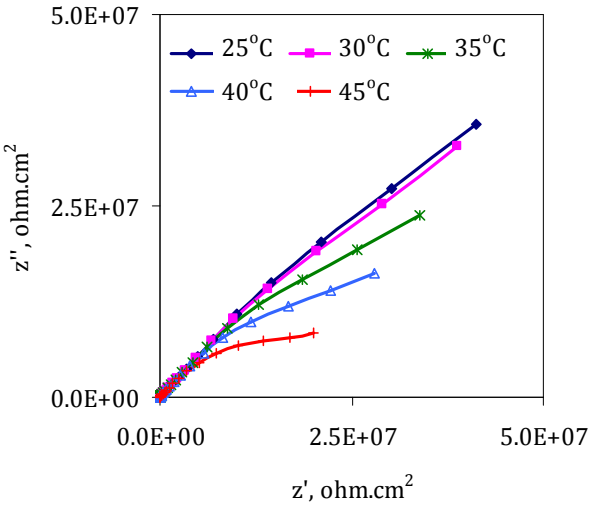

Figure 4.40 - Nyquist plots at various temperatures for 2-CE coating after 3 days immersion at 50°C in (a) KCl ; (b) NaCl and (c) LiCl solution

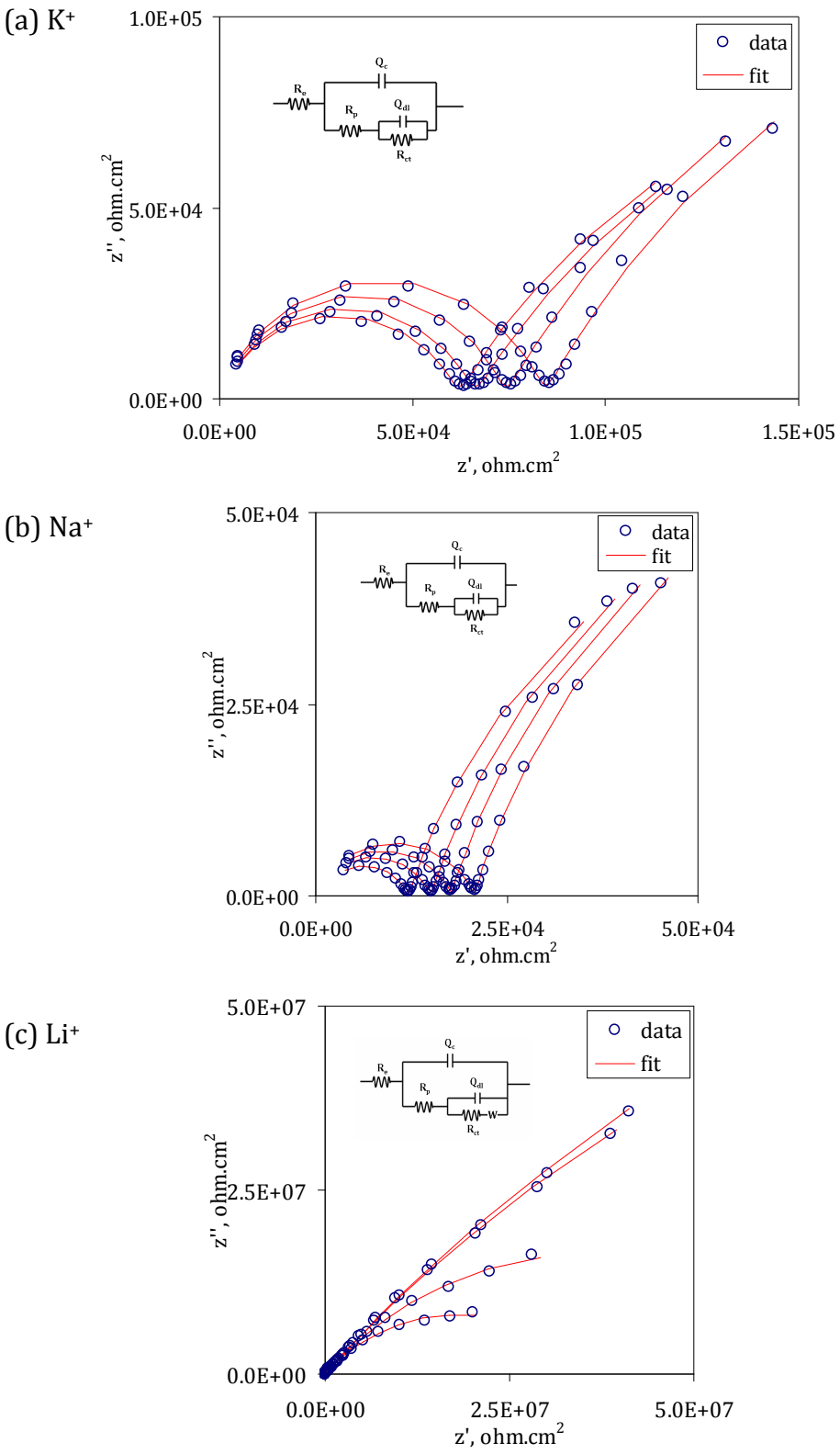

Figure 4.41 - Experimental (o) and simulated (-) Nyquist plot of 2-CE coating after 3 days immersion at 50°C in (a) KCl ; (b) NaCl and (c) LiCl solution

Table 4.6 - Parameters for 2-component epoxy coating from fitting of EIS after 3 days immersion at 50°C in KCl solution

T (°C)	Q_c $(Fcm^{-2})^n$	Q_c (%error)	n	R_p ($ohm.cm^2$)	R_p (%error)	Q_{dl} $(Fcm^{-2})^n$	Q_{dl} (%error)	n	R_{ct} ($ohm.cm^2$)	R_{ct} (%error)	X^2
25	4.36E-09	12.99	0.81	8.40E+04	1.36	1.27E-05	4.87	0.69	3.95E+05	35.76	6.12E+04
30	4.62E-09	14.63	0.80	7.39E+04	1.53	1.34E-05	5.08	0.69	3.80E+05	37.34	7.09E+04
35	4.92E-09	15.63	0.80	6.91E+04	1.64	1.40E-05	5.36	0.68	3.63E+05	39.26	7.74E+04
40	5.65E-09	14.27	0.79	6.59E+04	1.53	1.57E-05	5.27	0.67	3.22E+05	38.12	6.31E+04
45	6.39E-09	19.34	0.79	6.33E+04	2.13	1.59E-05	7.26	0.65	3.13E+05	51.32	1.13E+03
50	7.03E-09	17.45	0.78	6.18E+04	1.90	1.53E-05	6.12	0.68	2.90E+05	38.86	9.95E+04

Table 4.7 - Parameters for 2-component epoxy coating from fitting of EIS after 3 days immersion at 50°C in NaCl solution

T (°C)	Q_c $(Fcm^{-2})^n$	Q_c (%error)	n	R_p ($ohm.cm^2$)	R_p (%error)	Q_{dl} $(Fcm^{-2})^n$	Q_{dl} (%error)	n	R_{ct} ($ohm.cm^2$)	R_{ct} (%error)	X^2
25	1.35E-08	11.32	0.75	2.07E+04	1.49	2.68E-05	1.46	0.75	1.82E+05	10.44	1.83E+04
30	1.39E-08	11.37	0.75	1.77E+04	1.60	2.74E-05	1.31	0.75	1.79E+05	9.34	1.62E+04
40	1.57E-08	12.21	0.74	1.52E+04	1.87	2.84E-05	1.29	0.74	1.68E+05	8.83	1.68E+04
45	1.86E-08	13.91	0.74	1.31E+04	2.22	2.95E-05	1.38	0.74	1.59E+05	9.19	1.99E+04
50	1.88E-08	17.18	0.75	1.17E+04	2.67	3.03E-05	1.64	0.75	1.56E+05	10.99	2.87E+04

Table 4.8 - Parameters for 2-component epoxy coating from fitting of EIS after 3 days immersion at 50°C in LiCl solution

T (°C)	Q_c $(Fcm^{-2})^n$	Q_c (%error)	n	R_p ($ohm.cm^2$)	R_p (%error)	Q_{dl} $(Fcm^{-2})^n$	Q_{dl} (%error)	n	R_{ct} ($ohm.cm^2$)	R_{ct} (%error)	X^2
25	5.56E-10	35.19	0.93	4.19E+05	37.01	2.06E-08	5.22	0.52	3.88E+08	63.96	7.56E+04
30	5.03E-10	43.42	0.94	3.39E+05	42.96	2.15E-08	5.21	0.52	2.99E+08	51.91	8.44E+04
35	5.64E-10	42.77	0.93	3.23E+05	38.23	2.29E-08	5.54	0.53	1.31E+08	26.74	9.24E+04
40	6.35E-10	43.52	0.93	2.99E+05	37.71	2.45E-08	5.67	0.53	7.27E+07	16.98	8.89E+04
45	7.35E-10	37.02	0.92	2.82E+05	30.81	2.63E-08	5.70	0.54	3.29E+07	9.63	6.73E+04

(a) K^+

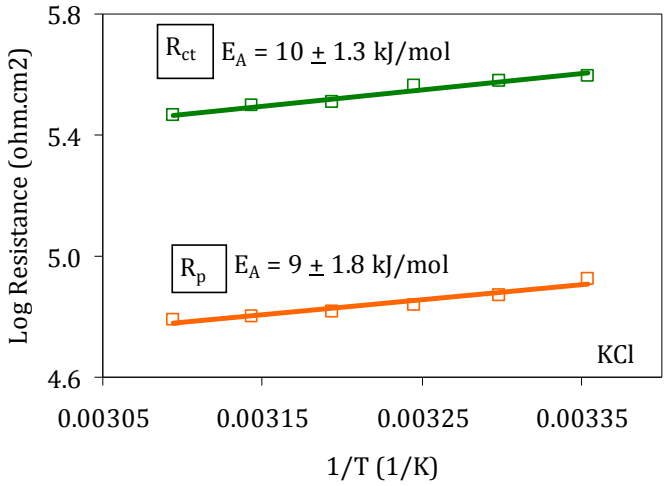

(a) Na^+

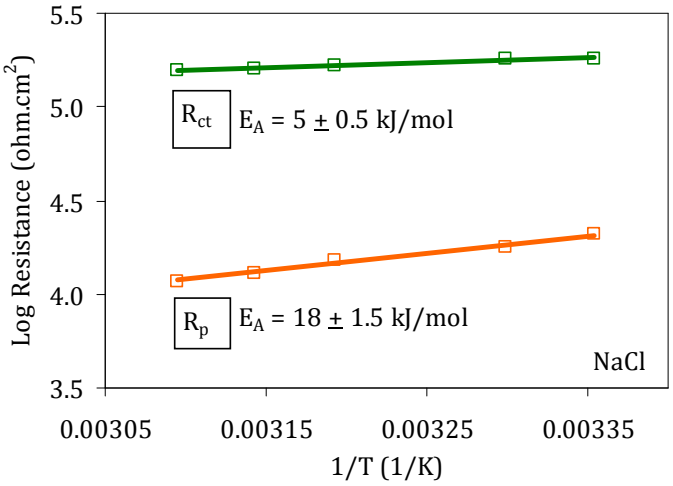

(a) Li^+

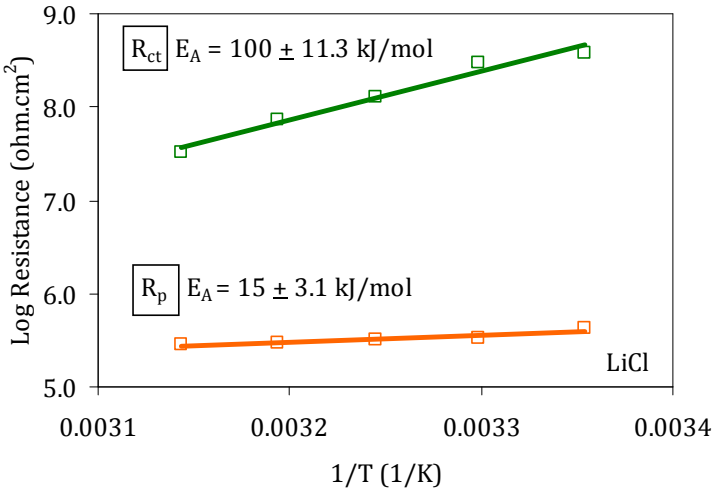

Figure 4.42 - Arrhenius plot of R_p and R_{ct} for 2-CE coating after 3 days immersion at 50°C in (a) KCl; (b) NaCl and (c) LiCl solution

Evolution with Time of EIS Plots for 1L-EP Coating

Figure 4.43 shows the Nyquist plots for the 1L-EP coating immersed in K^+, Na^+ and Li^+ solutions. The presence of two semicircles is seen at 1 day for the coating immersed in the K^+ solution (**Figure 4.43a**) and the Na^+ solution (**Figure 4.43b**). In **Figure 4.43c**, the degradation is slower in Li^+ solution, with indication of a second semicircle emerging only at 7 days. **Figure 4.44** shows the Bode plots for the 1L-EP coating immersed in the respective 0.5M chloride solutions at 50°C. All coated panels show almost pure capacitive behaviour before the temperature was raised to 50°C. After the first day of immersion at 50°C, all coated panels started to show some degradation.

The impedance modulus at the lowest frequencies decreases (by about two orders of magnitude) for coated panels immersed in Na^+ and K^+ solutions. The coated panels in Na^+ and K^+ solutions were further degraded with further decrease in the impedance modulus over the period of immersion. The presence of blisters were observed for coated panels exposed in K^+ and Na^+ solutions by 5 days of immersion. For coated panel immersed in the Li^+ solution, the impedance drops about one order of magnitude on the first day immersion in 50°C. As exposure time is increased, the impedance modulus at low frequency continued to decrease which indicates a degradation of the coating with the penetration of Li^+ ions within the coating film.

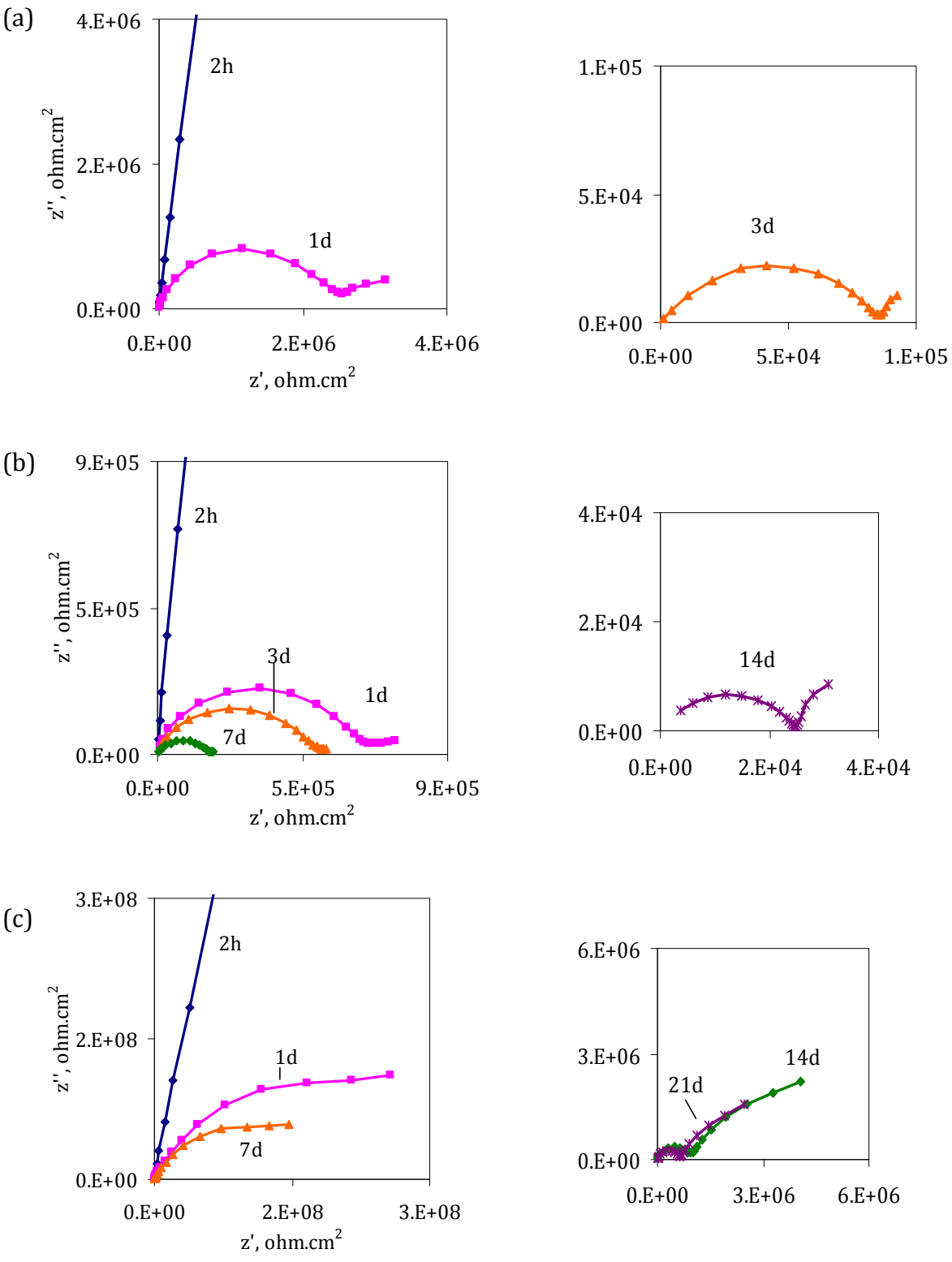

Figure 4.43 – Nyquist plots for 1L-EP coating measured at 21°C and exposed at 50°C and immersed in (a) 0.5MKCl; (b) 0.5MNaCl and (c) 0.5MLiCl solution

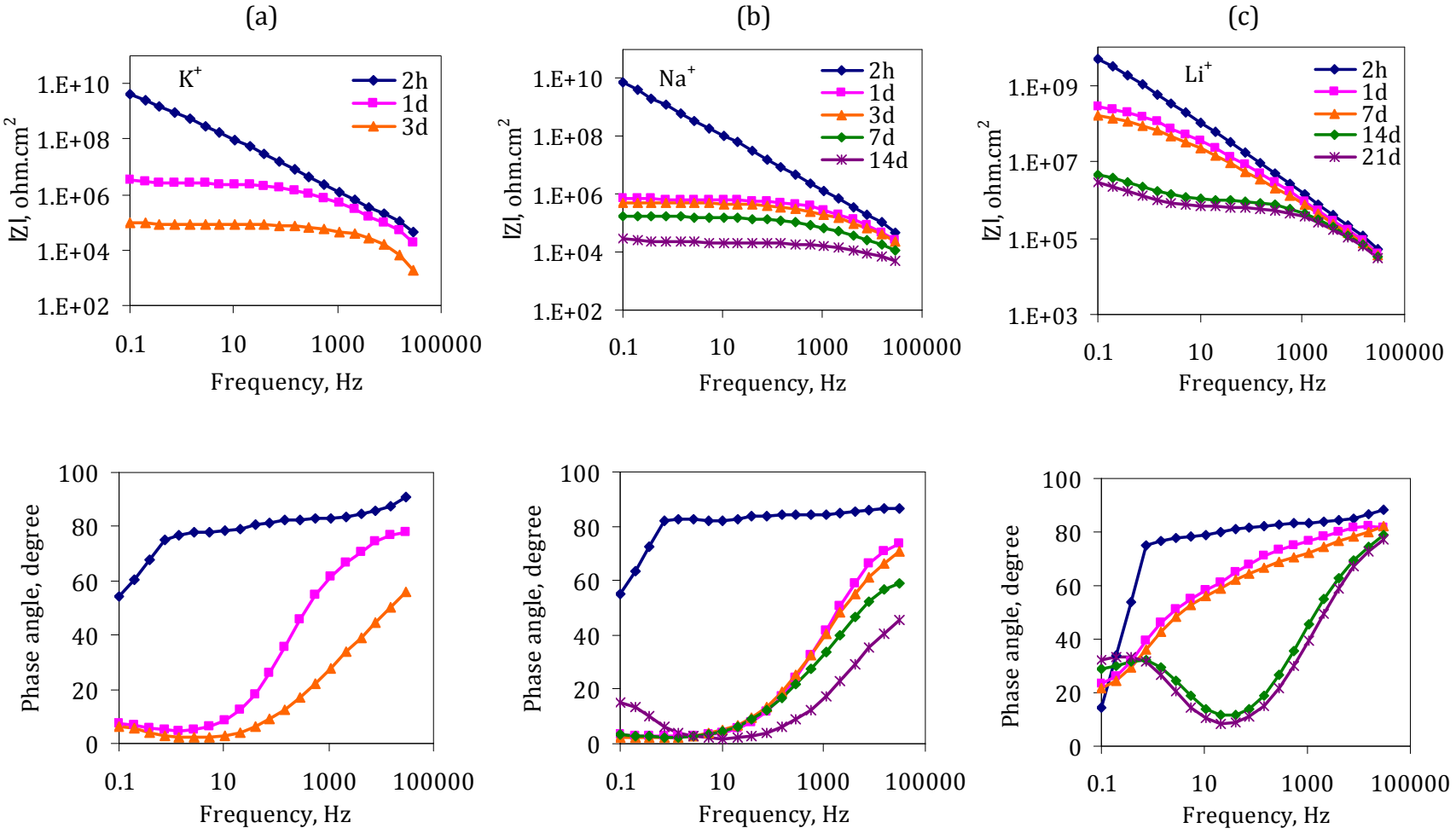

Figure 4.44 - Bode plots for 1L-EP coating measured at 21°C and exposed at 50°C and immersed in

(a) 0.5MKCl; (b) 0.5MNaCl and (c) 0.5MLiCl solution

Evolution of 1L-EP Coating Parameter with Time

Circuit values for coated panel in K^+ are not obtainable as a good fitting of the semicircle was very hard to achieve. **Figure 4.45** shows the values of coating resistance for duplicate panels of the 1L-EP coating in Na^+ and Li^+ solutions. After the first day immersion, the resistance decreases for all the samples. This is a consequence of the high temperature that accelerated the diffusion/migration of the cations into the coating. As immersion time increases, the resistance continues to decrease for all samples. The slow rate of decrease of coating resistance during the entire exposure period for coating in the Li^+ solution indicates that coatings have not deteriorated and low Li^+ ion mobility slows the failure of the coating.

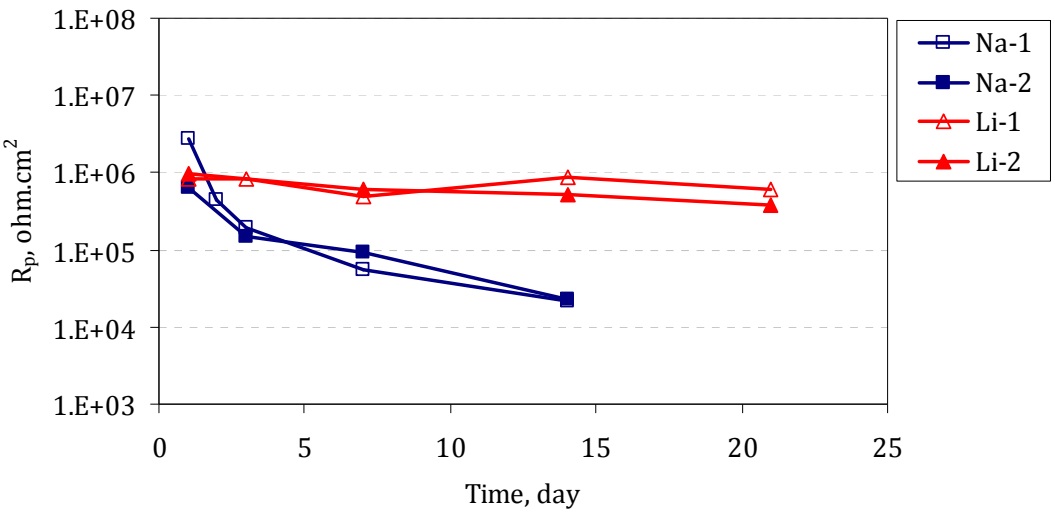

Figure 4.46 - Evolution of coating resistance with time for 1L-EP coating (duplicate panels) immersed in Na^+ and Li^+ solutions

The evolution of the coating capacitance against immersion time is summarised in **Figure 4.46**. Generally there is an increasing trend for all coated panels, except one coated panel immersed in a Na^+ solution that drops by day 14. However the corresponding coating resistance is behaving normally (decreasing over time). The increase in capacitance over the period is normally related to the water accumulation in the coating.

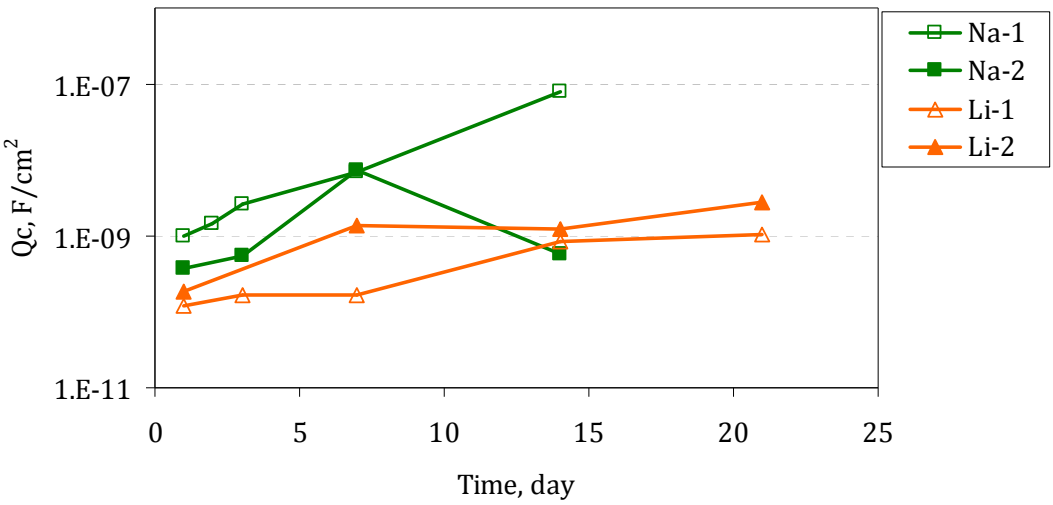

Figure 4.46 - Evolution of coating capacitance with time for 1L-EP coating (duplicate panels) immersed in Na^+ and Li^+ solutions

Temperature Dependence of 1L-EP Coating in KCl solution

Figure 4.47 shows the impedance spectra obtained for the 1L-EP coating at different temperatures after 3 days of exposure in the K^+ solution. From these spectra the strong influence of temperature on the impedance of the coating is evident. To determine the activation energies for ion migration, this semicircle is fitted to an appropriate

equivalent circuit. Even though the second semicircle is apparent, Nyquist plots are too difficult to fit using the ZSimpWin software. "Circle fit" from the ACM software was used instead to fit the first semicircle and the summary of the fitted parameters are given in **Table 4.9**. The plot of log R_p versus reciprocal temperature is shown in **Figure 4.48**.

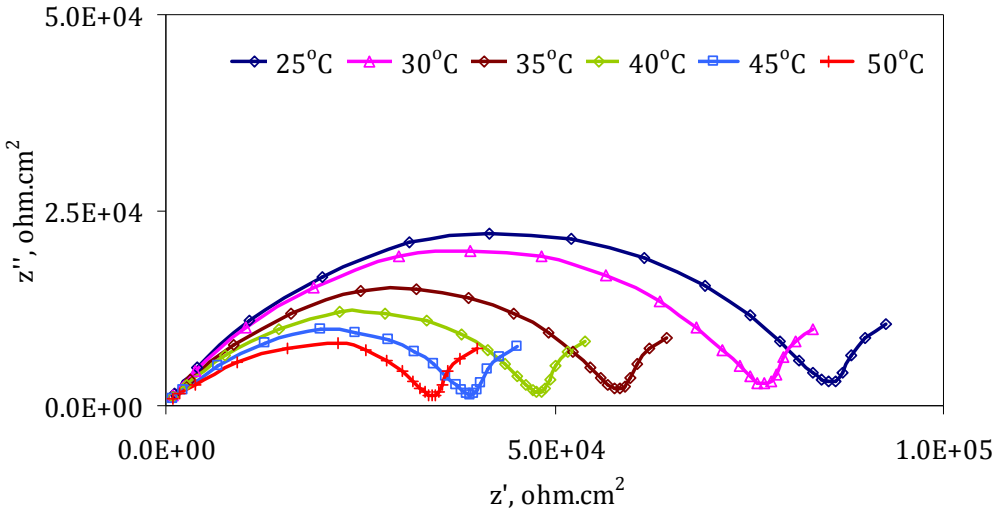

Figure 4.47 – Nyquist plots at various temperatures for 1L-EP coating (Panel 1) after 3 days exposure at 50°C in KCl solution

Table 4.9 – Parameters for 1L-EP coating (Panel 1) from fitting of EIS after 3 days exposure at 50°C; fitted circuit: circle fit from ACM software

T (°C)	C_c (F)	R_p (ohm.cm²)
25	1.04E-07	8.71E+04
30	1.16E-07	7.86E+04
35	7.55E-08	5.86E+04
40	8.77E-08	4.82E+04
45	9.88E-08	3.92E+04
50	1.15E-07	3.45E+04

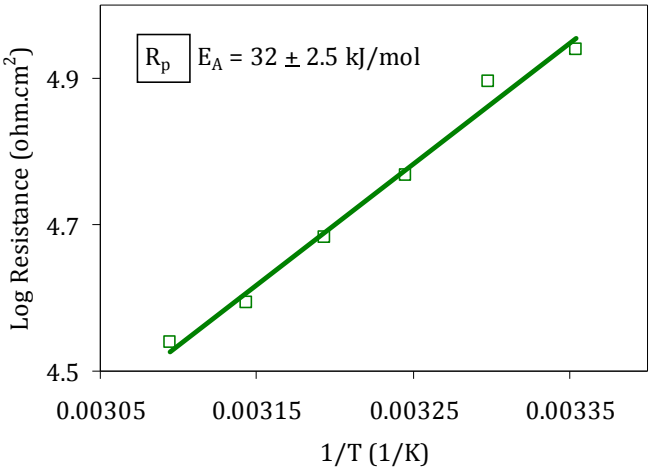

Figure 4.48 - Arrhenius plot R_p for 1L-EP coating (Panel 1) after 3 days of exposure at 50°C in KCl solution

Figure 4.49 shows the impedance spectra obtained for another set of 1L-EP coatings at different temperatures after 3 days of exposure in K^+ solution. Noticed there is a good resemblance of this figure with the earlier Nyquist plots in **Figure 4.47**.

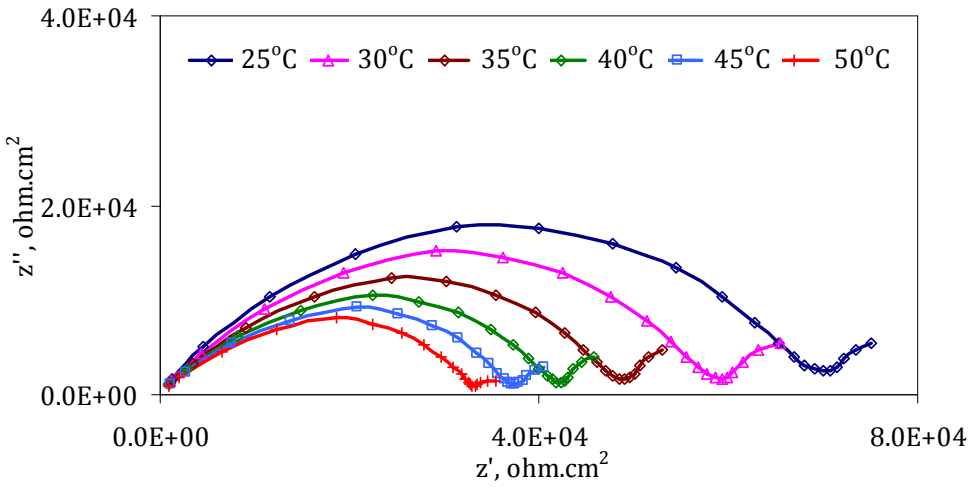

Figure 4.49 – Nyquist plots at various temperatures for 1L-EP coating (Panel 2) after 3 days exposure at 50°C in KCl solution

As before, this semicircle is fitted with circle fit from ACM software as Nyquist plots are too difficult to fit using ZSimpWin. The summary of the fitted parameters are given in **Table 4.10**. The Arrhenius plot of log R_p versus the reciprocal of temperature in **Figure 4.50** shows the activation energy is 24 kJmol^{-1}.

Table 4.10 – Parameters for 1L-EP coating (Panel 2) from fitting of EIS after 3 days exposure at 50^{o}C; fitted circuit: circle fit from ACM software

T (^{o}C)	C_c (F)	R_p (ohm.cm^2)
25	5.559E-08	6.945E+04
30	5.240E-08	5.800E+04
35	6.894E-08	4.835E+04
40	7.871E-08	4.168E+04
45	8.577E-08	3.692E+04
50	1.033E-07	3.312E+04

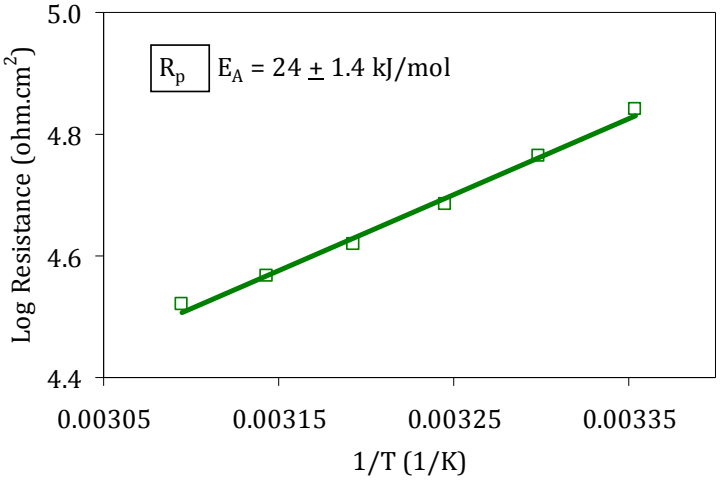

Figure 4.50 - Arrhenius plot R_p for 1L-EP coating (Panel 2) after 3 days of exposure at 50^{o}C in KCl solution

Temperature Dependence of 1L-EP Coating in NaCl solution

Figures 4.51 to **4.53** shows the impedance spectra obtained for the 1L-EP coating at different temperatures after 3, 7 and 14 days exposure in the Na^+ solution. From these spectra the strong influence of temperature on the impedance of the coating is evident. It is again noticeable that the low frequency semicircle shows a larger change with temperature than the high frequency semicircle. To determine the activation energies for ion migration and the corrosion process, this semicircle is fitted to an appropriate equivalent circuit. The summary of the fitted parameters are given in **Tables 4.11** to **4.13**. The plot of log R_p and R_{ct} versus the reciprocal of temperature are shown in **Figures 4.54** to **4.56**.

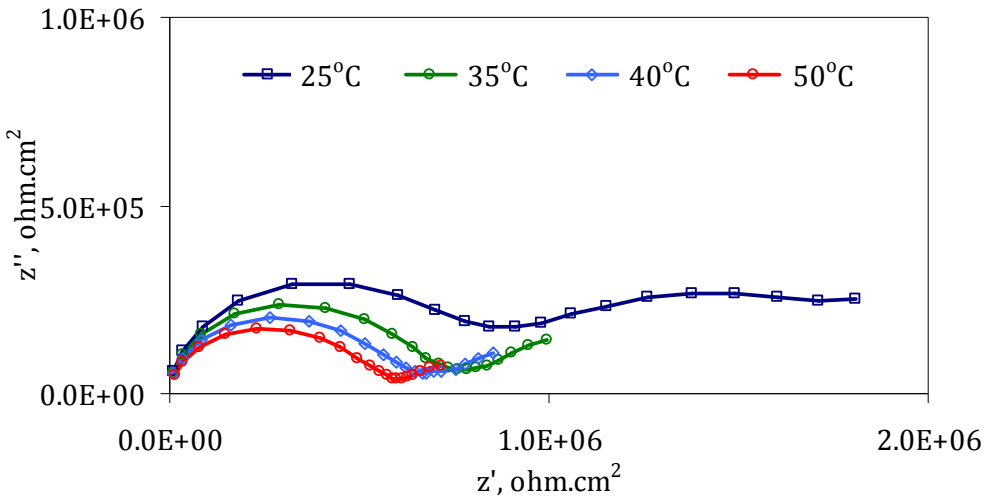

Figure 4.51 – Nyquist plots at various temperatures for 1L-EP coating after 3 days exposure at 50°C in NaCl solution

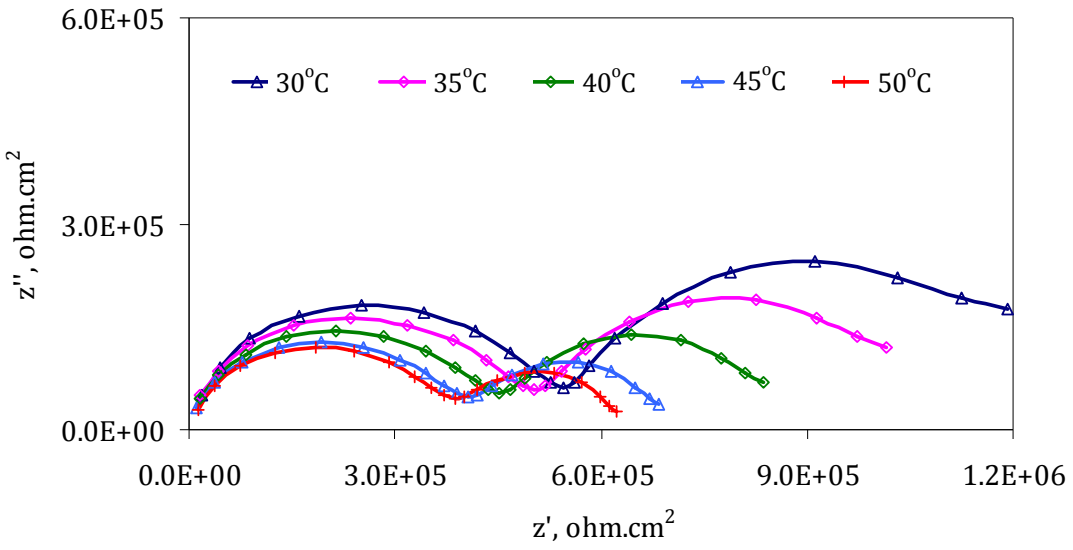

Figure 4.52 – Nyquist plots at various temperatures for 1L-EP coating after 7 days exposure at 50°C in NaCl solution

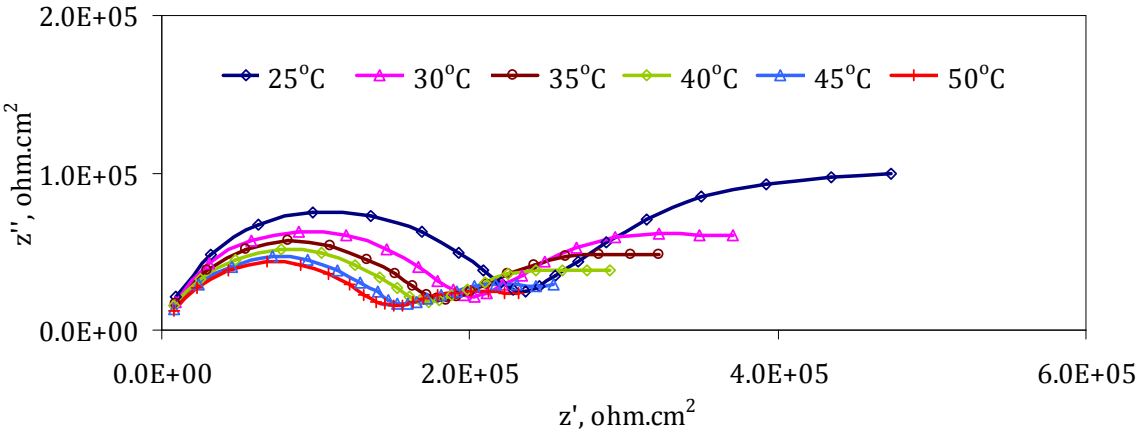

Figure 4.53 – Nyquist plots at various temperatures for 1L-EP coating after 14 days exposure at 50°C in NaCl solution

Table 4.11 – Parameters for 1L-EP coating from fitting of EIS after 3 days exposure at 50°C

Fitted circuit: [RQ][RQ]

T (°C)	Q_c $(Fcm^{-2})^n$	Q_c (%error)	n	R_p ($ohm.cm^2$)	R_p (%error)	Q_{dl} $(Fcm^{-2})^n$	Q_{dl} (%error)	n	R_{ct} ($ohm.cm^2$)	R_{ct} (%error)	X^2
25	3.50E-10	41.10	0.89	7.06E+05	11.89	2.09E-07	28.65	0.53	1.96E+06	18.95	5.40E+03
35	4.92E-10	41.53	0.86	6.41E+05	10.90	1.05E-06	51.48	0.47	1.14E+06	54.91	4.63E+03
40	6.28E-10	40.60	0.84	5.61E+05	11.12	1.21E-06	52.40	0.46	9.54E+05	54.39	5.14E+03
50	8.02E-10	48.02	0.83	4.85E+05	15.18	9.19E-07	64.27	0.48	7.41E+05	53.18	5.27E+03

Table 4.12 – Parameters for 1L-EP coating from fitting of EIS after 7 days exposure at 50°C

Fitted circuit: [RQ][RQ]

T (°C)	Q_c $(Fcm^{-2})^n$	Q_c (%error)	n	R_p ($ohm.cm^2$)	R_p (%error)	Q_{dl} $(Fcm^{-2})^n$	Q_{dl} (%error)	n	R_{ct} ($ohm.cm^2$)	R_{ct} (%error)	X^2
30	8.62E-10	15.71	0.81	5.06E+05	3.01	4.92E-07	14.24	0.64	1.37E+06	10.52	1.94E+03
35	9.30E-10	17.12	0.81	4.64E+05	3.46	5.30E-07	17.26	0.63	1.14E+06	11.48	2.14E+03
40	1.16E-09	17.50	0.79	4.15E+05	3.84	5.85E-07	20.18	0.62	9.08E+05	12.00	2.04E+03
45	9.54E-10	43.58	0.83	3.48E+05	11.68	6.51E-07	46.07	0.54	7.41E+05	29.05	7.38E+03
50	1.29E-09	39.56	0.81	3.39E+05	11.57	6.62E-07	51.91	0.56	6.62E+05	30.05	7.54E+03

Table 4.13 – Parameters for 1L-EP coating from fitting of EIS after 14 days exposure at 50°C

Fitted circuit: [RQ][RQ]

T (°C)	Q_c $(Fcm^{-2})^n$	Q_c (%error)	n	R_p ($ohm.cm^2$)	R_p (%error)	Q_{dl} $(Fcm^{-2})^n$	Q_{dl} (%error)	n	R_{ct} ($ohm.cm^2$)	R_{ct} (%error)	X^2
25	1.14E-09	59.33	0.84	2.00E+05	13.69	2.41E-06	37.87	0.41	8.27E+05	84.74	9.38E+03
30	1.08E-09	87.75	0.86	1.59E+05	17.90	2.99E-06	37.90	0.34	6.43E+05	79.63	1.08E+02
35	1.13E-09	92.25	0.87	1.39E+05	17.23	3.50E-06	40.54	0.31	5.68E+05	74.92	1.17E+02
40	1.09E-09	84.68	0.88	1.27E+05	15.27	3.43E-06	42.81	0.30	4.49E+05	53.05	1.06E+02
45	1.15E-09	91.14	0.89	1.12E+05	16.41	3.50E-06	52.99	0.29	3.60E+05	47.13	1.19E+02
50	1.16E-09	95.91	0.89	1.03E+05	17.49	3.43E-06	60.76	0.29	3.10E+05	42.50	1.25E+02

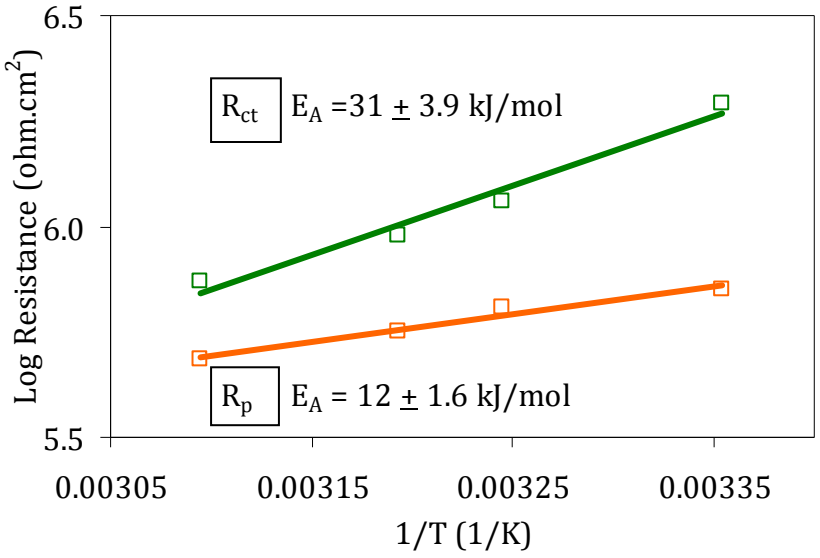

Figure 4.54 - Arrhenius plot of R_p and R_{ct} for 1L-EP coating after 3 days of exposure at 50°C in NaCl solution

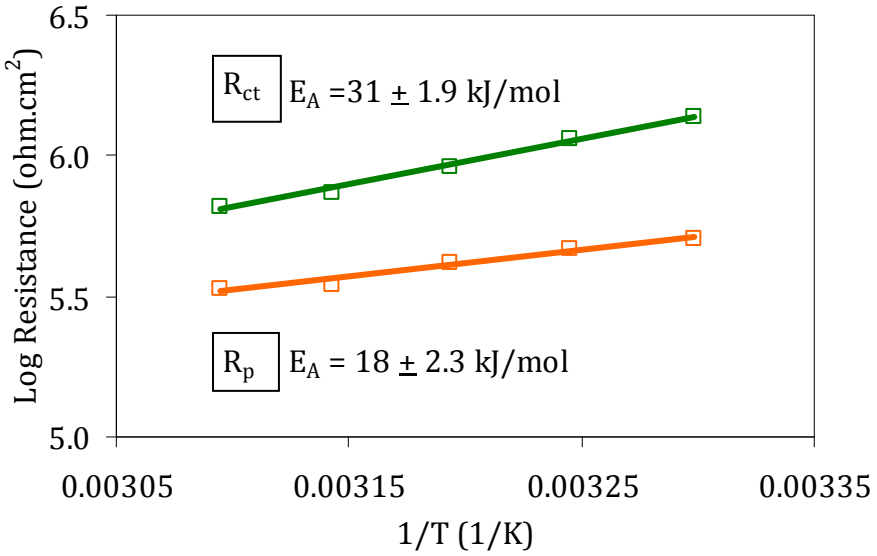

Figure 4.55 - Arrhenius plot of R_p and R_{ct} for 1L-EP coating after 7 days of exposure at 50°C in NaCl solution

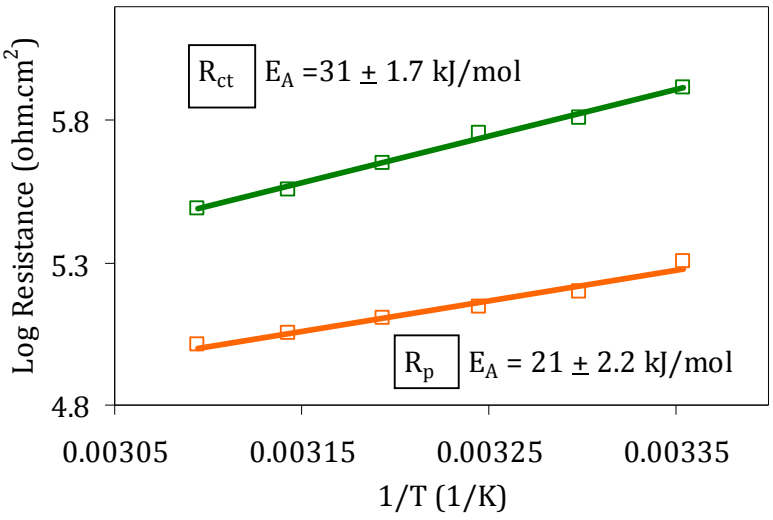

Figure 4.56 - Arrhenius plot of R_p and R_{ct} for 1L-EP coating after 14 days of exposure at 50°C in NaCl solution

Temperature Dependence of 1L-EP Coating in LiCl solution

Figures 4.57 and **4.58** show the impedance spectra obtained for the 1L-EP coating at different temperatures after 3 and 7 days exposure. From these spectra the strong influence of temperature on the impedance of the coating is evident. The second semicircle at low frequency is not seen clearly for impedance spectra for 3 and 7 days, thus is not suitable for analysis. However, by 14 days exposure (**Figure 4.59**) two distinct semicircles are seen. It is noticeable that the low frequency semicircle shows a larger change with temperature than the high frequency semicircle. To assess the influence of temperature on the ion conduction and corrosion process, the semicircles from **Figures 4.59** and **4.60** are fitted to an appropriate equivalent circuit. The summary of the fitted parameters is given in **Tables 4.14** and **4.15**. The plot of log R_p

and R_{ct} versus 1/T are shown in **Figures 4.61** and **4.62** and the straight line of R_p and R_{ct} represent ion conduction in the film and the corrosion process respectively.

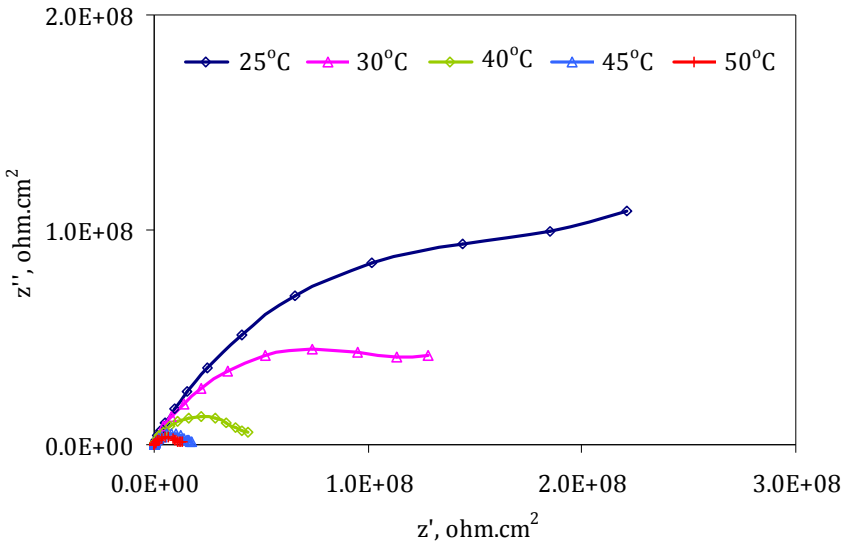

Figure 4.57 – Nyquist plots at various temperatures for 1L-EP coating after 3 days exposure at 50°C in LiCl solution

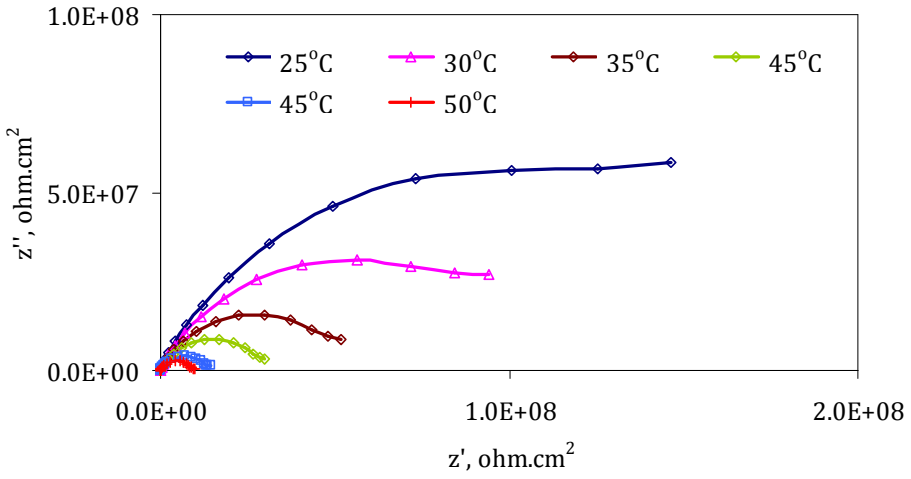

Figure 4.58 – Nyquist plots at various temperatures for 1L-EP coating after 7 days exposure at 50°C in LiCl solution

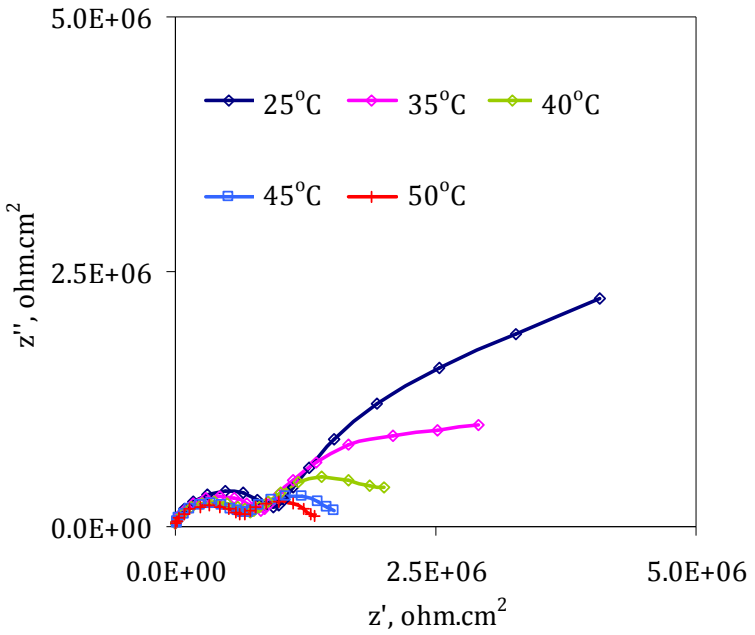

Figure 4.59 – Nyquist plots at various temperatures for 1L-EP coating after 14 days exposure at 50°C in LiCl solution

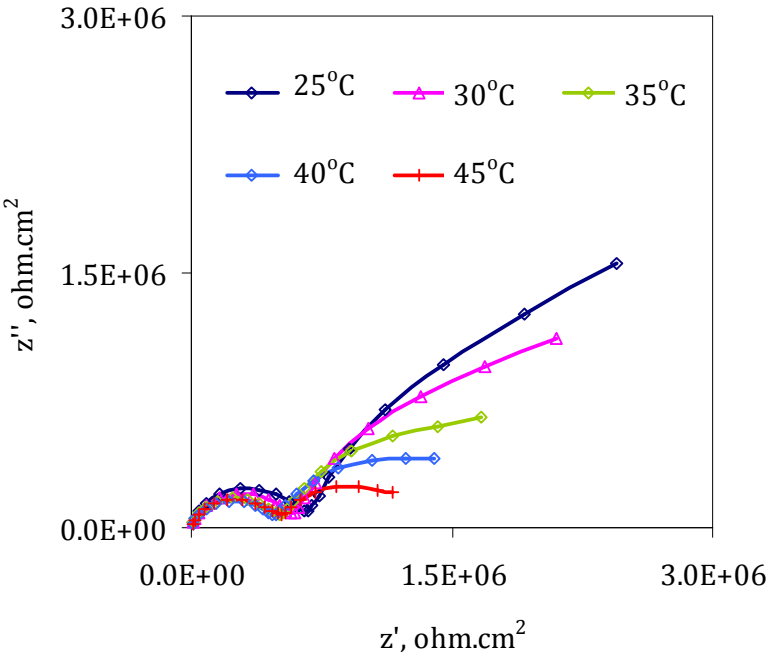

Figure 4.60 – Nyquist plots at various temperatures for 1L-EP coating after 21 days exposure at 50°C in LiCl solution

Table 4.14 – Parameters for 1L-EP coating from fitting of EIS after 14 days exposure at 50°C

Fitted circuit: R[Q[R[QR]]]

T (°C)	Q_c $(Fcm^{-2})^n$	Q_c (%error)	n	R_p ($ohm.cm^2$)	R_p (%error)	Q_{dl} $(Fcm^{-2})^n$	Q_{dl} (%error)	n	R_{ct} ($ohm.cm^2$)	R_{ct} (%error)	X^2
25	8.63E-10	19.83	0.85	8.80E+05	4.24	2.18E-07	8.40	0.63	8.46E+06	20.98	3.31E+03
35	1.06E-09	20.63	0.84	7.52E+05	4.75	2.67E-07	10.72	0.59	3.88E+06	16.05	3.05E+03
40	1.28E-09	22.87	0.83	6.52E+05	5.74	3.03E-07	15.04	0.58	1.89E+06	14.14	3.10E+03
45	1.55E-09	23.72	0.82	5.89E+05	6.47	3.23E-07	18.63	0.57	1.17E+06	13.47	2.83E+03
50	1.55E-09	27.45	0.82	5.45E+05	8.23	3.37E-07	22.59	0.54	9.62E+05	15.46	3.16E+03

Table 4.15– Parameters for 1L-EP coating from fitting of EIS after 21 days exposure at 50°C

Fitted circuit: R[Q[R[QR]]]

T (°C)	Q_c $(Fcm^{-2})^n$	Q_c (%error)	n	R_p ($ohm.cm^2$)	R_p (%error)	Q_{dl} $(Fcm^{-2})^n$	Q_{dl} (%error)	n	R_{ct} ($ohm.cm^2$)	R_{ct} (%error)	X^2
25	1.07E-09	22.33	0.84	6.19E+05	4.11	3.88E-07	20.36	0.67	5.18E+06	75.73	3.49E+03
30	1.21E-09	23.26	0.83	5.48E+05	4.21	4.24E-07	21.64	0.67	3.37E+06	59.53	3.43E+03
35	1.43E-09	24.30	0.82	4.82E+05	4.56	4.97E-07	23.40	0.65	2.11E+06	46.54	3.29E+03
40	1.60E-09	25.71	0.81	4.40E+05	5.05	5.67E-07	24.95	0.62	1.58E+06	40.71	3.29E+03
45	1.61E-09	51.85	0.82	4.45E+05	14.01	6.69E-07	70.50	0.53	1.09E+06	96.15	1.19E+02

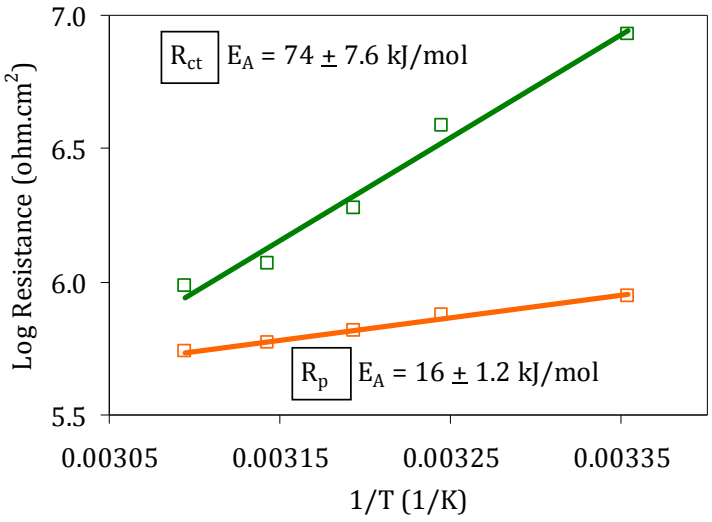

Figure 4.61 - Arrhenius plot of R_p and R_{ct} for 1L-EP coating after 14 days of exposure at 50°C in LiCl solution

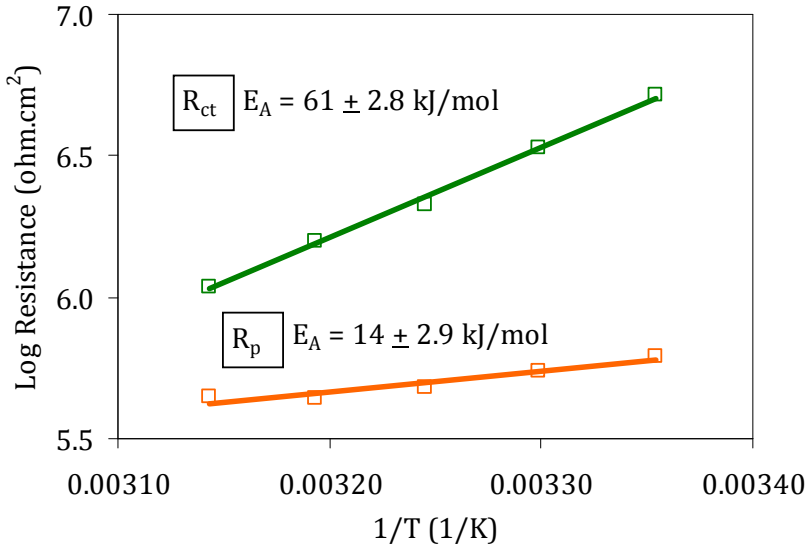

Figure 4.62 - Arrhenius plot of R_p and R_{ct} for 1L-EP coating after 21 days of exposure at 50°C in LiCl solution

Activation Energy for 2-CE and 1L-EP Coating Exposed in K^+, Na^+ and Li^+ solutions

Table 4.16 displays the summary of activation energies determined for ion conduction (calculated from R_p) and for the corrosion process (calculated from R_{ct}) for the 2-CE coating after 3 days of exposure in K^+, Na^+ and Li^+ solutions. It can be seen that the activation energy for ion conduction is lower than the activation energy for the corrosion process for coated metal in the Li^+ solution only. Referring to **Table 4.17**, agreement between the activation energy for ion conduction and the cation size is not good; larger cation size (Li^+) should generate a larger E_A, due to its difficulty in penetrating the coating. **Figure 4.63** presents the activation energy determined for ion conduction and for the corrosion process for the 1L-EP coating after various exposure times in K^+, Na^+ and Li^+ solutions. In this investigation, lower activation energy values for ion transport for both Na^+ (12–21 $kJmol^{-1}$) and Li^+ (14–16 $kJmol^{-1}$) were observed compared to the corrosion process, Na^+ (31 $kJmol^{-1}$) and Li^+ (61–74 $kJmol^{-1}$).

Table 4.16 – Activation energy for 2-CE coating after 3 days of exposure in K^+, Na^+ and Li^+ solutions

Ion		K^+	Na^+	Li^+
Activation energy, kJ/mol	R_p	9	18	15
	R_{ct}	10	5	100

Table 4.17 - Hydrate ionic radii for K^+, Na^+ and Na^+ [168]

Ion	K^+	Na^+	Li^+
Hydrated ionic radii, nM	0.232	0.276	0.340

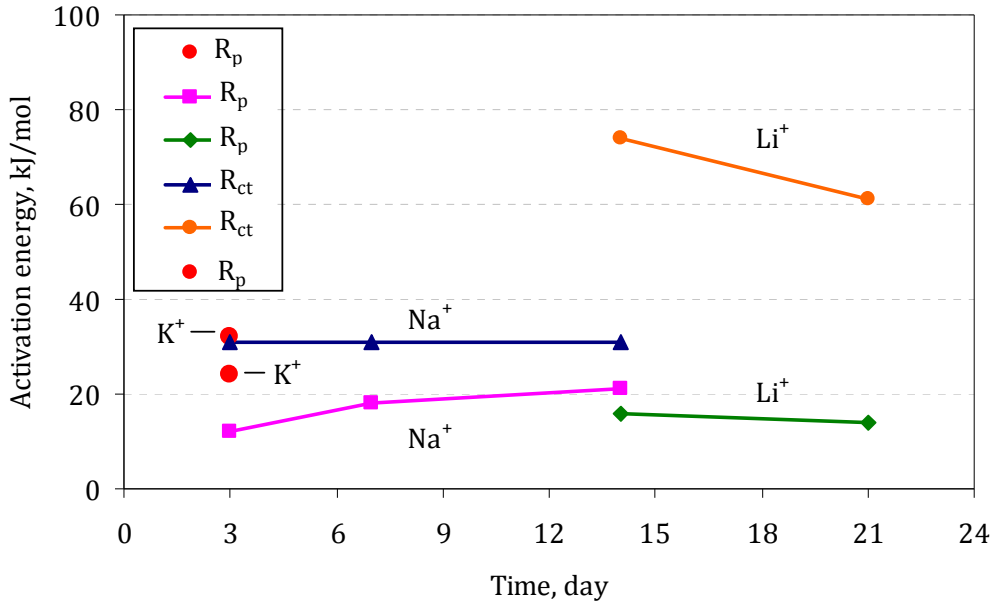

Figure 4.63 - Activation energies for ion conduction and corrosion process for 1L-EP coating exposed in K^+, Na^+ and Li^+ solutions

Notice that a small increase of activation energy for ion transport of Na^+ was observed as the immersion period increased. On the other hand, a slight decrease of activation energy for ion transport of Li^+ was observed over the period. The calculated activation energy for ion transport in the K^+ solution is surprisingly high at 24–32 $kJmol^{-1}$. This result is unexpected as the activation energy ranking found in **Figure 4.63** for ion conduction is $E_ALi^+ < E_ANa^+ < E_AK^+$. The ranking does not correlate well with the cation size (**Table 4.17**) as it is expected that the bigger the cation, the larger the E_A due to its difficulty in penetrating the coating. But the activation energies generated from this study seem to go down with size. It is suggested that the penetration of cation through the coating at the cathode region is being limited by the more mobile anion i.e. OH^- generated by oxygen reduction and that the measured impedance may reflect changes at the cathode.

4.3.9 Blister Study using Scanning Kelvin Probe

In this work the SKP was used to measure the potential distribution underneath a blister area. Two types of SKP scan were conducted; an area scan and a line scan. Area scans allow mapping of electrochemical potentials, identifying anodic and cathodic regions underneath the blister and its surrounding. In addition, line scans were used to create potential profiles of the coating surface on a metal substrate. The automatic height control during scanning is also able to provide the increase in height between the coating and the metal substrate. SKP topography from different line scans of the blister area was able to measure independently the blister height and its potential.

SKP Area Scan of Blister on Coated Metal Exposed in NaCl Solution

Figure 4.64a is a coated panel with blisters after 21 days exposure in 3% NaCl solution. Cathodic reduction of oxygen in a solution containing Na^+ will generate an alkali environment therefore cathodic blistering would be expected to occur preferentially. A SKP potential map is presented in **Figure 4.64b** for the area marked with the dashed blue box. It can be seen that the blue patch in the centre has the most positive potential and this is believed to be the blister area. In addition, orange and green areas denote the presence of anodic regions surrounding it. This result shows that the blister has formed at a cathode due to alkali but anodes form nearby (not remote). However, the area underneath the blister revealed shining bare metal without the presence of any corrosion product due to passivation in alkali (**Figure 4.65**). **Figure 4.66** shows the proposed schematic representations of coated metal exposed to

NaCl solution. Sodium cations migrate through the coating at cathodic areas. They carry ionic current and combine with OH^- causing NaOH to accumulate at the metal surface. The result is strongly alkaline within the cathodic area. As osmotic forces drive water through the coating to the alkaline solution, the coating is deformed upward which then generates a blister.

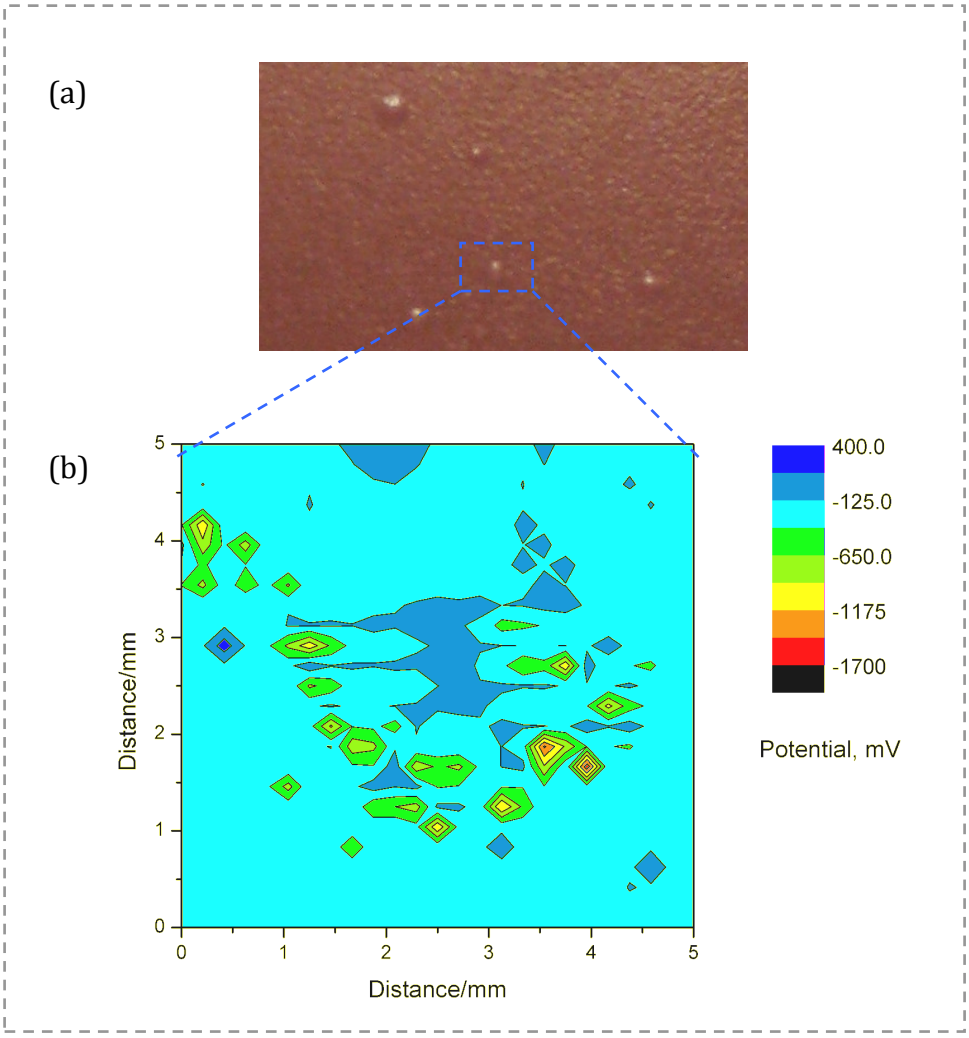

Figure 4.64 – Blister feature and surrounding area imaged with (a) optical microscopy, (b) SKP relative potential map for PCE coating after 21 days of exposure to NaCl solution (sample area is 5mm x 5mm)

Figure 4.65 - Image of area underneath a blister on a PCE coating exposed to NaCl solution (size 5mm x 5mm)

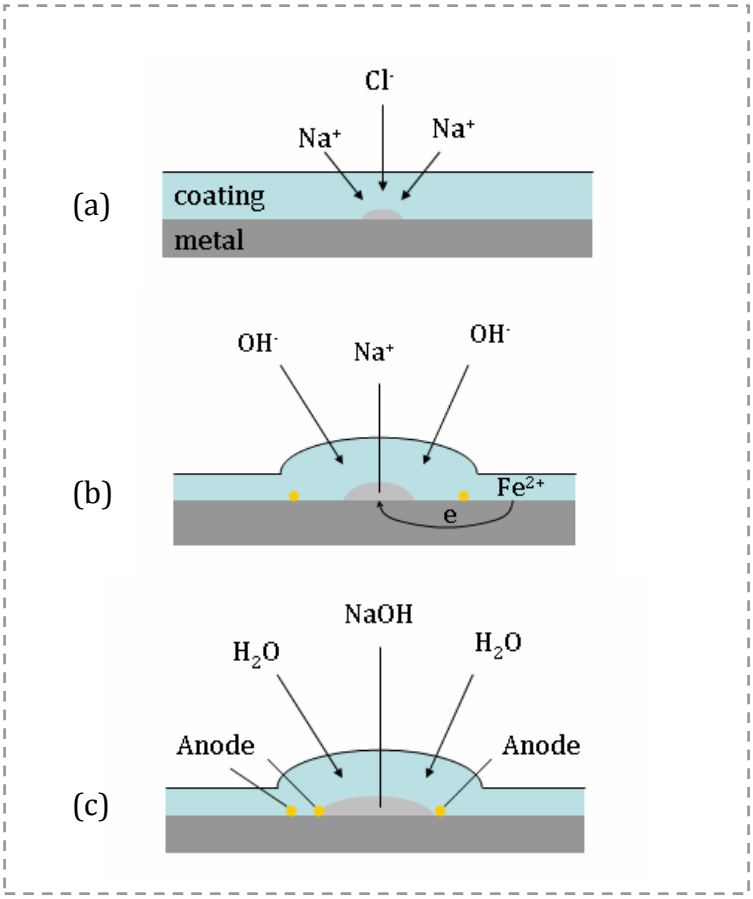

Figure 4.66 - Schematic representations of coated metal exposed to NaCl solution (a) initially, (b) formation of alkali region and (c) blistering due to osmosis

SKP Line Scan of Blister on Coated Metal Exposed in NaCl Solution

The same blister area was further investigated by using a SKP line scan. The scan was conducted based on the diagram in **Figure 4.67**. Six lines labelled A to F were scanned over the blister area with line E at the centre of the blister.

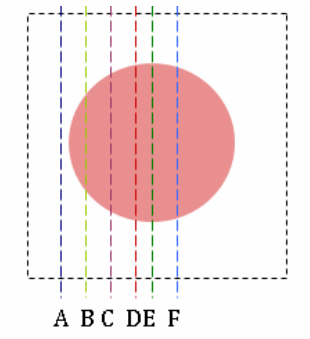

Figure 4.67 – Position of line scan using SKP over a blister on coated panel immersed in NaCl solution (line scan length is 5mm)

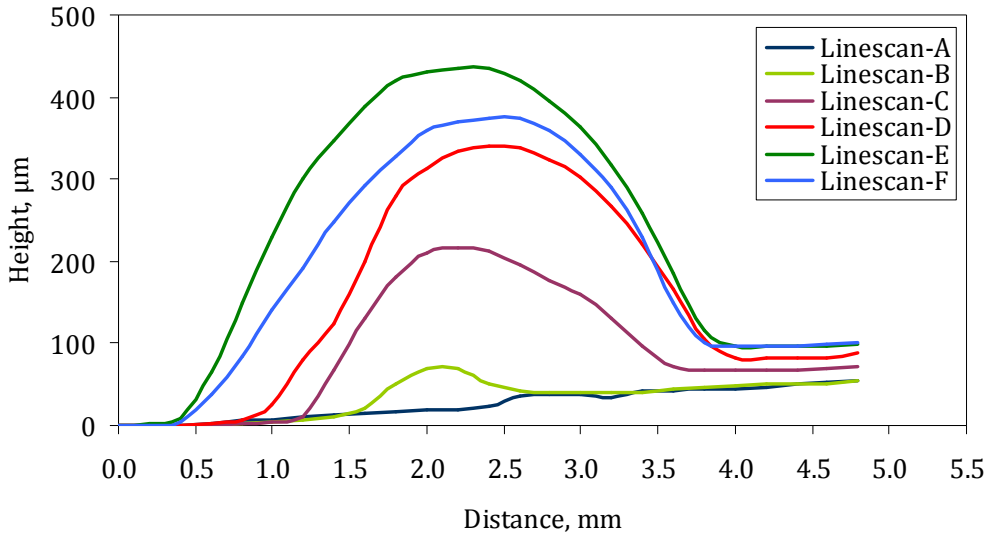

Figure 4.68 - Blister height according to its respective position of PCE coating exposed to NaCl solution

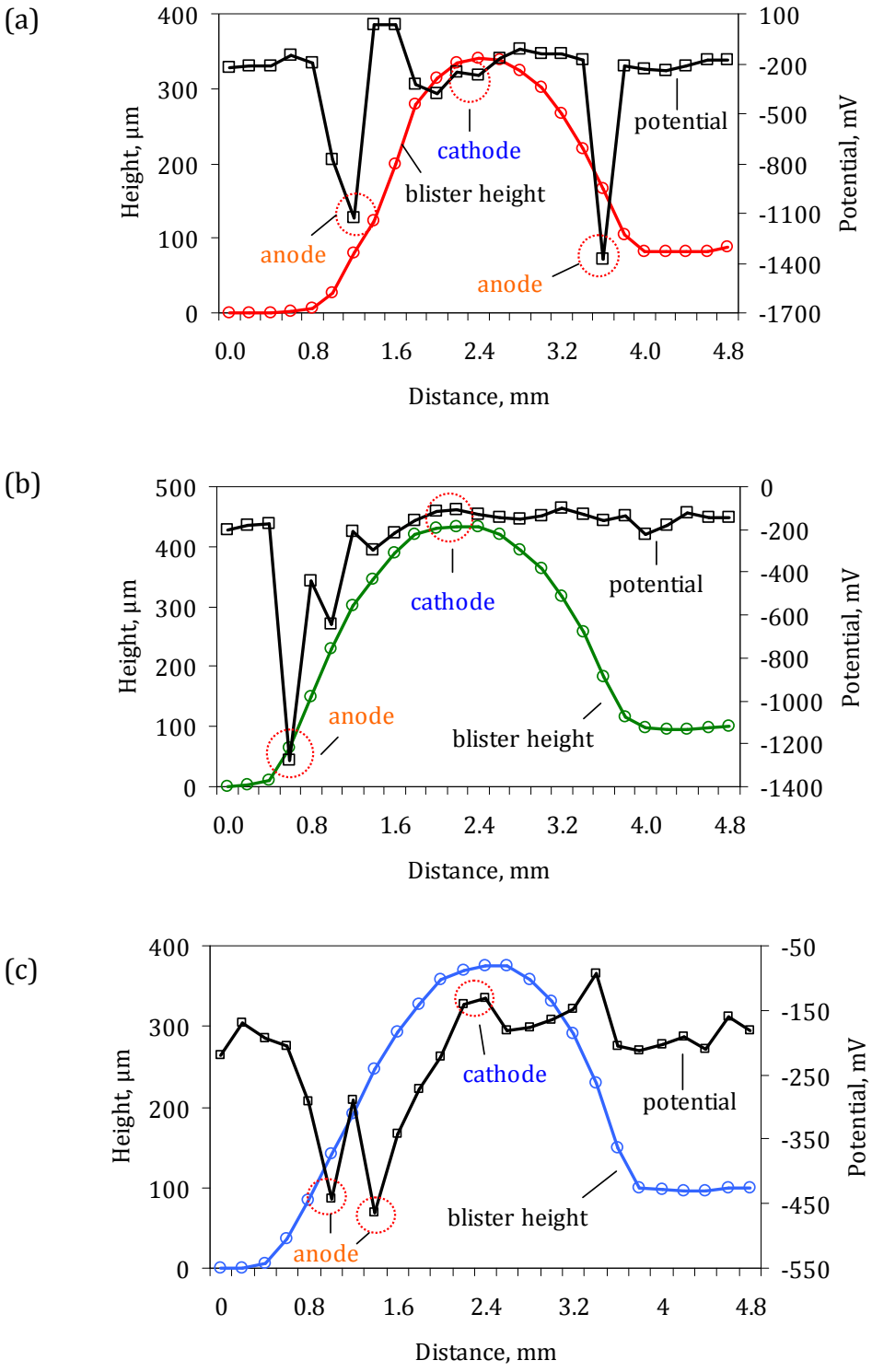

Figure 4.69 - Blister height and potential measured for PCE coating exposed to NaCl solution (a) Linescan-D, (b) Linescan-E and (c) Linescan-F

The explanation given here is focusing on the area where there is an increase in blister height from the metal surface. **Figure 4.68** shows the coating profile corresponding to the measured potentials. Notice that Linescan-E has the maximum height which confirms its position as the centre of the blister. As the line moves away from the blister centre, the height of the blister is greatly reduced. This indicates that the detachment of the coating from metal surface is lower at the edge of the blister.

Figure 4.69 shows the potential measured for Linescan D, E and F. It can be seen that all of them show the cathodic region lying in a similar position where the blister height is at its greatest. Anodic regions were observed at specific areas surrounding the blister.

SKP Area Scan of Blister on Coated Metal Exposed in NH_4Cl Solution

It is interesting to extend this technique to blister formation on a coated panel exposed to 3% NH_4Cl solution. **Figure 4.70a** is a coated panel with blisters after 13 days exposure in NH_4Cl solution. A SKP scan was conducted on the selected area as mapped out by the blue dashed box drawn on the coated panel. **Figure 4.70b** shows an SKP potential map for the metal underneath the blister. The lowest (most negative) potential corresponds to areas of anodic activity (red colour). The highest (more positive) potential represents cathodic activity (blue colour). Notice the presence of orange patches in the image and small bits of red area which have the most negative potential and these correspond to the blister area.

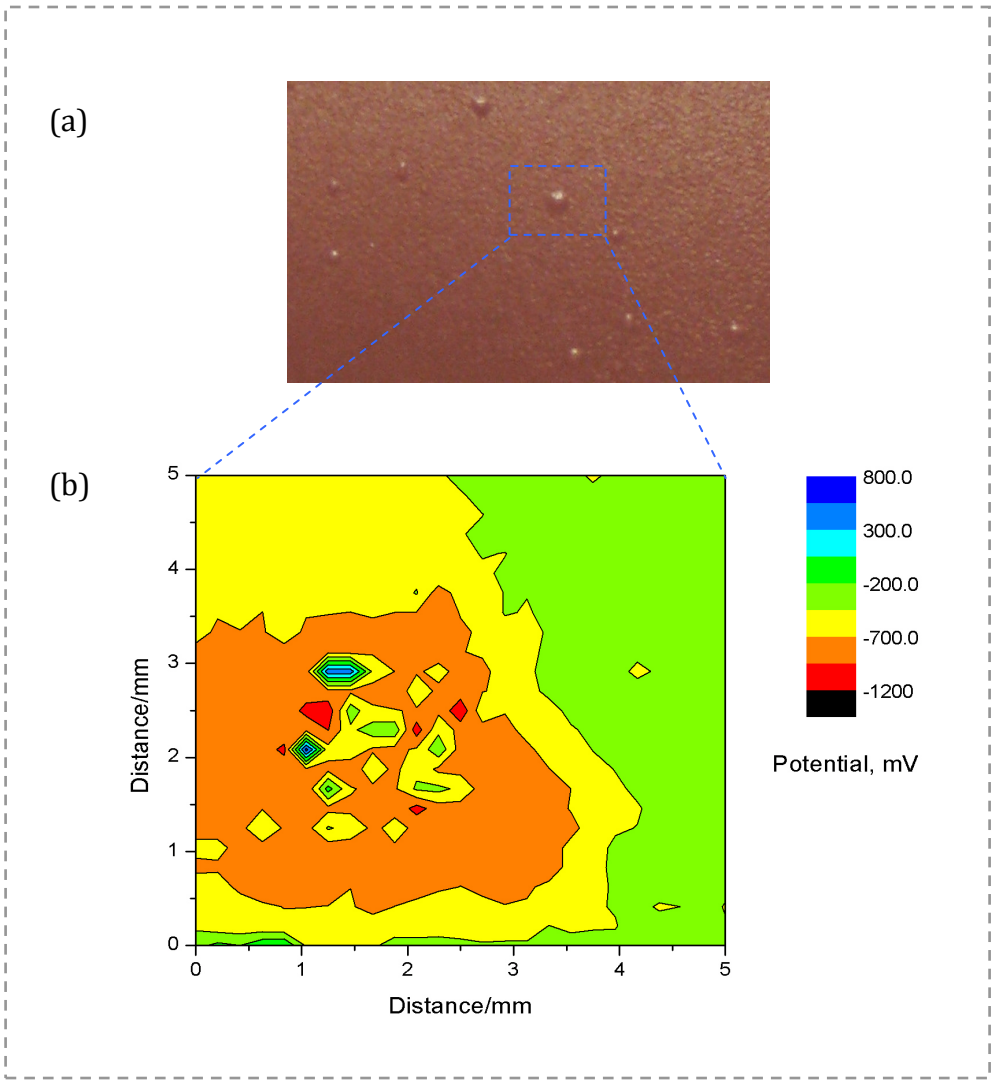

Figure 4.70– Blister feature and surrounding area imaged with (a) optical microscopy, (b) SKP relative potential map for PCE coating after 13 days of exposure to NH_4Cl solution (sample area is 5mm x 5mm)

It is interesting to observe the colour changes of the area surrounding the blister. The colour changes from green towards yellow and orange which corresponds to a more negative potential as it moves towards the blister area. Notice the appearance of blue and green patches which indicate the presence of cathodic activity within the anodic

region. There is a possibility that this cathodic region may start as anodes initially. In the previous studies by Sykes and Doherty [149, 169], where a defect on a thin lacquer coating on electro-chrome coated steel was examined, they observed a gradual change from an anode region to a cathode region. They attributed this shift to the corrosion products formed in the defects becoming the cathode reactant.

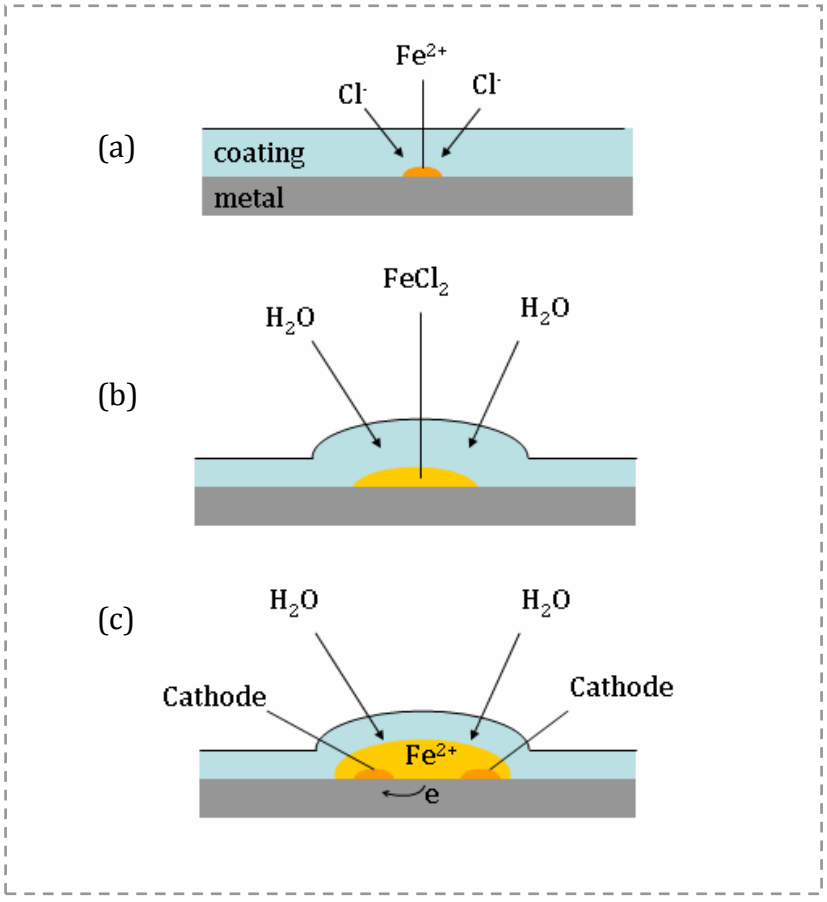

Figure 4.71 - Schematic representations of coated metal exposed to NH_4Cl solution (a) initially, (b) corrosion initiation and (c) after blistering

Figure 4.71 shows the proposed schematic representations of coated metal exposed to NH_4Cl solution. Initially anodic attack on the metal produces Fe^{2+} which then combines

with the chloride anion to form $FeCl_2$. As water starts coming in, $FeCl_2$ is diluted and Fe^{2+} combines with water to form iron hydroxide which is then oxidized by oxygen to rust (FeOOH). Rust becomes established on the metal surface and becomes the cathodic reactant. New anodes then develop within the blister and brown rust is gradually reduced to black magnetite. This result is confirmed when the area underneath the blister was revealed at the end of the test; it was corroded with corrosion products suggesting anodic detachment (**Figure 4.72**). Notice the presence of brown rust on top of the green rust.

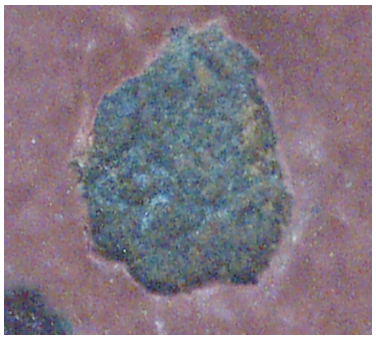

Figure 4.72 - Corrosion products underneath the blister of PCE coating exposed to NH_4Cl solution (size 5mm x 5mm)

SKP Line Scan of Blister on Coated Metal Exposed in NH_4Cl Solution

The same blister area was further investigated using a SKP line scan which could provide a profile of the coating height corresponding to the potential measured on the metal surface. The scan was conducted based on the diagram in **Figure 4.73**. Five lines labelled 1 to 5 were scanned over the blister area with line 3 at the centre of the blister.

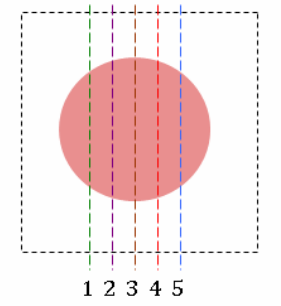

Figure 4.73– Schematic of the line scan position over a blister area on coated panel immersed in NH_4Cl solution (line scan length is 5mm)

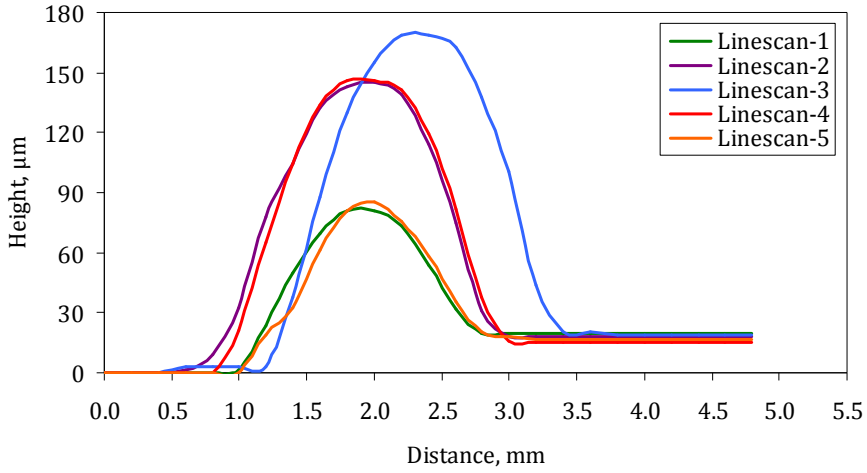

Figure 4.74- Blister height according to its respective line scan position for PCE coating exposed to NH_4Cl solution

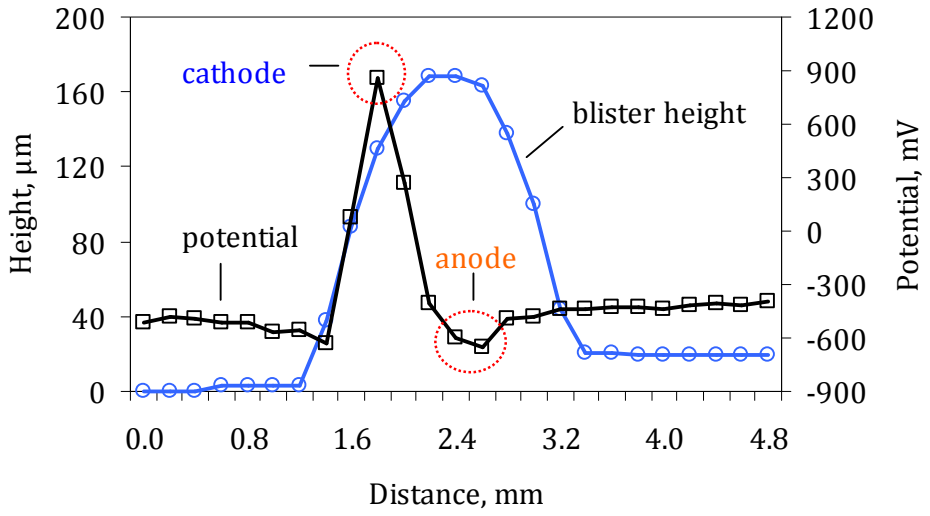

Figure 4.75 - Blister height and its potential for Linescan-3 of PCE coating exposed to NH_4Cl solution

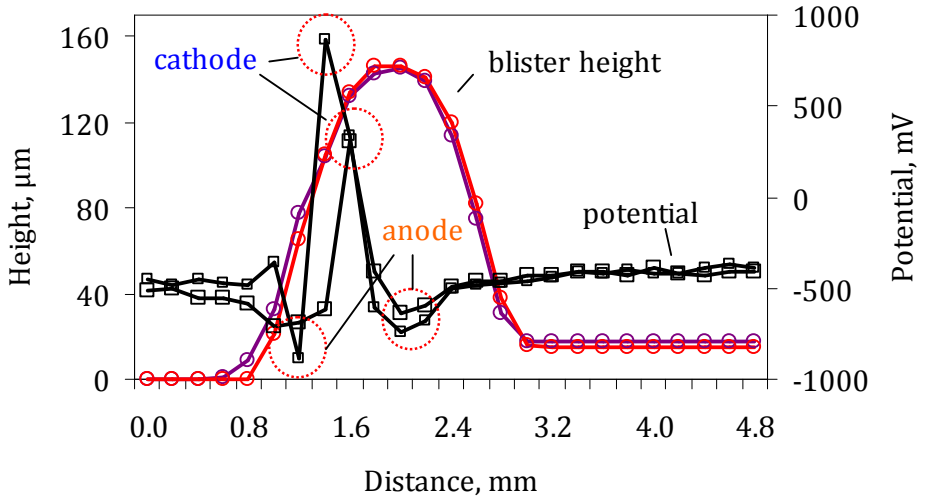

Figure 4.76 - Blister height and its potential for Linescan-2 and Linescan-4 of PCE coating exposed to NH_4Cl solution

Figure 4.74 shows the coating height from the substrate area and corresponds to the measured potential value according to the respective line scan position. It was observed that Linescan-3 has the greatest height which confirms its position as the

centre of the blister. The explanation given here is applies to the area where there is an increase in blister height from the metal surface. The potential and the measured blister height of Linescan-3 are presented in **Figure 4.75**. It can be seen that when the blister height is at its greatest, the potential is at the most negative which denotes anodic activity. Notice however the presence of a more positive cathodic region which suggests that the anode and cathode appear side by side within the blister area. According to Funke [82], the areas underneath a blister with plugged pores are anodic, with cathodic edges due to differential aeration. Similar results were observed from Linescan-2 and Linescan-4 as presented in **Figure 4.76**. Notice the anode and cathode areas appear within the same blister region which demonstrated the existence of anodic and cathodic areas on iron corroding as shown previously in the SKP area scan.

4.4 Conclusions

- Tests at high temperature show that the time for observing coating degradation was greatly reduced.

- The activation energies determined for ion transport and the corrosion process for the PCE coating are 14–25 $kJmol^{-1}$ and 35–49 $kJmol^{-1}$, whereas for the 1L-EP coating, activation energies are 27–30 $kJmol^{-1}$ and 28–48 $kJmol^{-1}$ respectively. These values show that the temperature dependence for ion transport exhibited different values from temperature dependence for the corrosion process, where the latter generates rather higher values. This suggests that ion conduction in the coating, as apparent in an AC measurement, cannot be controlling the corrosion rate.

- Although the effect of heating is partially reversible the coatings do show a degree of irreversible behaviour. Some coatings show reversible behaviour if adequate time is allowed for the water to desorb from the coating.

- The temperature dependence for ion conduction through the coating for a coated panel does not correlate with the size of the cation. This result is unexpected because of the activation energy ranking for ion conduction; $Li^+ < Na^+ < K^+$. It is expected that cation size should influence ion

conduction/migration in the film but activation energies generated from this study seems to go down with ion size.

- For blisters formed on coated panel immersed in NaCl solution, SKP potential map reveals that the blister has formed at a cathode due to alkali but anodes form nearby (not remote). This is supported by line scans which show the presence of an anode at the edge of the blister. It is possible, given that the metal underneath the blister is still bright; that the blister has began to overlap anodes formed around the edge of the blister.

- SKP potential map on a blister forming on a coated panel immersed in NH_4Cl solution reveals the presence of cathodic regions within the anodic areas. It is suggested that there is a possibility that this cathodic region may start as an anode initially, but corrosion products become the cathode reactants.

CHAPTER 5

MULTILAYER COATINGS WITH INHIBITIVE PIGMENTS

5.1 Introduction

In the field, multilayer coatings[5] are generally used for corrosion protection. Multilayer coatings often have a thickness more than 250μm and a typical stacking sequence would consist of a metal substrate, primer, intermediate and top coat layers (**Figure 5.1**). The primer layer may provide inhibition or provide galvanic protection, while the intermediate may provide barrier protection. The top coats can provide gloss, colour and UV protection. In this work, zinc phosphate pigmented primer with top coatings were tested to observe whether the same conclusion derived for coating systems i.e. two component epoxy and epoxy-phenolic in **Section 4.3.5** holds for a real system used in the field.

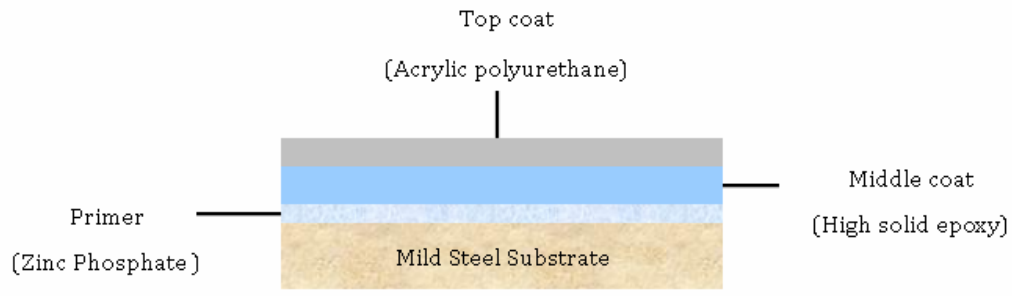

Figure 5.1 - Schematic diagram of a multilayer coatings consisting of primer, middle and top coating

[5] Also referred as 'real system' or 'full system' throughout the thesis

5.2 Materials

In this study, a primer containing inhibiting pigment (zinc phosphate) is under investigation. For simplicity panels are identified as ZP-FS. Details of the coating are listed in **Table 5.1**.

Table 5.1 – Zinc phosphate full system coating information

System	Primer	Middle	Top
ZP-FS	Zinc phosphate epoxy[1]	High solid epoxy[2]	Polyurethane[3]
Thickness, DFT	50µm	180µm	60µm

[1]A two component epoxy anti-corrosive primer pigmented with zinc phosphate
[2]A low VOC, high solids, high build, two-component epoxy coating, pigmented with micaceous iron oxide
[3]A two component acrylic polyurethane finish

5.3 Results and Discussion

5.3.1 Exposure at Ambient Temperature, 21°C and 50°C

Figure 5.2 shows Bode and Nyquist plots for the ZP-full system coating after different periods of exposure at ambient temperature, 21°C. Throughout the 30 days of immersion, the impedance modulus |Z| at the low frequency limit displayed very high values (>10^9 ohm.cm^2). Only one time constant could be observed from the Nyquist plot. This kind of impedance response is characteristic of a coating system in very good condition. Since a period of 30 days immersion of ZP-full system coatings show excellent protective properties, longer monitoring has been conducted where the

coatings were exposed to 3% sodium chloride solution for a one-year period at room temperature, and the EIS result is shown in **Figure 5.3**. The coating only starts to degrade after 4 months of immersion which motivates us to speed up the degradation reaction by exposing the samples at higher temperature of immersion.

Figure 5.4 shows Bode and Nyquist plots of ZP-full system coating after different periods of exposure at 50°C. Degradation is very much faster at 50°C with the presence of a second semi-circle by 7 days (**Figure 5.4c**). The impedance drops from 10^8ohm.cm^2 down to 10^6ohm.cm^2 over a 30 day period. This indicates that the protective properties of coating system gradually decreased due to a faster degradation process during exposure at high temperature.

Impedance spectra from **Figures 5.2** and **5.4** were fitted with an equivalent circuit R[Q[R[QR]]]. **Figure 5.5** shows the evolution of coating resistances with immersion time for tests at 21 and 50°C. As expected, the values of coating resistance at 50°C drop even faster during early immersion.

Open circuit potential (OCP) variation is also interesting to look at. **Figure 5.6** shows time dependent behaviour of OCP for the same coated panel. Notice this figure had a good resemblance to **Figure 5.5**. For coating tested at 50°C, as the coating resistances drop, the OCP values also drop. According to Mahdavian and Attar [57], OCP values drop when the surface becomes active or any passive layer start to break down thus the coating becomes more permeable to OH^- and Cl^- ions. But cathodic inhibition can also contribute to a fall in OCP.

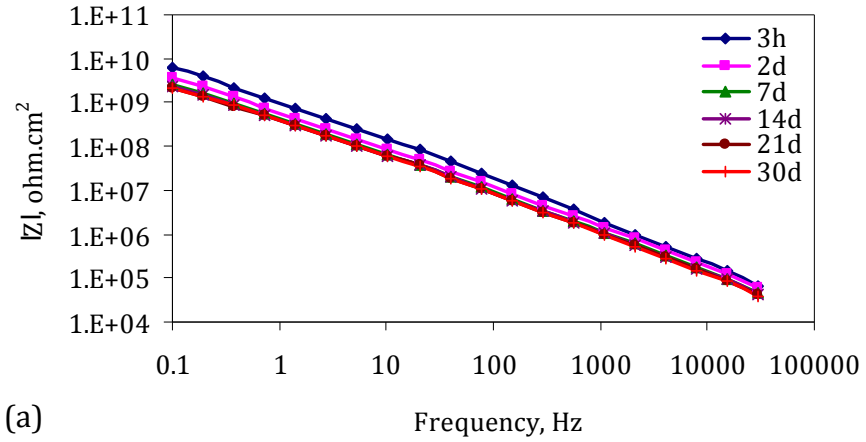

(a)

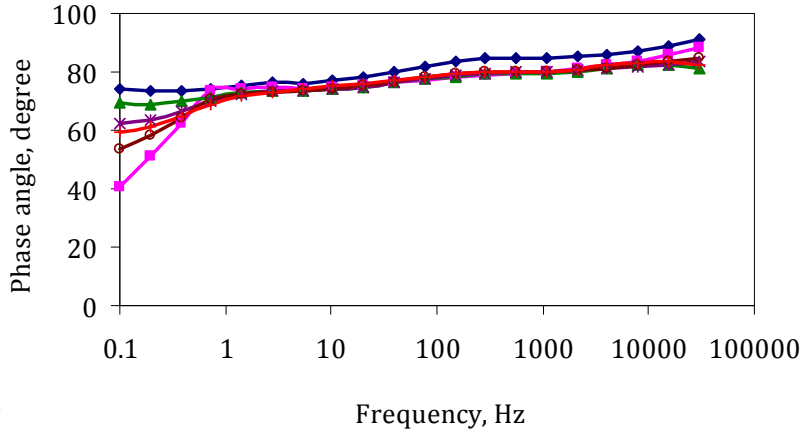

(b)

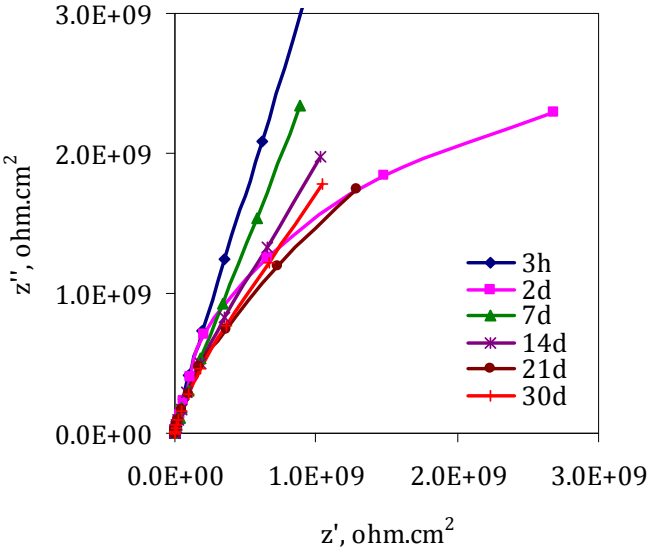

(c)

Figure 5.2- Bode and Nyquist plot for ZP-full system coating tested at 21°C

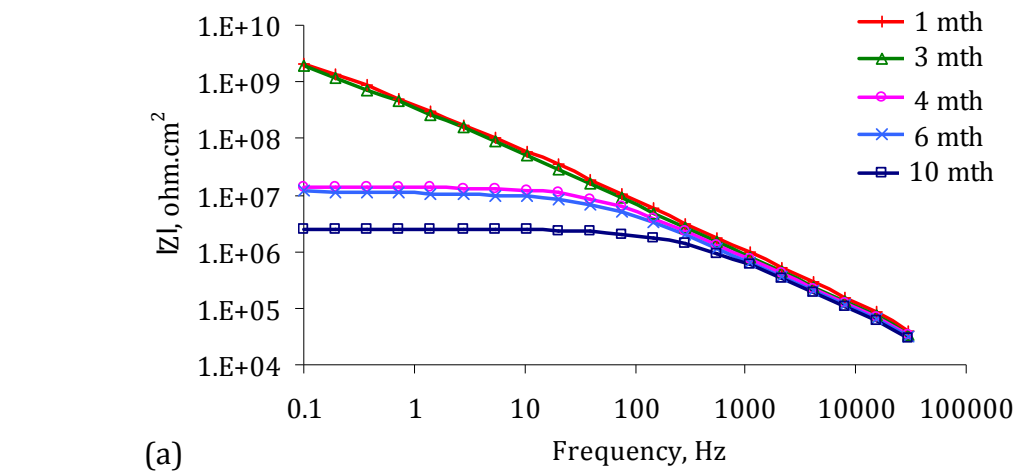

(a)

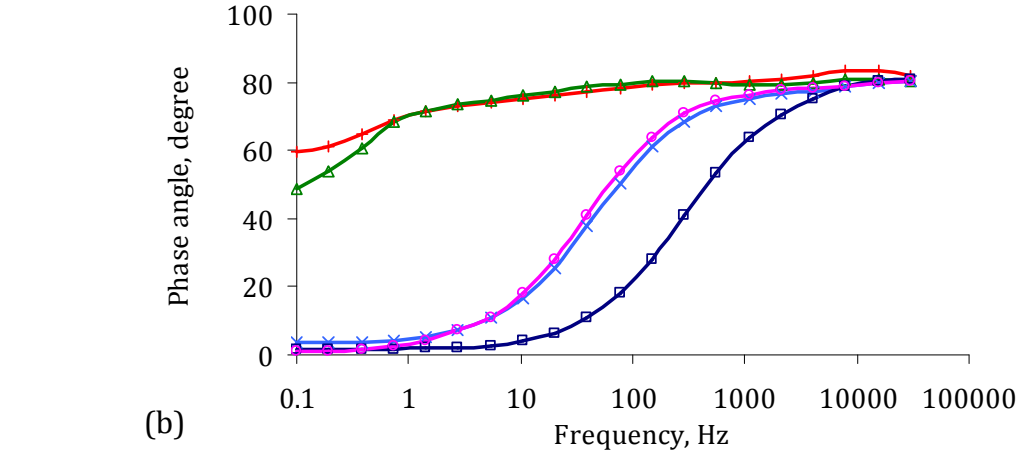

(b)

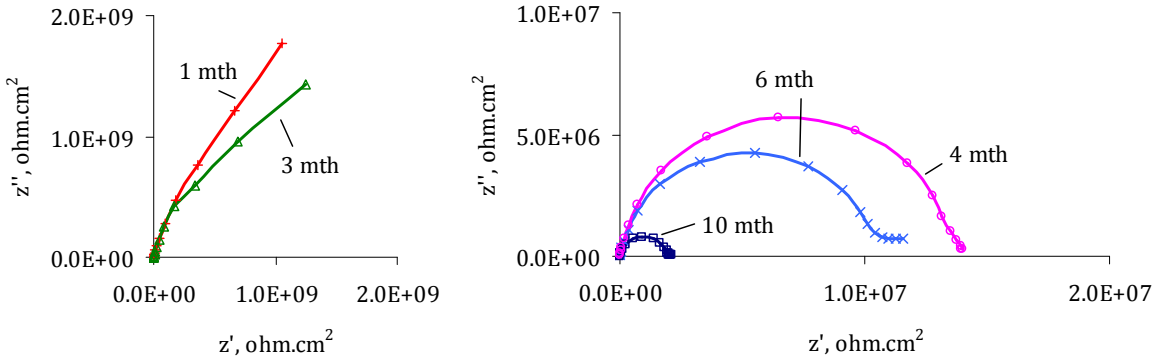

(c)

Figure 5.3 - Bode and Nyquist plot for ZP-full system coating after 1, 3, 4, 6 and 10 months exposed at 21°C

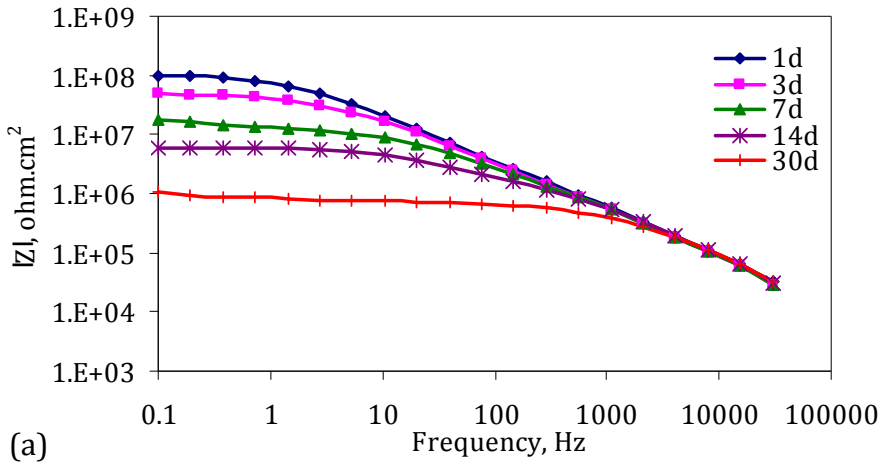

(a)

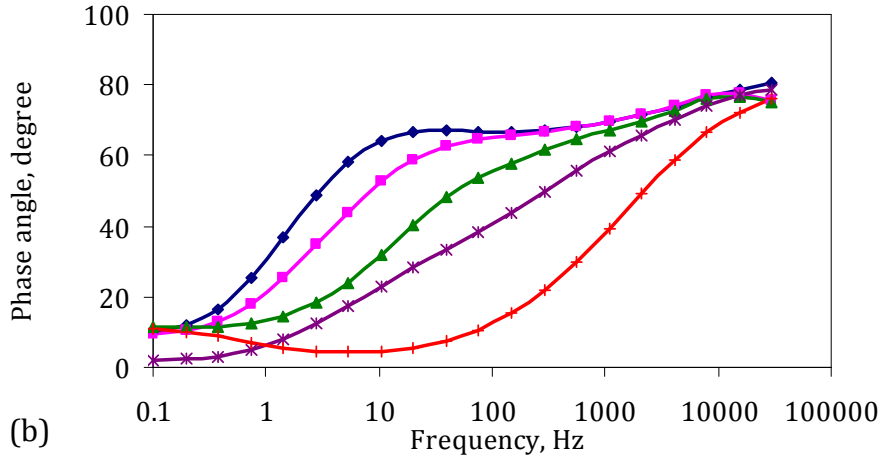

(b)

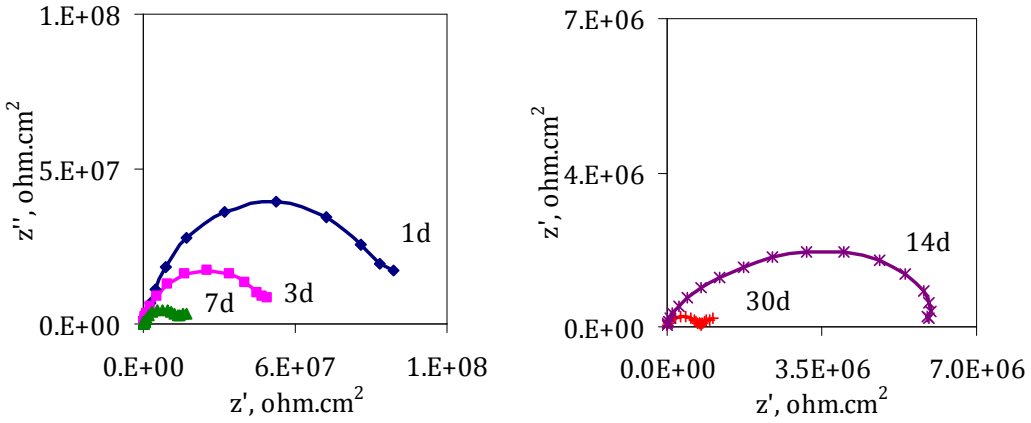

(c)

Figure 5.4 - Bode and Nyquist plot for ZP-full system coating tested at 50°C

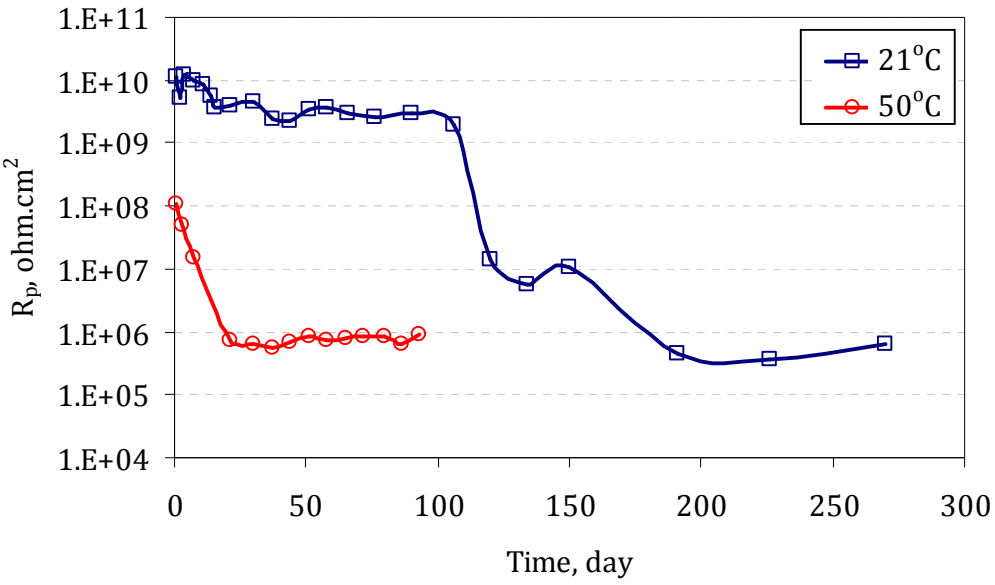

Figure 5.5 – Variation of coating resistance against immersion time for ZP-full system coating exposed at 21 and 50°C

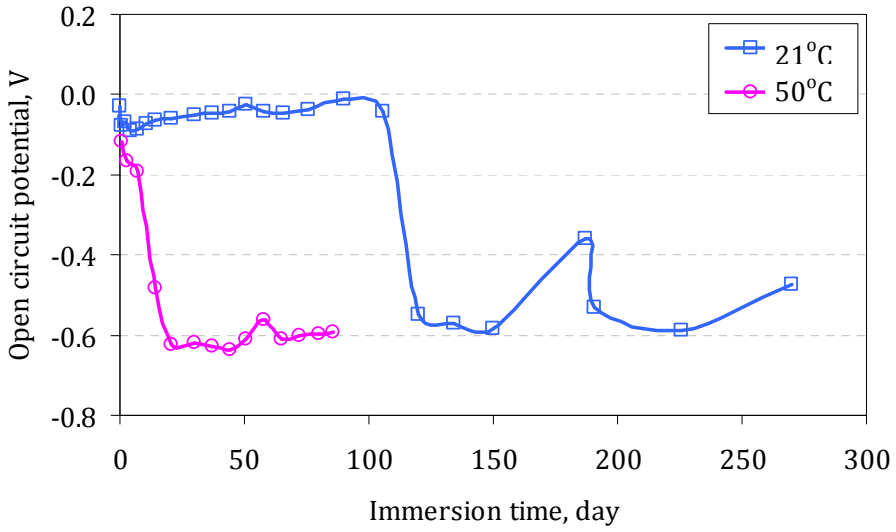

Figure 5.6 - Variation of OCP against immersion time for ZP-full system coatings exposed at 21 and 50°C

5.3.2 Assessment of Coating Behaviour Exposed at Constant 50°C and (50°C-E_A)[6]

EIS data for coated panel exposed at constant 50°C and (50°C-E_A) for a certain period were observed to see whether any significant difference arises from both tests. This is to be certain that imposing a short period of test where the panel is left to cool down (50°C-E_A) does not differ greatly from tests at constant 50°C. **Figure 5.7** shows the impedance spectra for duplicate samples when measured at 50°C and (50°C-E_A) after various exposure periods. These figures hardly show any significant difference between coated panels exposed at constant 50°C and (50°C-E_A) during early immersion test, but it is interesting to note that at longer immersion test, more effect seems to come from the test at constant 50°C. It is not possible to draw statistically significant conclusions on the basis of the duplicate tests, but this result would be reasonable. The conclusion would be reasonable because high temperature speed up degradation, so if we cool down from time to time degradation will be slower.

[6]Coated panel is exposed at 50°C but slowly cooled to ambient temperature to determine activation energy, E_A

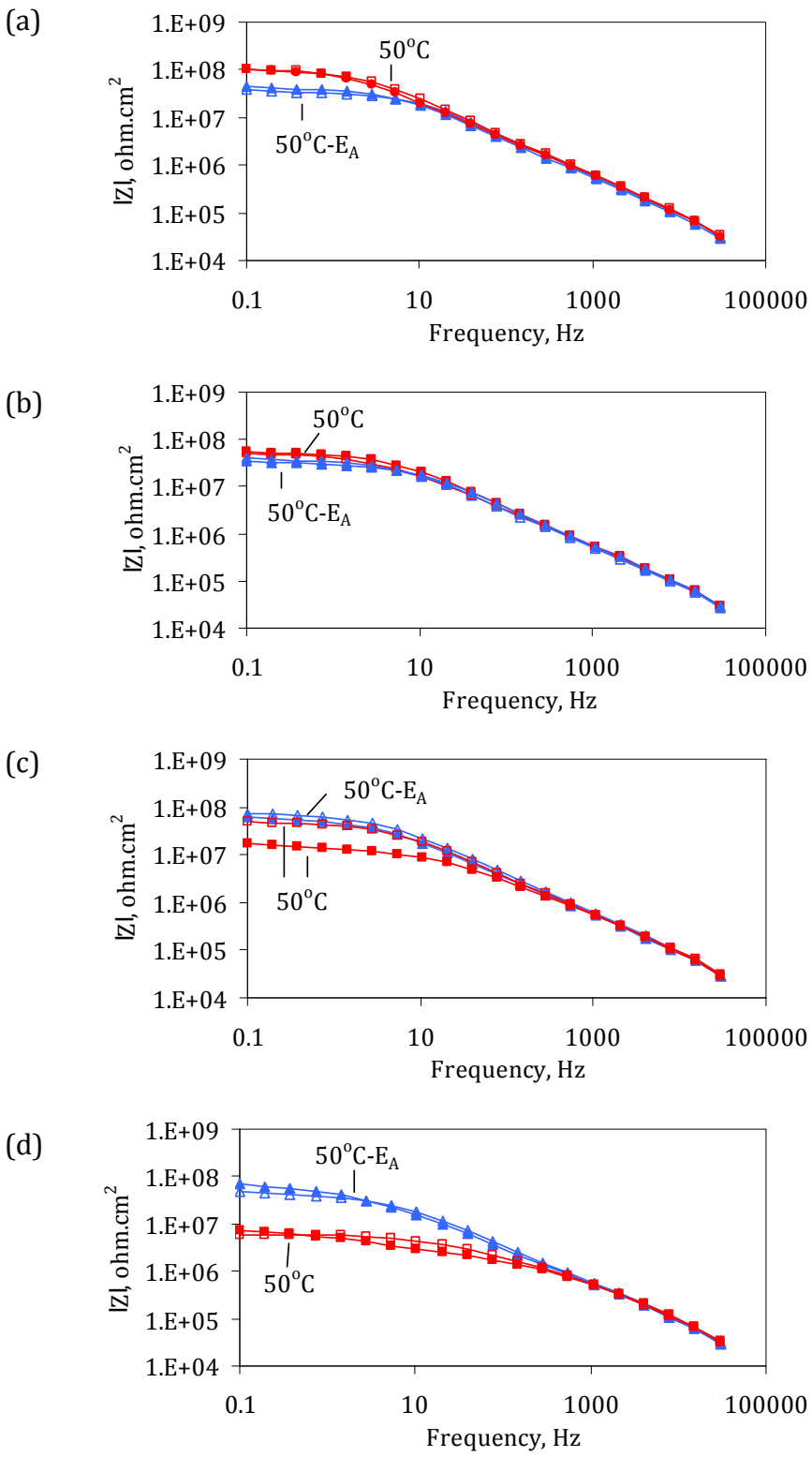

Figure 5.7- Bode plot for ZP-full system coating after (a) 1 day, (b) 3 days, (c) 7 days and (d) 14 days of exposure at constant 50°C and (50°C-E_A)

5.3.3 Temperature Dependence of Coating Parameter

Figures 5.8 to **5.13** show the effect of changing temperature on the EIS response of ZP-full system coating in 3% NaCl solution after 7, 14, 30, 46, 70 and 180 days exposure at 50^{o}C. From these figures the influence of temperature on the impedance of the coating is obvious where higher temperature generates a much smaller semicircle size. No second semicircle can be observed even after 6 months of immersion. Because of the absence of the second semicircle, it is difficult to distinguish whether the curves represent ionic diffusion through the coating or corrosion reaction at interface or both.

The impedance spectra were then fitted with an appropriate equivalent circuit using ZSimpWin software. However, the circuit with one time constant R[QR] was having difficulty in fitting the data at lower frequency values as shown in **Figures 5.14** and **5.16**. So, another equivalent circuit consisting two time constants, R[Q[R[QR]]] is used and a better fit was observed (**Figures 5.15** and **5.17**). Thus, two time constants were now used to fit all the curves and the fitted parameters are summarized in **Tables 5.2** to **5.7**. According to these tables, the coating resistances, R_p are about 10^5–10^6ohm.cm^2 and this is unlikely as the coating tested here is a very thick coating (290μm). On the other hand the charge transfer resistance values, R_{ct} is very high (10^7–10^{10}ohm.cm^2). It can be suggested that the curve is being dominated by the charge transfer resistance that the coating resistance value is a small fraction but that seems unlikely. Plotting logarithm of charge transfer resistance, R_{ct} against 1/T may perhaps give some answers. **Figures 5.18** to **5.23** display the Arrhenius plots in which activation energy is calculated by multiplying the slope by the gas constant.

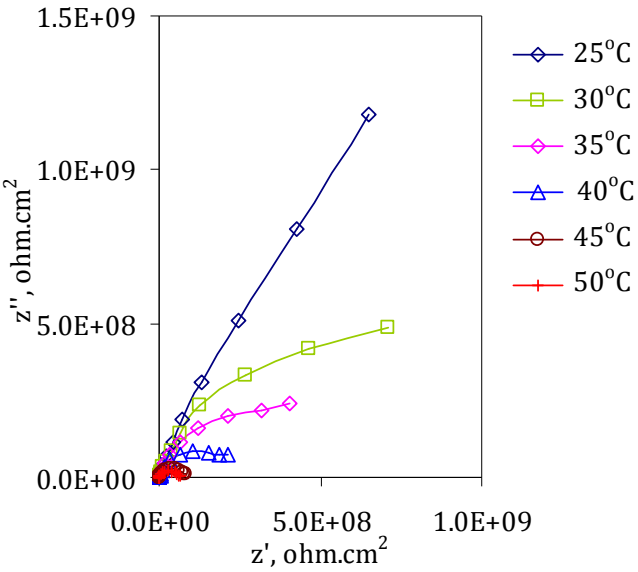

Figure 5.8 - Nyquist plots at various temperatures for ZP-full system coating after 7 days of exposure at 50°C

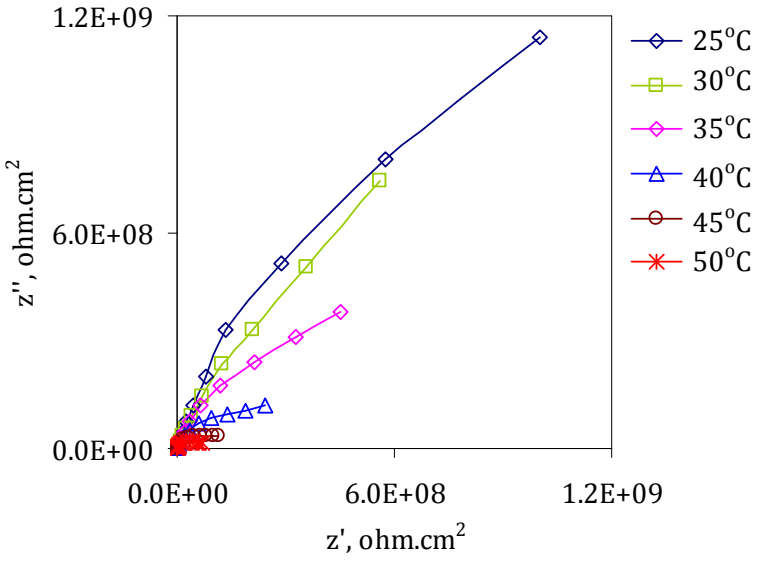

Figure 5.9 - Nyquist plots at various temperatures for ZP-full system coating after 14 days of exposure at 50°C

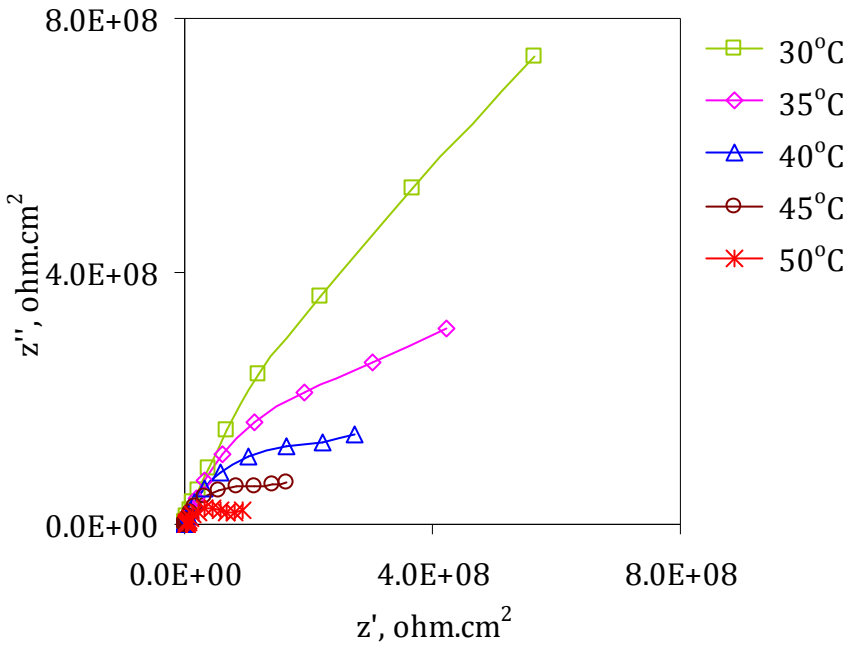

Figure 5.10 - Nyquist plots at various temperatures for ZP-full system coating after 30 days of exposure at 50°C

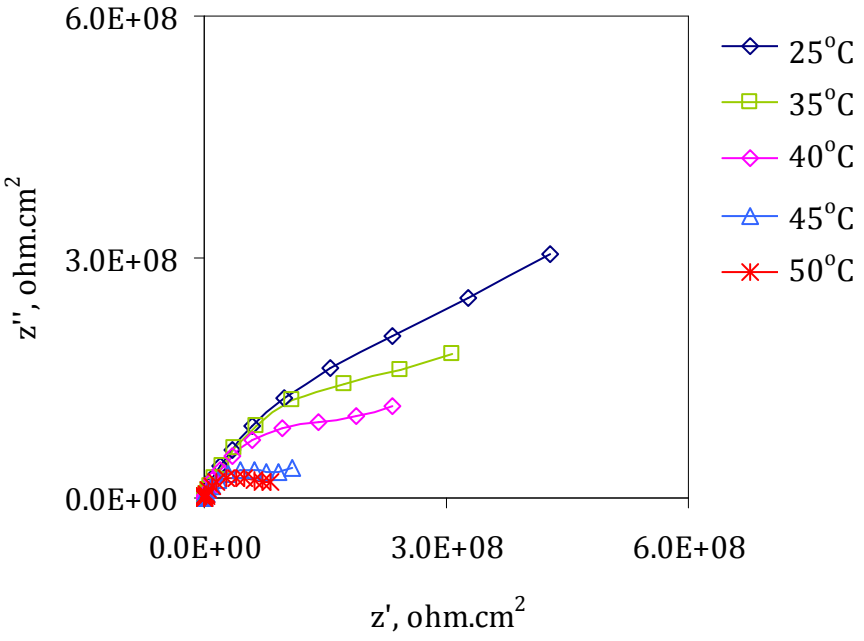

Figure 5.11 - Nyquist plots at various temperatures for ZP-full system coating after 46 days of exposure at 50°C

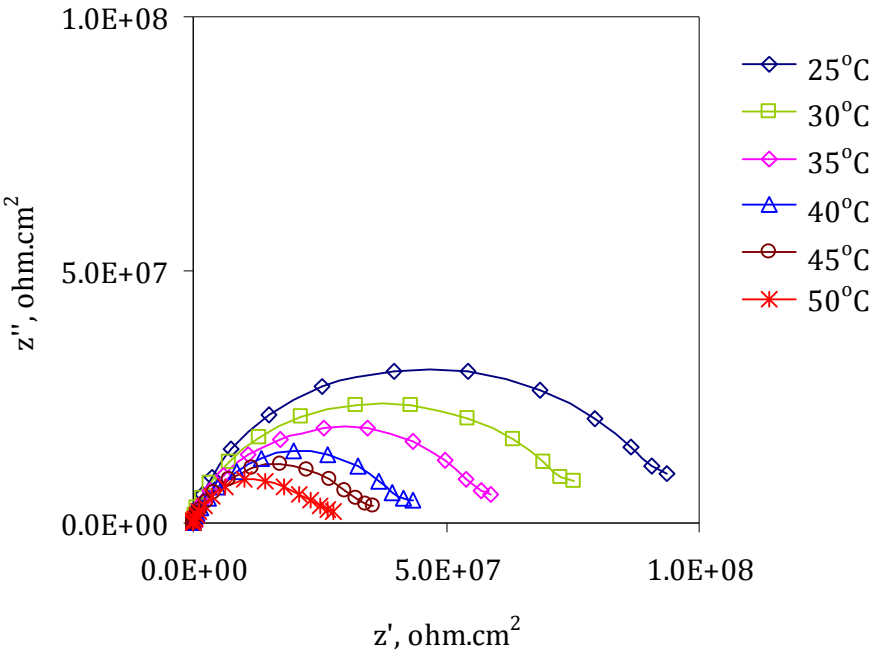

Figure 5.12 - Nyquist plots at various temperatures for ZP-full system coating after 70 days of exposure at 50°C

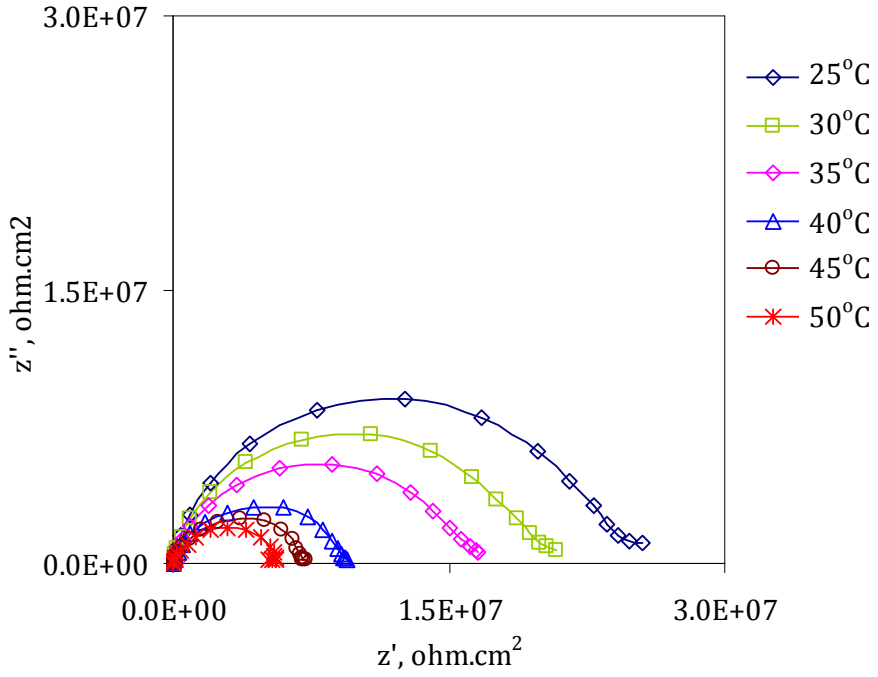

Figure 5.13 - Nyquist plots at various temperatures for ZP-full system coating after 180 days of exposure at 50°C

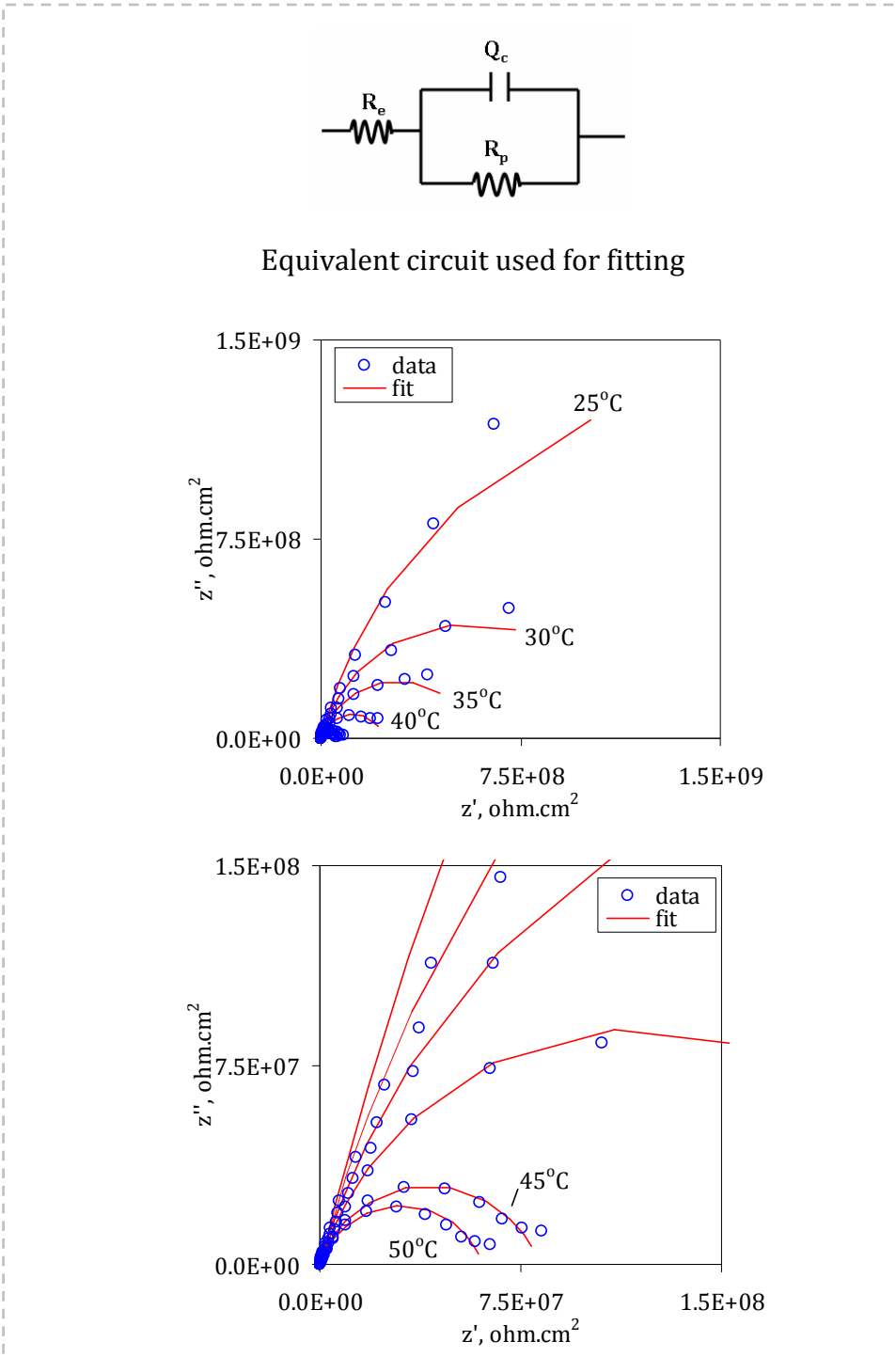

Figure 5.14 - Experimental (o) and simulated (-) Nyquist plot of ZP-full system coating exposed at various temperatures after 7 days of exposure at 50°C using equivalent circuit R[QR]

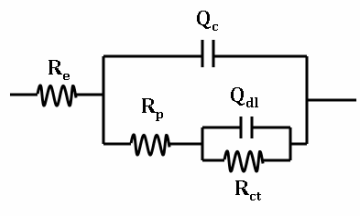

Equivalent circuit used for fitting

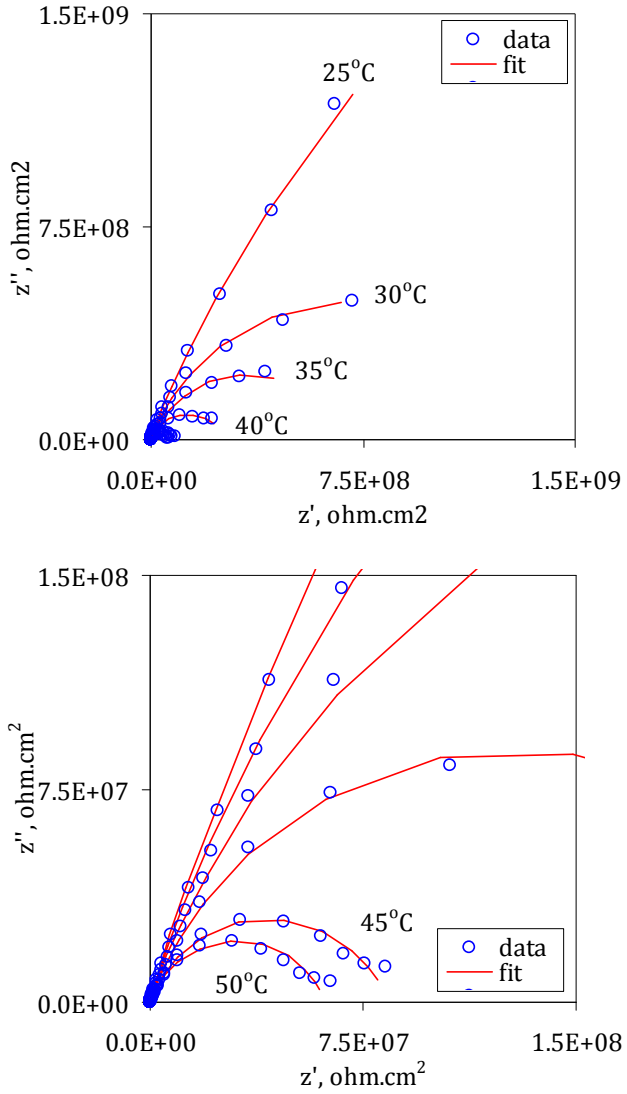

Figure 5.15 - Experimental (o) and simulated (-) Nyquist plot of ZP-full system coating exposed at various temperatures after 7 days of exposure at 50°C using equivalent circuit R[Q[R[QR]]]

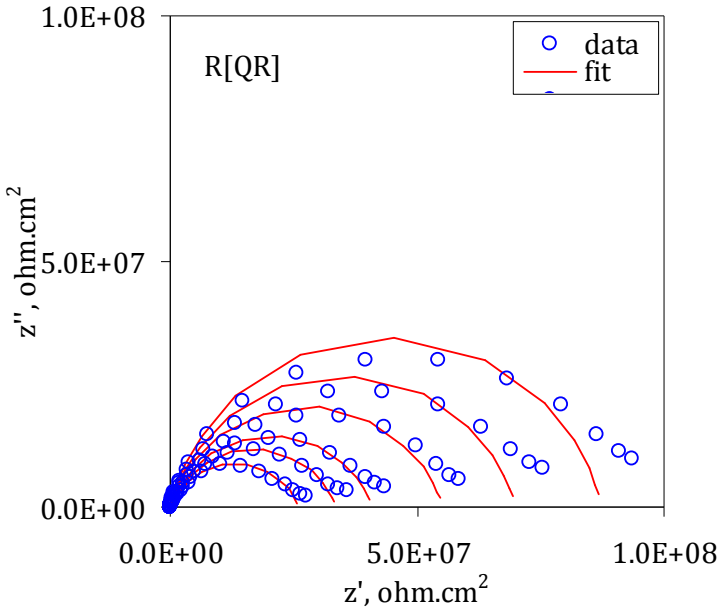

Figure 5.16 – Experimental (o) and simulated (-) Nyquist plot for ZP-FS coating after 70 days of exposure at 50°C fitted with R[QR]

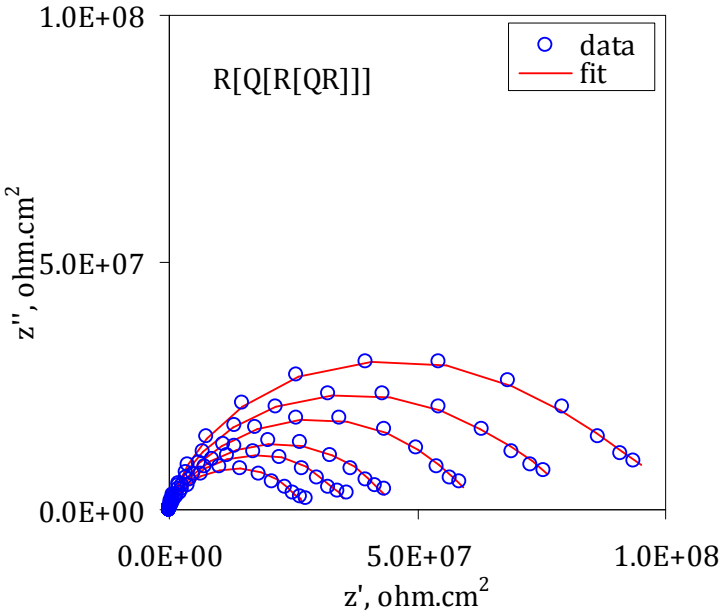

Figure 5.17 – Experimental (o) and simulated (-) Nyquist plot for ZP-FS coating after 70 days of exposure at 50°C fitted with R[Q[R[QR]]]

Table 5.2 - Best fitting parameters for ZP-FS coating after 7 days of exposure at 50°C

Fitted circuit:R[Q[R[QR]]]

T (°C)	Q_c (Fcm^{-2})^n	Q_c (%error)	n	R_p ($ohm.cm^2$)	R_p (%error)	Q_{dl} (Fcm^{-2})^n	Q_{dl} (%error)	n	R_{ct} ($ohm.cm^2$)	R_{ct} (%error)	X^2
25	1.40E-10	76.94	1	1.04E+06	120.9	8.13E-10	11.29	0.70	1.09E+10	40.99	1.73E-03
30	1.49E-10	63.43	1	1.15E+06	75.37	9.43E-10	10.44	0.72	1.43E+09	8.49	2.89E-03
35	1.56E-10	68.73	1	8.84E+05	74.14	1.27E-09	8.79	0.71	6.97E+08	6.22	2.59E-03
40	1.65E-10	67.52	1	7.50E+05	61.49	1.53E-09	9.092	0.71	2.65E+08	4.47	2.85E-03
45	2.11E-10	58.73	0.98	6.42E+05	46.15	1.74E-09	10.93	0.73	8.36E+07	3.07	2.35E-03
50	1.84E-10	63.02	1	5.35E+05	44.54	1.90E-09	10.40	0.73	6.17E+07	2.94	2.44E-03

Table 5.3 - Best fitting parameters for ZP-FS coating after 14 days of exposure at 50°C

Fitted circuit:R[Q[R[QR]]]

T (°C)	Q_c (Fcm^{-2})^n	Q_c (%error)	n	R_p ($ohm.cm^2$)	R_p (%error)	Q_{dl} (Fcm^{-2})^n	Q_{dl} (%error)	n	R_{ct} ($ohm.cm^2$)	R_{ct} (%error)	X^2
25	1.30E-10	85.86	1	1.17E+06	122.9	6.97E-10	14.54	0.72	4.34E+09	16.9	2.68E-03
30	1.39E-10	81.19	1	9.27E+05	119.5	1.17E-09	7.63	0.68	3.94E+09	22.94	1.79E-03
35	1.42E-10	96.28	1	7.77E+05	111.3	1.37E-09	8.53	0.68	1.19E+09	10.27	2.65E-03
40	1.56E-10	92.96	1	6.74E+05	88.27	1.94E-09	9.81	0.68	3.49E+08	11.55	3.47E-03
45	1.88E-10	64.66	0.99	6.07E+05	49.66	2.11E-09	11.2	0.71	1.04E+08	7.27	2.36E-03
50	1.75E-10	110.3	1	4.22E+05	79.66	2.84E-09	11.8	0.69	7.00E+07	6.64	3.79E-03

Table 5.4 - Best fitting parameters for ZP-FS coating after 30 days of exposure at 50°C

Fitted circuit:R[Q[R[QR]]]

T (°C)	Q_c $(Fcm^{-2})^n$	Q_c (%error)	n	R_p ($ohm.cm^2$)	R_p (%error)	Q_{dl} $(Fcm^{-2})^n$	Q_{dl} (%error)	n	R_{ct} ($ohm.cm^2$)	R_{ct} (%error)	X^2
30	1.35E-10	68.61	1	1.08E+06	103	1.15E-09	6.58	0.67	4.30E+09	21.91	1.58E-03
35	1.41E-10	75.02	1	9.32E+05	83.29	1.49E-09	7.19	0.68	9.63E+08	9.01	2.78E-03
40	5.57E-10	41.06	0.88	4.32E+06	77.29	1.30E-09	20.27	0.66	4.12E+08	6.59	2.34E-03
45	5.62E-10	75.24	0.88	1.95E+06	113.2	1.74E-09	27.22	0.66	2.11E+08	6.46	3.59E-03
50	2.09E-09	68.97	0.75	2.38E+06	28.91	1.32E-09	65.11	0.51	9.89E+07	9.62	4.71E-03

Table 5.5 - Best fitting parameters for ZP-FS coating after 46 days of exposure at 50°C

Fitted circuit:R[Q[R[QR]]]

T (°C)	Q_c $(Fcm^{-2})^n$	Q_c (%error)	n	R_p ($ohm.cm^2$)	R_p (%error)	Q_{dl} $(Fcm^{-2})^n$	Q_{dl} (%error)	n	R_{ct} ($ohm.cm^2$)	R_{ct} (%error)	X^2
25	3.06E-10	211.3	0.92	3.00E+06	5216	1.59E-09	21.38	0.45	1.80E+09	59.43	2.55E-03
35	1.40E-10	105.7	1	7.81E+05	136.8	1.75E-09	6.66	0.65	5.61E+08	7.95	2.61E-03
40	1.47E-10	87.51	1	7.98E+05	95.74	2.01E-09	7.03	0.66	3.54E+08	6.41	3.12E-03
45	1.62E-10	95.89	1	6.15E+05	78.22	2.61E-09	9.65	0.68	1.25E+08	5.50	4.76E-03
50	1.67E-10	89.33	1	5.40E+05	65.95	2.78E-09	9.51	0.68	8.73E+07	4.58	4.03E-03

Table 5.6 - Best fitting parameters for ZP-FS coating after 70 days of exposure at 50°C

Fitted circuit:R[Q[R[QR]]]

T (°C)	Q_c (Fcm^{-2})^n	Q_c (%error)	n	R_p ($ohm.cm^2$)	R_p (%error)	Q_{dl} (Fcm^{-2})^n	Q_{dl} (%error)	n	R_{ct} ($ohm.cm^2$)	R_{ct} (%error)	X^2
25	3.29E-10	242.1	0.89	1.50E+06	1.84+E04	1.58E-09	548.4	0.42	1.05E+08	256.5	1.23E-03
30	3.36E-10	106.8	0.90	1.21E+06	2605	1.97E-09	90.15	0.46	8.33E+07	33.42	1.10E-03
35	2.17E-10	115.5	0.94	5.21E+05	364.1	1.97E-09	14.34	0.58	6.24E+07	2.65	1.06E-03
40	1.16E-10	181.7	1	3.12E+05	182.5	2.45E-09	8.26	0.64	4.51E+07	1.97	9.53E-04
45	1.24E-10	139.8	1	3.67E+05	110.1	2.73E-09	6.34	0.65	3.62E+07	2.17	1.27E-03
50	1.43E-10	121.8	0.99	3.62E+05	81.99	3.06E-09	7.73	0.66	2.73E+07	2.49	1.61E-03

Table 5.7 - Best fitting parameters for ZP-FS coating after 180 days of exposure at 50°C

Fitted circuit:R[Q[R[QR]]]

T (°C)	Q_c (Fcm^{-2})^n	Q_c (%error)	n	R_p ($ohm.cm^2$)	R_p (%error)	Q_{dl} (Fcm^{-2})^n	Q_{dl} (%error)	n	R_{ct} ($ohm.cm^2$)	R_{ct} (%error)	X^2
25	5.09E-10	18.38	0.90	1.19E+07	105.9	2.19E-09	112.2	0.87	2.46E+07	101.4	2.91E-03
30	5.82E-10	14.72	0.89	7.88E+06	108.1	1.95E-09	74.79	0.87	2.01E+07	72.2	3.09E-03
35	6.65E-10	27.73	0.91	3.50E+06	110.8	1.48E-09	26.4	0.87	1.60E+07	33.25	5.17E-03
40	7.67E-10	35.17	0.91	1.58E+06	88.33	1.59E-09	18.44	0.86	9.23E+06	19.8	3.36E-03
45	7.96E-10	43.66	0.91	9.20E+05	75.52	1.62E-09	18.52	0.85	7.08E+06	12.63	3.03E-03
50	1.35E-09	42.45	0.88	5.07E+05	72.84	1.96E-09	17.62	0.83	5.57E+06	8.52	2.31E-03

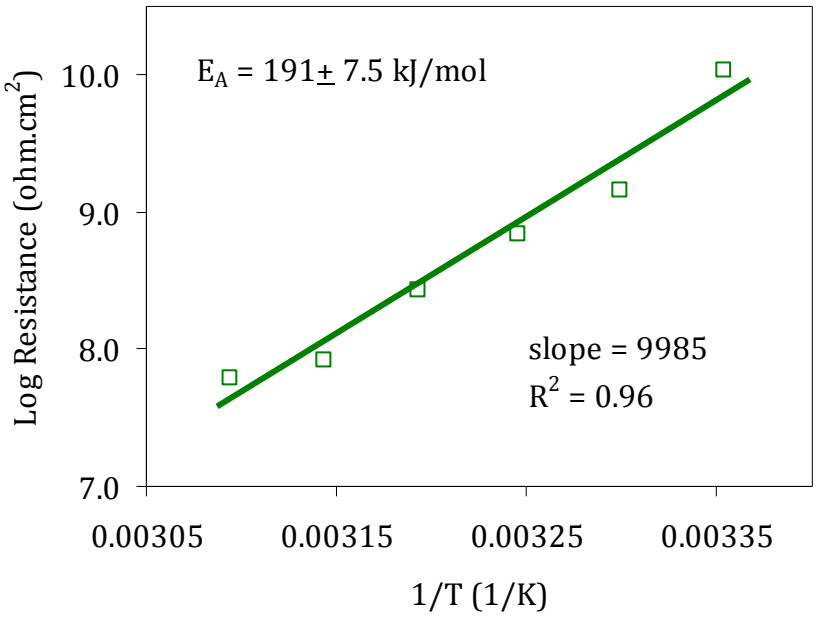

Figure 5.18 – Arrhenius plot of ZP-FS coating after 7 days of exposure for 'R_{ct}'

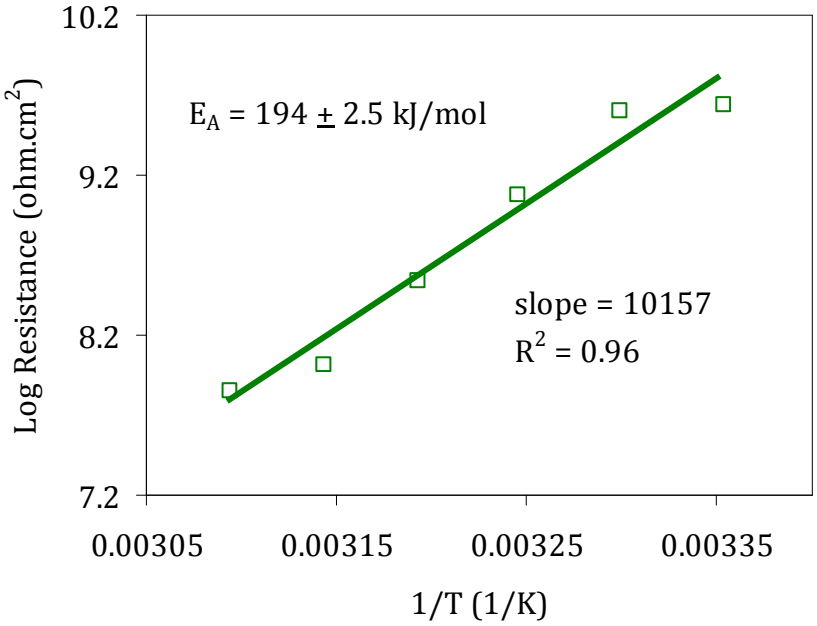

Figure 5.19 – Arrhenius plot of ZP-FS coating after 14 days of exposure for 'R_{ct}'

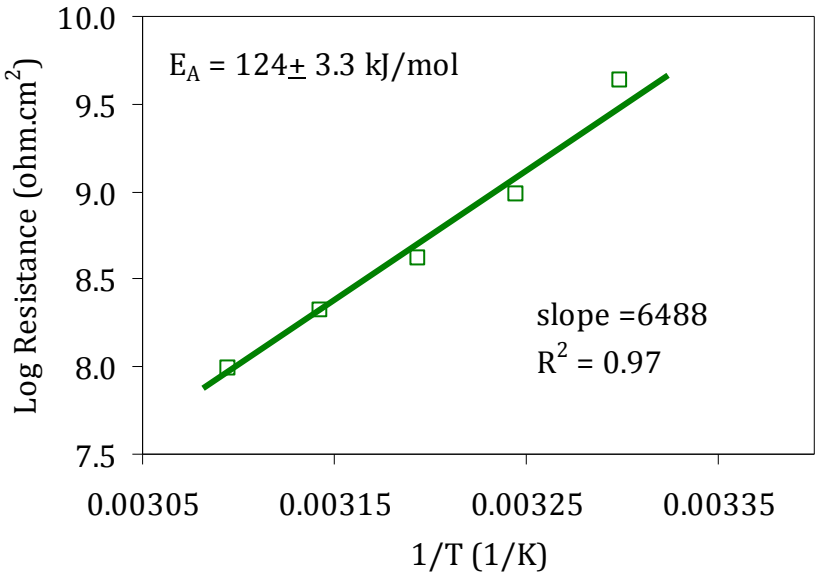

Figure 5.20– Arrhenius plot of ZP-FS coating after 30 days of exposure for 'R_{ct}'

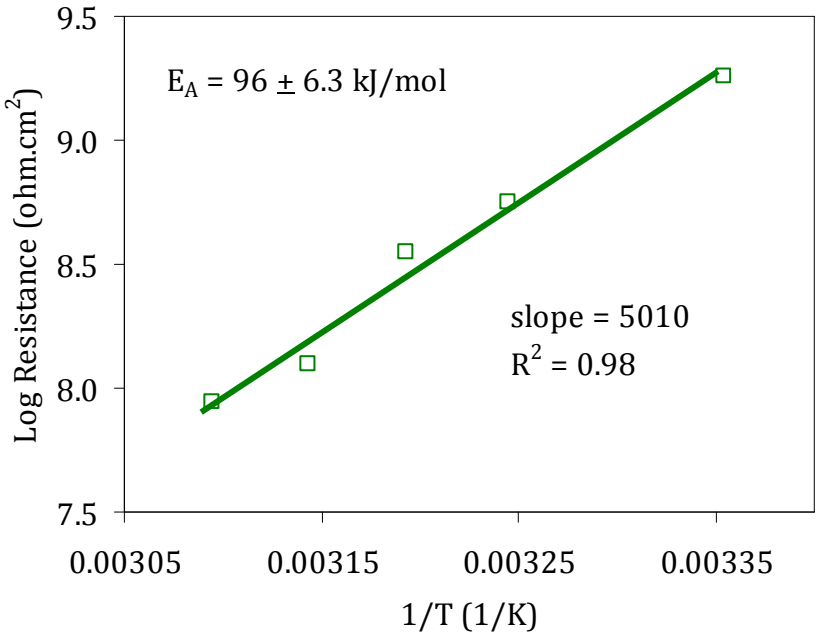

Figure 5.21 – Arrhenius plot of ZP-FS coating after 46 days of exposure for 'R_{ct}'

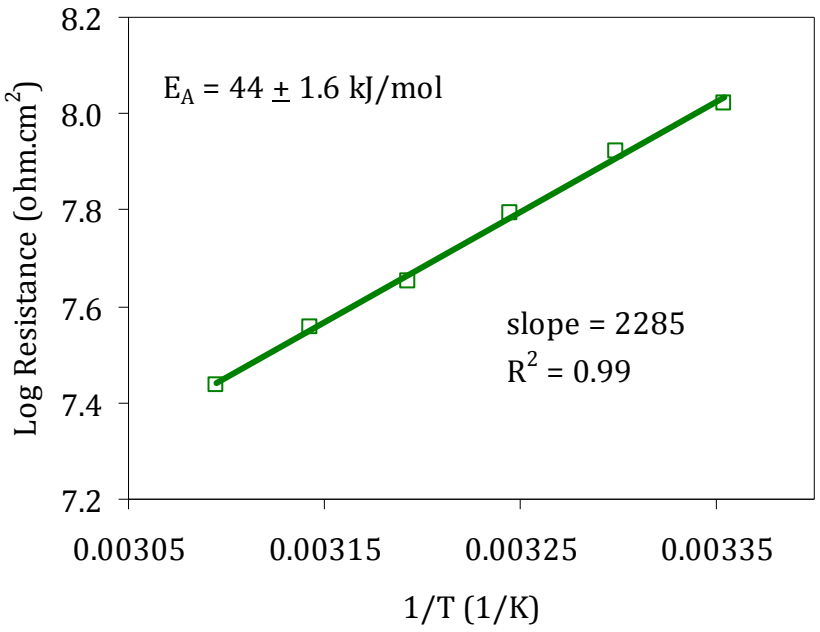

Figure 5.22 – Arrhenius plot of ZP-FS coating after 70 days of exposure for 'R_{ct}'

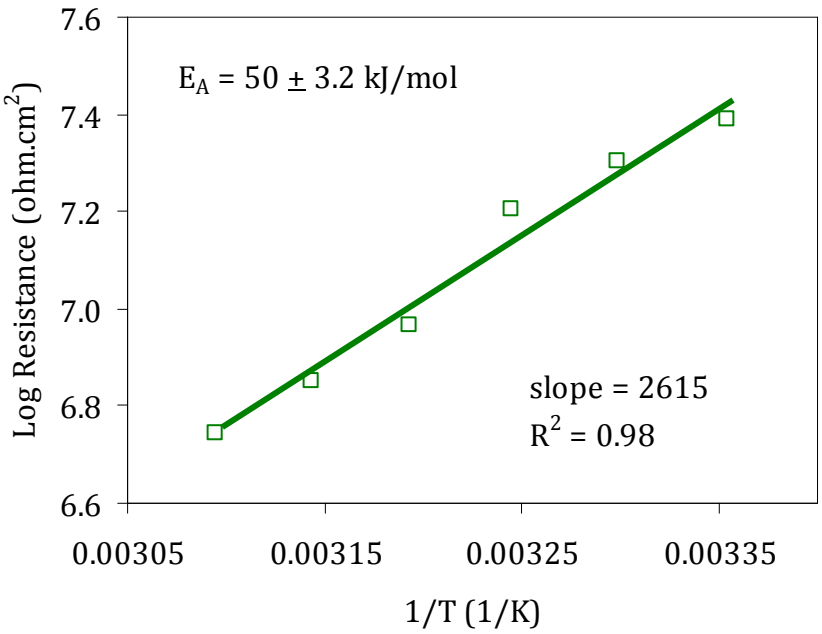

Figure 5.23 – Arrhenius plot of ZP-FS coating after 180 days of exposure for 'R_{ct}'

Table 5.8 – Summary of activation energy, E_A values, calculated from 'R_{ct}'

Time, day	7	14	30	46	70	180
E_A, $kJmol^{-1}$	191	194	124	96	44	50
Error, $\pm$	7.5	2.5	3.3	6.3	1.6	3.2

Table 5.8a – Summary of activation energy, E_A values, calculated from 'R_{ct}' of other panel

Time, day	3	21	30	46	70	90
E_A, $kJmol^{-1}$	134	139	133	120	130	135
Error, $\pm$	7.7	2.9	18.1	13.7	6.9	6.9

As presented in **Tables 5.8** and **5.8a**, the activation energies calculated from 'R_{ct}' are giving large values. From this test, only the larger resistance can be measured with certainty from the impedance spectra and it is uncertain whether it is the coating or corrosion reaction at the interface (only one semicircle is presence in the impedance spectra). According to the findings in **Section 4.3.5**, high activation energy was generated from the charge transfer resistance. So there is a possibility that since the activation energies generated in this test were high that the response of the impedance spectra is being dominated by the charge transfer resistance. High activation energies were generated from the high resistance value and this would be evidence that this high resistance is related to the charge transfer resistance. However, Ochs and Vogelsang [160] have shown increasing values of activation energy with coating thickness, based on values of 'coating resistance' of coated panels. As this test is unable to distinguish for certain between the coating and the corrosion at the interface, it is unable to test the link between them. Nevertheless the activation energy generated

from this test is larger than before and in agreement with Ochs and Vogelsang's [160] observation, but here we link the behaviour to the electrochemical process rather than to ion transport in the paint.

5.4 Conclusions

- Only one semicircle is apparent in the impedance spectra but fitting with one time constant gave large errors, so two time constants were used and a better fit was observed. However the coating resistances, R_p are about 10^5–10^6ohm.cm^2 and this is unlikely as the coating tested here is very thick (290μm). But high charge transfer resistance, R_{ct} values were observed.

- Activation energies determined from charge transfer resistance gave large values (44–191 kJmol^{-1}). According to previous study (**Section 4.3.5**) high activation energy was generated from the charge transfer resistance. So there is a possibility that since the activation energies in this test were high that the response of the impedance spectra is being dominated by the charge transfer resistance.

- As this test is unable to distinguish for certain between the coating and the corrosion at the interface, it is unable to test any link between them. But the activation energy generated from this test is larger than before and in agreement with Ochs and Vogelsang's [160] observation, but here we link the behaviour to the electrochemical process rather than to ion transport in the paint.

CHAPTER 6

MULTILAYER COATINGS WITH SACRIFICIAL PIGMENTS

6.1 Introduction

In this work, multilayer coatings[7] with sacrificial pigment in the primer were tested to observe whether the same conclusions derived for a primer coating system hold for a real system used in the field. Similar middle and top coatings were used to the multilayer coating in **Chapter 5**, but the primer used here is zinc rich paint (**Figure 6.1**). It is expected that the zinc rich paint does not form a barrier coating for the metal substrate rather it will be the most active component of the 'substrate' in the electrochemistry. The outer 2 coats (180µm middle and 60µm topcoat) will form the barrier layer.

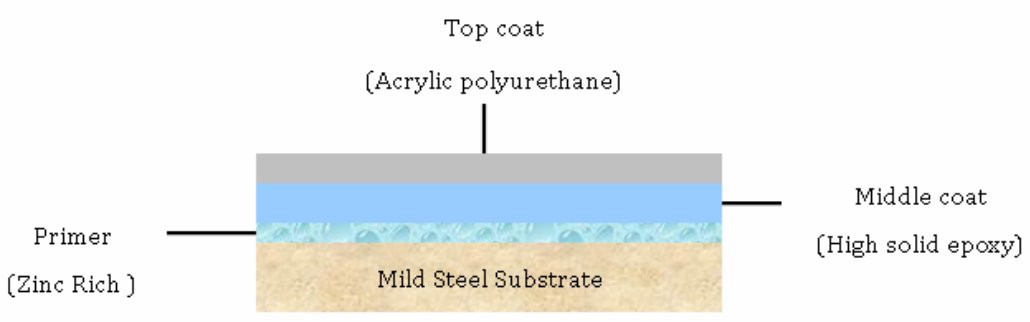

Figure 6.1 - Schematic diagram of a multilayer coating consisting of primer, middle and top coating

[7] Also referred as 'real system' or 'full system' throughout the thesis

In this work, the electrochemical activity of the zinc rich primer (coupled to the steel substrate) plus the barrier properties of those two topcoats were my concern. Thus, steel with zinc rich primer alone was tested first to identify characteristics of its electrochemical (sacrificial action) behaviour.

6.2 Materials

In this study, two types of zinc rich coatings, zinc rich primer and zinc rich full system are under investigation. For simplicity, panels are identified as ZRP and ZR-FS respectively. Details of ZR-FS coating are listed in **Table 6.1**.

Table 6.1 – Zinc rich full system coating information

System	Primer	Middle	Top
ZR-FS	Zinc rich epoxy[1]	High solid epoxy[2]	Acrylic polyurethane[3]
Thickness, DFT	50µm	180µm	60µm

[1]A two component zinc rich epoxy primer containing 81% zinc
[2]A low VOC, high solids, high build, 2-component epoxy coating, pigmented with micaceous iron oxide
[3]A two component acrylic polyurethane finish

6.3 Results and Discussion for Zinc Rich Primer Coating (ZRP) Alone

6.3.1 Visual Inspection

Optical micrographs as seen in **Figure 6.2** show the results of galvanic activity on the surface of the ZRP coating surface before and after exposure up to 22 days in 3% NaCl

solution. **Figure 6.2b** shows the presence of small 'white' particles, probably zinc oxide which starts to build up on the coating surface after 2 days of exposure. By day 19, the presence of blisters was noted and with time, these blisters grow, and unlike normal blisters, they are rough and not smooth (**Figure 6.2c**).

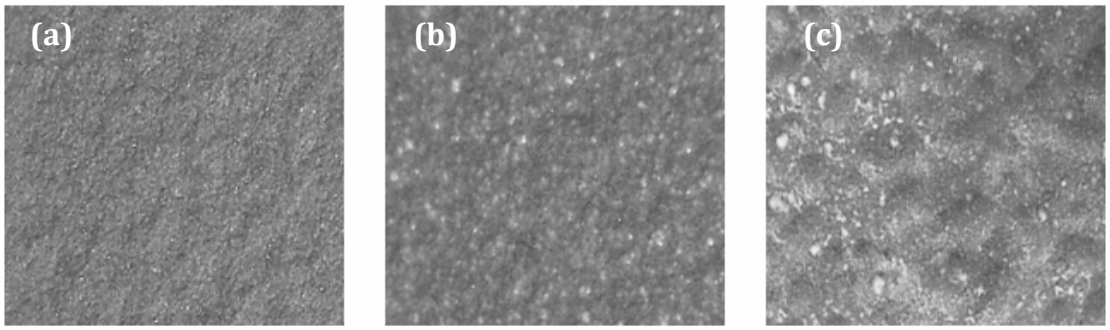

Figure 6.2 – Optical image showing the formation of corrosion product on the surface of ZRP coating after (a) 0 day; (b) 2 days; (c) 22 days of exposure

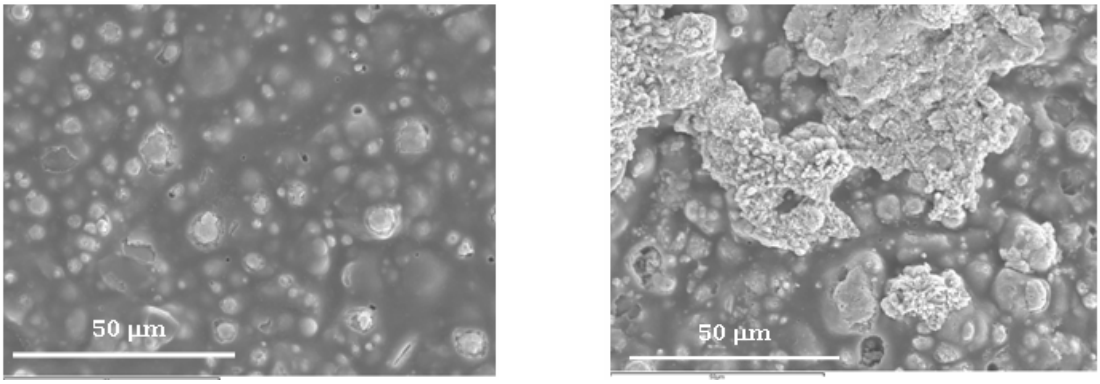

(a) (b)

Figure 6.3 – Top view SEM micrograph of ZRP coating; (a) before exposure (b) after 22 days of exposure

Figure 6.3 shows top view SEM images of ZRP coated panel before and after exposure. The changes of the surface morphology of the coated panel were seen with the presence of bright particles. The observed bright particles on the coating surface as seen in **Figure 6.3b** are likely to be corrosion product from zinc that has been consumed in order to protect the metal substrate.

6.3.2 Preliminary Analysis for Coated Panel Exposed at 21°C

After an hour of exposure, the modulus of impedance shows a plateau at low frequency (**Figure 6.4a**), while the Nyquist plot shows two semicircles (**Figure 6.4b**). This indicates that the coating is highly porous and permeable. The potentials recorded were -0.96 V_{SCE} and -0.98 V_{SCE} which suggests that zinc particles are already starting to corrode.

There are disagreements in the literature concerning the analysis and interpretation of the impedance spectra. For some authors, the semicircle at higher frequency corresponds to undefined charge transfer process while the semicircle at low frequency is related to oxygen diffusion [61, 170, 171]. Other studies conclude that semicircle at low frequency is related to the charge transfer for zinc dissolution, whereas the high frequency range shows the dielectric properties of the polymeric matrix [64, 172]. An active electrode acts as R_p in parallel with C_{dl} (one semicircle), so for ZRP panels we don't expect two, but sometimes oxide films/passivity generates a more complicated diagram thus the coating does not behave like a simple zinc electrode.

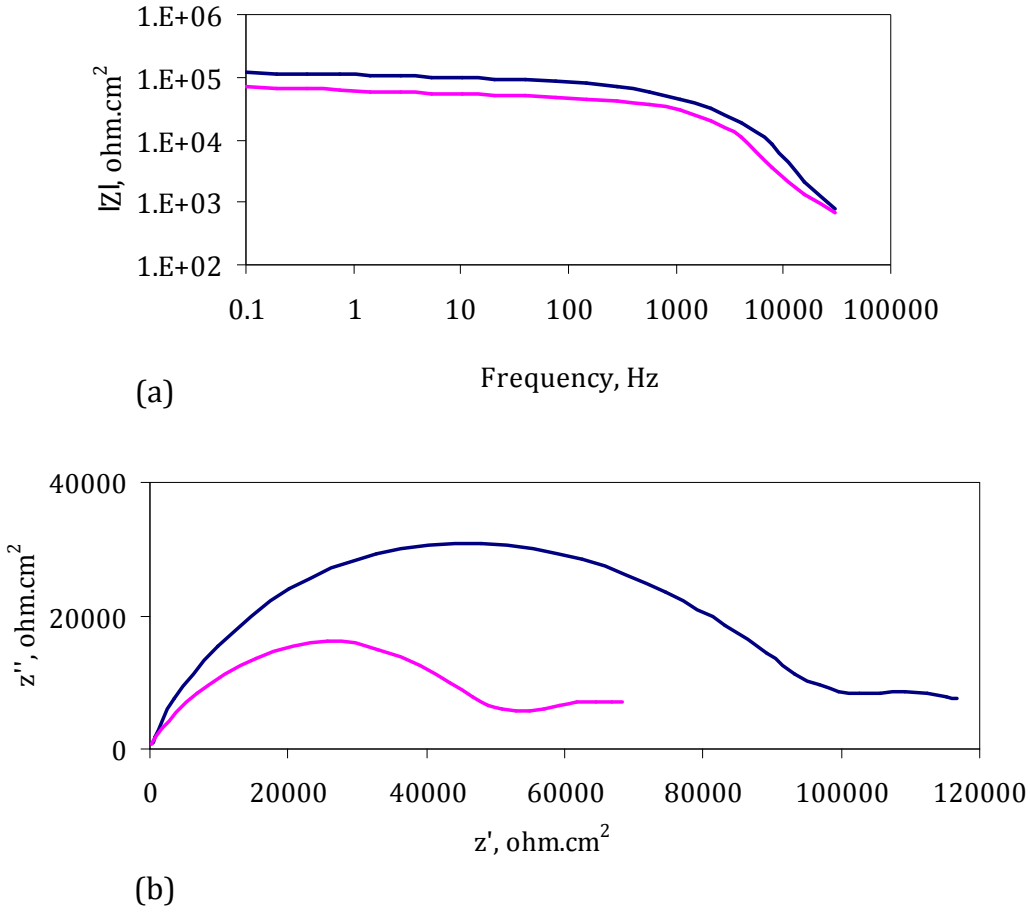

Figure 6.4 – Bode (a) and Nyquist (b) plots obtained for ZRP coating (2 replicates) after 1-hour exposure at ambient temperature

6.3.3 Bode Plot Evolution with Time

Impedance spectra for the ZRP coating characterises anodic activity of the zinc pigment, rather than the corrosion behaviour of the steel or barrier properties of the coating. This is illustrated in **Figure 6.5**, where impedance modulus, |Z|, at low frequency decreases steadily until on the 8th day, when it starts to increase again. This pattern indicates increasing activity at first that subsequently decreases again. This

behaviour agrees with the results obtained by Feliu et al. [61] where they attribute the behaviour to active zinc dissolution at first then as the effective surface area of zinc decreases and pores are plugged by the zinc corrosion product, an increase in impedance taken place.

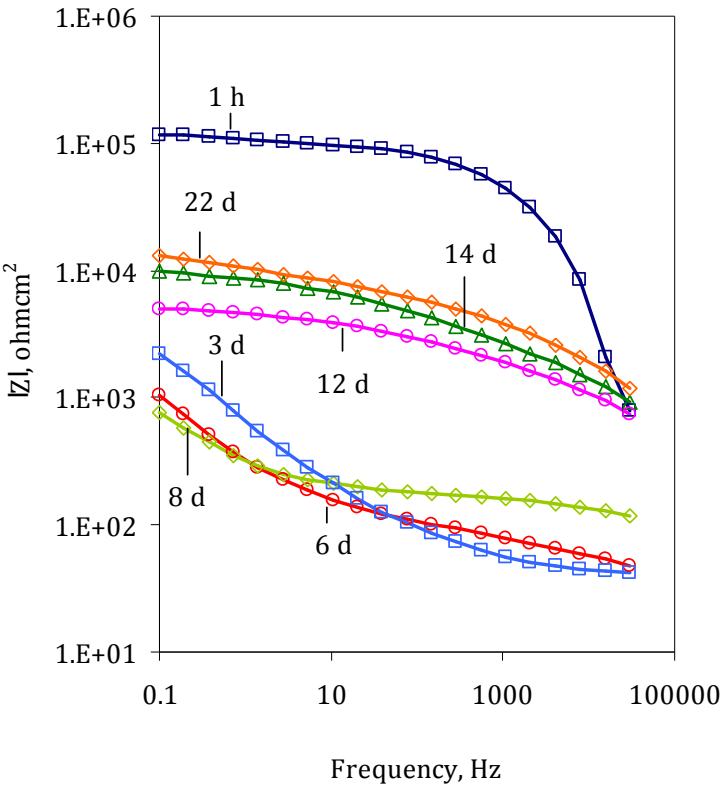

Figure 6.5 – Bode plot evolution with immersion time measured at 21°C for ZRP coating after exposure at 50°C

6.3.4 Nyquist Plot Evolution with Time

Impedance spectra obtained for zinc rich primer system normally show one or two semicircles [61]. The impedance response of zinc rich primer coating is often very complex, difficult to interpret and no definite explanation is available [60] . **Figures 6.6**

and **6.7** show a summary of the Nyquist plots obtained at different times after exposure at 50°C. Since the two panels show comparable behaviour, only Nyquist plots from **Figure 6.6** are discussed in detail.

During early immersion, **Figures 6.6a**, **6.6b** and **6.6c** show a trend towards the formation of straight-line tails of about 45° slope at low frequency. These tails are possibly connected with a diffusion process through a layer of infinite thickness (Warburg impedance). Another study has shown that the insoluble corrosion products plugging the pores and perforations in the film lead to the appearance of the diffusion tail [173]. Notice that the impedance values are decreasing as immersion time increases. After 12 days of exposure, Nyquist plots show a different shape; the diffusion tail disappeared and possibly two semicircles or even a third semicircle appear (**Figures 6.6d**, **6.6e** and **6.6f**). The values of open circuit potential also start to rise above the protection potential for steel (-0.85V_{SCE}) by 12 days. Notice that the impedance values are also getting bigger. It is suggested that the corrosion current supplied by zinc is getting smaller thus an increase in impedance values were observed.

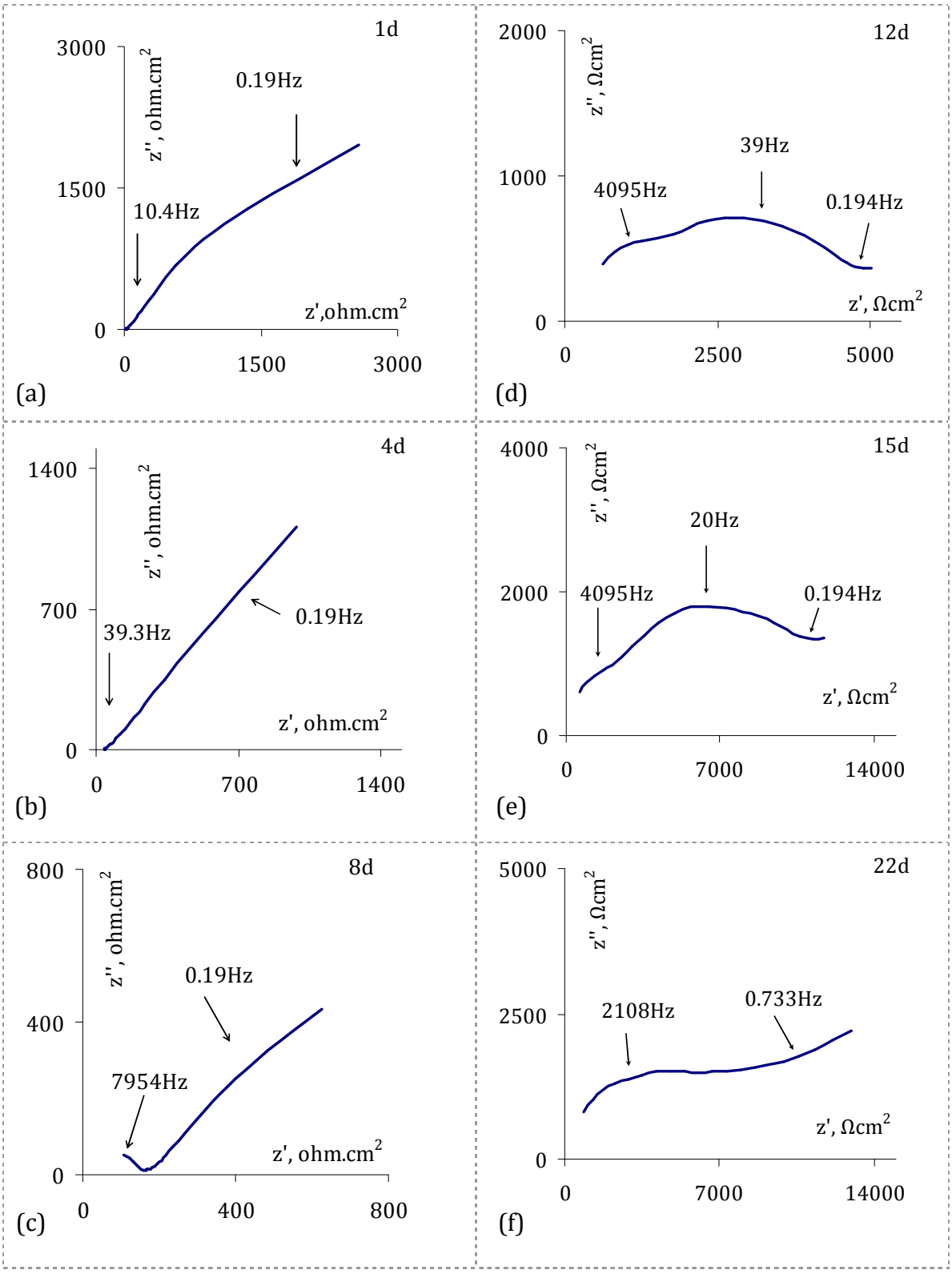

Figure 6.6 – Nyquist plots evolution with immersion time for ZRP coating after exposure at 50°C and measured at 21°C (Panel 1)

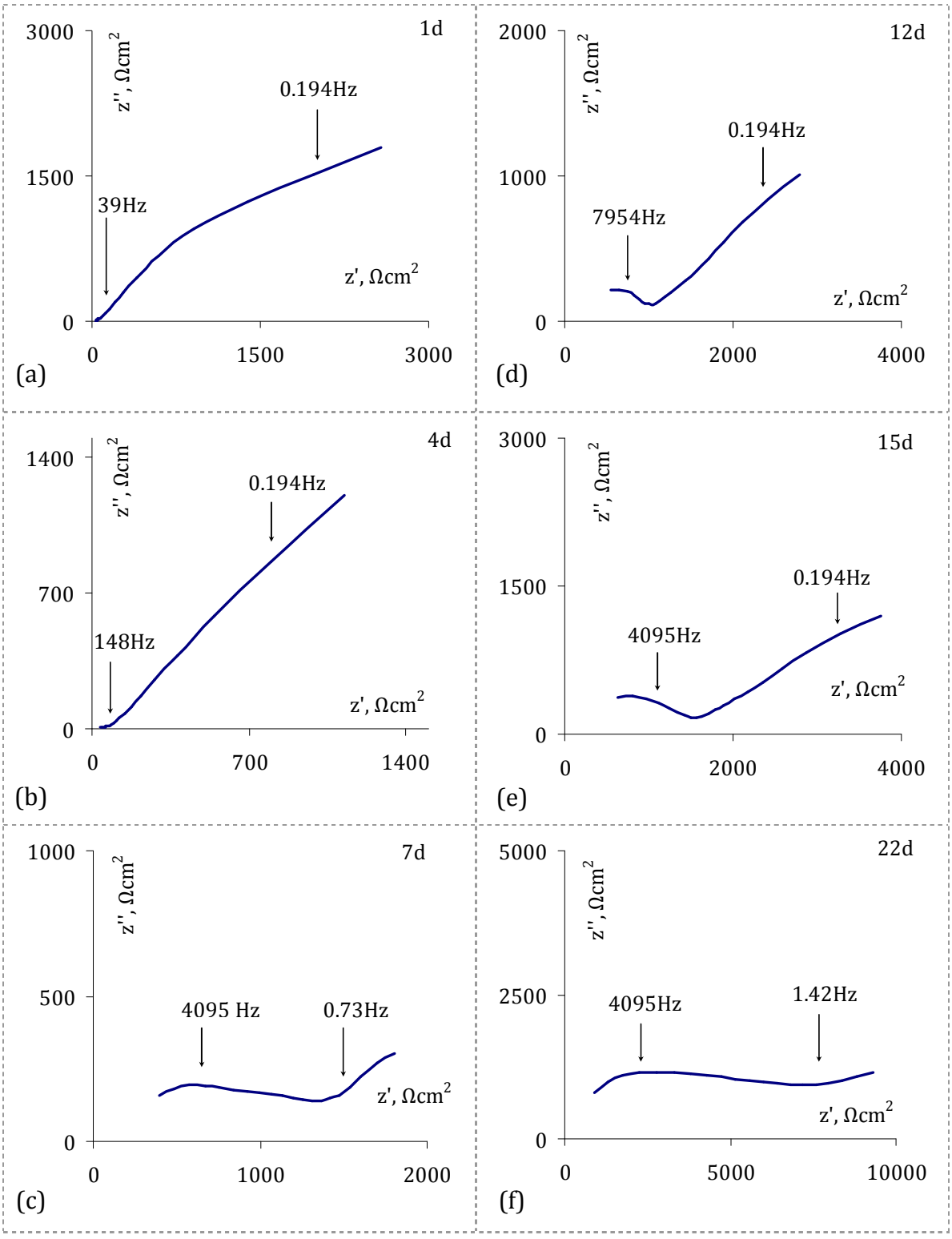

Figure 6.7 – Nyquist plots evolution with immersion time for ZRP coating after exposure at 50°C and measured at 21°C (Panel 2)

6.3.5 Open Circuit Potential Measurements

The exposure time dependence of the open circuit potential (OCP) was used as a simple tool for the evaluation of corrosion protection by ZRP coatings. ZRP coating can only protect the steel cathodically when the zinc particles in the primer have electrical contact with the steel substrate. According to Abreu et al. [68], the potential evolution is in close relationship with the variation of the ratio of active areas (zinc/steel). In other words, the upwards shift of the potential corresponds to the decrease of the electro-active zinc area, which means the decrease of the cathodic protection intensity. The effect of temperature changes on the potential of the saturated calomel electrode (SCE) raises a concern. When the temperature is changing, the level of concentration of saturated KCl solution inside the calomel electrode is also changing so that small relative potential shifts will take place. This will affect the potential reading that is being measured.

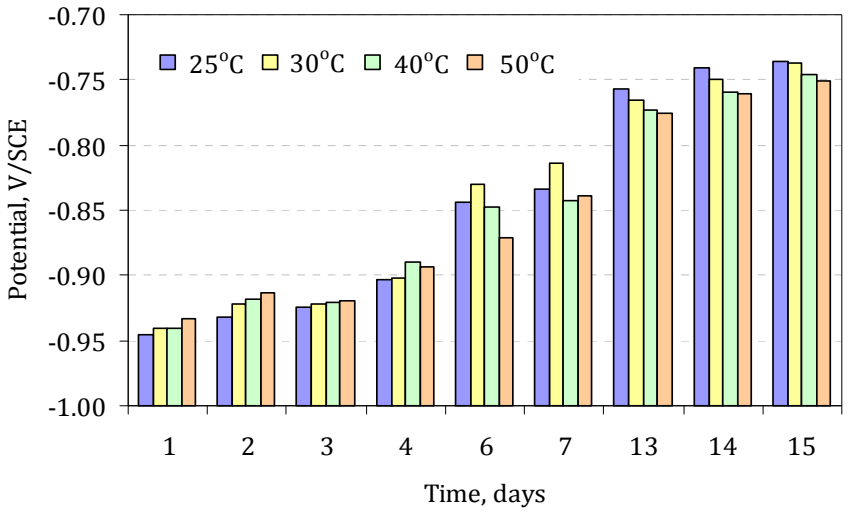

Figure 6.8 – The effect of changing temperature on the potential measurements over time for ZRP coating

The histogram in **Figure 6.8** compares the effect of changing temperature on the potential measurements of the coated metal with respect to SCE over time. It is evident that the potential measured on the coated metal at different temperatures are quite stable for each day and only small changes relative to potential shifts were observed. Therefore OCP measured in this study is an appropriate indication to evaluate the cathodic protection duration provided by ZRP coatings.

The duration of protection potential for steel (E_{PP}) is given as being the time during which the potential remains lower than free corrosion potential of steel (-0.65V_{SCE}) [174], however it is often taken in practical as being the time which the potential remains lower than -0.85V_{SCE} [68]. The ZRP coated panel potentials are monitored up to 22 days and presented in **Figure 6.9**.

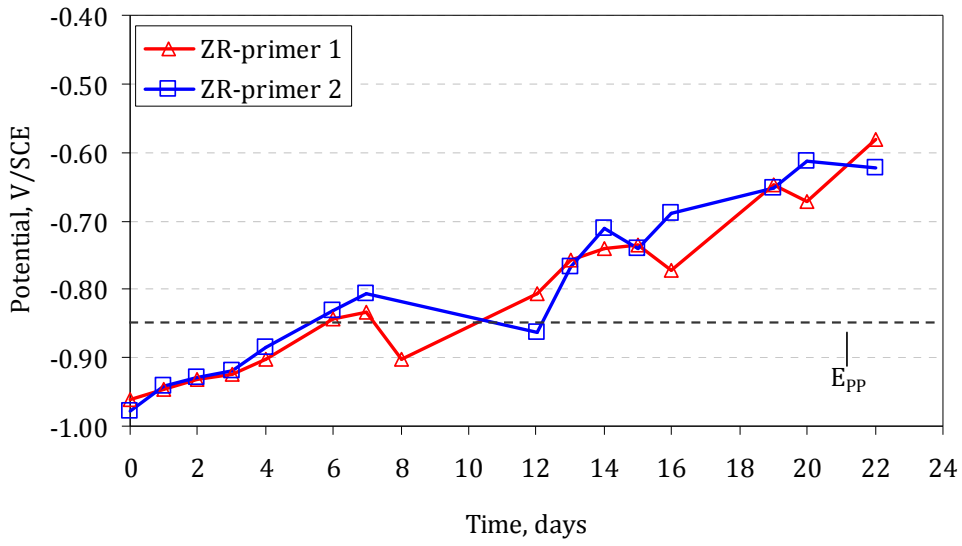

Figure 6.9 – Evolution of corrosion potential measured at 21°C with time for ZRP coating exposed in 3% NaCl solution for 22 days at 50°C

Due to the high permeability of ZRP coatings, immediately upon immersion in the electrolyte the potential is about -0.98V_{SCE}, a value which is close to the potential of zinc in sea water. This indicates clearly that the zinc particles were actively consumed to provide initial galvanic protection to the steel. Notice that the potential passed the E_{PP} value by 6 days. By 22 days, contact between zinc and steel may have been lost as the potential recorded is closed to the corrosion potential of steel.

Figure 6.10 presents the suggested model based on the corrosion potential variation with time of ZRP coating [68]. Two main periods can be distinguished;

Period I: Corrosion potential is close to that of zinc, but shifts to a less negative value indicating that there is an electrical connection between the zinc particles and the steel substrate. Corrosion potential value increases to about – 0.75V_{SCE} where stabilization is reached and this period is known as the 'transition' period.

Period II: After the transition period, the corrosion potential continues to rise until reaching a potential value over which the cathodic protection is no longer efficient. Both periods correspond to a decrease of the zinc-to-steel area ratio due to zinc corrosion. However at the end of period II, contact is lost between zinc and steel causing the potential measured to be close to the corrosion potential of steel. Zinc corrosion products seal the pores near the steel substrate and continue giving protection to the metal substrate via a barrier effect.

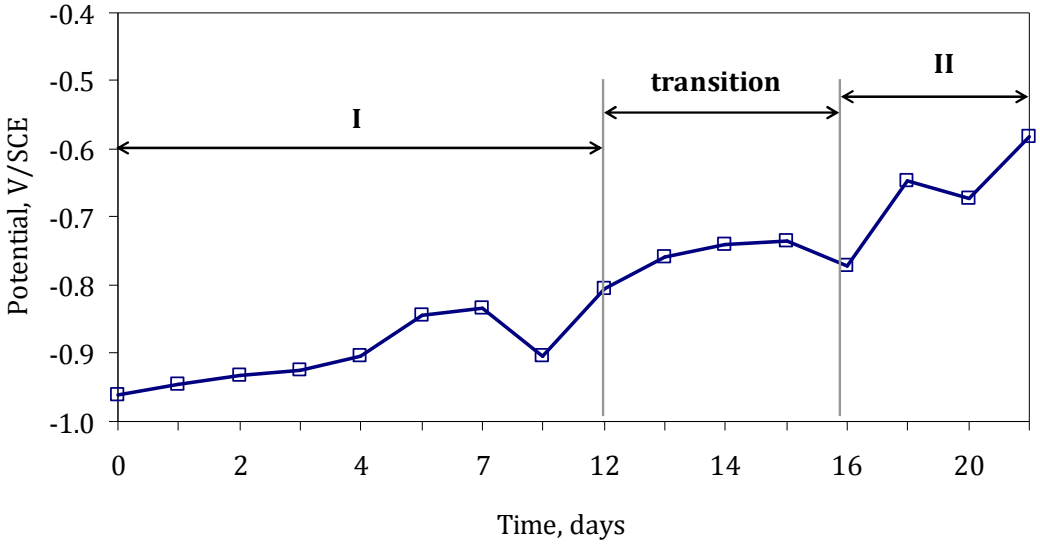

Figure 6.10 – Model to represent the variation of corrosion potential for ZRP coating with exposure time

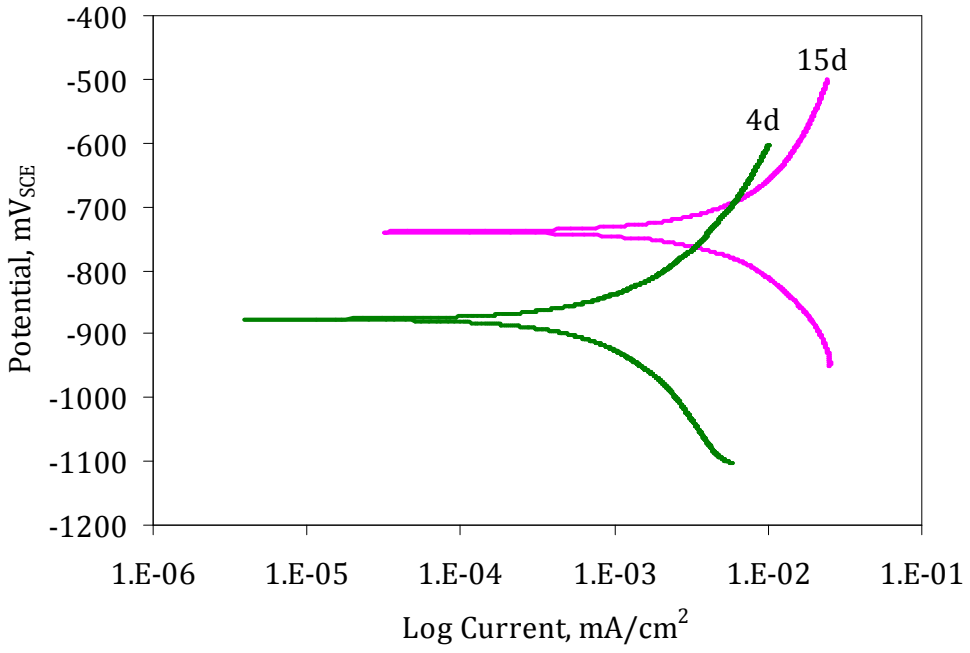

Figure 6.11– Polarization curve of ZRP coating measured at 21°C after 4 and 15 days of exposure at 50°C

The polarization curves of ZRP coated steel after 4 and 15 days of immersion are shown in **Figure 6.11**. The values of the corrosion potential, E_{corr}, are in agreement with the OCP measurements. Current densities at E_{corr}, determined for the two curves by extrapolating the Tafel lines at E_{corr}, are 8.02 x 10^{-4} $mAcm^{-2}$ and 5.09 x 10^{-3} $mAcm^{-2}$ for 4 and 15 days respectively. It can be seen that there is a large increase in cathodic current and only small increase in the anodic current. It appears then that the upwards shift in potential and increased i_{corr} arise from an increasing cathodic area.

6.3.6 Temperature Dependence of Impedance

Figures 6.12 to **6.15** show the effect of changing temperature on the EIS response of ZRP coating in 3% NaCl solution after 1, 4, 7 and 14 days exposure at 50°C. It is interesting to observe that the effect of changing temperature is barely noticeable on the impedance spectra after 1 and 4 days of immersion. However by day 7 the effect of changing temperature becomes much clearer. Even though the effect of temperature on the size of the 'semicircle' is apparent in **Figures 6.14** and **6.15**, Nyquist plots are difficult to fit. Only the first semicircle could be fitted using "circle fit" from the ACM software and the fitted parameters are summarized in **Table 6.2**. Logarithm of R_p is then plotted against reciprocal of temperature (**Figure 6.16**) and the activation energies measured are in the range of 32–34 $kJmol^{-1}$.

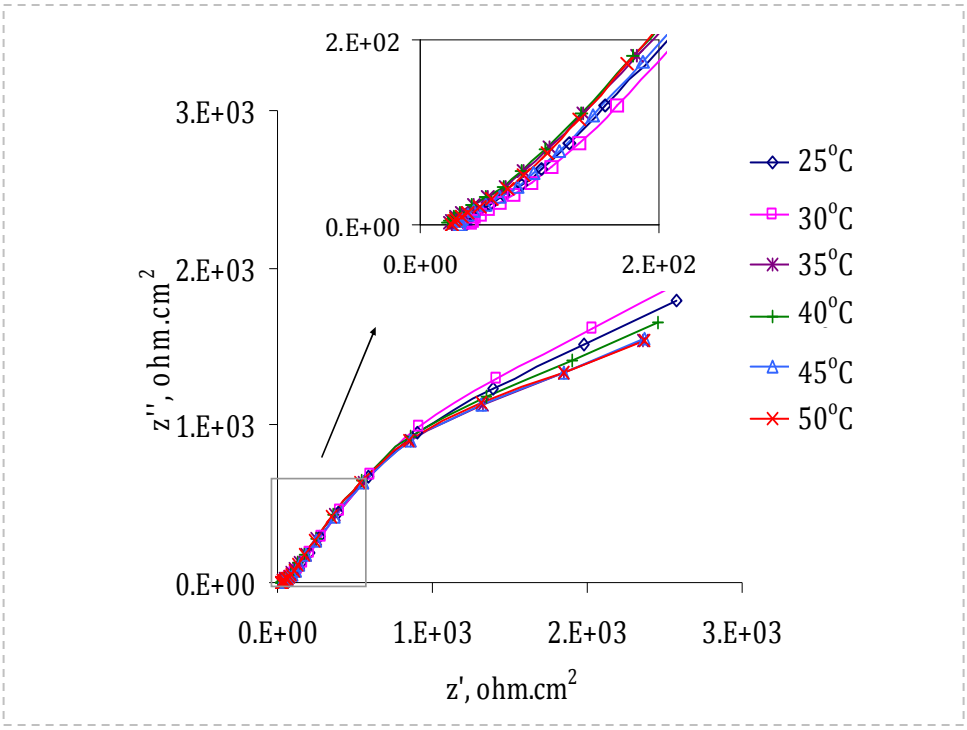

Figure 6.12 – Nyquist plots for ZRP coating at various temperatures after 1 day of exposure at 50°C

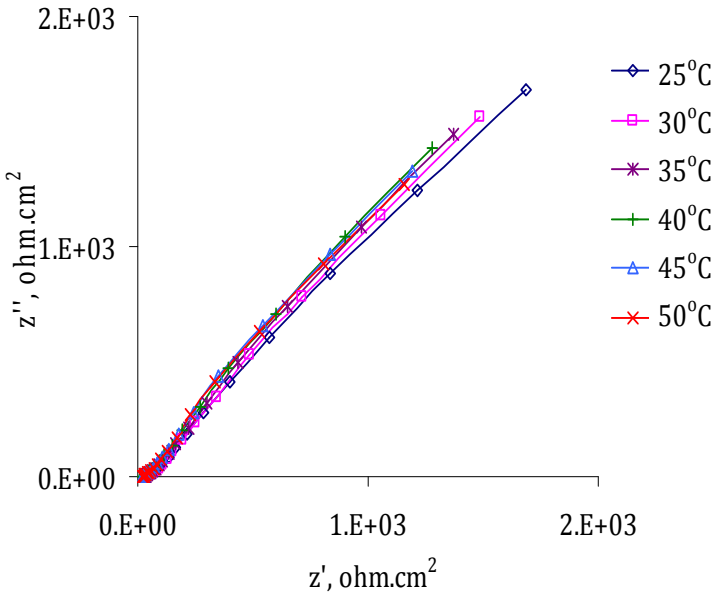

Figure 6.13 – Nyquist plots for ZRP coating at various temperatures after 4 days of exposure at 50°C

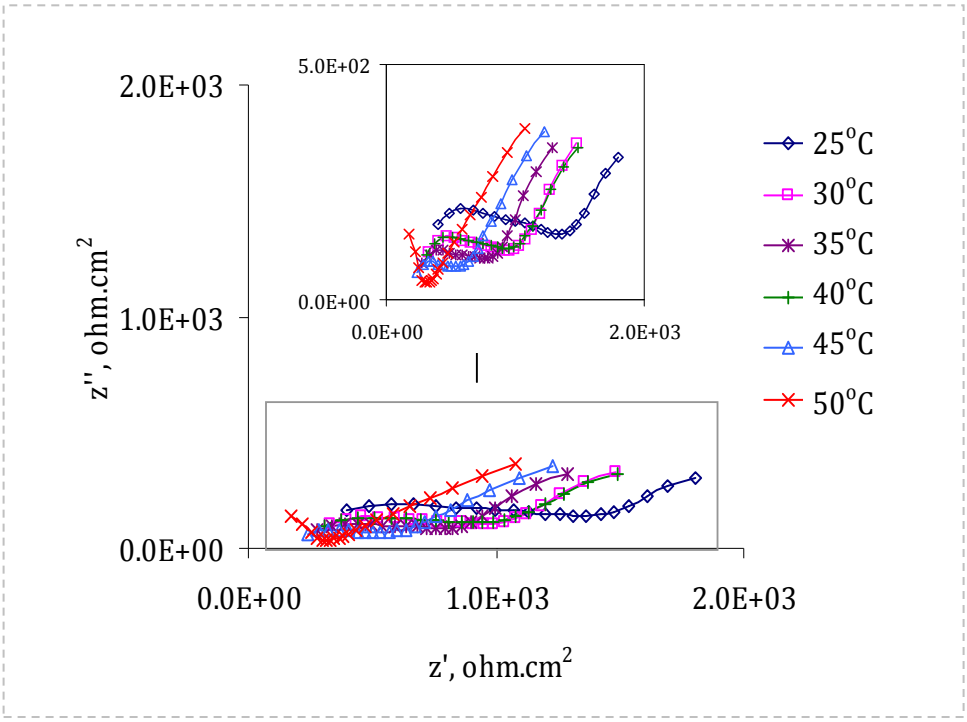

Figure 6.14 – Nyquist plots for ZRP coating at various temperatures after 7 days of exposure at 50°C

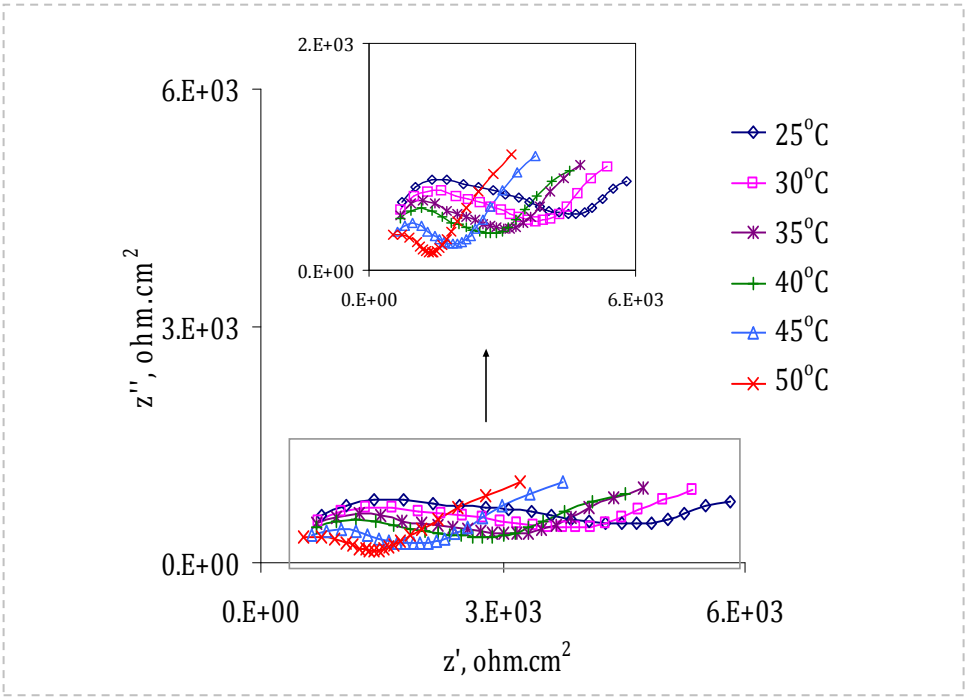

Figure 6.15 – Nyquist plots for ZRP coating at various temperatures after 14 days of exposure at 50°C

Table 6.2 – Parameters for ZRP coating from fitting of EIS after (a) 7 days and (b) 14 days at 50°C; fitted circuit: circle fit from ACM software

T (°C)	C_{dl} (F)	R_{ct} (ohm.cm²)
25	1.19E-05	1.15E+03
30	7.15E-06	6.37E+02
35	1.04E-05	5.42E+02
40	4.81E-06	5.74E+02
45	1.25E-05	3.86E+02
50	1.97E-07	2.82E+02

(a)

T (°C)	C_{dl} (F)	R_{ct} (ohm.cm²)
25	9.74E-07	3.45E+03
30	1.04E-06	3.01E+03
35	4.58E-07	2.19E+03
40	3.45E-07	2.07E+03
45	3.01E-07	1.45E+03
50	2.19E-07	1.25E+03

(b)

(a)

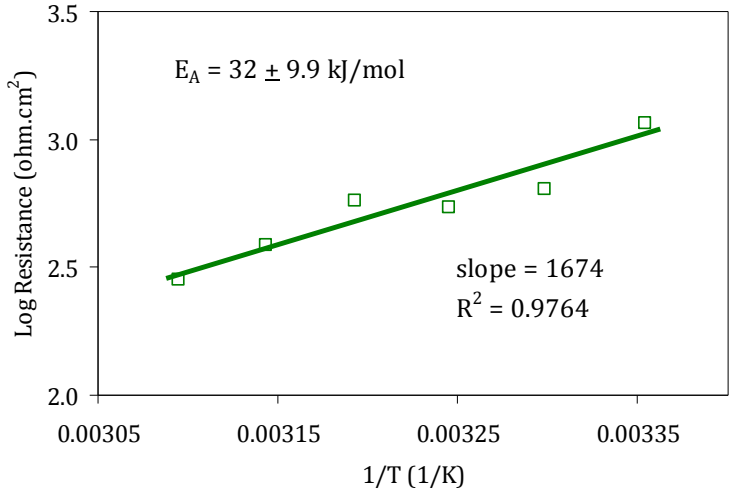

(b)

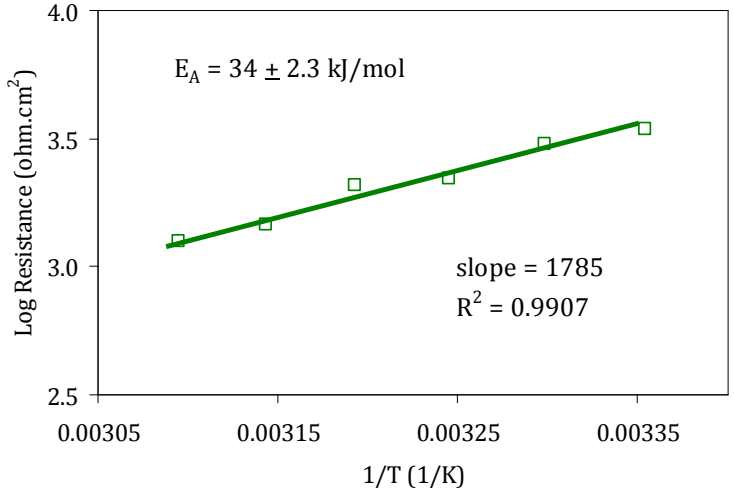

Figure 6.16 - Arrhenius plot for ZRP coating after (a) 7 days and (b) 14 days of exposure at 50°C

6.4 Results and Discussion for Zinc Rich Full System (ZR-FS)

6.4.1 EIS Diagram for Exposure at 21 and 50°C

Figure 6.17 shows Bode and Nyquist plots of ZR-FS coating after different periods of exposure at ambient temperature, 21°C. The plots show a steady decrease in impedance modulus, |Z| at low frequency. Two distinct semicircles are seen by 7 days; semicircle size becomes smaller over time.

Figure 6.18 shows Bode and Nyquist plots of ZR-FS coating after different periods of exposure at 50°C. Degradation is much faster at 50°C with indication of a second semicircle at 3 days compared to ambient temperature (**Figure 6.17c**).

Results corresponding to the trend of coating resistance, R_p, for both temperatures are shown in **Figure 6.19**. The resistance for coated panel in both tests dropped over time and, as expected, the values of coating resistance at 50°C dropped even faster during early immersion.

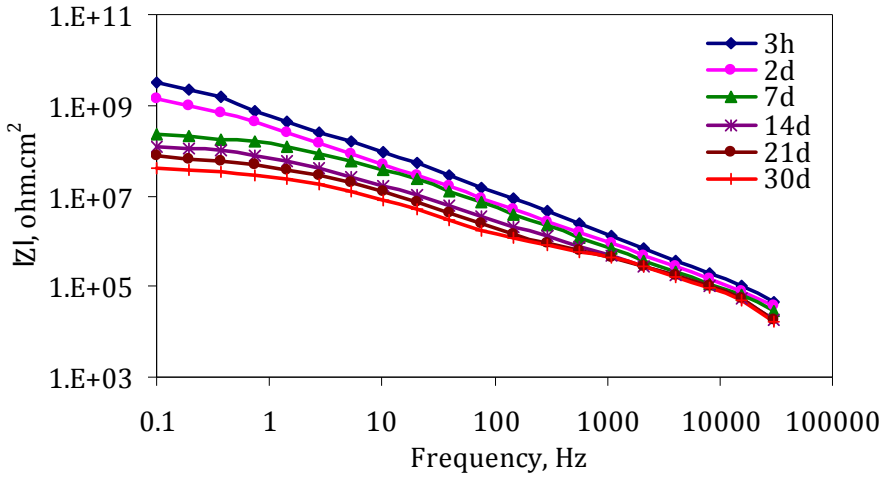

(a)

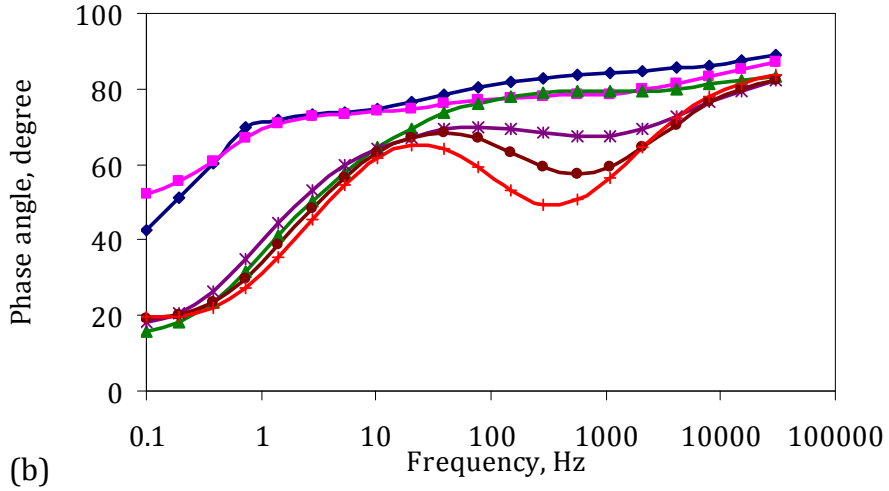

(b)

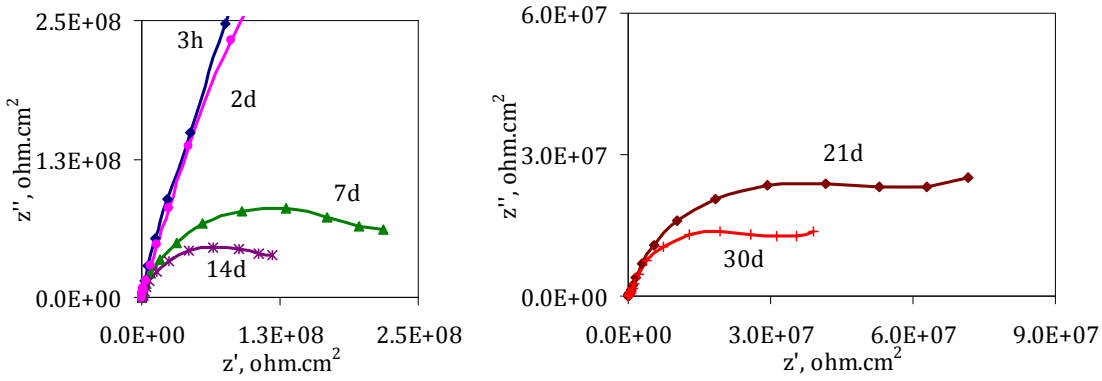

(c)

Figure 6.17 - Bode and Nyquist plot for ZR-FS coating tested at 21°C

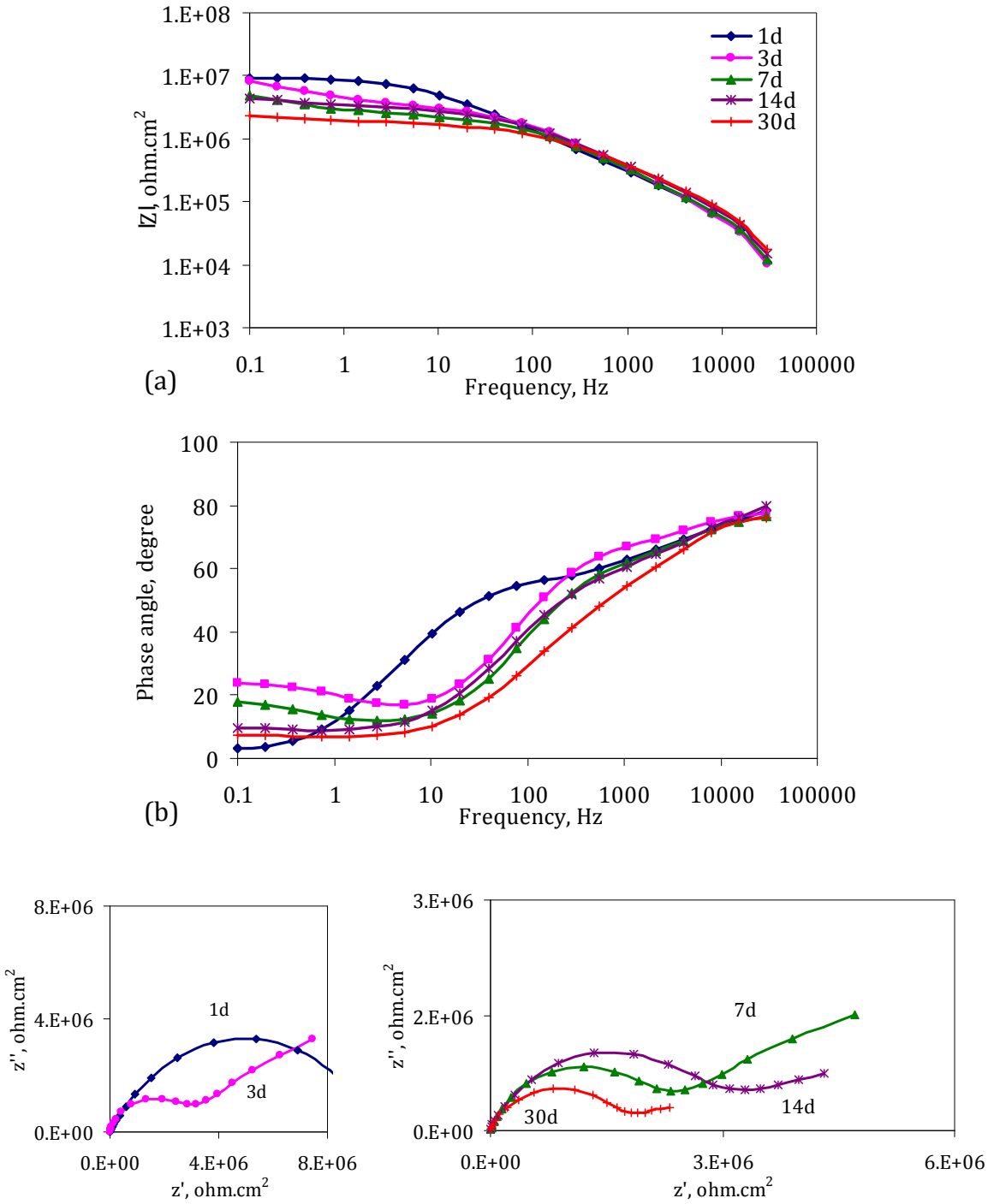

Figure 6.18- Bode and Nyquist plot for ZR-FS coating tested at 50°C

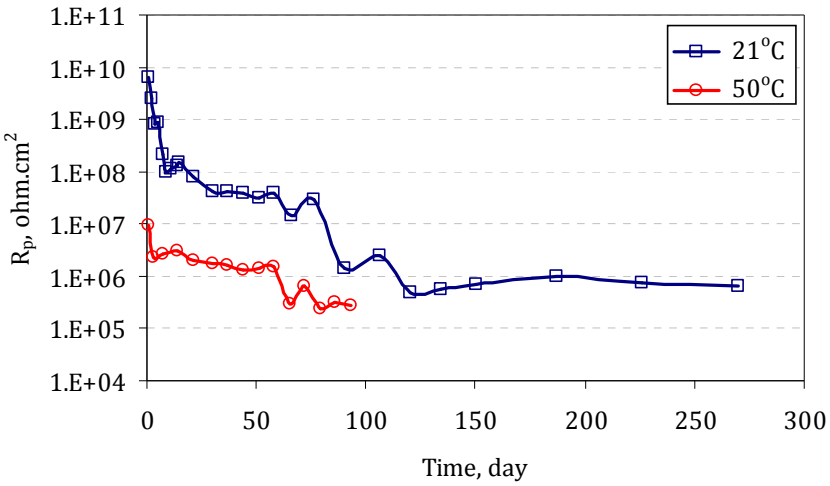

Figure 6.19 – The dependence of R_p on exposure time for ZR-FS coating

6.4.2 Open Circuit Potential Measurement

Figure 6.20 displays the open circuit potential (OCP) measured over time for ZR-FS coated panels (duplicate sets) exposed at 21 and 50°C. It is interesting to note that the two panels tested at 21°C reacted differently during early immersion. During the first 21 days of immersion panel 1 had an unstable potential which varied between -0.3 and -0.8 V_{SCE} before reaching a stationary value close to the corrosion potential of steel. In contrast panel 2 shows potential values close to the zinc potential during early immersion but rapidly increased reaching the corrosion potential of steel by 21 days. Panels 3 and 4 tested at 50°C gave comparable potential values. Their values were fluctuating in the range of -0.45 to -0.65V_{SCE} which is similar to the potential for a coated steel substrate. In this study, the number of days during which the coated panel exhibits more negative potential than E_{PP} (-0.85V_{SCE}) in 3% NaCl solution is used for judgment of how long zinc rich primer coatings provide full cathodic protection to the

steel substrate. According to these results, it is evident that OCP of ZR-FS never lies in cathodic protection region (below -0.85V_{SCE}). The potential measured for ZR-FS coating will be however a compromise between the zinc-steel galvanic couple (anode and cathode) as suggested by Mayne [132] which has been explained in **Section 3.4.2**. Anode potential may give reading at -0.95V_{SCE}, and cathode potential may be a very much higher.

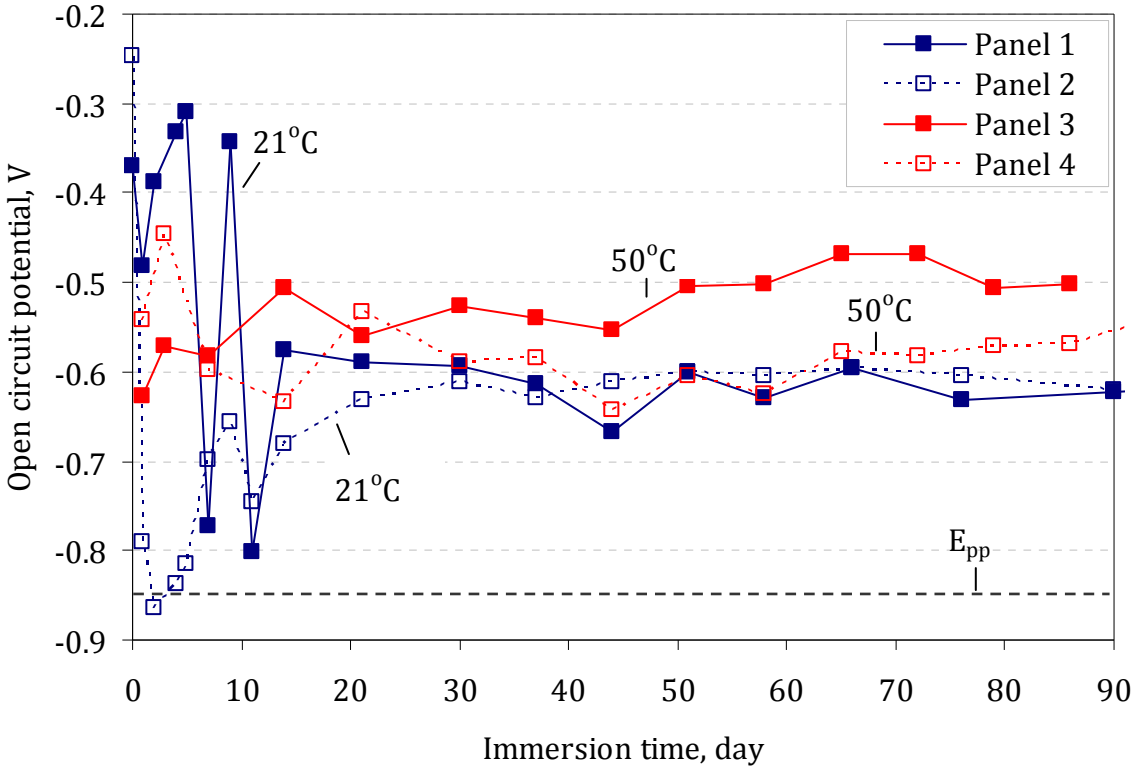

Figure 6.20 – Evolution of OCP values with immersion time for ZR-FS coated panels

6.4.3 Effect of Signal Amplitude – A Test of the Circuit Model

ZRP (primer only) gave two semicircles (**Figure 6.4**) and here again two semicircles were observed (**Figure 6.21**) for the ZR-FS (full system). The first semicircle was

expected to be the top coating over the zinc rich epoxy primer and the second semicircle corresponded to the electrochemical activity of the zinc rich primer coupled to the steel substrate. To be certain a test is conducted to investigate the effect of changing the signal amplitude on the semicircles as a way of identifying the different features displayed in Nyquist plots. EIS spectra were taken at amplitudes ranging from 20 mV to 120 mV. The resulting Nyquist plots are presented in **Figure 6.21**. It is clear from this figure that changing the applied potential only changes the shape of the second semicircle.

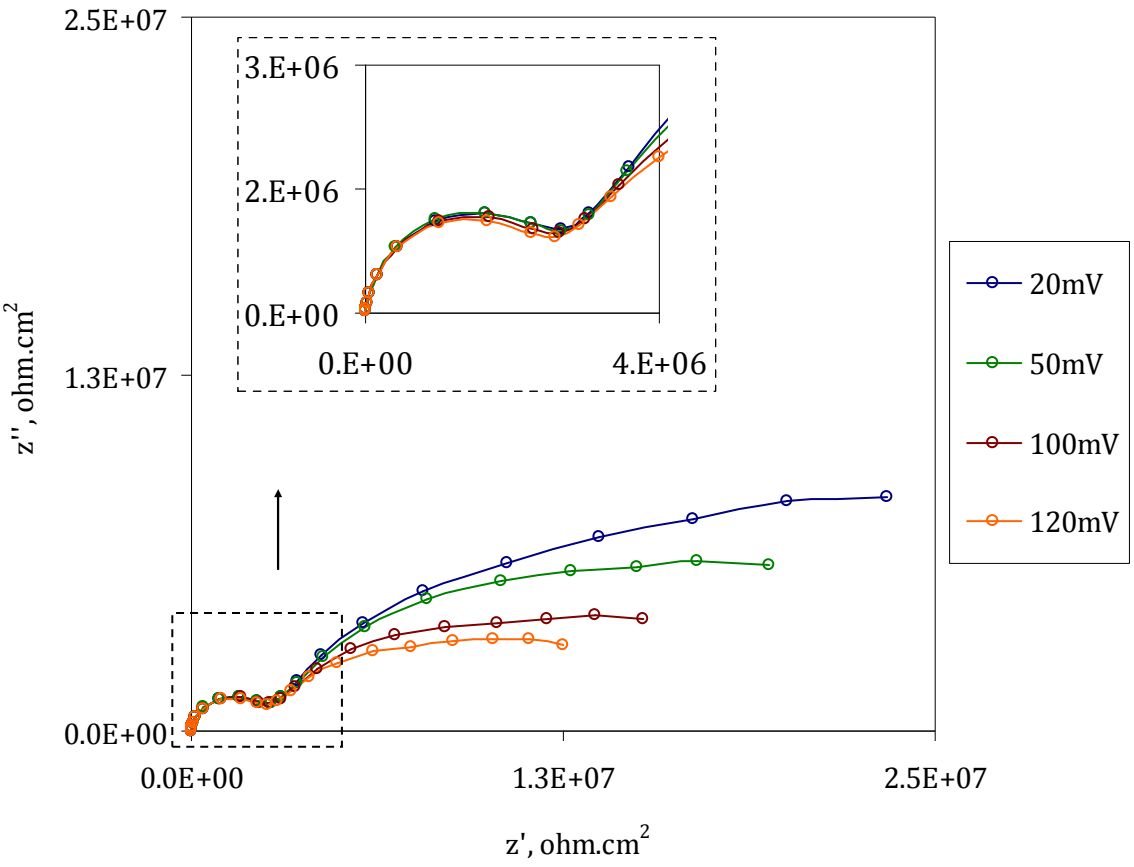

Figure 6.21 - Nyquist plot at various applied potential for ZR-FS coating

All the curves were fitted with ZSimpWin software using R[Q[R[QR]]] circuit combination and the fitted values are displayed in **Table 6.3**. Notice that the coating resistance and capacitance does not change. However, the charge transfer resistance decreases as increasing potential was applied. This is consistent with the polarisation behaviour of the electrode due to the non-linearity between the potential and the current.

Table 6.3 Effect of changing the applied potential on the resistance and capacitance values measured for ZR-FS coating exposed to 3% NaCl solution

Amplitude mV	Q_c $(Fcm^{-2})^n$	n	R_p ohm.cm^2	Q_{dl} $(Fcm^{-2})^n$	n	R_{ct} ohm.cm^2
20	3.70E-10	0.95	2.07E+06	6.48E-08	0.51	3.48E+07
50	3.60E-10	0.95	2.06E+06	6.31E-08	0.51	2.54E+07
100	3.30E-10	0.96	1.96E+06	7.91E-08	0.47	1.95E+07
120	3.63E-10	0.95	2.09E+06	7.73E-08	0.52	1.16E+07

6.4.4 Assessment of EIS Data Exposed at constant 50^{o}C vs. (50^{o}C-E_A)[8]

EIS data for coated panels exposed at constant 50^{o}C and (50^{o}C-E_A) for a certain periods were observed to see whether any significant difference arises from both tests. This is to be certain that imposing a short period of test where the panel is left to cool down (50^{o}C-E_A) does not deviate much compared to tests at constant 50^{o}C. **Figures 6.22** and **6.23** show the impedance spectra for duplicate samples when measured at 50^{o}C and

[8] Coated panel is exposed at 50^{o}C but slowly cooled to ambient temperature to determine activation energy, E_A

($50^{o}C$-E_A) after various exposure periods. There is no consistent difference between the two types of tests.

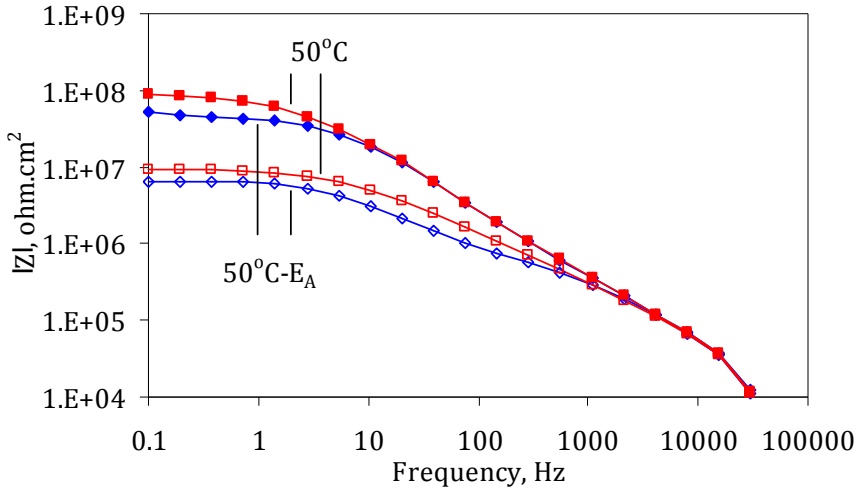

Figure 6.22– Bode plot for ZR-FS coating after 1 day of exposure

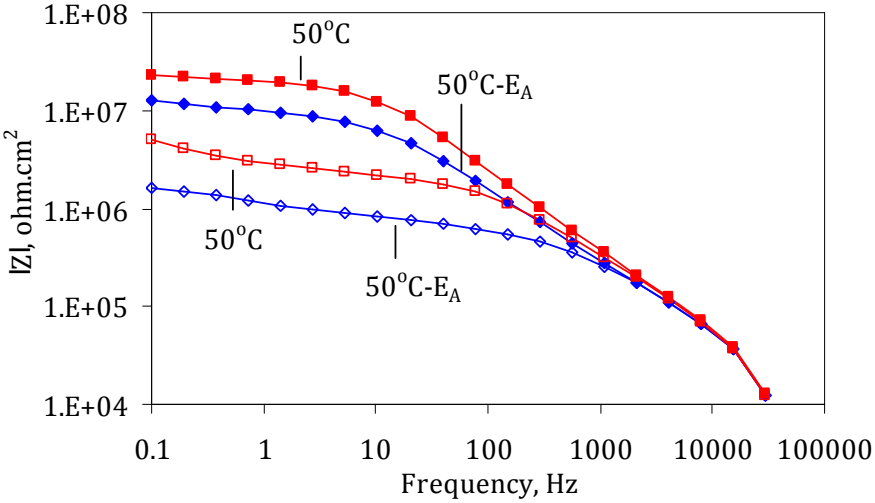

Figure 6.23– Bode plot for ZR-FS coating after 7 days of exposure

6.4.5 Temperature Dependence of Coating Parameters

Figures 6.24 to **6.28** show the effect of changing temperature on the EIS response of ZR-FS coating (panel 1) after 3, 7, 14, 21 and 30 days exposure at 50°C. The size of both semicircles decreases as temperature rises. The presence of a Warburg impedance is noticed in the Nyquist plot (data at 25 to 45°C) but not for data at 50°C as presented in **Figure 6.24**. Thus data from 25 to 45°C are fitted with circuit combination R[Q[R[Q[RW]]]] whereas data at 50°C circuit R[Q[R[QR]]] is used instead. It can be seen in **Figure 6.29** that the measured data fit quite well with the simulation. This shows the chosen equivalent circuit is apparently appropriate to determine the coating parameters for the respective data. Impedance spectra for day 7 to day 30 are fitted with a combination circuit of [RQ][RQ] rather than the classical R[Q[R[QR]]] because the latter gave a larger error. Justification on using an equivalent circuit of [RQ][RQ] has been explained in **Section 3.3.4**. **Figure 6.30** shows the good agreement between the measured data and fitted for the first semicircle. Notice that the fitting program has difficulty in fitting the second semicircle but nevertheless the fitted parameter values seem reasonable though in some cases the error is large (**Tables 6.4** to **6.8)**.

Accordingly, the parameters, coating resistance, R_p and charge transfer resistance, R_{ct} are then plotted against reciprocal of temperature for each table. The Arrhenius plots in **Figures 6.31** to **6.35**, display a straight line where activation energy is calculated by multiplying the slope with the gas constant, R.

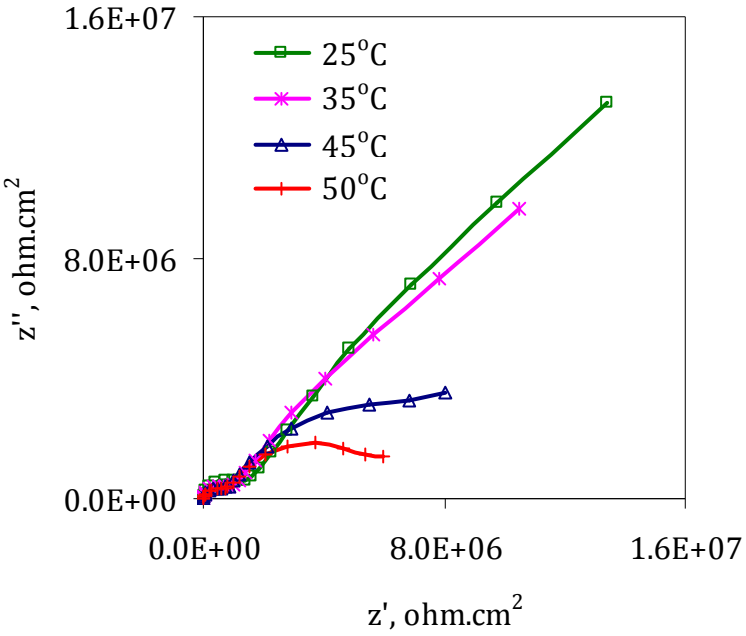

Figure 6.24 – Nyquist plots at various temperatures for ZR-FS (panel 1) coating after 3 days of exposure at 50°C

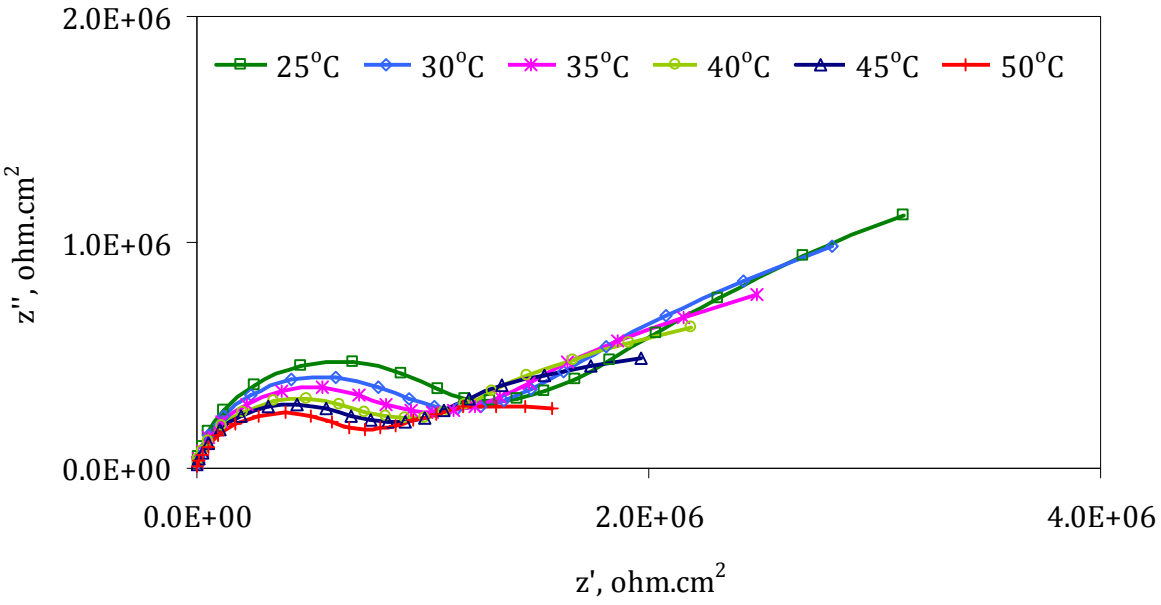

Figure 6.25 – Nyquist plots at various temperatures for ZR-FS (panel 1) coating after 7 days of exposure at 50°C

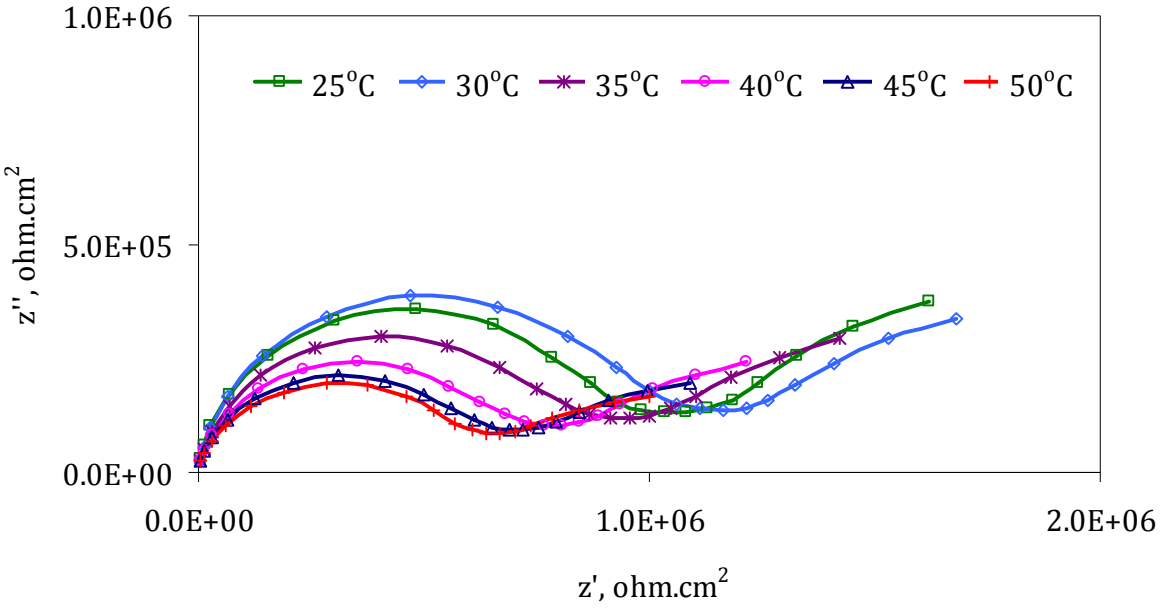

Figure 6.26 - Nyquist plots at various temperatures for ZR-FS coating (panel 1) after 14 days of exposure at 50°C

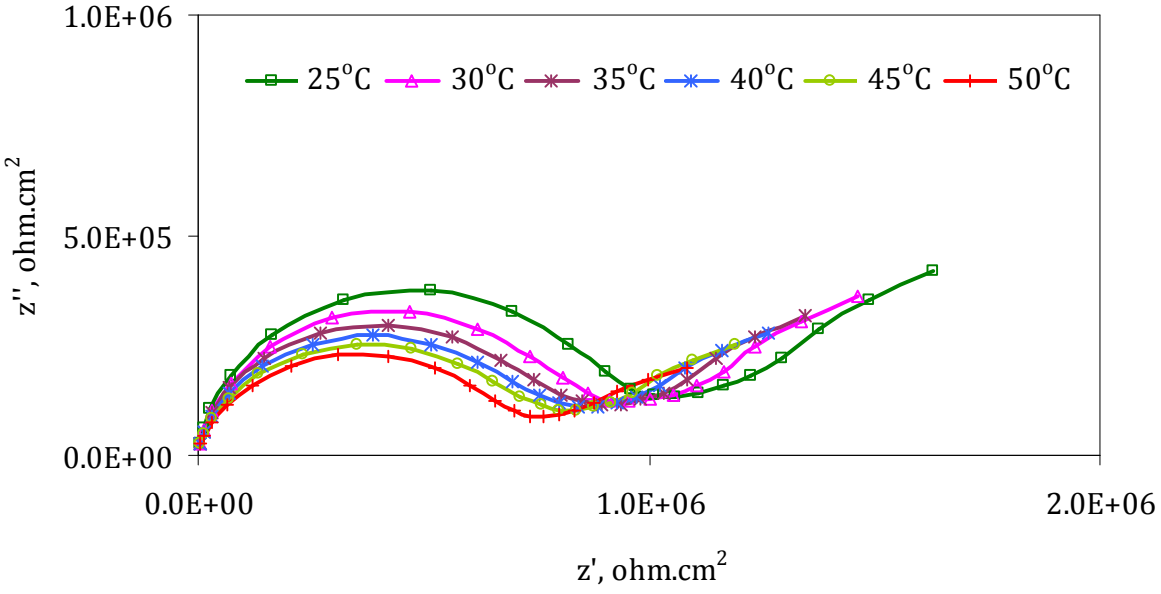

Figure 6.27 - Nyquist plots at various temperatures for ZR-FS coating (panel 1) after 21 days of exposure at 50°C

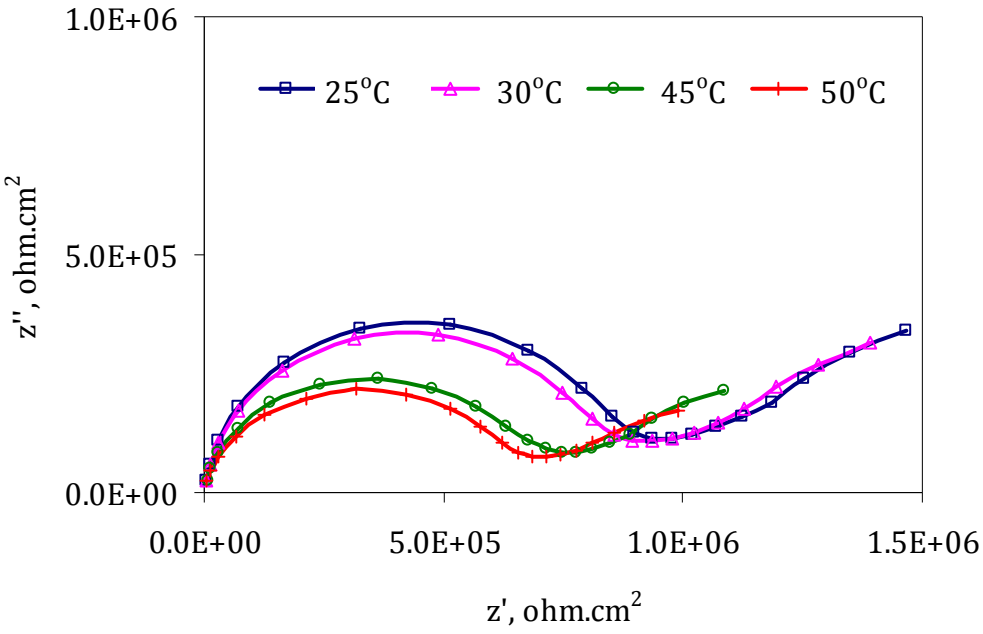

Figure 6.28 - Nyquist plots at various temperatures for ZR-FS coating (panel 1) after 30 days of exposure at 50°C

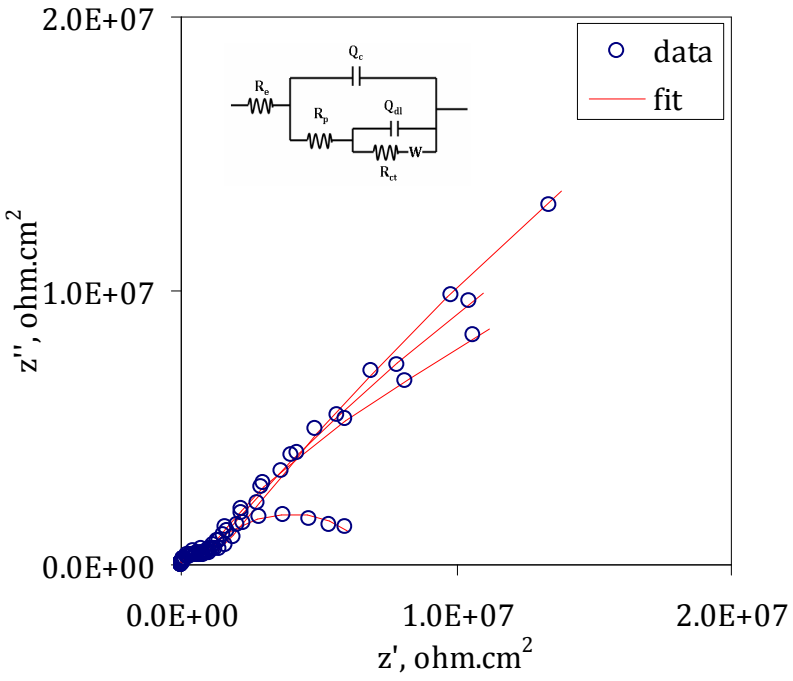

Figure 6.29 - Experimental (o) and simulated (-) Nyquist plot of ZR-FS coating (Panel 1) exposed at various temperatures after 3 days of exposure at 50°C

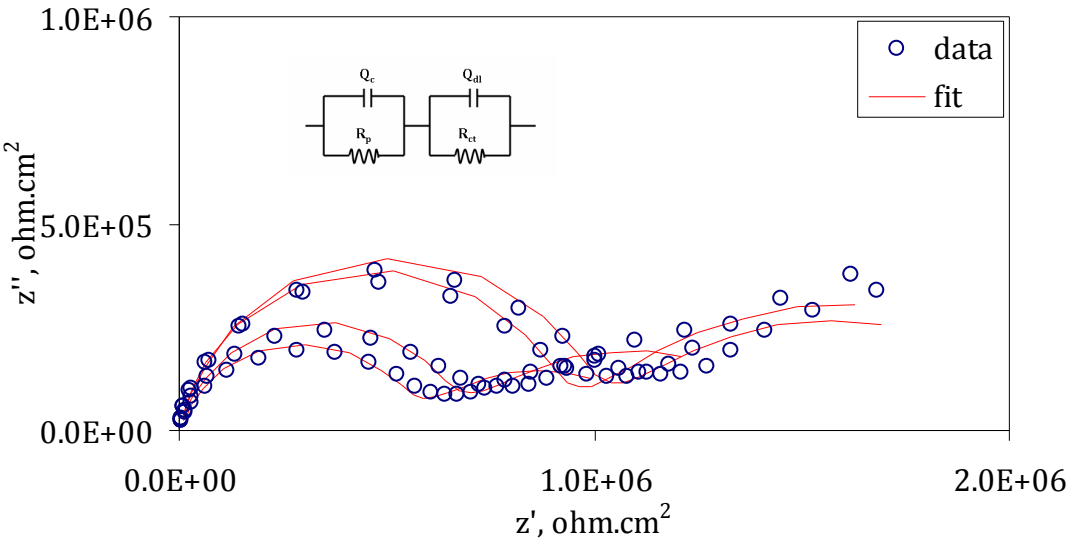

Figure 6.30 – Experimental (o) and simulated (-) Nyquist plot of ZR-FS coating (Panel 1) exposed at various temperatures after 14 days of exposure at 50°C

Table 6.4 – Best fitting parameters for ZR-FS coating (panel 1) after 3 days exposure at 50°C

Fitted circuit: R[Q[R[Q[RW]]]] for data 25-40°C; R[Q[R[Q[R]]] for data at 50°C

T (°C)	Q_c $(Fcm^{-2})^n$	Q_c (%error)	n	R_p ($ohm.cm^2$)	R_p (%error)	Q_{dl} $(Fcm^{-2})^n$	Q_{dl} (%error)	n	R_{ct} ($ohm.cm^2$)	R_{ct} (%error)	W	X^2
25	4.48E-10	38.10	0.95	1.17E+06	15.66	6.40E-08	28.96	0.59	1.28E+08	394.8	1.89E-07	1.59E+02
35	4.87E-10	49.03	0.95	7.71E+05	17.62	7.72E-08	19.72	0.58	5.61E+07	113.9	1.02E-07	1.77E+02
40	7.11E-10	49.54	0.92	7.13E+05	19.05	6.06E-08	40.73	0.63	2.14E+07	134.5	1.17E-07	1.81E+02
50	9.52E-10	49.69	0.90	6.36E+05	18.50	6.49E-08	22.84	0.63	6.71E+06	17.34	-	1.77E+02

Table 6.5 – Best fitting parameters for ZR-FS coating (panel 1) after 7 days exposure at 50°C

Fitted circuit: [RQ][RQ]

T (°C)	Q_c $(Fcm^{-2})^n$	Q_c (%error)	n	R_p ($ohm.cm^2$)	R_p (%error)	Q_{dl} $(Fcm^{-2})^n$	Q_{dl} (%error)	n	R_{ct} ($ohm.cm^2$)	R_{ct} (%error)	X^2
25	8.27E-10	28.69	0.88	1.16E+06	8.99	3.04E-07	18.56	0.56	3.86E+06	33.86	6.93E+03
30	1.03E-09	28.67	0.87	1.02E+06	9.44	3.32E-07	18.90	0.56	3.40E+06	33.79	6.83E+03
35	1.25E-09	31.04	0.86	9.14E+05	10.92	3.42E-07	21.93	0.57	2.59E+06	32.83	7.86E+03
40	1.60E-09	30.18	0.84	8.00E+05	11.13	3.71E-07	20.98	0.56	2.18E+06	29.71	6.73E+03
45	1.57E-09	53.00	0.85	7.15E+05	19.14	3.60E-07	35.96	0.56	1.77E+06	42.55	1.89E+02
50	2.13E-09	53.59	0.83	6.20E+05	22.59	3.45E-07	42.38	0.58	1.15E+06	39.48	1.83E+02

Table 6.6 – Best fitting parameters for ZR-FS coating (panel 1) after 14 days exposure at 50°C

Fitted circuit: [RQ][RQ]

T (°C)	Q_c $(Fcm^{-2})^n$	Q_c (%error)	n	R_p (ohm.cm^2)	R_p (%error)	Q_{dl} $(Fcm^{-2})^n$	Q_{dl} (%error)	n	R_{ct} (ohm.cm^2)	R_{ct} (%error)	X^2
25	8.05E-10	25.82	0.88	9.88E+05	7.72	7.87E-07	31.20	0.54	1.18E+06	48.57	5.38E+03
30	7.16E-10	25.99	0.88	9.07E+05	7.13	8.59E-07	27.04	0.52	1.42E+06	51.44	5.03E+03
35	1.06E-09	29.18	0.86	7.90E+05	8.97	8.41E-07	31.68	0.53	1.04E+06	47.59	5.99E+03
40	1.38E-09	30.81	0.84	6.50E+05	9.81	8.96E-07	43.96	0.52	8.89E+05	30.82	5.79E+03
45	1.84E-09	30.06	0.82	5.88E+05	10.52	9.57E-07	33.03	0.53	7.38E+05	44.50	5.84E+03
50	2.42E-09	28.52	0.80	5.54E+05	10.82	1.04E-06	33.89	0.53	6.41E+05	45.09	5.52E+03

Table 6.7 – Best fitting parameters for ZR-FS coating (panel 1) after 21 days exposure at 50°C

Fitted circuit: [RQ][RQ]

T (°C)	Q_c $(Fcm^{-2})^n$	Q_c (%error)	n	R_p (ohm.cm^2)	R_p (%error)	Q_{dl} $(Fcm^{-2})^n$	Q_{dl} (%error)	n	R_{ct} (ohm.cm^2)	R_{ct} (%error)	X^2
25	5.41E-10	30.85	0.91	9.22E+05	7.83	8.19E-07	30.24	0.51	1.55E+06	57.82	6.98E+03
30	7.20E-10	28.04	0.88	8.33E+05	7.49	9.12E-07	27.95	0.51	1.34E+06	52.89	5.43E+03
35	9.17E-10	30.36	0.87	7.75E+05	8.62	9.46E-07	31.26	0.51	1.12E+06	53.83	6.15E+03
40	1.15E-09	31.62	0.85	7.30E+05	9.58	9.61E-07	33.57	0.51	9.65E+05	53.06	6.48E+03
45	1.52E-09	31.11	0.83	6.98E+05	10.14	1.05E-06	34.64	0.52	8.76E+05	56.05	6.34E+03
50	2.16E-09	28.35	0.80	6.58E+05	10.45	1.20E-06	37.85	0.53	6.99E+05	59.67	6.07E+03

Table 6.8– Best fitting parameters for ZR-FS coating (panel 1) after 30 days exposure at 50°C

Fitted circuit: [RQ][RQ]

T (°C)	Q_c $(Fcm^{-2})^n$	Q_c (%error)	n	R_p ($ohm.cm^2$)	R_p (%error)	Q_{dl} $(Fcm^{-2})^n$	Q_{dl} (%error)	n	R_{ct} ($ohm.cm^2$)	R_{ct} (%error)	X^2
25	5.10E-10	28.35	0.91	8.58E+05	6.85	9.52E-07	28.50	0.50	1.33E+06	53.47	5.48E+03
30	5.77E-10	29.29	0.90	8.20E+05	7.24	1.00E-06	30.07	0.50	1.21E+06	55.01	5.73E+03
45	1.28E-09	29.25	0.84	6.54E+05	8.69	1.23E-06	32.50	0.50	7.92E+05	53.86	5.09E+03
50	1.86E-09	28.11	0.82	6.13E+05	9.69	1.34E-06	38.58	0.52	6.16E+05	58.96	5.64E+03

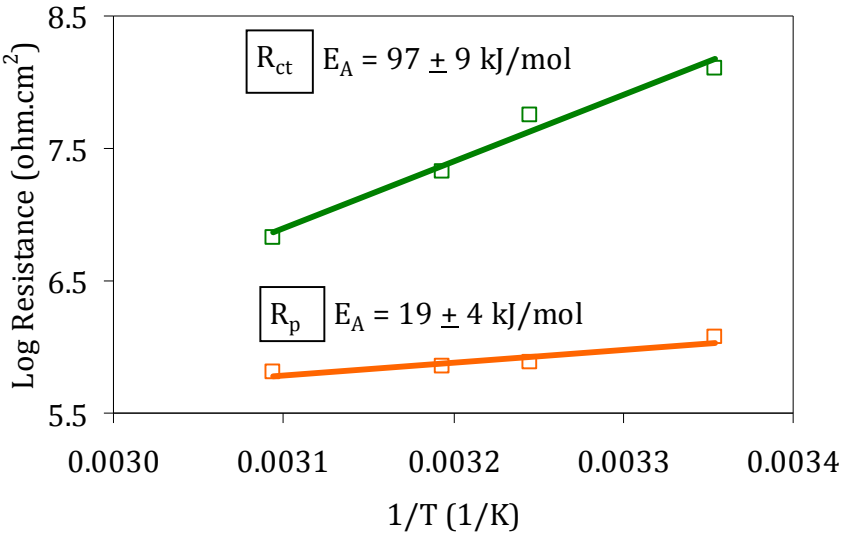

Figure 6.31 – Arrhenius plots of R_p and R_{ct} for ZR-FS coating (panel 1) after 3 days of exposure at 50°C

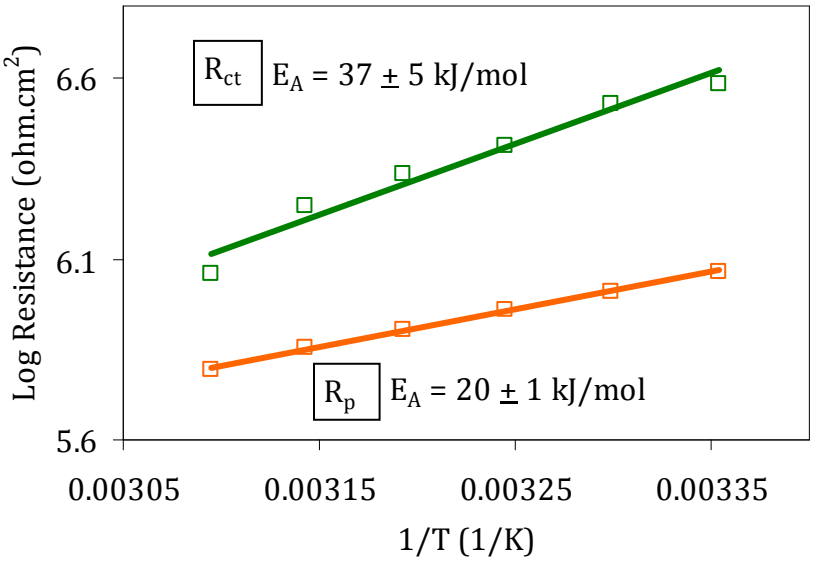

Figure 6.32 – Arrhenius plots of R_p and R_{ct} for ZR-FS coating (panel 1) after 7 days of exposure at 50°C

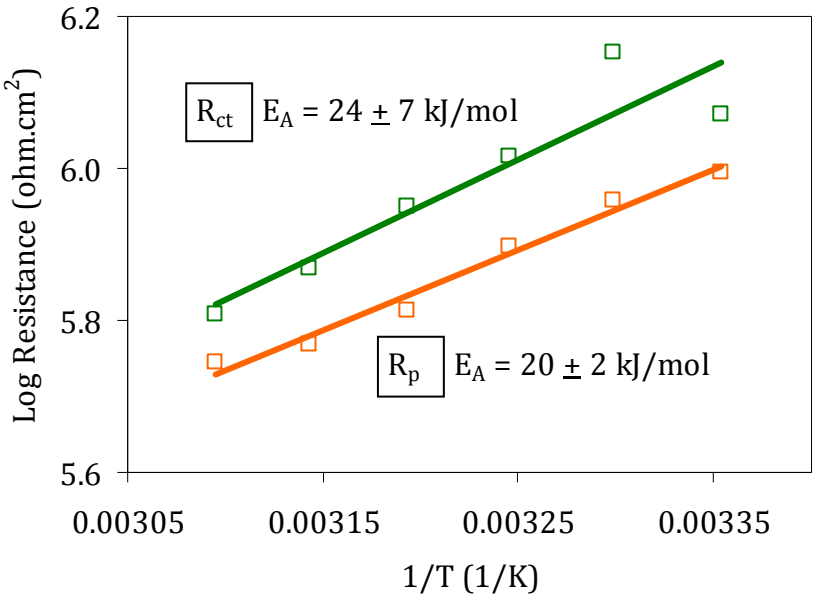

Figure 6.33 – Arrhenius plots of R_p and R_{ct} for ZR-FS coating (panel 1) after 14 days of exposure at 50°C

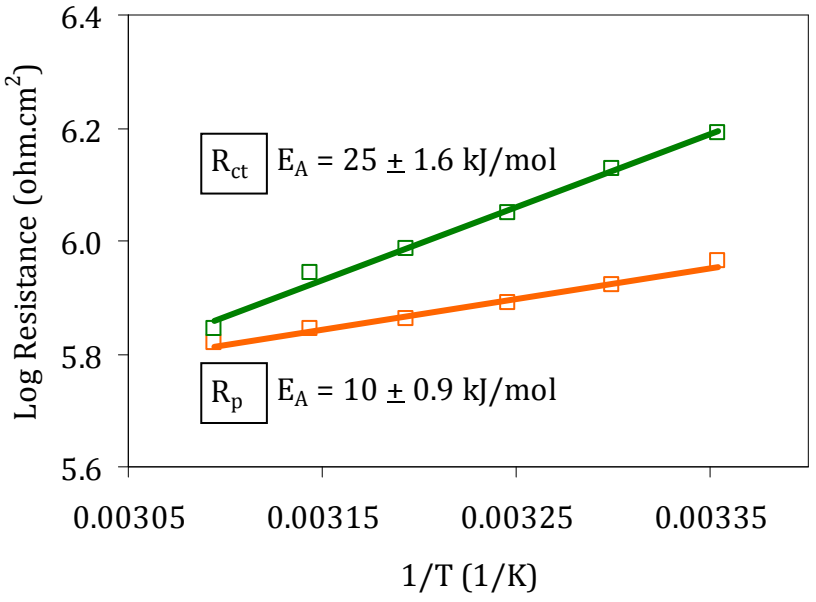

Figure 6.34 – Arrhenius plots of R_p and R_{ct} for ZR-FS coating (panel 1) after 21 days of exposure at 50°C

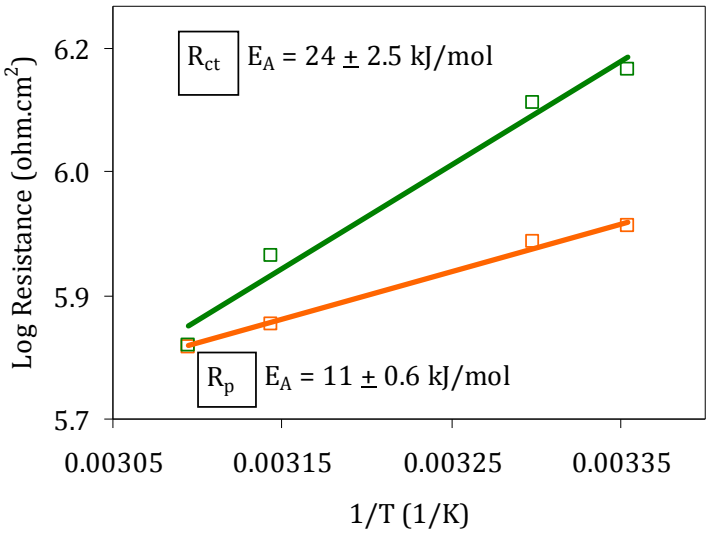

Figure 6.35 – Arrhenius plots of R_p and R_{ct} for ZR-FS coating (panel 1) after 30 days of exposure at 50°C

Figures 6.36 to **6.40** show the effect of changing temperature on the EIS response of ZR-FS coating (panel 2) after 1, 3, 14, 21 and 35 days exposure at 50°C. The size of the semicircle decreases as temperature rises. It can be seen from **Figures 6.36** and **6.37** that the presence of a low frequency semicircle is hardly noticeable. By day 14, the second semicircle is clearer and perhaps with a Warburg diffusion (**Figure 6.38**). Data from day 1 and 3 are fitted with a combination circuit R[Q[R[QR]]]. It can be seen in **Figure 6.40** that the measured data fit really well with the simulation. Impedance spectra for 14 and 21 days are fitted with a combination circuit R[Q[R[Q[RW]]]] while for day 35 the R[Q[R[QR]]] circuit is used instead. The chosen circuit shows a good fit (**Figures 6.42** and **6.43**). The fitted parameters are summarized in **Tables 6.9** to **6.13**. It can be seen from **Table 6.13** that the n values for Q_{dl} become smaller (n<0.5). The parameters, coating resistance, R_p, and charge transfer resistance, R_{ct}, are then plotted as log resistance against the reciprocal temperature for each table. The Arrhenius plots

(**Figures 6.44** to **6.48)** display a straight line where activation energy is calculated by multiplying the slope with the gas constant, R.

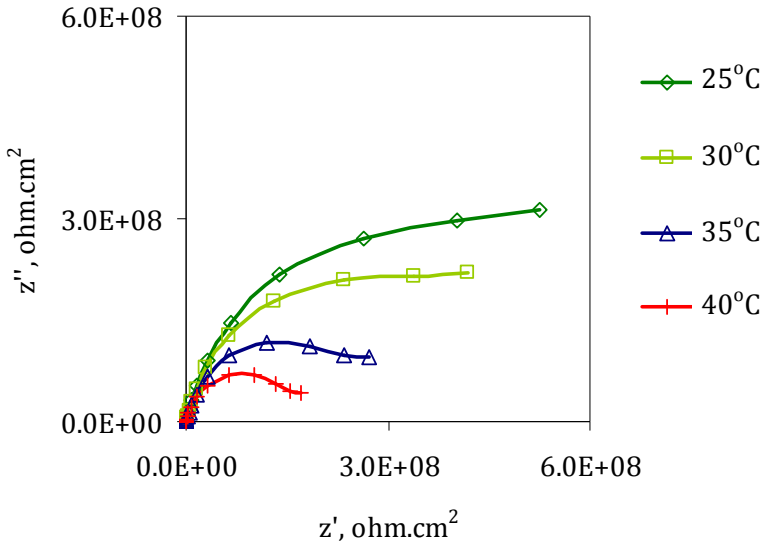

Figure 6.36 - Nyquist plots at various temperatures for ZR-FS coating (panel 2) after 1 day of exposure at 50°C

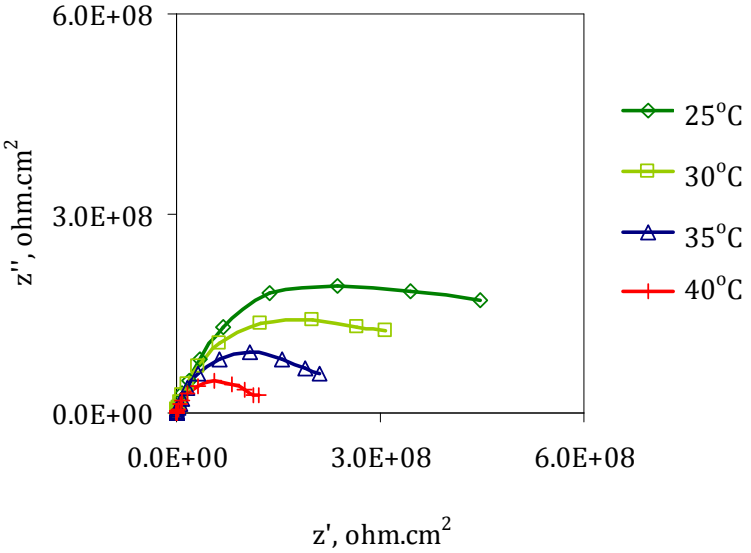

Figure 6.37 - Nyquist plots at various temperatures for ZR-FS coating (panel 2) after 3 days of exposure at 50°C

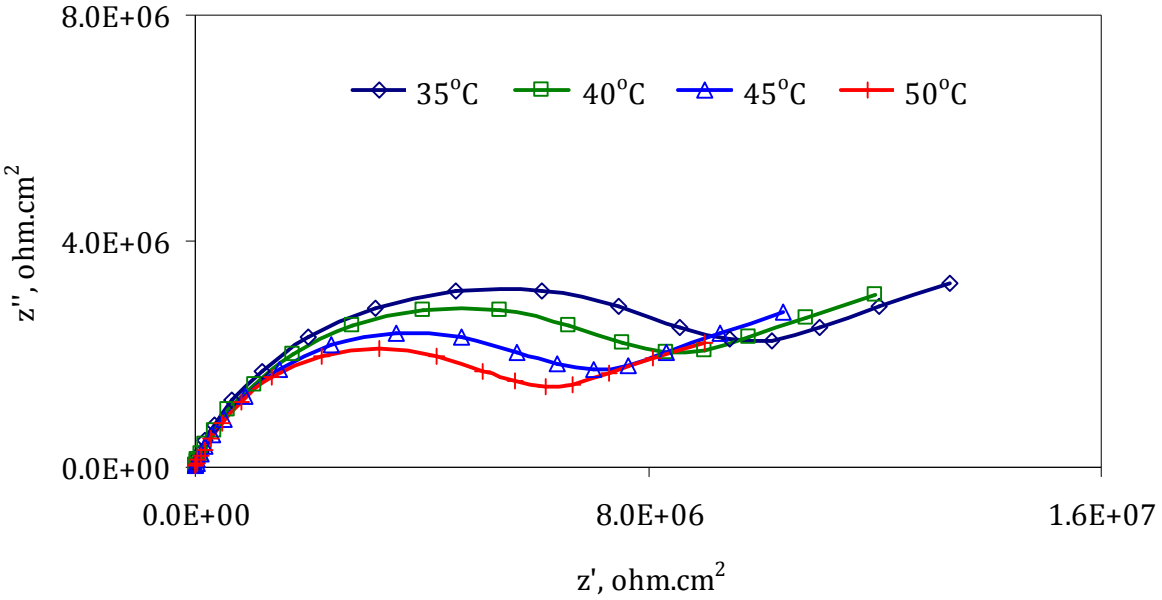

Figure 6.38 - Nyquist plots at various temperatures for ZR-FS coating (panel 2) after 14 days of exposure at 50°C

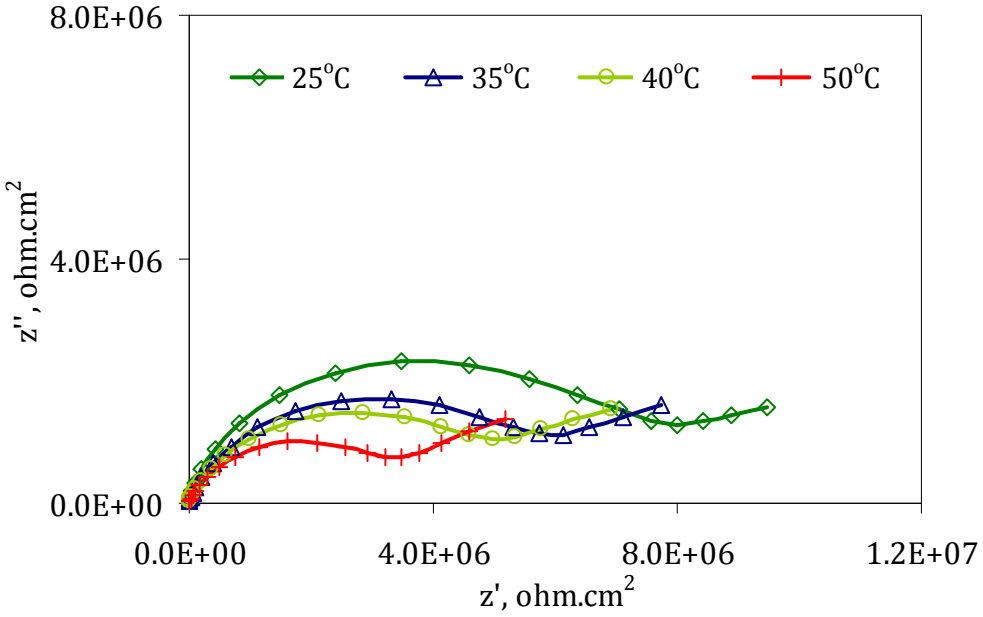

Figure 6.39 - Nyquist plots at various temperatures for ZR-FS coating (panel 2) after 21 days of exposure at 50°C

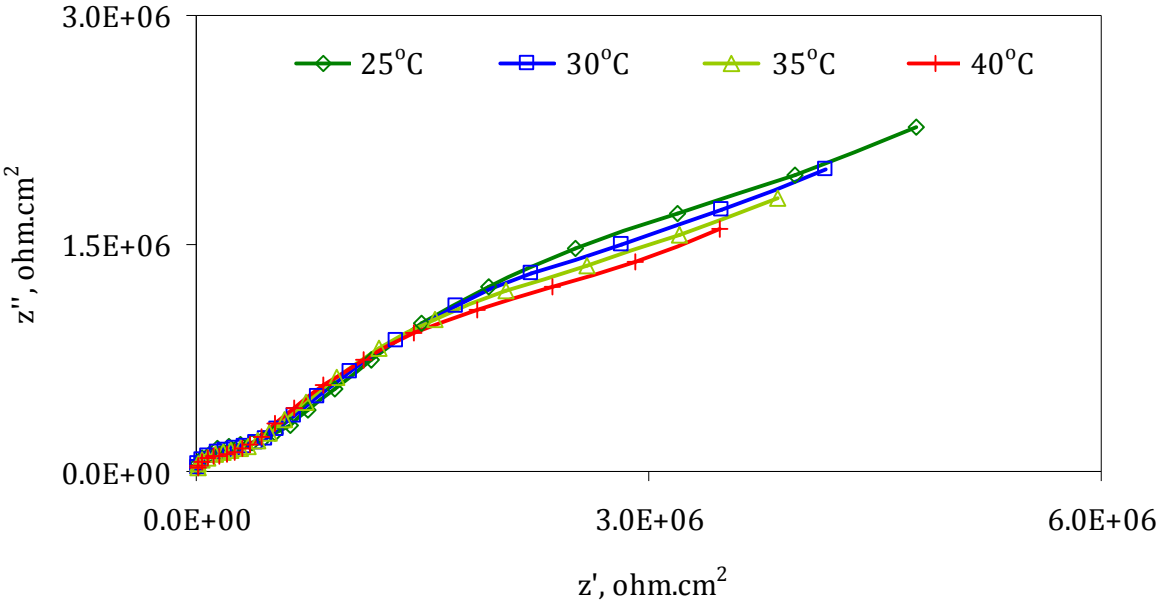

Figure 6.40 - Nyquist plots at various temperatures for ZR-FS coating (panel 2) after 35 days of exposure at 50°C

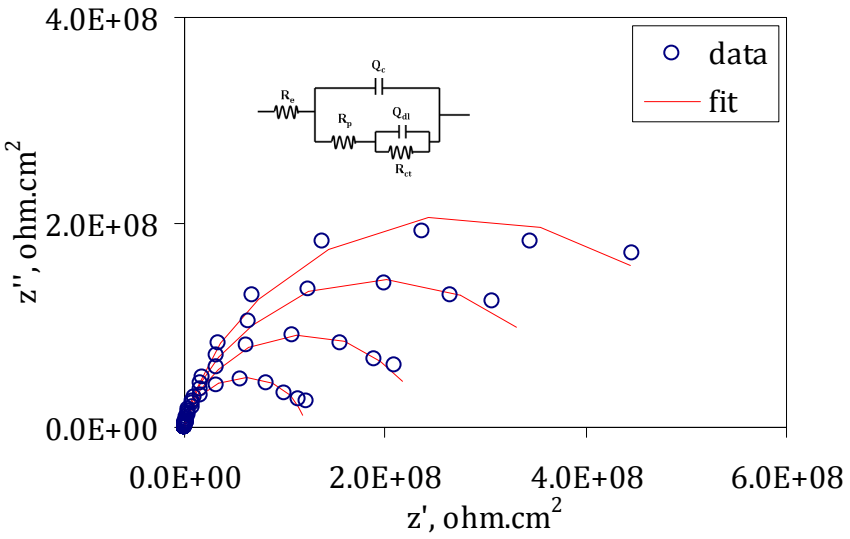

Figure 6.41 – Experimental (o) and simulated (-) Nyquist plot of ZR-FS coating (Panel 2) exposed at various temperatures after 3 days of exposure at 50°C

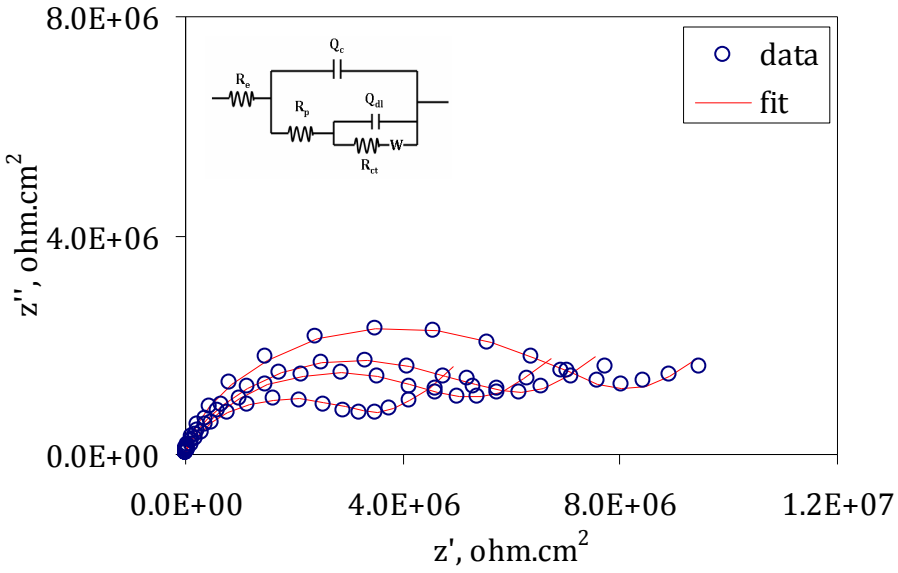

Figure 6.42 – Experimental (o) and simulated (-) Nyquist plot of ZR-FS coating (Panel 2) exposed at various temperatures after 21 days of exposure at 50°C

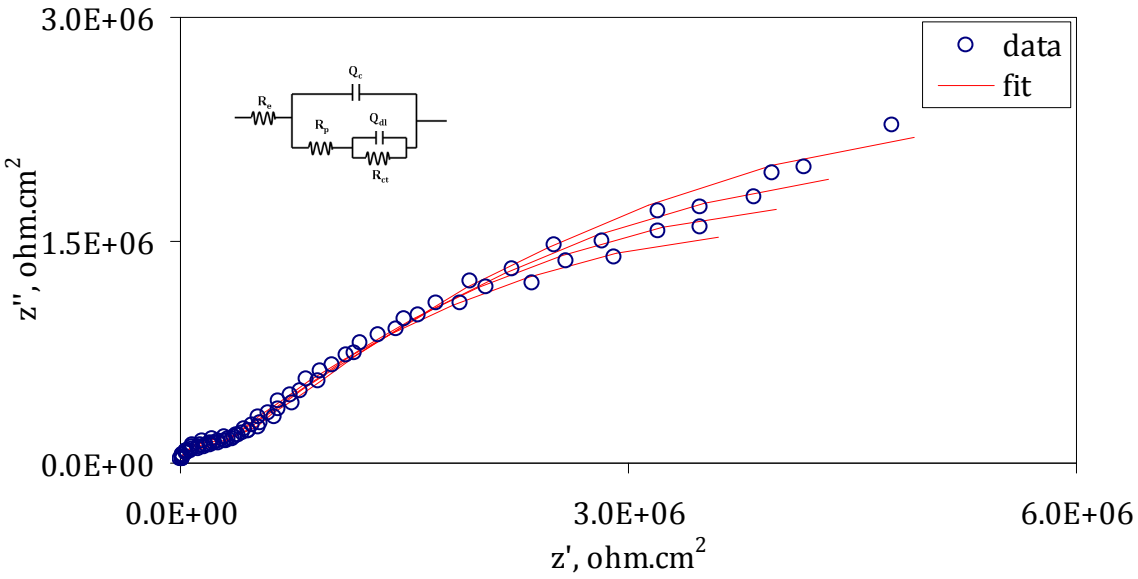

Figure 6.43 – Experimental (o) and simulated (-) Nyquist plot of ZR-FS coating (Panel 2) exposed at various temperatures after 35 days of exposure at 50°C

Table 6.9 – Best fitting parameters for ZR-FS coating (panel 2) after 1 day exposure at 50°C; Fitting circuit: [R[Q[R[QR]]]

T (°C)	Q_c $(Fcm^{-2})^n$	Q_c (%error)	n	R_p ($ohm.cm^2$)	R_p (%error)	Q_{dl} $(Fcm^{-2})^n$	Q_{dl} (%error)	n	R_{ct} ($ohm.cm^2$)	R_{ct} (%error)	X^2
25	3.00E-10	174.8	0.98	1.63E+06	591.2	7.87E-10	55.36	0.68	8.96E+08	17.89	1.50E+02
30	2.46E-10	141.5	1	1.07E+06	271.4	9.35E-10	35.81	0.72	6.30E+08	12.33	1.34E+02
35	2.60E-10	115.8	1	9.61E+05	171.9	1.02E-09	33.81	0.75	3.26E+08	9.56	1.41E+02
40	2.72E-10	119.7	1	7.69E+05	150.0	1.06E-09	37.80	0.77	1.84E+08	8.12	1.44E+02

Table 6.10 – Best fitting parameters for ZR-FS coating (panel 2) after 3 days exposure at 50°C; Fitting circuit: [R[Q[R[QR]]]

T (°C)	Q_c $(Fcm^{-2})^n$	Q_c (%error)	n	R_p ($ohm.cm^2$)	R_p (%error)	Q_{dl} $(Fcm^{-2})^n$	Q_{dl} (%error)	n	R_{ct} ($ohm.cm^2$)	R_{ct} (%error)	X^2
25	2.50E-10	147.9	1	1.19E+06	335.9	8.58E-10	39.52	0.71	5.77E+08	11.83	1.37E+02
30	2.57E-10	135.3	1	9.95E+05	239.3	1.04E-09	34.09	0.73	4.03E+08	10.65	1.41E+02
35	2.69E-10	131.2	1	8.33E+05	192.8	1.13E-09	35.03	0.74	2.44E+08	9.13	1.46E+02
40	2.83E-10	140.6	1	6.65E+05	178.0	1.26E-09	38.54	0.75	1.28E+08	8.09	1.55E+02

Table 6.11 – Best fitting parameters for ZR-FS coating (panel 2) after 14 days exposure at 50°C; Fitting circuit: [R[Q[R[Q[RW]]]]

T (°C)	Q_c $(Fcm^{-2})^n$	Q_c (%error)	n	R_p ($ohm.cm^2$)	R_p (%error)	Q_{dl} $(Fcm^{-2})^n$	Q_{dl} (%error)	n	R_{ct} ($ohm.cm^2$)	R_{ct} (%error)	W	X^2
35	1.88E-10	169	1	2.39E+05	220.7	5.50E-09	21.98	0.59	1.03E+07	4.21	2.77E-07	5.84E+03
40	1.94E-10	109.6	1	2.16E+05	105.0	5.78E-09	10.11	0.61	8.93E+06	2.98	2.87E-07	4.23E+03
45	2.04E-10	102.8	1	1.88E+05	75.22	5.80E-09	8.06	0.64	7.32E+06	2.99	3.05E-07	5.33E+04
50	2.14E-10	106	1	1.69E+05	64.77	5.49E-09	8.42	0.66	6.30E+06	3.09	3.66E-07	6.91E+03

Table 6.12 – Best fitting parameters for ZR-FS coating (panel 2) after 21 days exposure at 50°C; Fitting circuit: [R[Q[R[Q[RW]]]]

T (°C)	Q_c $(Fcm^{-2})^n$	Q_c (%error)	n	R_p (ohm.cm²)	R_p (%error)	Q_{dl} $(Fcm^{-2})^n$	Q_{dl} (%error)	n	R_{ct} (ohm.cm²)	R_{ct} (%error)	W	X^2
25	1.81E-10	136.7	1	4.80E+05	250.7	6.65E-09	32.65	0.55	7.79E+06	17.30	5.78E-07	2.50E+03
35	1.89E-10	122.7	1	2.43E+05	155.1	9.42E-09	16.64	0.56	6.12E+06	6.63	5.61E-07	5.88E+04
40	1.95E-10	109.8	1	2.04E+05	111.4	1.06E-08	12.26	0.57	5.30E+06	5.05	5.62E-07	5.09E+04
50	2.27E-10	159.5	0.99	1.36E+05	116.8	1.26E-08	13.73	0.58	3.52E+06	5.21	5.85E-07	6.33E+04

Table 6.13– Best fitting parameters for ZR-FS coating (panel 2) after 35 days exposure at 50°C; Fitting circuit: [R[Q[R[QR]]]

T (°C)	Q_c $(Fcm^{-2})^n$	Q_c (%error)	n	R_p (ohm.cm²)	R_p (%error)	Q_{dl} $(Fcm^{-2})^n$	Q_{dl} (%error)	n	R_{ct} (ohm.cm²)	R_{ct} (%error)	X^2
25	6.12E-10	30.69	0.90	2.99E+05	9.932	1.54E-07	6.02	0.47	1.18E+07	14.59	1.53E+03
30	6.80E-10	31.59	0.89	2.53E+05	9.665	1.73E-07	5.69	0.47	1.03E+07	13.38	1.38E+03
35	7.38E-10	34.23	0.89	2.17E+05	10.06	1.83E-07	5.64	0.47	9.00E+06	12.45	1.39E+03
40	6.65E-10	38.17	0.90	1.74E+05	10.75	2.00E-07	5.51	0.47	8.02E+06	11.87	1.36E+03

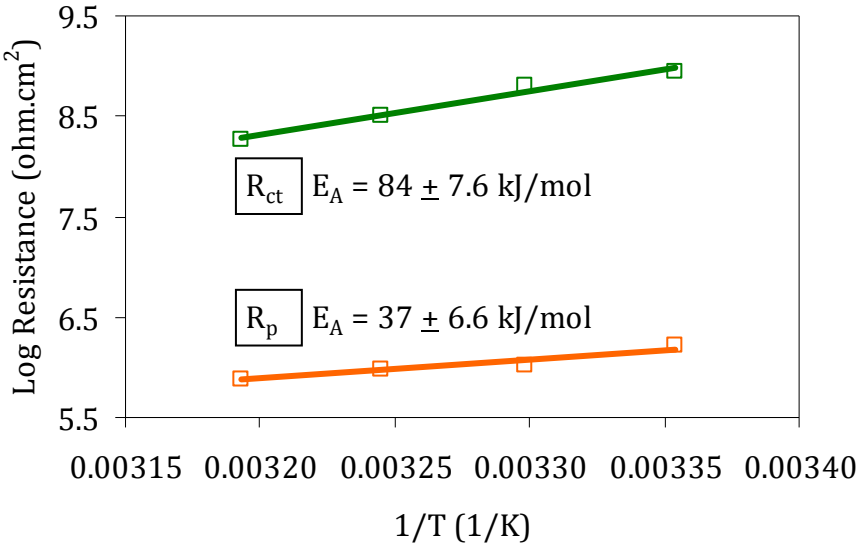

Figure 6.44 – Arrhenius plots of R_p and R_{ct} for ZR-FS coating (panel 2) after 1 day of exposure at 50°C

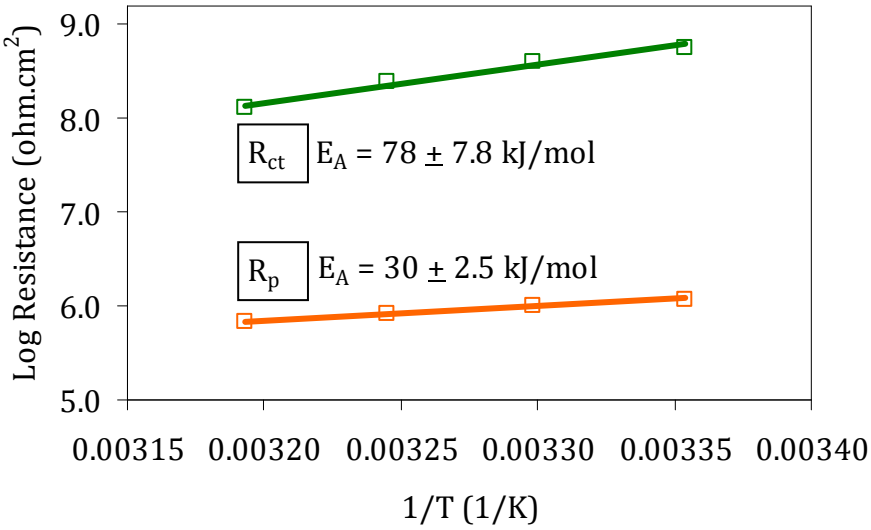

Figure 6.45 – Arrhenius plots of R_p and R_{ct} for ZR-FS coating (panel 2) after 3 days of exposure at 50°C

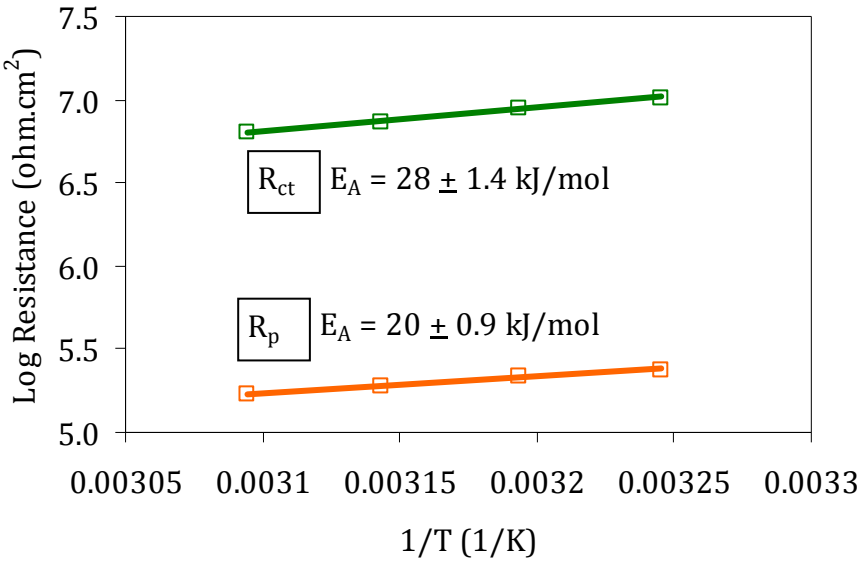

Figure 6.46 – Arrhenius plots of R_p and R_{ct} for ZR-FS coating (panel 2) after 14 days of exposure at 50°C

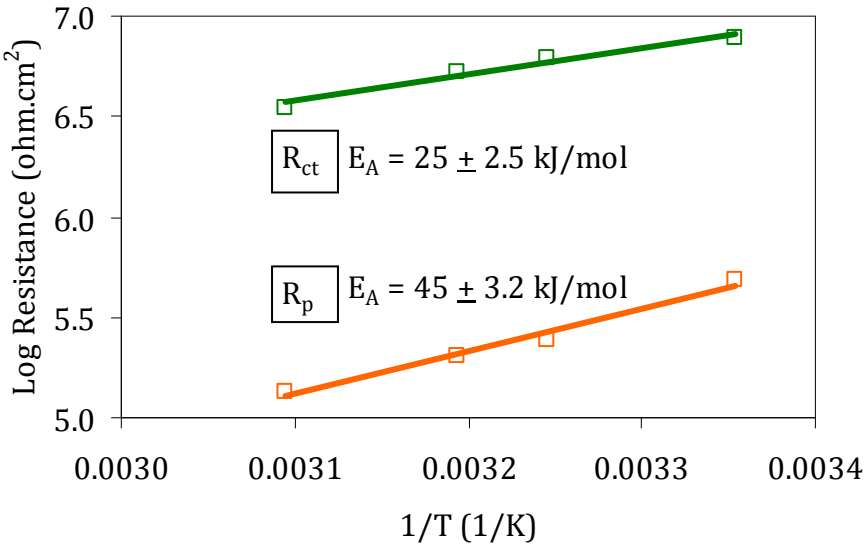

Figure 6.47 – Arrhenius plots of R_p and R_{ct} for ZR-FS coating (panel 2) after 21 days of exposure at 50°C

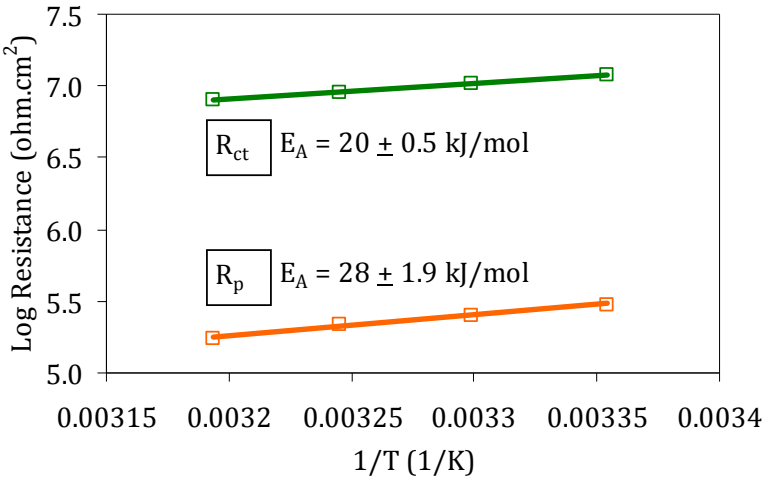

Figure 6.48 – Arrhenius plots of R_p and R_{ct} for ZR-FS coating (panel 2) after 35 days of exposure at 50°C

6.4.6 Activation Energies for Ion Conduction and Corrosion Process

The effect of temperature on ion transport through the film and the corrosion process are then summarized. **Figures 6.49** and **6.50** show the trend of activation energy determined for ion conduction in the film (from R_p) and corrosion process (from R_{ct}). Note that in the early stages the error in R_p is large. Both figures show that the activation energy for the corrosion process is very much higher than ion conduction during early immersion. This finding is similar to earlier experiments (**Section 4.3.5**). It is evident from both figures that the activation energy for the corrosion process is decreasing over time, and at the end of the exposure, they are quite similar. It is suggested that at this stage ion transport in the coating might be controlling the corrosion process. In the beginning the activation energy values get smaller over time because of coating degradation. If we compare these results with those in **Chapter 5**,

we see that R_p values for 2 coats of ZR-FS coating are similar to those for the first semi-circles on the thicker ZP-FS coating; suggesting that the interpretation offered is correct. However the high activation energy values seen in those tests were not seen here.

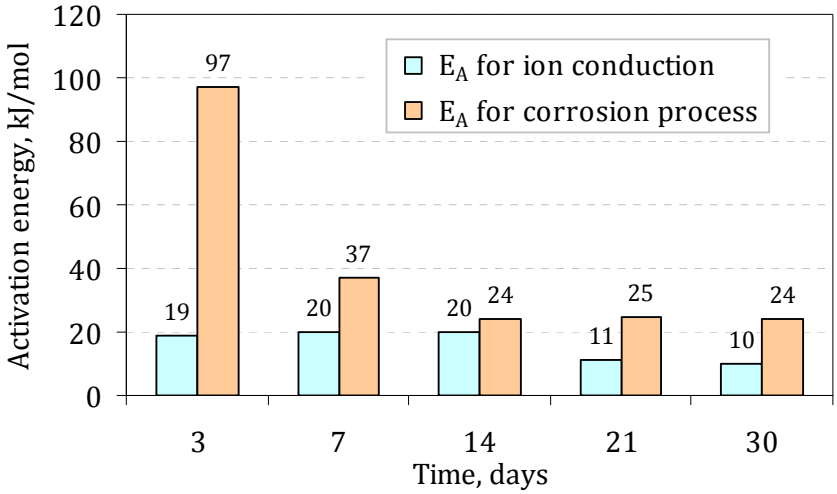

Figure 6.49 – Evolution with time of activation energy for ion conduction and corrosion process for ZR-FS coating (panel 1)

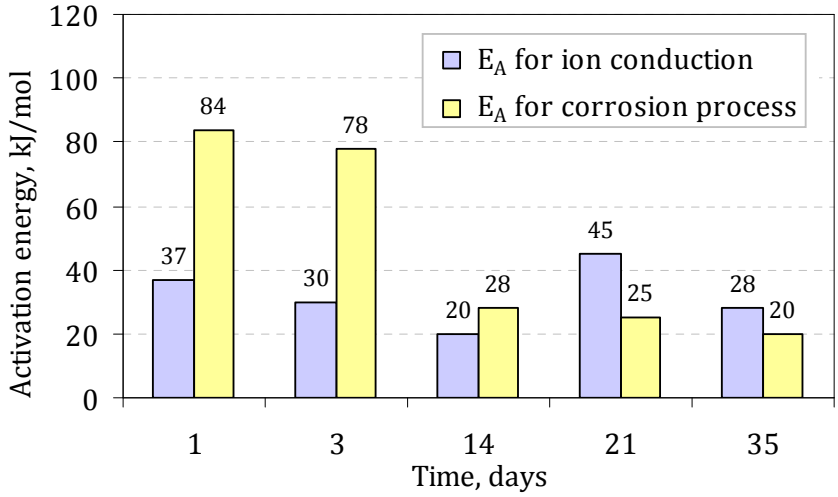

Figure 6.50 – Evolution with time of activation energy for ion conduction and corrosion process for ZR-FS coating (panel 2)

6.5 Conclusions

- The shapes of Nyquist plots for zinc rich primer coating generated in this study were quite complex. During early immersion Warbug diffusion was observed and afterwards the plot changed to a two semicircle curve.

- Degradation of zinc rich full system coating is faster at high temperature when compared to tests conducted at ambient temperature.

- The activation energies generated from the higher frequency semicircle for zinc rich full system coatings is about 19–37 $kJmol^{-1}$. It is believed that this value corresponds to ion transport into the coating.

- The activation energies generated for the corrosion process are very much higher than that for ion conduction for a full system coating. The initial activation energy generated from the charge transfer resistance is large (78–97 $kJmol^{-1}$). However, over the period a decrease in activation energy value was noted for the corrosion process, which suggested that ionic resistance of the coating system can eventually account for the effect of temperature on corrosion rate.

CHAPTER 7

TESTING ON FREE FILM

7.1 Introduction

The proposition that corrosion rate is controlled by the ionic resistance of an organic coating has been tested and discussed in the earlier chapter (**Chapter 4**). The calculated activation energy for coating resistance is significantly lower than the activation energy for the charge transfer resistance. This suggests that ion conduction in the coating, as apparent in an AC measurement, cannot be controlling the corrosion rate. In this chapter, further investigation on how the coating resistance behaves was done using only free films to confirm that ion conduction in the paint coating generates a simple impedance response and to determine the activation energy for ion conduction in undegraded coating.

'Free film' refers to paint films which had been carefully removed from the substrate (glass, plastic or smooth metal) whereas 'attached films' are those that are still adhered to the metal substrate. Several factors, which include the effects of the metal substrate or reaction at the coating/metal interface towards the electrochemical properties of the coating, can be eliminated by studying the free standing films. Permeation of the coating with ions or water has been precisely studied with free standing films by Castela and Simoes [175]. There are two main features which are of interest in the free

films studied; their resistive behaviour and their dielectric properties. However, the aim of free film study in this work is mainly to observe any changes in resistance with time and to characterise the response of the films under the immersion conditions when the surrounding temperature is altered (lower and higher than ambient temperature) to determine activation energy.

7.2 Experimental Details

In this work, epoxy-phenolic free standing film with 150μm thickness is being tested. A two-electrode arrangement was used, with one Ag/AgCl electrode acted as both counter electrode and reference electrode and the other as working electrode. Further information on cell arrangement can be found in **Section 3.6**. The spectrum was obtained using two frequency ranges; for tests at high temperature a 1Hz–30 kHz frequency range, whereas for tests at different concentrations of NaCl solution a 0.1Hz–30 kHz frequency range was used. In all cases, a 10 mV AC voltage at the open circuit potential was applied.

In addition to exposure at ambient temperature, another free film was exposed at 40^{o}C and EIS measurements were taken across a range of temperatures (21 to 40^{o}C). Then the same film at 21^{o}C was cooled with ice and EIS measurements were taken across a range of temperatures (10 to 21^{o}C). Tests on free films were then extended to immersion in different chloride cation solutions: NaCl, KCl and LiCl. In another experiment to test for 'D' or 'I' character the free film was kept in 0.1% NaCl solution for a week while impedance measurements were made, after which the solution was

changed for a more concentrated one (2% and 3% NaCl solution). At the end of the test, the film was re-immersed in 0.1% NaCl solution.

The EIS spectra were analyzed using a model circuit in **Figure 7.1** which was composed of a resistor, R_p, in parallel with a CPE, Q_c, in series with the solution resistance, R_e, labelled as R[QR].

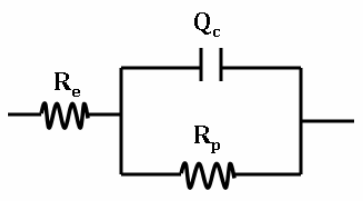

Figure 7.1 - Equivalent electric circuit for free film immersed in salt solution [1]

7.3 Results and Discussion

7.3.1 Other Free Film Studies

The importance of free film behaviour should not be under estimated as earlier work [1, 119, 176] involving free film investigations resulted in markedly different behaviour to attached films. However, work by Walter on free films generates similar behaviour to attached films such that the water uptake on the free film increases with immersion time. He also found that the failure time of free film is decreasing with increasing chloride ion concentration [1, 129]. He attributed the similarity between free and attached film to the paint film degradation which is caused predominantly by the solution and not by secondary effects such as the build-up of alkalinity in the

accumulated water layer at the metal/film interface on the attached films caused by cathodic reduction of oxygen.

Kendig et al. [177] compared polybutadiene coatings prepared as freestanding and attached films with various surface preparations. They observed a distinct pattern between them where the freestanding films maintained a high and constant resistance, whereas the resistance of attached films decrease with immersion time. They suggested that the degradation behaviour of an attached film is due to the accumulation of corrosion products at the coating/metal interface. On the other hand, studies conducted by both Kittel et al. [178] and Castela et al. [119] showed inferior properties for the resistance of a freestanding film compared with that of an identical film applied to a metallic substrate.

Free films have been frequently used to investigate the permeability properties and the water uptake by paint films, with a view to correlate this data with the corrosion protective properties of the paint. The comparison between water uptake of free and attached films has been the subject of many studies. For their studies, D'Alkaine et al. [176] used free film from sand blasted substrates and found that films applied to a steel substrate showed a higher rate of water uptake than free films or film applied to a glass substrate. They suggested that there must be a special interaction between the water in the film and the metal substrate. On the other hand, Corti et al. [39] measured a higher water uptake for freestanding films than for attached films applied to steel or glass. They attributed this difference to the different level of residual stress from curing in free and attached films. These agreed with those obtained by Castela and co-

workers who also observed a greater water uptake for PVC freestanding films in comparison with attached films [119].

7.3.2 Behaviour of Free Film Exposed in 3% NaCl at 21°C

The corresponding Nyquist plots for free film exposed at ambient temperature up to 3 weeks immersion is presented in **Figure 7.2**. As the immersion time increased, the size of semicircle become smaller and the impedance value dropped. It was observed that over 22 days, the film resistance remained above $10^8 \Omega cm^2$ which indicates that the film is still in a very good condition.

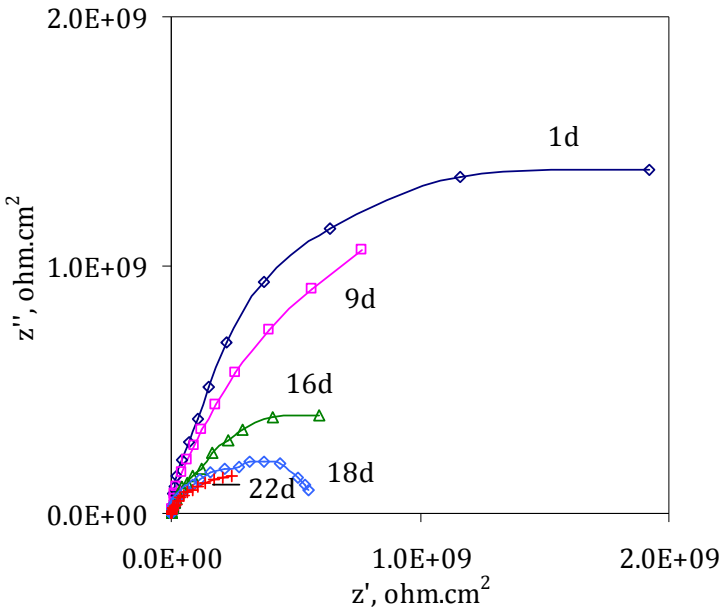

Figure 7.2 – Impedance spectra for free film at various exposure times in 3% NaCl solution

As shown in **Figure 7.3** as immersion time increased, the film resistance decreased while capacitance increased. The change with immersion time indicates that water sorption decreases film resistance and increases the capacitance of the film. It is suggested that the changes in the film resistance with time could be attributed to the permeation of the water and ions into the film. The steady increase in Q_c suggests continuing water uptake.

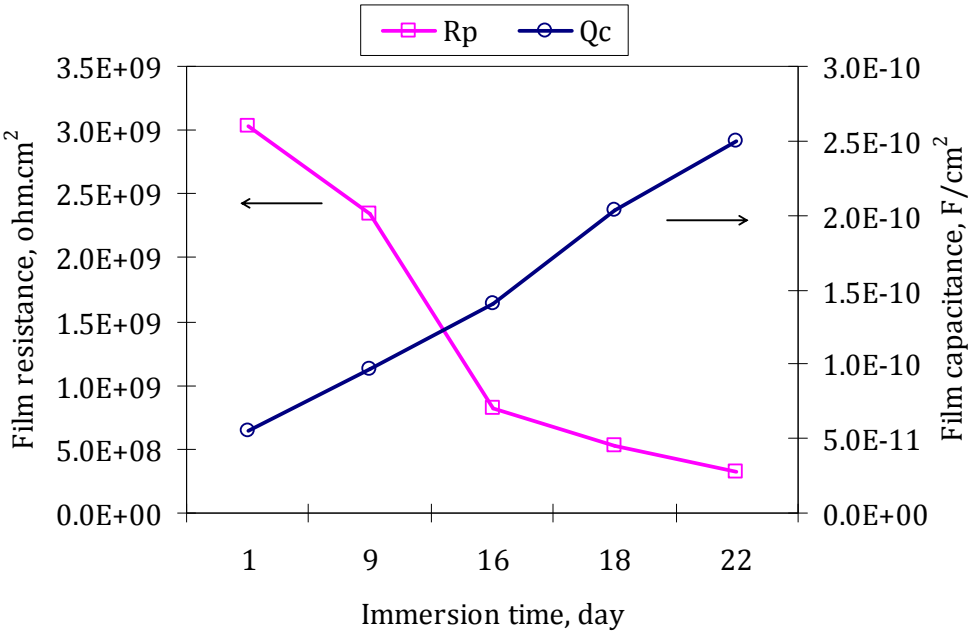

Figure 7.3 – The change in film resistance and capacitance with immersion time in 3% NaCl solution

7.3.3 Behaviour of Free Film Exposed in Different Solution Concentrations

Figure 7.4 presents the impedance spectra obtained in the various NaCl concentrations; 0.1%, 2% and 3%. For each concentration the film was allowed to

stabilize for a week. After the end of the test in 3% solution, the film was again re-immersed in the 0.1% solution until stabilization. It was observed that the impedance increased again when the free film was re-immersed in 0.1% NaCl solution, approaching the impedance spectra recorded initially.

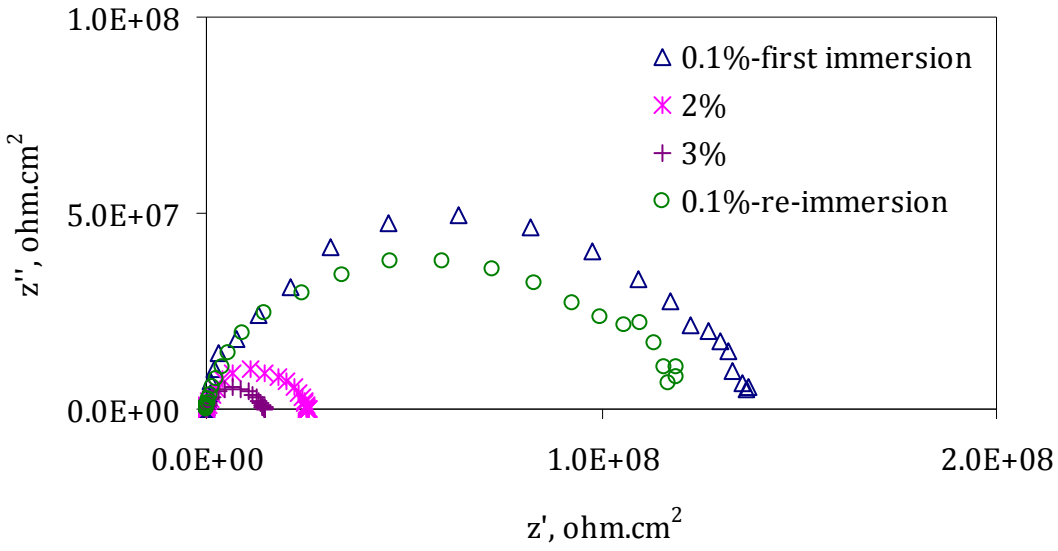

Figure 7.4 - Nyquist plot of a free film exposed in a different concentration of NaCl solution

The film resistance is plotted as a function of NaCl concentration and is presented in **Figure 7.5**. It was observed that the resistance of the film decreased with increasing concentration of the solution. This clearly indicates that the film has a direct dependence (lower solution conductance leads to a higher film resistance) revealing a D-type behaviour [33]. The film resistance decreases considerably when exposed to a stronger chloride solution (2% and 3%) but when placed back in the weaker chloride solution (0.1%) the resistance increased and recovered to almost where it was initially.

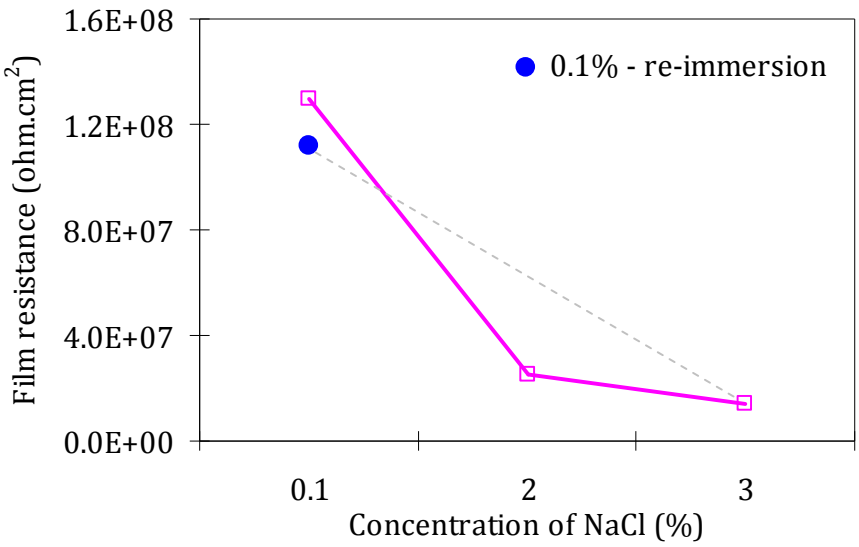

NaCl conc. (%)	0.1	2	3
R_p (ohm.cm^2)	1.30E+08	2.50E+07	1.43E+07
R_p (ohm.cm^2)	1.12E+08		

Figure 7.5 - Film resistance as a function of NaCl concentration

7.3.4 Behaviour of Free Film Exposed in Different Metal Cations

Wang and Leidheiser [165] , Fürbeth and Stratmann [139-141] and Sharman [179] have investigated the link between cation mobility, blistering and delamination rate. The smaller the hydrated cation, the greater was the rate of delamination growth which is due to an easier ion transport along the metal-polymer interface. A similar test was carried out in this work where the influence of the cation mobility on the electrochemical behaviour of free standing films was studied.

Free film was exposed to different metal cations at high temperature to see how the size of hydrated cation affects the activation energy for ion conduction in the coating. The films were exposed to 0.5M chloride solution with different cations (K^+, Na^+ and Li^+). The film was exposed to 40^{o}C chloride solution and EIS measurements were taken as the solution slowly cooled down to room temperature. After the test ended, the same film was exposed to 10^{o}C chloride solution (cooled with ice) and EIS measurements were also taken as the solution slowly warmed up to room temperature. This test is conducted to obtain the activation energy without heating the film which could possibly causing over-curing and solvent loss.

Figure 7.6 shows typical EIS responses for free standing film at various temperatures (40^{o}C to room temperature) during exposure to K^+, Na^+ and Li^+ solution. Notice that the shape of the semicircle in the Nyquist plots becomes smaller at higher temperature.

To assess the influence of the temperature on the ion conduction, these semicircles were fitted with an equivalent circuit using ZSimpWin software. However, with one time constant, R[QR], it was difficult to fit the data at lower frequency values as shown in **Figure 7.7a**. So another equivalent circuit consisting two time constants, R[Q[R[QR]]], was used and a better agreement was observed between the experimental data and the fit (**Figure 7.7b**). The two time constants model circuit fit the EIS spectra better which is probably due to the presence of pigment in the free film. Thus two time constants were now used to fit all the impedance spectra (**Figure 7.8**) and the fitted parameters are summarized in **Tables 7.1** to **7.3**. As two time constants were used, and considering that free film is normally based on one time constant system, the film resistance should be taken as the sum of R_1 and R_2 together. Notice that R_1 is very much smaller than R_2, thus adding those values together does not make any significant difference, so the film resistance is based solely on R_2 values.

The values of log (film resistance), R_2 are then plotted against 1/T, where T is in Kelvin. A good straight line in **Figure 7.9** shows that the film resistance does obey the Arrhenius equation across the full temperature range, thus enabling the activation energy to be calculated.

(a) K^+

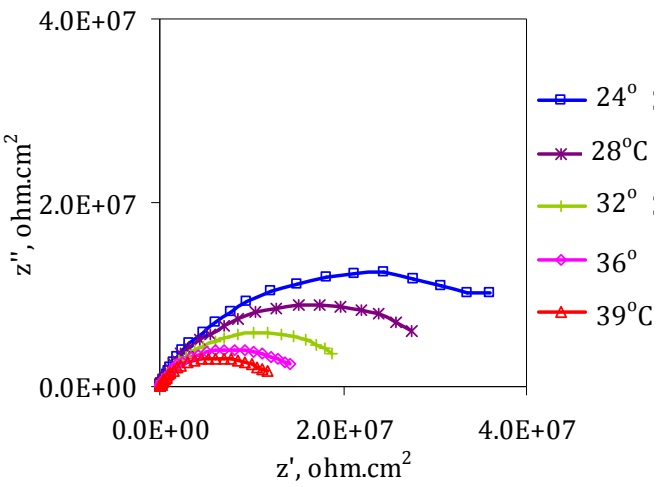

(b) Na^+

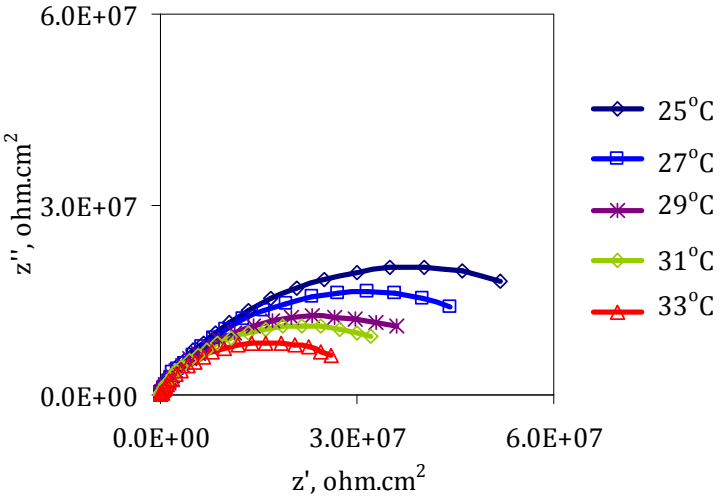

(c) Li^+

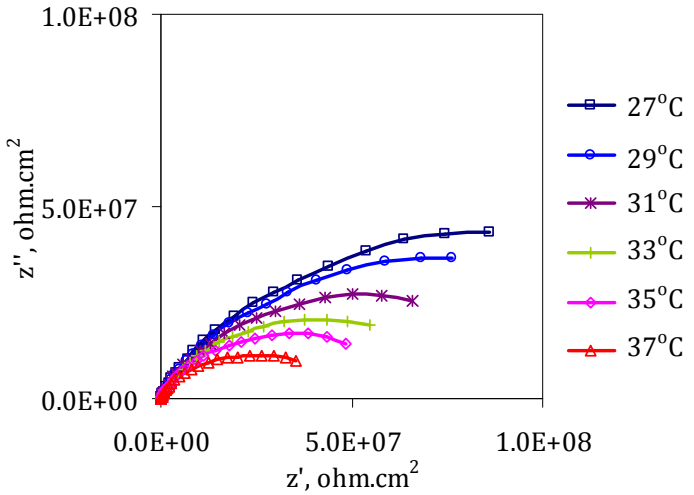

Figure 7.6 - Nyquist plot at various temperatures for free film exposed at 40°C in K^+, Na^+, and Li^+ solution

(a)

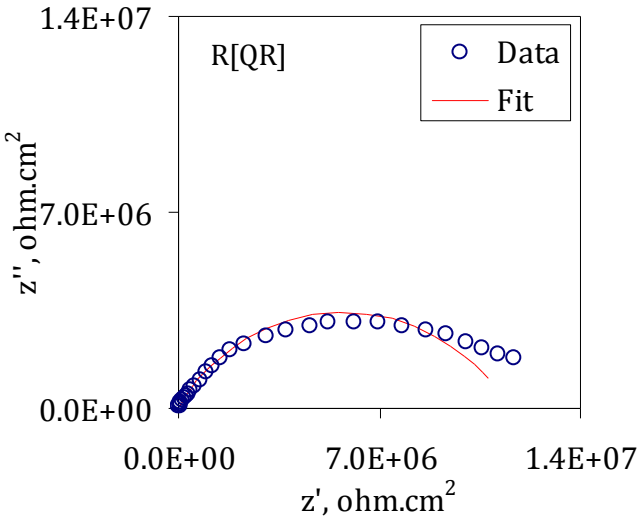

(b)

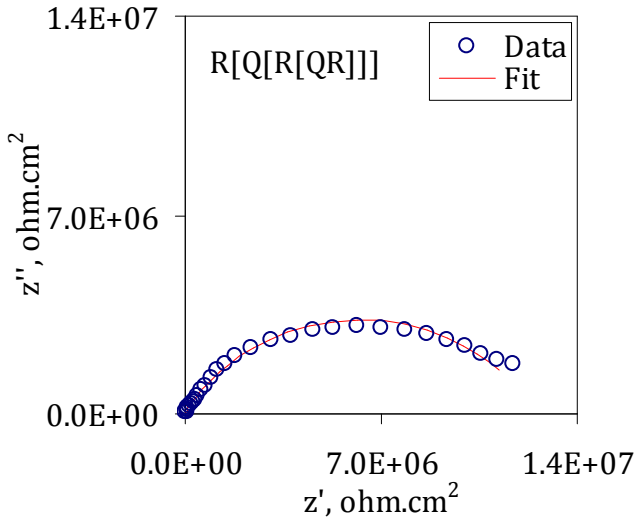

Figure 7.7 – Experimental (o) and simulated (-) Nyquist plot for free film exposed at 40°C in KCl solution

(a) K^+

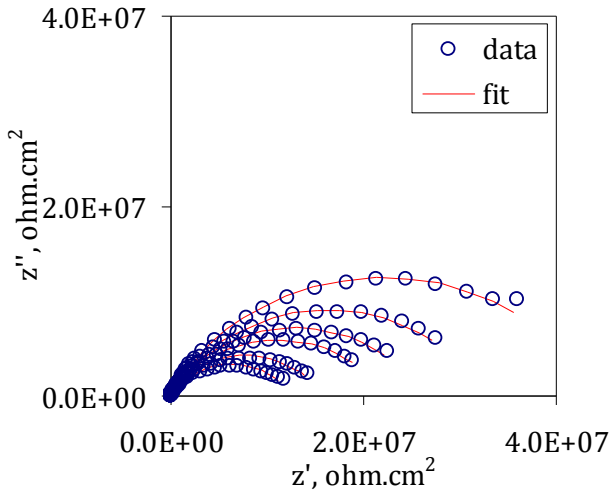

(b) Na^+

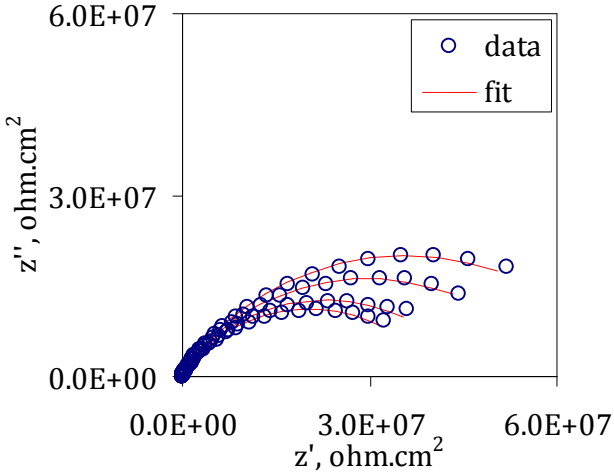

(c) Li^+

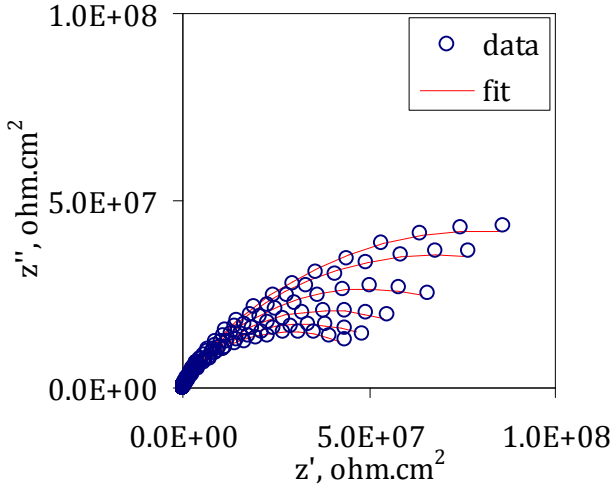

Figure 7.8 – Experimental (o) and simulated (-) Nyquist plot at various temperatures for free film exposed at 40°C in K^+, Na^+ and Li^+ solution

Table 7.1 – Best fitting parameters for free film exposed at 40°C in KCl solution

Fitting circuit:R[Q[R[QR]]]

T (°C)	Q_1 (Fcm^{-2})^n	Q_1 (%error)	n	R_1 (ohm.cm^2)	R_1 (%error)	Q_2 (Fcm^{-2})^n	Q_2 (%error)	n	R_2 (ohm.cm^2)	R_2 (%error)	X^2
24	6.19E-11	134.4	1	5.50E+05	88.11	2.46E-09	6.52	0.62	4.44E+07	3.12	2.76E+02
28	6.46E-11	172.0	1	4.44E+05	116.4	2.99E-09	8.49	0.60	3.29E+07	2.85	2.46E+02
30	6.69E-11	135.7	1	4.37E+05	83.22	3.34E-09	6.82	0.61	2.60E+07	2.76	2.23E+02
32	3.70E-11	174.0	1	4.14E+04	541.3	3.73E-09	10.81	0.61	2.24E+07	3.49	3.20E+02
36	7.38E-11	164.3	1	3.68E+05	98.71	4.47E-09	9.19	0.59	1.55E+07	3.57	3.01E+02
39	7.44E-11	247.7	1	2.86E+05	148.5	5.28E-09	13.46	0.59	1.25E+07	3.82	2.76E+02

Table 7.2 – Best fitting parameters for free film exposed at 40°C in NaCl solution

Fitting circuit:R[Q[R[QR]]]

T (°C)	Q_1 (Fcm^{-2})^n	Q_1 (%error)	n	R_1 (ohm.cm^2)	R_1 (%error)	Q_2 (Fcm^{-2})^n	Q_2 (%error)	n	R_2 (ohm.cm^2)	R_2 (%error)	X^2
25	5.58E-11	169.8	1	5.04E+05	119.0	2.34E-09	6.98	0.61	7.31E+07	3.54	2.06E+02
27	5.65E-11	237.3	1	4.49E+05	166.4	2.55E-09	10.44	0.60	5.99E+07	4.13	2.98E+02
29	5.90E-11	183.5	1	4.42E+05	118.5	2.87E-09	7.72	0.60	4.65E+07	3.13	2.40E+02
31	6.20E-11	149.7	1	4.71E+05	99.71	3.05E-09	6.83	0.60	4.11E+07	2.92	2.19E+02
33	3.56E-11	268.2	1	3.42E+04	870.5	3.50E-09	9.24	0.59	3.25E+07	3.63	2.63E+02

Table 7.3 – Best fitting parameters for free film exposed at 40°C in LiCl solution

Fitting circuit:R[Q[R[QR]]]

T (°C)	Q_1 $(Fcm^{-2})^n$	Q_1 (%error)	n	R_1 (ohm.cm²)	R_1 (%error)	Q_2 $(Fcm^{-2})^n$	Q_2 (%error)	n	R_2 (ohm.cm²)	R_2 (%error)	X^2
27	9.59E-11	257.4	0.94	1.01E+06	405.9	1.97E-09	17.12	0.55	1.69E+08	12.13	3.99E+02
29	9.53E-11	257.0	0.94	9.73E+05	361.5	2.08E-09	15.61	0.58	1.41E+08	9.87	4.38E+02
31	7.20E-11	179.5	0.97	8.47E+05	174.2	2.09E-09	8.95	0.58	1.01E+08	5.47	3.84E+02
33	5.97E-11	160.7	0.99	7.47E+05	139.6	2.34E-09	8.25	0.59	7.86E+07	4.59	3.44E+02
35	6.94E-11	230.6	0.98	6.15E+05	227.5	2.67E-09	13.30	0.57	6.66E+07	4.58	2.82E+02
37	7.17E-11	208.5	0.97	6.37E+05	183.2	2.77E-09	10.85	0.58	5.80E+07	4.41	3.49E+02
39	3.59E-11	290.5	1	1.20E+04	1687	3.06E-09	13.47	0.58	4.60E+07	5.58	2.88E+02

(a) K^+

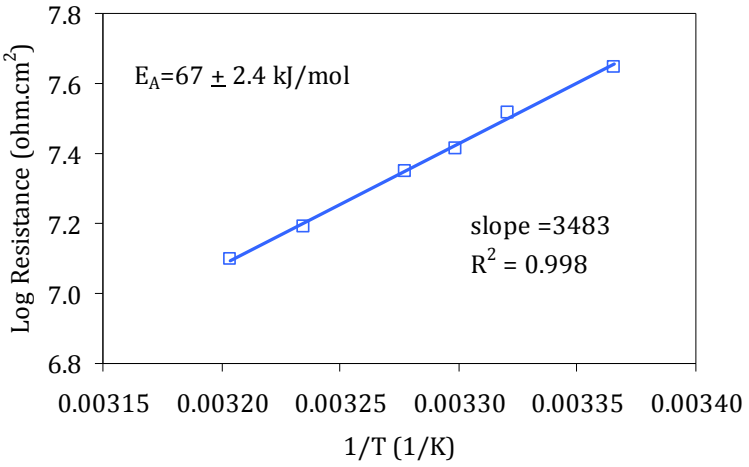

(b) Na^+

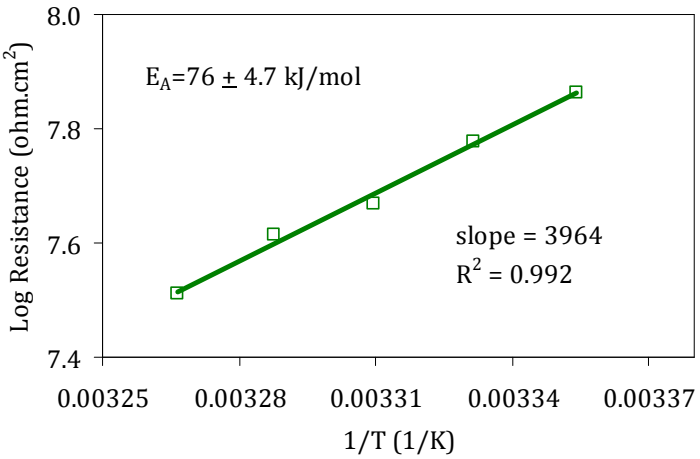

(c) Li^+

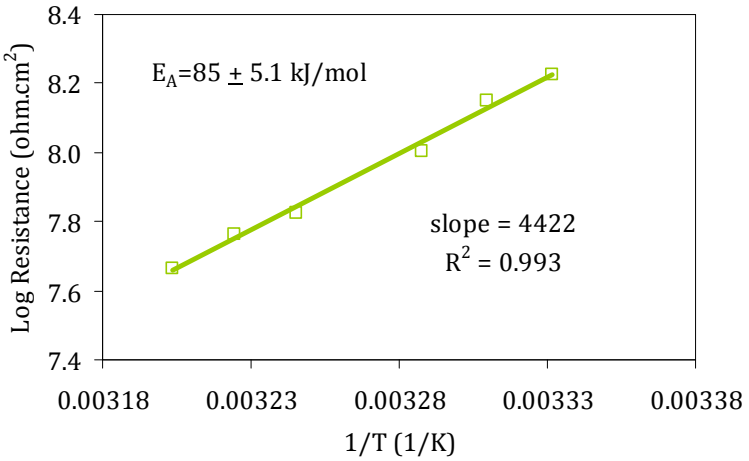

Figure 7.9 - Arrhenius plot for free film exposed at 40°C in K^+, Na^+ and Li^+ solution

(a) K^+

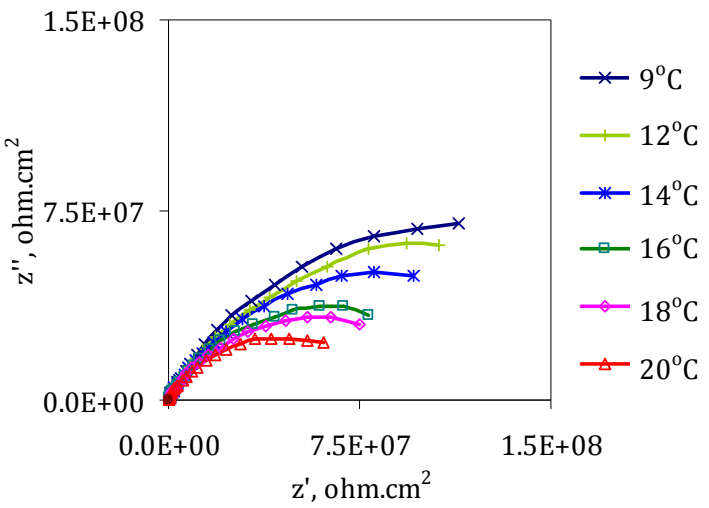

(b) Na^+

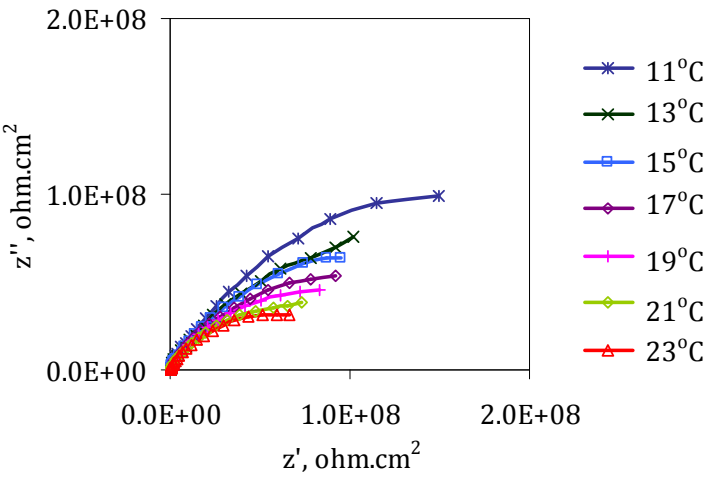

(c) Li^+

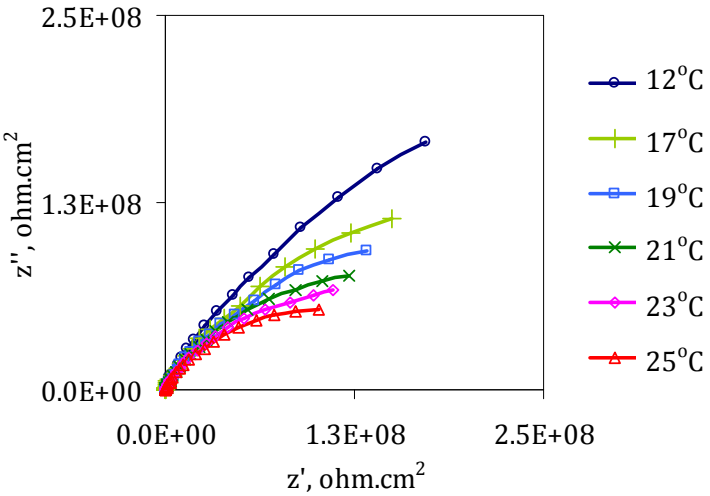

Figure 7.10 - Nyquist plot at various temperatures for free film exposed at 10°C in K^+, Na^+, and Li^+ solution

(a) K^+

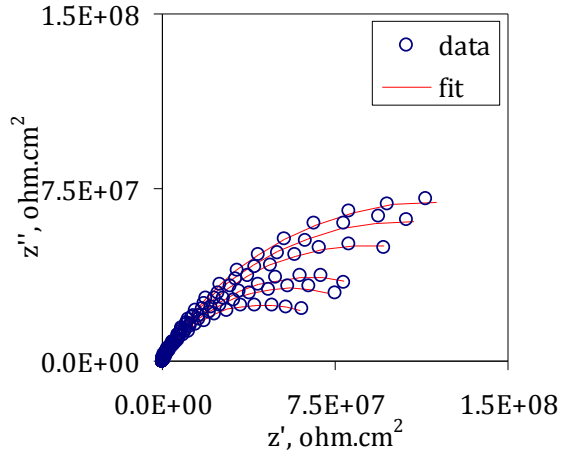

(b) Na^+

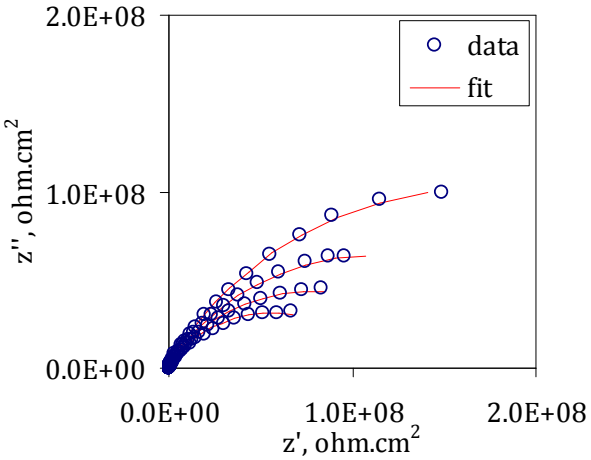

(c) Li^+

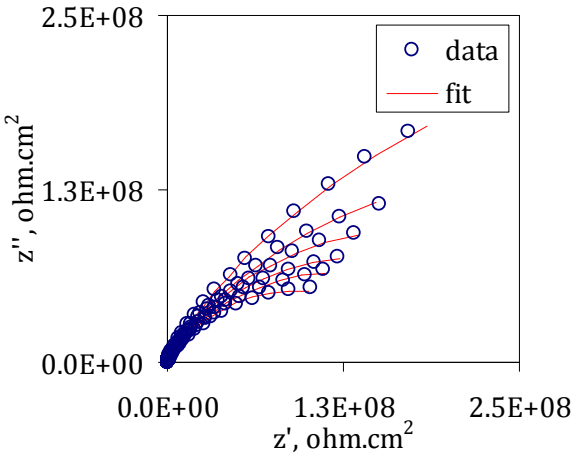

Figure 7.11 - Experimental (o) and simulated (-) Nyquist plot at various temperatures for free film exposed at 10°C in K^+, Na^+ and Li^+ solution

Table 7.4 – Best fitting parameters for free film exposed at 10°C in KCl solution

Fitting circuit:R[Q[R[QR]]]

T (°C)	Q_1 $(Fcm^{-2})^n$	Q_1 (%error)	n	R_1 ($ohm.cm^2$)	R_1 (%error)	Q_2 $(Fcm^{-2})^n$	Q_2 (%error)	n	R_2 ($ohm.cm^2$)	R_2 (%error)	X^2
9	4.85E-11	162.5	1	7.92E+05	133.0	1.27E-09	5.77	0.63	2.43E+08	6.91	2.99E+02
12	4.97E-11	162.1	1	7.45E+05	129.7	1.36E-09	5.78	0.63	2.13E+08	6.39	2.99E+02
14	5.05E-11	155.0	1	6.72E+05	128.3	1.52E-09	6.17	0.62	1.80E+08	5.62	1.98E+02
16	6.84E-11	123.3	0.98	7.85E+05	97.1	1.67E-09	4.81	0.62	1.29E+08	4.06	2.28E+02
18	2.99E-11	467.9	1	2.80E+04	1494	1.69E-09	8.26	0.64	1.12E+08	6.73	3.04E+02
20	3.25E-11	396.6	1	3.19E+04	1304	1.96E-09	9.36	0.63	8.80E+07	6.20	3.69E+02

Table 7.5 – Best fitting parameters for free film exposed at 10°C in NaCl solution

Fitting circuit:R[Q[R[QR]]]

T (°C)	Q_1 $(Fcm^{-2})^n$	Q_1 (%error)	n	R_1 ($ohm.cm^2$)	R_1 (%error)	Q_2 $(Fcm^{-2})^n$	Q_2 (%error)	n	R_2 ($ohm.cm^2$)	R_2 (%error)	X^2
11	4.65E-11	128.0	1	9.16E+05	95.59	1.11E-09	4.39	0.64	3.57E+08	7.30	3.04E+02
13	1.02E-10	327.4	0.92	1.46E+04	3547	1.62E-09	17.08	0.57	3.13E+08	31.82	8.58E+02
15	3.09E-11	299.1	1	3.80E+04	1085	1.43E-09	7.85	0.64	2.28E+08	9.80	4.31E+02
17	4.90E-11	180.4	1	6.13E+05	140.8	1.64E-09	6.85	0.62	1.87E+08	6.86	2.28E+02
19	5.19E-11	145.4	1	7.02E+05	108.1	1.72E-09	5.44	0.62	1.56E+08	5.28	2.74E+02
21	3.11E-11	423.9	1	2.99E+04	1453	1.79E-09	8.99	0.63	1.28E+08	8.02	3.55E+02
23	3.11E-11	298.1	1	3.78E+04	983.6	1.99E-09	7.96	0.63	1.13E+08	6.48	3.51E+02

Table 7.6 – Best fitting parameters for free film exposed at 10°C in LiCl solution

Fitting circuit:R[Q[R[QR]]]

T (°C)	Q_1 $(Fcm^{-2})^n$	Q_1 (%error)	n	R_1 (ohm.cm^2)	R_1 (%error)	Q_2 $(Fcm^{-2})^n$	Q_2 (%error)	n	R_2 (ohm.cm^2)	R_2 (%error)	X^2
13	8.47E-11	186.8	0.94	2.04E+06	386.1	1.03E-09	10.12	0.57	9.37E+08	34.04	4.63E+02
17	1.35E-10	295.1	0.90	1.65E+06	1306	1.44E-09	37.47	0.51	6.48E+08	75.87	9.02E+02
19	7.05E-11	175.4	0.96	1.31E+06	230.9	1.31E-09	8.15	0.59	3.65E+08	12.84	4.01E+02
21	3.32E-11	261.2	1	3.59E+04	1276	1.36E-09	10.29	0.61	2.81E+08	12.99	4.66E+02
23	6.75E-11	243.5	0.97	8.62E+05	363.5	1.55E-09	16.81	0.58	2.54E+08	16.56	4.22E+02
25	3.54E-11	245.4	0.99	3.60E+04	1143	1.53E-09	9.79	0.61	1.93E+08	9.60	3.93E+02

(a) K^+

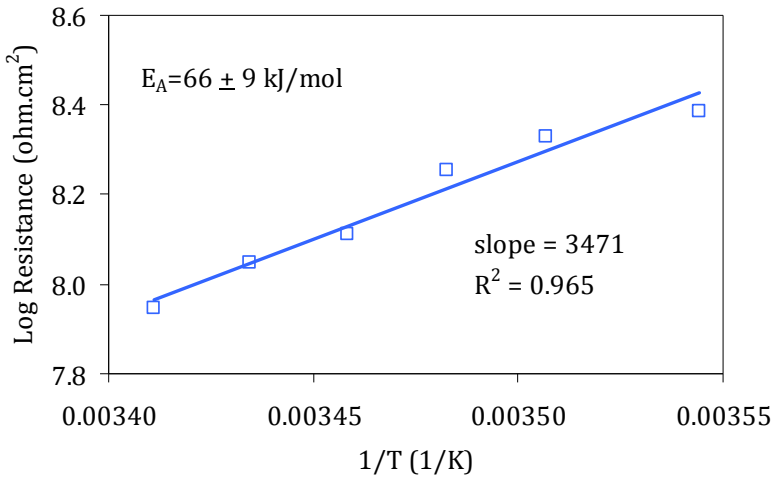

(b) Na^+

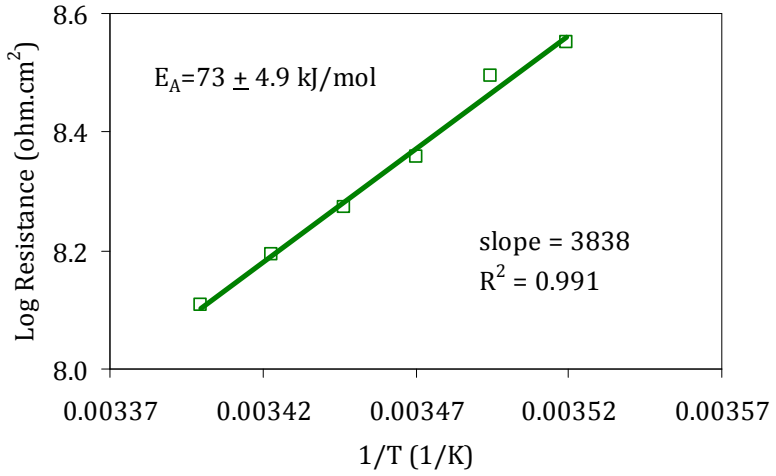

(c) Li^+

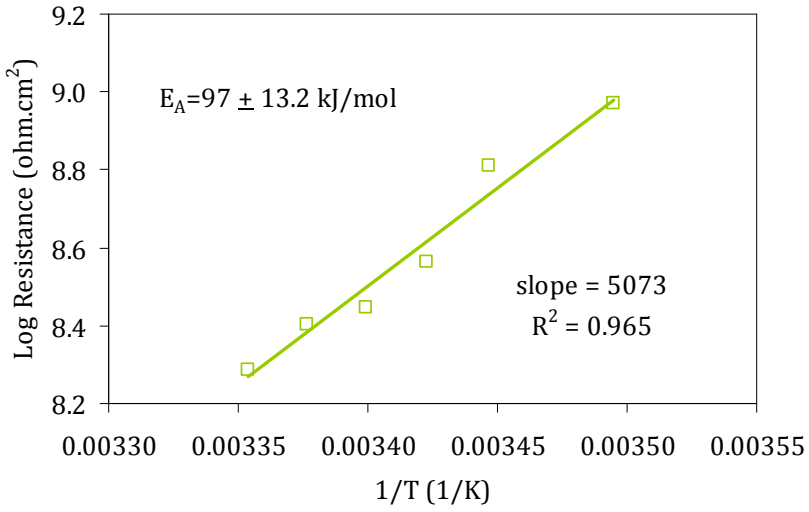

Figure 7.12- Arrhenius plot for free film exposed at 10°C in K^+, Na^+ and Li^+ solution

From **Figure 7.9**, it is obvious that free film exposed to K^+ solution generates the lowest activation energy of 67 $kJmol^{-1}$ and this is followed by free film exposed to Na^+ solution of 76 $kJmol^{-1}$. Free film exposed to Li^+ solution generates the highest activation energy of 85 $kJmol^{-1}$. All three values are substantially higher than the activation energies from film resistance on metal samples with the same coating (**Figure 4.64**).

Figure 7.10 shows typical EIS responses for freestanding film at various temperatures during exposure to K^+, Na^+ and Li^+ solution (cooled with ice). The semicircle decreases in sizes at higher temperature. Again the impedance spectra are fitted to fitting software (ZSimpWin) to determine the film resistance. However, again the semicircle cannot be fitted with one time constant**.** Thus an equivalent circuit with two time constants again was used for fitting, which showed a better agreement between the experimental data and the fit (**Figure 7.11)**.

The fitted parameters are summarized in **Tables 7.4** to **7.6**. Log (film resistance), R_2 is then plotted against 1/T. **Figure 7.12** displays a similar trend of activation energy to before with free film in K^+ solution generating the lowest value (66 $kJmol^{-1}$), followed by free film in Na^+ solution (73 $kJmol^{-1}$) and free film in Li^+ solution (97 $kJmol^{-1}$). These results are in agreement with the size of hydrated ionic radii (**Table 4.18**), where Li^+ has the biggest size followed by Na^+ and K^+. It is therefore likely that the largest cation, in this case Li^+, has the most difficulty in penetrating the film thus resulting in a higher activation energy value.

A summary of activation energy values generated from free film exposed at 40°C (mark with a red star) and 10°C in different cation solutions are presented in **Figure 7.13**. Notice that similar activation energy values are obtained, irrespective of whether the film is heated or cooled. It is interesting that the activation energy values gathered here (66–97 kJ/mol) are bigger than the activation energies determined from coating resistance for coated panels. Furthermore the activation energies generated by these free films are in the range of activation energies calculated from charge transfer resistance on those samples.

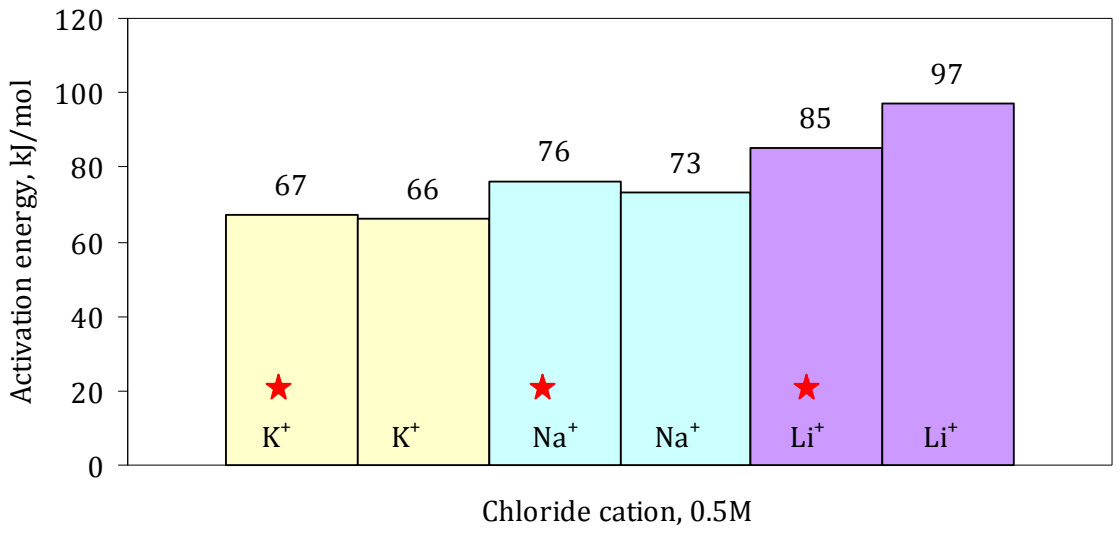

Figure 7.13 – Activation energy calculated for free film exposed in K^+, Na^+ and Li^+ solution

7.3.5 Behaviour of Free Film Exposed at Ambient Temperature and 50°C

Previous experiences on free films exposed at ambient temperature resulted in a relatively constant value of film resistance over an immersion period of days or even weeks [136, 177]. In this work, the film is exposed at both ambient temperature and 50°C immersion test.

Initially the free film was exposed at ambient temperature for 48 hours before taking the EIS measurement. Then the film was exposed at 50°C and after taking EIS measurement the film was left to cool at ambient temperature. The coating performance was monitored for a week. **Figure 7.14** shows the Nyquist plot which represent the impedance spectra at stages before and during exposure at 50°C and when the film was left to cool at ambient condition. Notice the drastic reduction in the semicircle size when the temperature is raised to 50°C. However when cooled to ambient temperature, the impedance rises close to the initial value. The spectrum was fitted with equivalent circuit R[RQ] and the fitted parameters are summarized in **Table 7.7**. It was observed that the film resistance dropped about two orders of magnitude when exposed at 50°C. Then it slowly rises up again to almost what it was after 168 hours at ambient condition. This is similar to the findings in **Section 4.3.7** for an attached film. However it is noticed that the free film recovers more slowly, more than 168 hours compared to an attached film which needed only 10 hours.

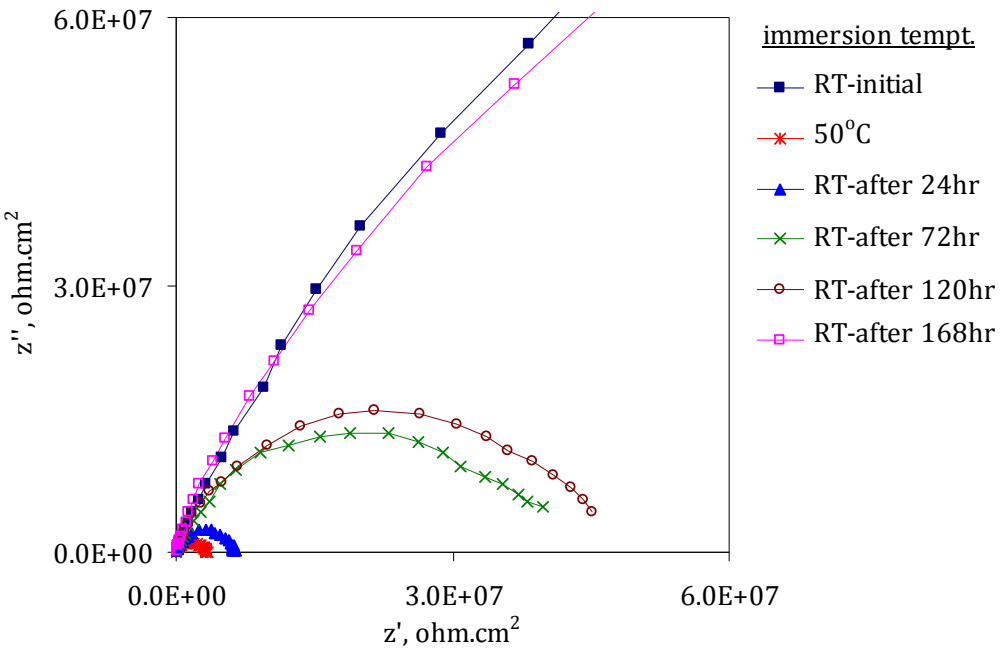

Figure 7.14 – Nyquist plot for free film after exposure at high temperature and left to cool at room temperature

Table 7.7 - Film resistance and capacitance data from fitting

Immersion temperature	Film resistance R_p (ohm.cm^2)	Film capacitance Q_c (F/cm^2)
RT-initial	3.87E+08	4.24E-10
50°C	3.24E+06	4.35E-10
RT-after 24hr	6.31E+06	2.76E-10
RT-after 72hr	3.83E+07	4.22E-10
RT-after 120hr	4.54E+07	3.78E-10
RT-after 168hr	2.80E+08	4.60E-10

7.4 Conclusions

- The resistance of epoxy-phenolic free standing films has been found to decrease very slowly with immersion time when the films were exposed at ambient temperature.

- The resistance of free films decreases with the increasing concentration of NaCl solution which indicates that the films behave as a D-type film.

- The impedance spectra in different metal cation shows one semicircle curve in the Nyquist plot but fitting with one time constant is not a good match; fitting with two time constants gives a much better fit.

- Activation energies calculated for free films exposed in different cations increase with the size of the hydrated ionic radii. Since Li^+ has the biggest size among them, Li^+ generates the highest activation energy (85–97 $kJmol^{-1}$) followed by Na^+ (73–76 $kJmol^{-1}$) and K^+ (66–67 $kJmol^{-1}$). These values are bigger than the activation energies determined from coating resistance for coated panels.

CHAPTER 8

IDENTIFICATION OF THE CONTROLLING MECHANISM FOR PROTECTION

8.1 Introduction

In the previous chapters, several coating systems on mild steel were exposed at 50°C and measured with electrochemical impedance spectroscopy (EIS) across a range of temperatures (25–50°C). EIS behaviour was fitted to a model circuit and changes in the coating resistance and charge transfer resistance with temperature were determined to deduce activation energies for the processes involved. The results showed that activation energies determined for ion conduction were lower than the values for the corrosion process which raises a question on whether it could possibly be ion conduction that is controlling the corrosion rate. Measurements of coating resistance on free films of the same coating generate systematically higher activation energy values for ion transport.

In this work, a potentiostatic pulse technique, PPT is adopted to monitor the current transient, which provides an alternative estimate of corrosion rate as a function of temperature and information on electrochemical processes on the metal substrate. Further EIS measurement to determine R_p yield another comparison of activation energy for ion conduction and the corrosion process as deduced in **Chapter 4** and **6**.

8.2 Experimental Details

In this work two different kinds of epoxy coatings were tested. They are a zinc rich full system (ZR-FS) and epoxy phenolic coating (1L-EP). Further information on the coatings has been described in **Table 3.1**. EIS measurements were conducted using a 3-electrode cell as described in **Section 3.3.2** and information on PPT can be found in **Section 3.5**.

8.3 Results and Discussion

8.3.1 Determination of iR-correction

The effect of uncompensated resistance is particularly important in transient studies, since the current/voltage curves are further distorted by alteration of the perturbation function. For instance, in potential step studies the actual potential drop across the interface may vary with time, even though the applied potential is constant, since the product iR is also a function of time (**Figure 8.1**).

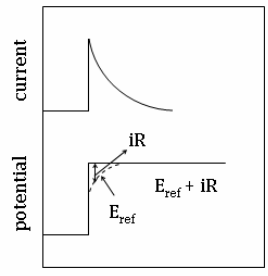

Figure 8.1 – Schematic representation of the effect of uncompensated resistance upon the potential/time profile of an electrode under potentiostatic control [180]

Table 8.1 – Data summarized for corrected potential-current transient

Column 1	Column 2	Column 3	Column 4	Column 5
E	ΔE	i(mA)	iR(mV)	ΔE, true
-529.95	100	6.05E-05	5.90E+01	-5.89E+02
-429.95	200	1.38E-04	1.34E+02	-5.64E+02
-329.95	300	2.19E-04	2.14E+02	-5.44E+02
-229.95	400	3.01E-04	2.93E+02	-5.23E+02
-129.95	500	3.87E-04	3.78E+02	-5.07E+02
-29.95	600	4.76E-04	4.64E+02	-4.94E+02

The corrected polarization curves are plotted on potential versus log current scale in **Figure 8.2**, which shows a more linear behaviour than the measured data. Extrapolation of the linear Tafel region E_{corr} would give i_{corr}.

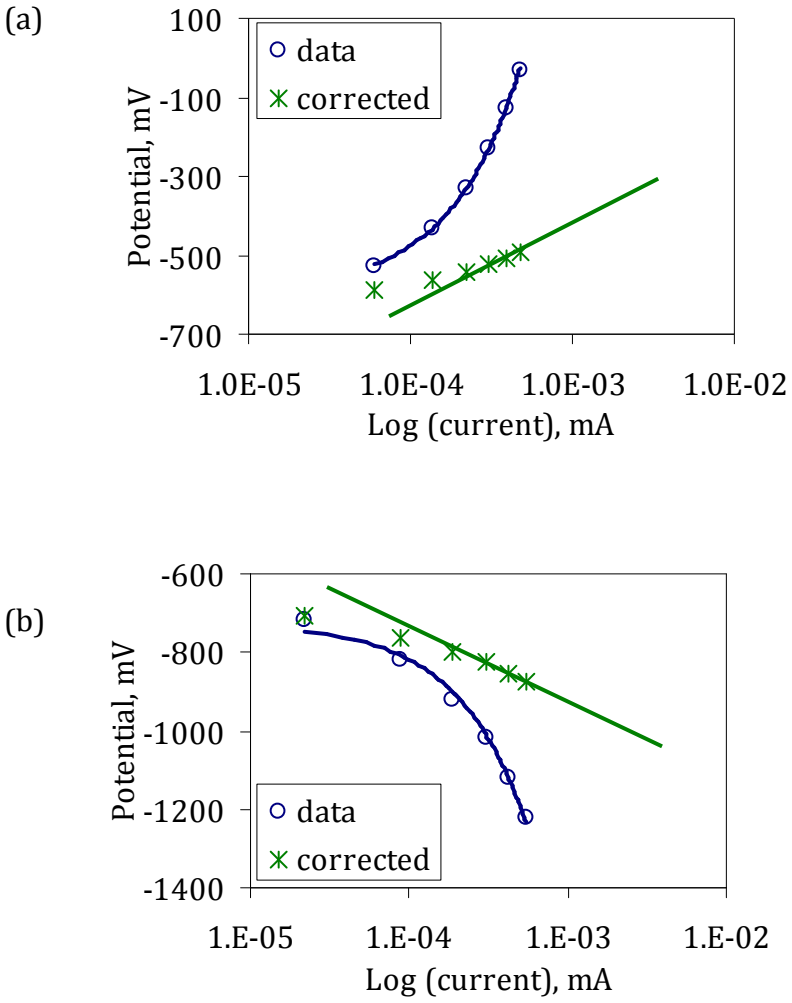

Figure 8.2 – Measured data and corrected potential-current transient for (a) anodic (b) cathodic polarization

8.3.2 Effect of Temperature on Coated Metal Measured with PPT

Figure 8.3 represents current transients at various temperatures when potential steps were applied. For both, i_{steady} is higher at high temperatures.

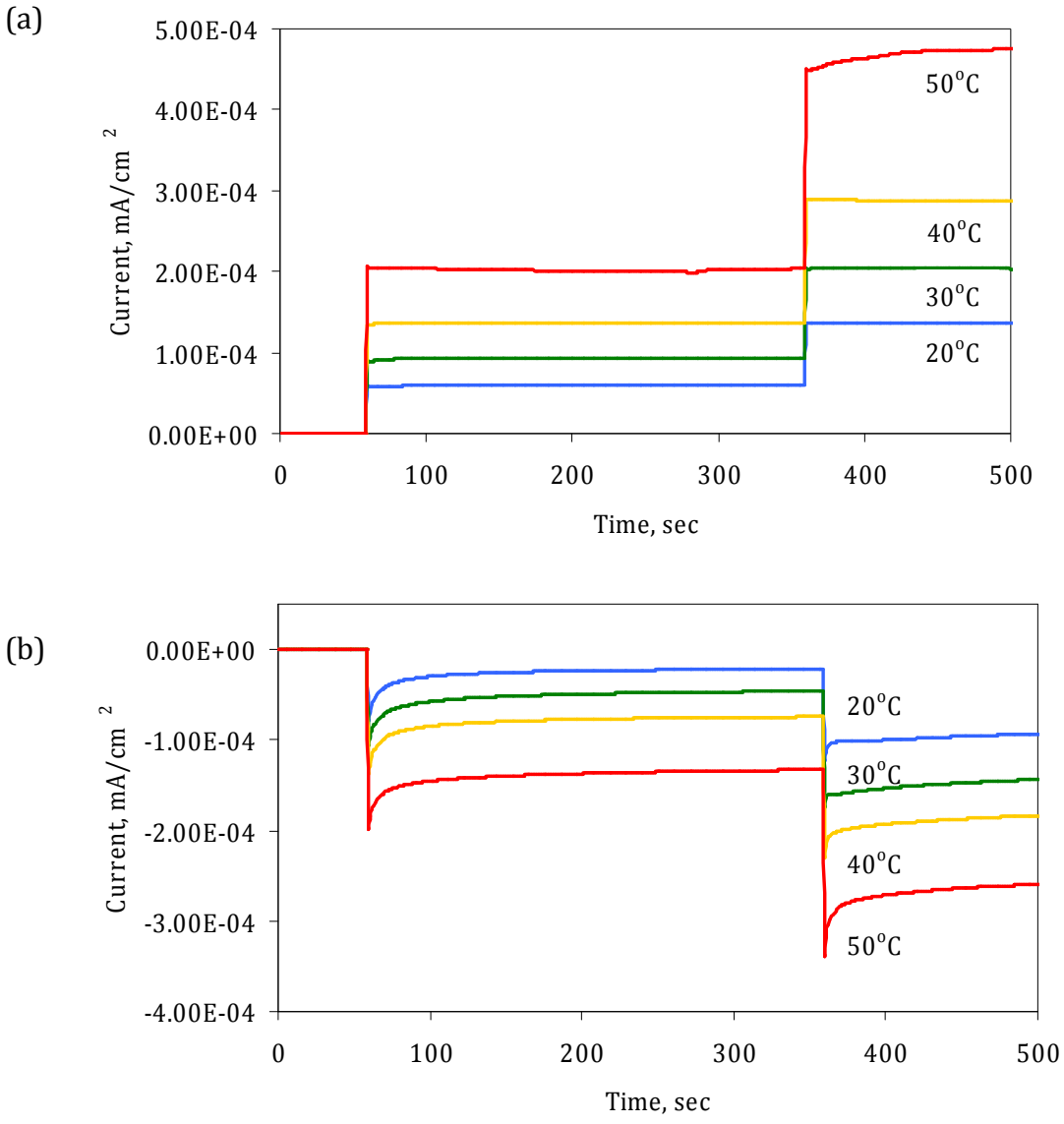

Figure 8.3 - The influence of temperature on current transient during (a) anodic (b) cathodic polarization

8.3.3 Effect of Temperature on ZR-FS Coating Measured with EIS

Figures 8.4 and **8.5** show impedance spectra recorded from the ZR-FS coated panel before the anodic and cathodic potentiostatic pulse measurements. Similar patterns were observed for both figures, where the radius of both semicircles in the Nyquist plot decreases with increasing temperatures. Notice the effect of temperature is more apparent on the low frequency semicircle.

To obtain the coating resistance, the impedance spectra was fitted to a fitting software, ZSimpWin with the model R[Q[R[QR]]]. The fitted parameters are listed in **Tables 8.2** and **8.3**. It was observed that coating and charge transfer resistance decreased with increasing of immersion temperature. As before logarithm of coating and charge transfer resistance are plotted against the reciprocal of temperature and the plots show linear behaviour (**Figures 8.6** and **8.7**). The activation energy determined for ion transport is 13–21 $kJmol^{-1}$ whereas for the corrosion process 50–51 $kJmol^{-1}$. It is clear that the activation energy for ion transport is very much lower than the activation energy for the corrosion process, so the effect of temperature on corrosion again cannot be explained by the change in film resistance. These finding is similar to the results gathered in **Figure 6.49**.

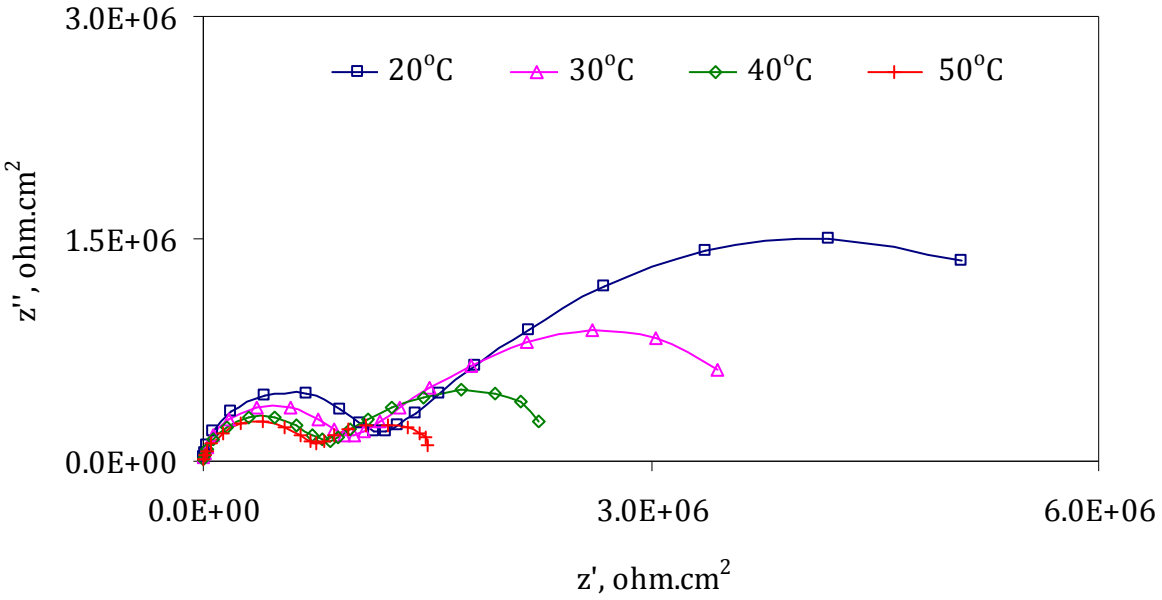

Figure 8.4– Nyquist plots for ZR-FS coating at various temperatures before anodic PPT

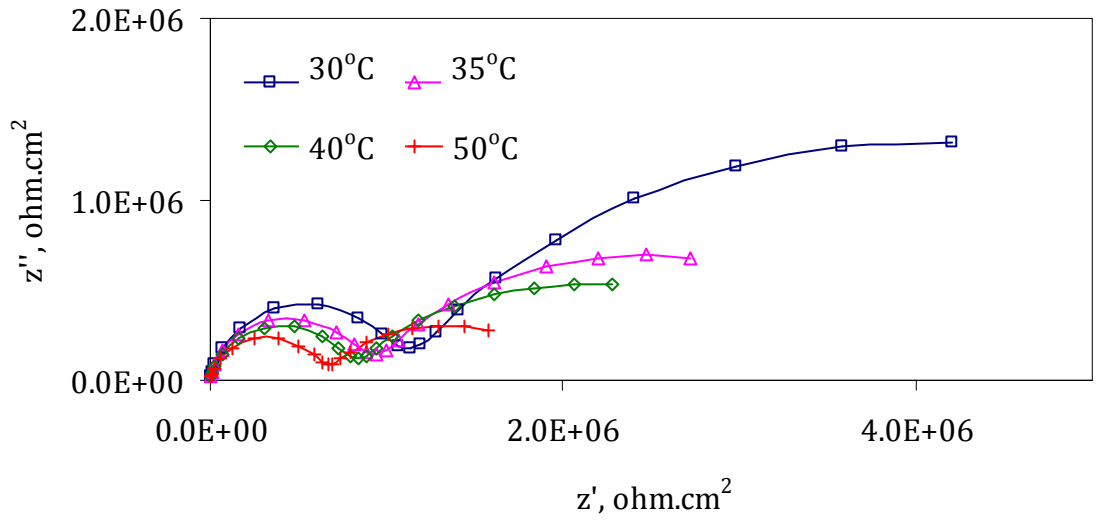

Figure 8.5– Nyquist plots for ZR-FS coating at various temperatures before cathodic PPT

Table 8.2– Parameters for ZR-FS coating from fitting of EIS result – anodic

Fitted circuit: R[Q[R[QR]]]

T (^oC)	Q_c ($Fcm^{-2})^n$	Q_c (%error)	n	R_p ($ohm.cm^2$)	R_p (%error)	Q_{dl} ($Fcm^{-2})^n$	Q_{dl} (%error)	n	R_{ct} ($ohm.cm^2$)	R_{ct} (%error)	X^2
20	6.68E-10	14.55	0.90	1.06E+06	3.89	4.84E-07	5.52	0.51	7.28E+06	16.11	2.47E+03
30	8.59E-10	15.21	0.89	8.66E+05	4.27	5.68E-07	6.68	0.49	3.99E+06	13.60	2.35E+03
40	1.18E-09	17.84	0.87	7.13E+05	5.61	6.49E-07	9.70	0.48	2.14E+06	13.71	2.75E+03
50	1.91E-09	17.96	0.84	6.57E+05	6.23	6.88E-07	14.55	0.50	1.05E+06	12.79	2.63E+03

Table 8.3 – Parameters for ZR-FS coating from fitting of EIS result – cathodic

Fitted circuit: R[Q[R[QR]]]

T (^oC)	Q_c ($Fcm^{-2})^n$	Q_c (%error)	n	R_p ($ohm.cm^2$)	R_p (%error)	Q_{dl} ($Fcm^{-2})^n$	Q_{dl} (%error)	n	R_{ct} ($ohm.cm^2$)	R_{ct} (%error)	X^2
30	9.08E-10	15.03	0.88	9.96E+05	4.11	5.82E-07	5.98	0.50	6.30E+06	18.14	2.66E+03
35	9.81E-10	17.97	0.88	7.95E+05	5.56	7.18E-07	8.38	0.45	3.55E+06	20.59	3.05E+03
40	1.21E-09	17.59	0.87	7.04E+05	5.87	8.86E-07	8.55	0.43	3.00E+06	23.28	2.63E+03
50	1.93E-09	17.40	0.84	5.82E+05	5.73	1.34E-06	10.03	0.43	1.71E+06	23.68	2.45E+03

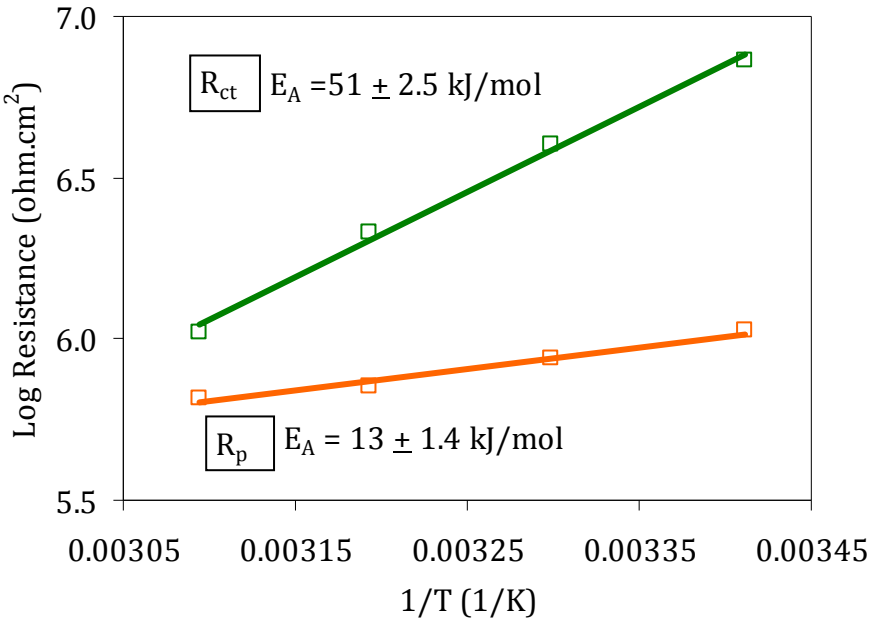

Figure 8.6 - Arrhenius plots of R_p and R_{ct} for ZR-FS coating before anodic PPT

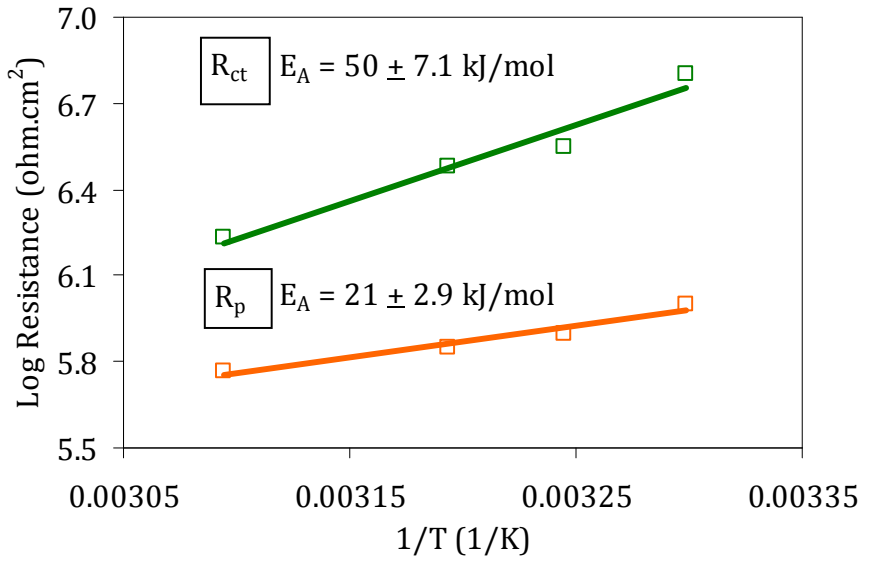

Figure 8.7- Arrhenius plots of R_p and R_{ct} for ZR-FS coating before cathodic PPT

8.3.4 Effect of Temperature on ZR-FS Coating Measured with PPT

The effect of temperature on the anodic and cathodic polarization after iR correction is presented in **Figure 8.8**. It can be seen that both anodic and cathodic curves are strongly affected by the temperature changes. The influence of temperatures changes is more evident on the cathodic curve (**Figure 8.8b**) where the cathodic current density becomes much larger as the temperature rises. The current density for each temperature is determined from the intersection of anodic and cathodic Tafel line and is listed in **Table 8.4**. Logarithm of current density is then plotted against reciprocal of temperature and a straight line indicates the parameter obeys the Arrhenius equation (**Figure 8.9**). The activation energy calculated from this plot is 43 ± 2.9 $kJmol^{-1}$.

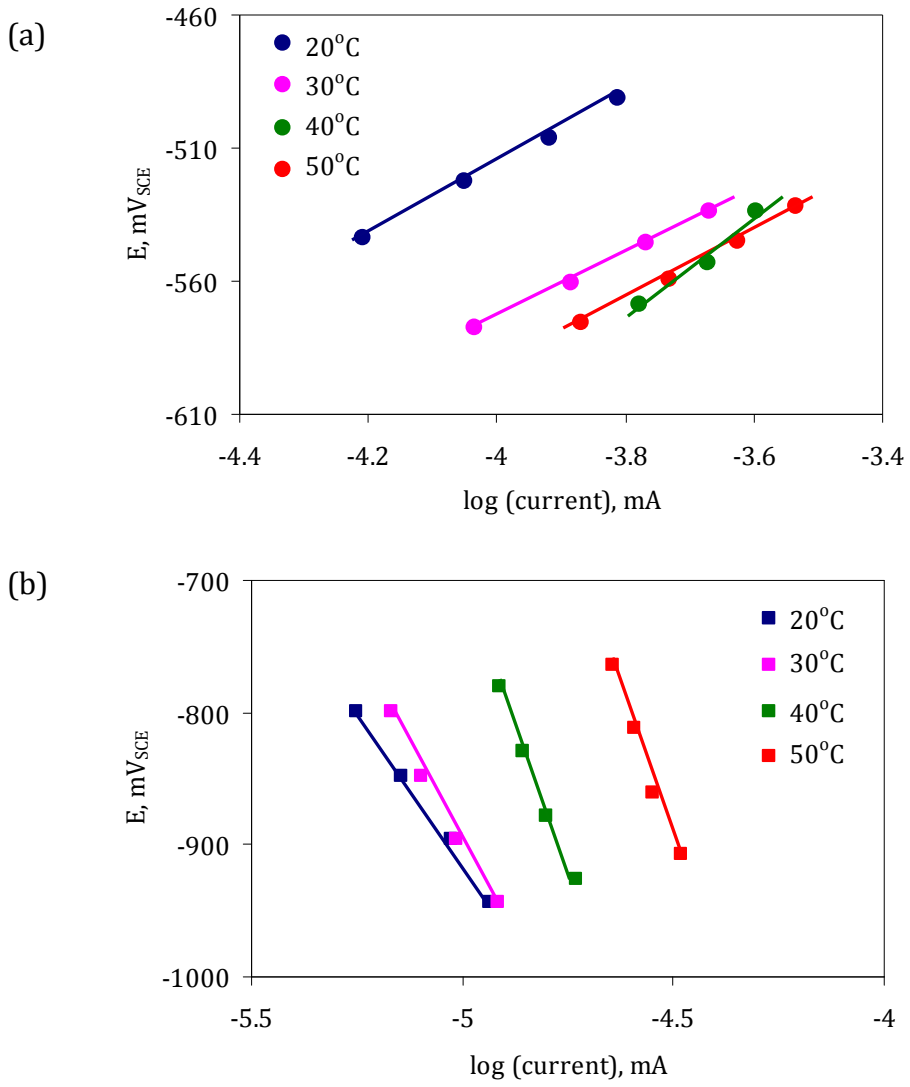

Figure 8.8 – Effect of temperature changes on (a) anodic (b) cathodic curves of ZR-FS coating

Table 8.4 Corrosion current for ZR-FS coating

Temperature, °C	Anodic		Cathodic		log i_{corr}, mA
	Slope	R^2	Slope	R^2	
20	130.86	0.99	429.25	0.99	-5.47
30	119.46	0.99	652.47	0.99	-5.28
40	124.45	0.99	882.43	0.99	-4.99
50	74.19	0.99	990.38	0.99	-4.77

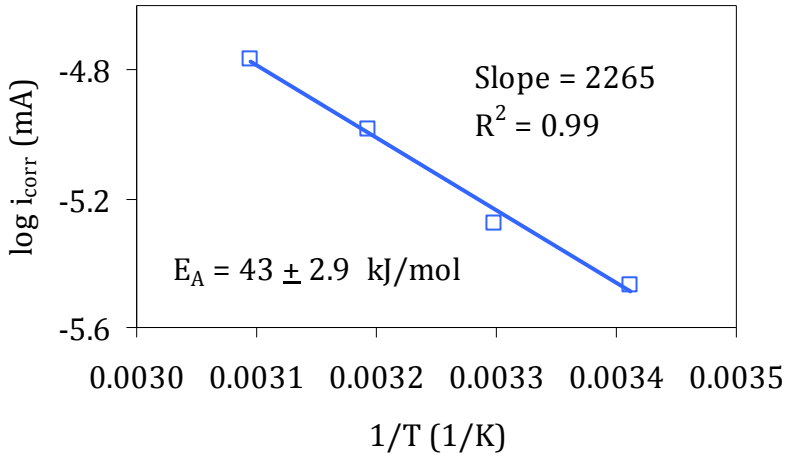

Figure 8.9 – Arrhenius plot calculated from anodic and cathodic Tafel line of ZR-FS coating

8.3.5 Effect of Temperature on 1L-EP Coating Measured with EIS Technique

In the impedance measurement, the result is expressed as a Nyquist plot at various immersion temperatures. **Figure 8.10** shows impedance spectra recorded from the 1L-EP coated panel before the anodic and cathodic potentiostatic pulse measurements. Notice the effect of temperature is more apparent on the low frequency semicircle. To obtain the coating resistance, the impedance spectra was fitted to a fitting software, ZSimpWin with the model R[Q[R[QR]]]. The fitted parameters are listed in **Table 8.5**. Logarithm of coating and charge transfer resistance is plotted against reciprocal of temperature and the plots show linear behaviour (**Figure 8.11**). The activation energy determined for ion transport (calculated from R_p) is 19 kJmol^{-1} and for the corrosion process (calculated from R_{ct}) is 34 kJmol^{-1}. These finding are similar to the results

gathered in **Table 4.6**, where the E_A for the corrosion process is significantly higher than E_A for ion transport.

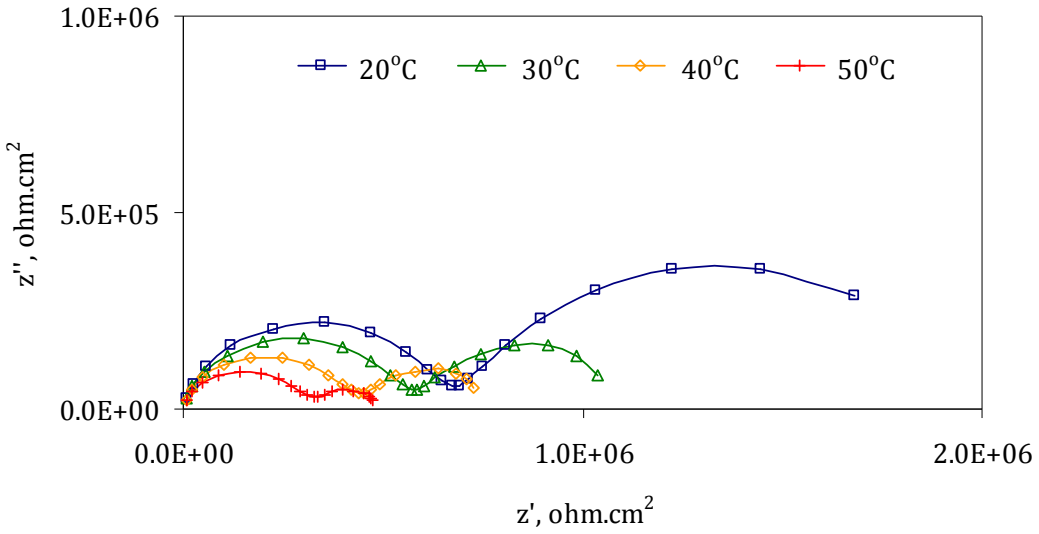

Figure 8.10– Nyquist plots for 1L-EP coating at various temperatures before PPT

Table 8.5 – Parameters for 1L-EP coated panel from fitting of EIS result

Fitted circuit: R[Q[R[QR]]]

T (^oC)	Q_c $(Fcm^{-2})^n$	Q_c (%error)	n	R_p ($ohm.cm^2$)	R_p (%error)	Q_{dl} $(Fcm^{-2})^n$	Q_{dl} (%error)	n	R_f ($ohm.cm^2$)	R_f (%error)	X^2
20	1.75E-09	18.66	0.80	7.00E+05	4.083	1.86E-06	11.65	0.57	2.20E+06	22.15	4.51E+03
30	2.24E-09	17.15	0.79	6.06E+05	4.459	2.26E-06	15.61	0.53	1.14E+06	20.89	3.12E+03
40	2.67E-09	20.16	0.78	4.61E+05	5.753	2.41E-06	18.62	0.49	8.87E+05	21.43	3.04E+03
50	3.24E-09	27.84	0.77	3.44E+05	23.91	2.08E-06	27.82	0.48	5.66E+05	23.91	3.19E+03

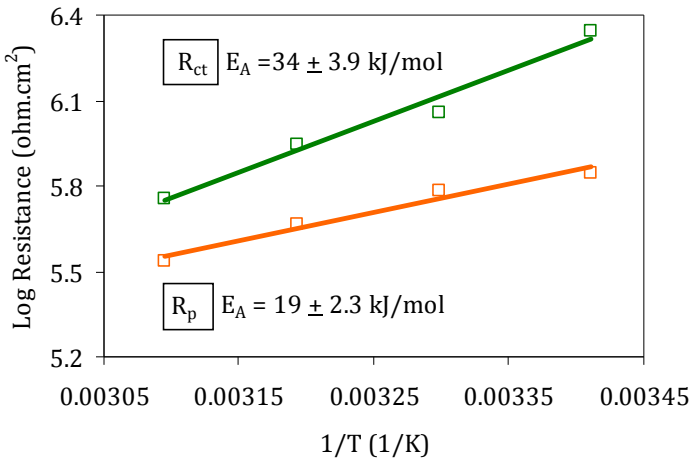

Figure 8.11 - Arrhenius plots of R_p and R_{ct} for 1L-EP coating before PPT

8.3.6 Effect of Temperature on 1L-EP Coating Measured with PPT

The effect of temperature on the anodic and cathodic polarization for 1L-EP coating after iR correction is presented in **Figure 8.12**. It can be seen that anodic curve is not strongly affected by the temperature changes (**Figure 8.12a**). The influence of temperature changes is more evident on the cathodic curve (**Figure 8.12b**) where the cathodic current density becomes larger as the temperature rises. Therefore data from the cathodic curves was analyzed further for generation of activation energy from the corrosion current density. The current density for each temperature was determined from the cathodic Tafel line at a fixed potential (E=-650mV) and is listed in **Table 8.6**. Logarithm of current density is then plotted against reciprocal of temperature and a straight line indicates the current obeys the Arrhenius Law (**Figure 8.13**). The activation energy calculated from this plot is 66 $\pm$ 2 $kJmol^{-1}$. This is much higher than

E_A for the film resistance and also higher than for that from R_{ct}. Increase in cathodic current generates smaller increase in i_{corr} because of the need to polarise the anode.

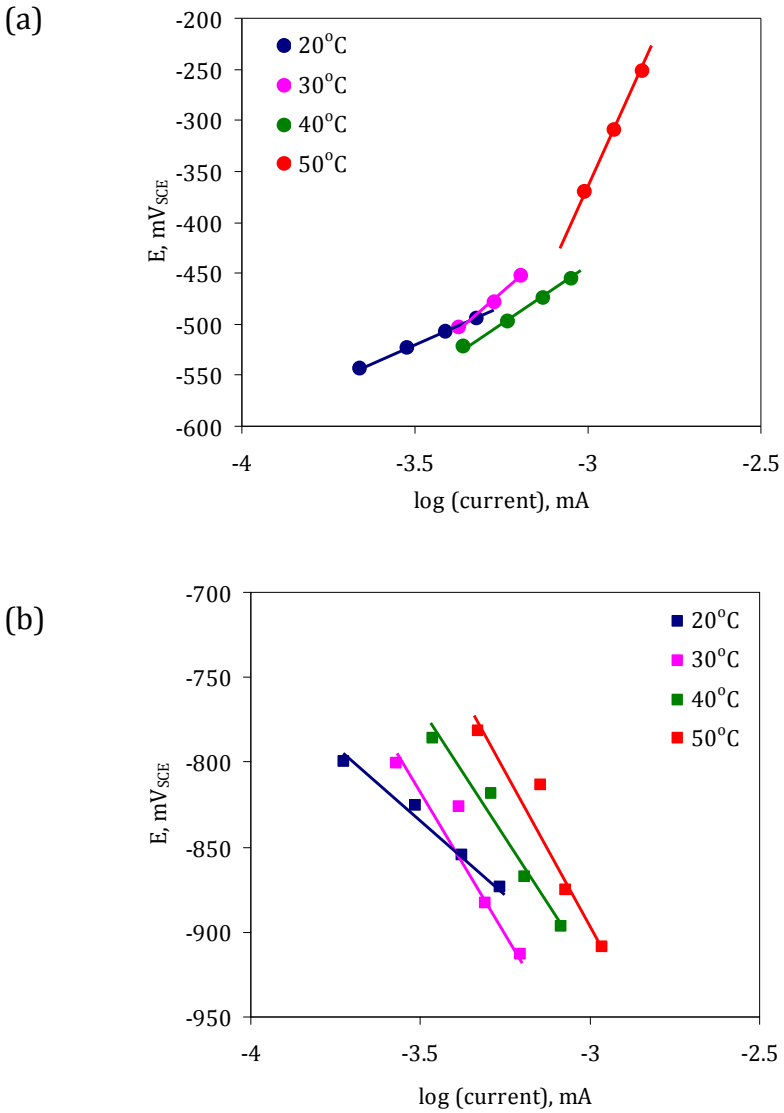

Figure 8.12– Effect of temperature changes on (a) anodic (b) cathodic curves of 1L-EP coating

Table 8.6 - Corrosion current determined from cathodic Tafel lines

Temperature, ^{o}C	Slope	R^2	log i_{corr}, mA
20	163.15	0.99	-5.06
30	317.19	0.91	-4.63
40	303.60	0.96	-4.30
50	356.74	0.91	-3.95

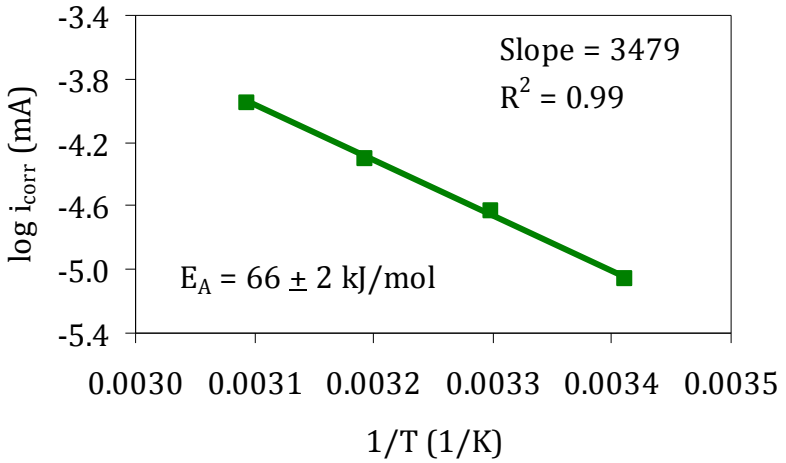

Figure 8.13 – Arrhenius plot calculated from cathodic Tafel lines

8.4 Summary

Two types of coating system have been tested to compare the activation energy generated from EIS and PPT tests. An overall summary of activation energies calculated from EIS test and PPT test is presented in **Table 8.7**. Notice that both E_A determined from EIS tests for the corrosion process (from R_{ct}) and from PPT tests are always higher than the E_A determined for ion transport (from R_p).

Table 8.7 – Activation energy determined from EIS and PPT test

Coating	EIS		PPT
	E_A, R_p (kJ/mol)	E_A, R_{ct} (kJ/mol)	E_A, i_{corr} (kJ/mol)
ZR-FS	13–21	50–51	43[a]
1L-EP	19	34	66[b]

[a]from i_{corr}
[b]from $i_{cathode}$

8.5 Conclusions

Measurement by PPT shows that the anode is less affected by the temperature changes than the cathode. E_A generated from the cathode gives higher activation energy than R_p and could accounts for the change in R_{ct}.

CHAPTER 9

CONCLUSIONS AND FURTHER WORK

This thesis has thrown new light into the significance of EIS measurements on coated metals. First, it will help to look at Mayne's model again on how paint protects metal from corrosion [19, 27, 29, 30]. Mayne suggested that paint coatings protect metal from corrosion by their high ionic resistance that limits ionic current flow from anode to cathode. When we look at this model, it seems unlikely that R_a and R_c will be the same and both will change over time as the coating degrades. Following Mayne's ideas on how coating protects metal as illustrated in **Figure 9.1**, the current has to pass through the coating at these two places in order for the corrosion process to occur.

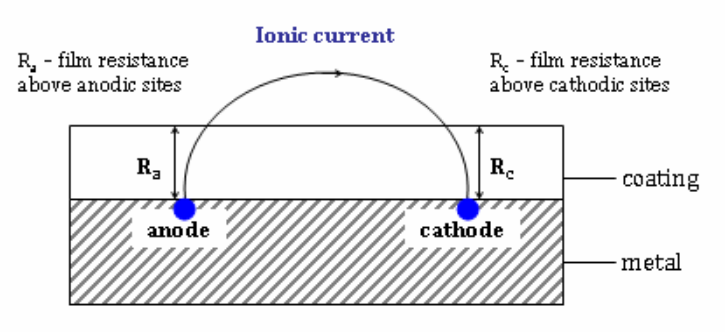

Figure 9.1 - Diagram illustrating Mayne's mechanism on how paint protect metal from corrosion through resistance inhibition

From **Chapter 4**, the Arrhenius plots of the temperature dependence for ion transport exhibited different values from the temperature dependence for the corrosion process

where the latter generates a significantly higher value (**Table 4.5**). This suggests that the coating resistance being measured here cannot be the factor controlling the corrosion rate. This raised a question then, what is controlling the corrosion rate? One option is still based on Mayne's resistance inhibition model where the current flows twice through the paint, where the lower resistance is being measured but actually the higher resistance is the one that is controlling the corrosion rate. In the EIS measurements R_a and R_c are in parallel, but in the corrosion cell they act in series.

Free film tests in **Chapter 7** showed that for an undegraded coating, film resistance remained high (**Figure 7.3**) and high activation energy is observed (**Figure 7.13**). This indicates that if the corrosion current returns through undegraded areas of coating of higher resistance, higher activation energy will be observed for R_{ct}. This also means that the lower resistance that is being measured doesn't tell whether the coating is still protective or not. Activation energy values for ion conduction in 'good' regions of the coating might well be intermediate between values characteristic of the pristine free film and the degraded areas of coating.

Another possibility is that the kinetic reaction on the electrode could be controlling the corrosion rate. In **Chapter 8**, the potentiostatic pulse technique (PPT) was used to investigate how the kinetics of the reaction on the electrode varies with temperature. The result shows that the anode is less affected by the temperature changes than the cathode. E_A generated from i_{corr} and $i_{cathode}$ measured by PPT give higher E_A than R_p and could account for the change in R_{ct} (**Table 8.7**).

In **Chapter 4**, the temperature dependence for conduction in the coating through cation mobility for a coated panel does not correlate with its hydrated ionic radii (**Table 4.16** and **4.17**). It was expected that a bigger cation (Li^+) will generate a bigger E_A, due to its difficulty to penetrate the coating at the cathode. The result on epoxy-phenolic coated panel proved otherwise that the E_A generated from this study seems to go down with size (**Figure 4.63**). However different findings arose from tests on epoxy-phenolic free film (**Figure 7.13**) where the results are in agreement with the size of the hydrated cation. For the results with a coated panel in different cations, it should be noted that we cannot tell if R_a or R_c (the film resistance at anode or cathode) is being measured. It is not expected that cations will penetrate at the anode. Even for R_c, it can be suggested that the penetration of cations through the coating at the cathode region has less effect than the more mobile anion i.e. OH^- generated by oxygen reduction.

In **Chapter 5**, a real coating system; multilayer coatings with inhibitive pigment i.e. zinc phosphate, in the primer were tested in high temperature immersion. This is to investigate whether the conclusion derived from **Chapter 4** where film resistance measured by EIS is not linked to the corrosion process, also applied with a real coating system. However findings from this test were unable to distinguish for certain between the coating resistance and the impedance of the corrosion reaction at the interface (only one semicircle is presence in the impedance spectra). Therefore it is unable to establish for certain any link between them for a zinc phosphate full system coating. However the activation energies generated from the second time constant in this test are larger (**Table 5.8**) than that for thinner coatings (**Table 4.5**), in agreement with

Ochs and Vogelsang [160]. The activation energies generated from this test are very much higher (44–191 $kJmol^{-1}$) than normally obtained for transport of ion in polymer coating (14–30 $kJmol^{-1}$), and is most likely to be related to the corrosion process.

Another type of real coating system, a multilayer coating with sacrificial pigment i.e. zinc-rich paint as the primer, was also tested in high temperature immersion. In contrast with the zinc phosphate full system, zinc-rich full system gave the same conclusion as the thinner coatings where the film resistance from EIS cannot be controlling the corrosion reaction. The activation energies generated for the corrosion process here (78–97 $kJmol^{-1}$) are very much higher than those of ion transport through the coating (19–37 $kJmol^{-1}$) during early immersion (**Figure 6.49** and **6.50**).

Further interesting findings come from the activation energy trends over time particularly for the corrosion process where the value is decreasing (**Figure 6.49** and **6.50**), so that at the end of exposure the values for R_p and R_{ct} become quite similar. It is suggested that at this stage ion transport in the coating might be controlling the corrosion process unlike at the beginning; the activation energy is getting smaller due to coating degradation. We can no longer distinguish different E_A values for conduction and corrosion.

Exposing the coated panel in high temperature immersion did speed up the coating failure and was particularly beneficial for thicker multilayer coatings. A separate test was conducted where the coated panel has been exposed to a heating and cooling test. The results show that water absorbed on heating recovers slowly after cooling.

However this only occurs if adequate time is allowed for the water to desorb from the coating.

The area underneath the blister formed on coated panel immersed in sodium chloride solution has been studied using a scanning Kelvin probe (SKP). In a solution containing Na^+ ions, cathodic reduction of oxygen generates an alkaline environment therefore cathodic blistering would be expected to occur preferentially underneath the blister. True to the expectation, SKP potential map shows that blister has formed at a cathode due to alkali but anodes form nearby (not remote). It is suggested that the blister has been overlapped by the anode around the edges as the area underneath the blister reveals a bright metal surface.

Scanning by Kelvin probe on a blister forming on a coated panel immersed in ammonium chloride solution shows the pattern of electrochemical activity in the blister is quite complex with both cathodic and anodic areas. It is suggested that there is a possibility that this cathodic region may start as an anode initially but corrosion products become the cathode reactant [149, 169].

Regarding further work there is scope for additional study in the following areas;

- The solution used in this study is mostly 3% sodium chloride which is more appropriate indication for a coated metal performance in a marine environment. Use of dilute Harrison solution (3.25% ammonium sulphate,

0.25% sodium chloride in distilled water) is more suitable for investigating the protection mechanism of a coated metal used in an industrial environment.

- It is also beneficial to carry out control experiments using a primer without an active inhibitive pigment as the full system, since experiments where the primer contains of an inhibitive pigment generate small values of R_p and large values of R_{ct}. This may help to understand better the role of zinc phosphate pigments as the primer.

- The investigations on a full system consisting of 3-layer coatings with sacrificial pigments as the primer should be extended to a 2-layer coatings where only the middle and top coating are applied on the metal substrate to compare with the zinc rich full system. This test may give a greater insight into the role of zinc rich paint as the primer.

- Further tests using the potentiostatic pulse technique on zinc phosphate pigmented primer vs. control experiment (primer without zinc phosphate) would be good to investigate the effect of temperature on the cathode in this case. This may give a better indication whether zinc phosphate is actively acting as the cathodic inhibitor underneath the intermediate coating during immersion at high temperature as the charge transfer resistance measured in this work is high.

References

1. G.W. Walter, *The Application of impedance methods to study the effects of water uptake and chloride ion concentration on the degradation of paint films - II. Free films and attached/free film comparisons.* Corrosion Science, 1991. 32(10): p. 1085-1103.

2. J. Titz, G.H. Wanger, H. Spahn, M. Ebert, K. Juttner, W.J. Lorenz, *Characterization of organic coatings on metal substrates by electrochemical impedance spectroscopy.* Corrosion, 1990. 46(3): p. 221.

3. M.G. Fontana, *Corrosion engineering.* 3rd Edition McGraw-Hill, New York, NY, 1986.

4. G.H. Koch, M.O.H. Bronngers, N.G. Thompson, Y.P. Virmani, J.H. Payer, *Corrosion cost and preventive strategies in the United States.* U.S. Department of Transportation, 2001.

5. P.A. Schweitzer, *Corrosion and corrosion protection handbook.* New York : M. Dekker, 1988.

6. D.A. Jones, *Principles and prevention of corrosion.* 2nd Edition, Macmillan Publishing Co., New York, NY, 1996.

7. H. Leidheiser, *Corrosion of painted metal - A review.* Corrosion 1982. 38(7): p. 374-383.

8. P. Marcus, J. Oudar, *Corrosion mechanisms in theory and practice.* Marcel Dekker, Inc, 1995.

9. P.A. Schweitzer, *Corrosion resistant linings and practice.* New York : M. Dekker, 2001.

10. J. Bently, *Organic film formers.* in paint and surface coating : Theory and practice, R. Lambourne, editor(s), Ellis Horwood Limited, Chichester, U.K., 1987.

11. R.W. Revie, *Uhlig's corrosion handbook.* John Wiley & Sons, 2000.

12. H.H. Uhlig, R.W. Revie, *Corrosion and corrosion control.* John Wiley & Sons, 1985.

13. R.A. Jeffs, W. Jones, *Additives for paint, in* paint and surface coatings: Theory and practice, R. Lambourne, editor(s), Ellis Horwood Limited, Chichester, U.K., 1987.

14. A. Forsgren, *Corrosion control through organic coatings.* CRC, Taylor & Francis, 2006.

15. J.H.W.d. Wit, *Inorganic and organic coatings.* in Corrosion Mechanisms in Theory and Practice, Marcus, P. and Oudar, J., Marcel Dekker, New York, NY, 594, 1995.

16. J.E.O. Mayne, *The mechanism of the protective action of paints.* in Corrosion Control Volume 2, L.L. Shreir, editor(s), Butterworth-Heinemann Ltd 1994.

17. G.W. Walter, *A critical review of the protection of metals by paints.* Corrosion Science, 1986. 26(1): p. 27-38.

18. G. Grundmeier, W. Schmidt, M. Stratmann, *Corrosion protection by organic coatings: Electrochemical mechanism and novel methods of investigation.* Electrochimica Acta, 2000. 45(15-16): p. 2515-2533.

19. J.E.O. Mayne, *The mechanism of the inhibition of the corrosion of iron and steel by means of paint.* Official Digest 1952. 24: p. 127.

20. H. Haagen, W. Funke, *Prediction of the corrosive protective properties of paint films by permeability data.* Journal of the Oil and Colour Chemists' Association, 1975. 58: p. 359 - 364.

21. M. Stratmann, R. Feser, A. Leng, *Corrosion protection by organic films.* Electrochimica Acta, 1994. 39(8-9): p. 1207-1214.

22. S. Guruviah, *The relationship between the permeation of oxygen and water through paint films and corrosion of painted mild steel.* Journal of the Oil and Colour Chemists' Association, 1970. 53: p. 669-679.

23. M. Morcillo, L. Hernandez, S. Feliu, S. Gimenez, *Underfilm corrosion of steel induced by saline contaminants at the metal/paint surface.* Journal of the Oil and Colour Chemists' Association, 1990. 73(1): p. 24 - 30.

24. R.C. Bacon, J.J. Smith, F.M. Rugg, *Electrolytic resistance in evaluating protective merit of coatings on metals.* Ind. Eng. Chem., 1948. 40(1): p. 161-167.

25. R.T. Ruggeri, T.R. Beck, *The transport properties of polyurethane paint* in Corrosion Control by Organic Coating, H. Leidheiser, editor(s) p 62, NACE, Houston, TX, 1981.

26. W.W. Kittelberger, A.C. Elm, *Diffusion of sodium chloride through various paint systems.* Ind. Eng. Chem., 1952. 44(2): p. 326-329.

27. J.E.O. Mayne, *Current view on how paint film prevent corrosion.* Journal of the Oil and Colour Chemists' Association, 1957. 40: p. 183-195.

28. W.W. Kittelberger, A.C. Elm, *Water immersion testing of metal protective paints.* Ind. Eng. Chem., 1947. 39(7): p. 876-881.

29. J.E.O. Mayne, *Paints for the protection of steel - A review of research into their modes of action.* British Corrosion Journal, 1970. 5.

30. J.E.O. Mayne, *The mechanism of the protection of iron and steel by paint.* Anti-Corrosion Methods and Materials, 1973. 20(10): p. 3-8.

31. C.C. Maitland, J.E.O. Mayne, *Factors affecting the electrolytic resistance of polymer film.* Official Digest, 1962. 34: p. 972-991.

32. B.W. Cherry, J.E.O. Mayne, *The interaction of divalent ions with varnish membranes.* Official Digest, 1965. 37: p. 13-27.

33. E.M. Kinsella, J.E.O. Mayne, *Ionic conduction in polymer films I. Influence of electrolyte on resistance.* British Polymer Journal, 1969. 1(4): p. 173-176.

34. A. Amirudin, D. Thieny, *Application of electrochemical impedance spectroscopy to study the degradation of polymer-coated metals.* Progress in Organic Coatings, 1995. 26(1): p. 1-28.

35. J.E.O. Mayne, D.J. Mills, *The effect of the substrate on the electrical resistance of polymer films.* Journal of the Oil and Colour Chemists' Association, 1975. 58: p. 155-159.

36. M. Kendig, J.Scully, *Basic aspects of electrochemical impedance application for the life prediction of organic coatings on metals.* Corrosion NACE, 1990. 46(1): p. 22-29.

37. G.W. Walter, *A review of impedance plot methods used for corrosion performance analysis of painted metals.* Corrosion Science, 1986. 26(9): p. 681-703.

38. J.E.O. Mayne, J.D. Scantlebury, *Ionic conduction in polymer films: II. Inhomogeneous structure of varnish films.* British Polymer Journal, 1970. 2(4): p. 240-243.

39. H. Corti, R. Fernández-Prini, D. Gómez, *Protective organic coatings: Membrane properties and performance.* Progress in Organic Coatings, 1982. 10(1): p. 5-33.

40. E.P.M. van Westing, *Determination of coating performance with impedance measurements.* DPhil Thesis, Delft University of Technology, 1992.

41. M.A. Hernández, F. Galliano, D. Landolt, *Mechanism of cathodic delamination control of zinc-aluminum phosphate pigment in waterborne coatings.* Corrosion Science, 2004. 46(9): p. 2281-2300.

42. A. Amirudin, C. Barreau, R. Hellouin, D. Thierry, *Evaluation of anti-corrosive pigments by pigment extract studies, atmospheric exposure and electrochemical impedance spectroscopy.* Progress in Organic Coatings, 1995. 25(4): p. 339-355.

43. J. Sinko, *Challenges of chromate inhibitor pigments replacement in organic coatings.* Progress in Organic Coatings, 2001. 42(3-4): p. 267-282.

44. S. Turgoose, Symposium on Anticorrosive Pigments, Binders & Paints, Paint Research Association, 1987.

45. M. Mahdavian, M.M. Attar, *Another approach in analysis of paint coatings with EIS measurement - Phase angle at high frequencies.* Corrosion Science, 2006. 48(12): p. 4152-4157.

46. B. del Amo, R. Romagnoli, V.F. Vetere, L.S. Hernández, *Study of the anticorrosive properties of zinc phosphate in vinyl paints.* Progress in Organic Coatings, 1998. 33(1): p. 28-35.

47. A. Kalendova, *Comparison of the efficiencies of anticorrosivepigments based on phosphates.* Pigment & Resin Technology, 2002. 31(6): p. 381.

48. J.D. Poindexter, *Corrosion: Fundamentals, testing, and protection.* ASM Handbook. Vol. 13A. 2003: ASM International.

49. J.A. Burkill, J.E.O. Mayne, *The limitation of zinc phosphate as an inhibitive pigment.* Journal of the Oil and Colour Chemists' Association, 1988. 71: p. 273.

50. R. Romagnoli, V.F. Vetere, *Heterogeneous reaction between steel and zinc phosphate.* Corrosion NACE, 1995. 51(2).

51. H. Leidheiser, *Mechanism of corrosion inhibition with special attention to inhibitors in organic coatings.* Journal of Coating Technology, 1981. 53(678): p. 29-39.

52. M.F. Clay, J.H. Cox, Journal of the Oil and Colour Chemists' Association, 1973. 56(13).

53. Z. Szklarsa-Smialowska, J. Mankowsky, British Corrosion Journal, 1969. 4(9): p. 271.

54. S. Turgoose, M. Hazza, Y.J. Qian, U.K. Corrosion' 86 Inst. Corr. Sci & Tech, 1986.

55. Pedro de Lima-Neto, A.P. de Araújo, W.S. Araújo, A.N. Correia, *Study of the anticorrosive behaviour of epoxy binders containing non-toxic inorganic corrosion inhibitor pigments.* Progress in Organic Coatings, 2008. 62(3): p. 344-350.

56. M. Beiro, A. Collazo, M. Izquierdo, X.R. Nóvoa, C. Pérez, *Characterisation of barrier properties of organic paints: the zinc phosphate effectiveness.* Progress in Organic Coatings, 2003. 46(2): p. 97-106.

57. M. Mahdavian, M.M. Attar, *Evaluation of zinc phosphate and zinc chromate effectiveness via AC and DC methods.* Progress in Organic Coatings, 2005. 53(3): p. 191-194.

58. R. Romagnoli, V.F. Vetere, *Non-pollutant corrosion inhibitive pigments: zinc-phosphate, a review* Corrosion Review, 1995. 13(1): p. 45-64.

59. M. Zubielewicz, W. Gnot, *Mechanisms of non-toxic anticorrosive pigments in organic waterborne coatings.* Progress in Organic Coatings, 2004. 49(4): p. 358-371.

60. J. S. Feliu, M. Morcillo, S. Feliu, *Deterioration of cathodic protection action of zinc-rich paint coatings in atmospheric exposure.* Corrosion, 2001. 57(7): p. 591-597.

61. J. Sebastian Feliu, R. Barajas, J.M. Bastidas, M. Morcillo, S. Felliu, *Study of protection mechanism of zinc rich paints by electrochemical impedance spectroscopy.* Electrochemical Impedance: Analysis and Interpretation, ASTM STP 1188, J.R. Scully, D.C. Silverman and M.W. Kending (eds) American Society for Testing and Materials, Philadelphia, 1993: p. 438-449.

62. J. S. Feliu, M. Morcillo, J.M. Bastidas, S. Feliu, *Evolution of the protective mechanisms of zinc rich paints during atmospheric exposure.* Journal of Coatings Technology, 1993. 65(826): p. 43-48.

63. R.A. Armas, C.A. Gervasi, A.D. Sarli, S.G. Real, J.R. Vilche, *Zinc-rich paints on steel in artificial seawater by electrochemical impedance spectroscopy.* Corrosion, 1992. 48(5): p. 379-383.

64. C.A. Gervasi, A.R. Di Sarli, E. Cavalcanti, O. Ferraz, E.C. Bucharsky, S.G. Real, J.R. Vilche, *The corrosion protection of steel in sea water using zinc-rich alkyd paints. An assessment of the pigment-content effect by EIS.* Corrosion Science, 1994. 36(12): p. 1963-1972.

65. A. Meroufel, S. Touzain, *EIS characterisation of new zinc-rich powder coatings.* Progress in Organic Coatings, 2007. 59(3): p. 197-205.

66. S. Feliu, Barajas, R., Bastidas, J.M., Morcillo, M., *Mechanism of cathodic protection of zinc-rich paints by electrochemical impedance spectroscopy. I. Galvanic stage.* Journal of Coatings Technology, 1989. 61(775): p. 63-69.

67. T.K. Ross, J. Wolstenholme, *Anti-corrosion properties of zinc dust paints.* Corrosion Science, 1977. 17(4): p. 341-351.

68. C.M. Abreu, M. Izquierdo, M. Keddam, X.R. Nóvoa, H. Takenouti, *Electrochemical behaviour of zinc-rich epoxy paints in 3% NaCl solution.* Electrochimica Acta, 1996. 41(15): p. 2405-2415.

69. H. Marchebois, M. Keddam, C. Savall, J. Bernard, S. Touzain, *Zinc-rich powder coatings characterisation in artificial sea water: EIS analysis of the galvanic action.* Electrochimica Acta, 2004. 49(11): p. 1719-1729.

70. S. González, V. Fox, S. R.M., *Laboratory evaluation of corrosion resistance at metallic substrates by an organic coating: delamination effects.* Journal of Adhesion Science and Technology, 2004. 18: p. 455-464.

71. W.M.Bos, *Prediction of coating durability - Early detection using electrochemical methods*. 2008: PhD Thesis, Delft Technology University.

72. H. Undrum, *Silicate and epoxy zinc primers: A review.* Journal of Protective Coatings and Linings, 2006: p. 52-57.

73. H. Leidheiser, W. Funke, *Water disbondment and wet adhesion of organic coatings on metals: A review and interpretation.* Journal of the Oil and Colour Chemists' Association, 1987. 70: p. 121.

74. W. Funke, *Letter to editor 'Wet Adhesion'.* Journal of the Oil and Colour Chemists' Association, 1986. 69: p. 78-79.

75. E. Koehler, *Underfilm corrosion currents as the cause of failure of protective organic coatings.* in Corrosion Control by Organic Coating, H. Leidheiser, editor(s) p 87, NACE, Houston, TX, 1981.

76. P. Walker, *Letter to editor 'Wet Adhesion'.* Journal of the Oil and Colour Chemists' Association, 1985. 68: p. 319.

77. W. Schwenk, *Adhesion loss of organic coatings causes and consequences for corrosion protection.* in corrosion control by organic coating, H. Leidheiser, editor(s) p103, NACE, Houston, TX, 1981.

78. K.R. Gowers, J.D. Scantlebury, *The influence on corrosion of the adhesion of a coating to a metal substrate.* Journal of the Oil and Colour Chemists' Association, 1987. 70: p. 64.

79. T. Nguyen, J.B. Hubbard, *Unified model for the degradation of organic coatings on steel in a neutral electrolyte.* Journal of Coatings Technology, 1996. 68(855).

80. D. Greenfield, D. Scantlebury, *The protective action of organic coating on steel: A review.* JCSE The Journal of Corrosion Science and Engineering, 2000. 3(5).

81. Z. Ahmad, *Principles of corrosion engineering and corrosion control.* Butterworth-Heinemann Ltd, 2006.

82. W. Funke, *Blistering of paint films and filiform corrosion.* Progress in Organic Coatings 1981. 9(1): p. 29 - 46.

83. J.E.O. Mayne, *The problem of painting steel.* Journal of Applied Chemistry, 1959. 9: p. 673-680.

84. E.L. Koehler, *The influence of contaminants on the failure of protective organic coatings on steel.* Corrosion, 1977. 33(6): p. 209.

85. M. Morcillo, *Soluble salts: Their effect on premature degradation of anticorrosive paints.* Progress in Organic Coatings, 1999. 36: p. 137-147.

86. J. Crossen, *Adhesion of organic coating and corrosion protection.* DPhil Thesis, University of Oxford 1997.

87. W. Funke, *Toward a unified view of the mechanism responsible for paint defects by metallic corrosion.* Ind. Eng. Chem. Prod. Res. Dev., 1985. 24(3): p. 343-347.

88. J.H.W.d. Wit, H.J.W. Lenderink, J.H.v.d. Weijde, E.P.M.v. Westing, *Mechanisms for delamination of organic coatings.* Materials Institute Delft, Delft University of Technology.

89. S. Brunner, R. Richner, U. Muller, O. Guseva, *Accelerated weathering device for service life prediction for organic coatings.* Polymer Testing, 2005. 24: p. 25-31.

90. J.W. Martin, T. Nguyen, E. Byrd, B. Dickens, N. Embree, *Relating laboratory and outdoor exposures of acrylic mealmine coatings - I. Cummulative damage model and laboratory exposure apparatus.* Polymer Degradation and Stability, 2002. 75: p. 193-210.

91. L. Fedrizzi, A. Bergo, F. Deflorian, L. Valentinelli, *Assessment of protective properties of organic coatings by thermal cycling.* Progress in Organic Coatings, 2003. 48(2-4): p. 271-280.

92. B.R. Appleman, *Survey of accelerated test methods for anti-corrosive coating performance.* Journal of Coating Technology, 1990. 67: p. 57-67.

93. O.Guseva, S. Brunner, P.Richner, *Service life prediction for aircraft coatings.* Polymer Degradation and Stability, 2003. 82: p. 1-13.

94. G.P. Bierwagen, L. He, J. Li, L. Ellingson, D.E. Tallman, *Studies of a new accelerated evaluation method for coating corrosion resistance - thermal cycling testing.* Progress in Organic Coatings, 2000. 39(1): p. 67-78.

95. G. Bierwagen, D. Tallman, J. Li, L. He, C. Jeffcoate, *EIS studies of coated metals in accelerated exposure.* Progress in Organic Coatings, 2003. 46(2): p. 149-158.

96. J.B. Harrison, T.C.K. Tickle, *New aspects of the atmospheric corrosion of steel and their implications.* Journal of the Oil and Colour Chemists' Association, 1962. 45(8): p. 571.

97. J.B. Harrison, *The realistic prediction of primer peformance-a case history.* Journal of the Oil and Colour Chemists' Association, 1979. 62: p. 18.

98. F.D. Timmins, *Avoiding paint failures by prohesion.* Journal of the Oil and Colour Chemists' Association, 1979. 62: p. 131.

99. I. N.Levine, *Physical chemistry*. 5th ed. 2002.

100. F. Rezaei, F. Sharif, A.A. Sarabi, S.M. Kasiriha, M. Rahmanian, E. Akbarinezhad, *Experimental evaluation of high solid polyurethane coating in the presence of salt at high temperature.* Materials and Corrosion, 2009. 60(No. 9999).

101. C.G. Oliveira, M.G.S. Ferreira, *Ranking high-quality paint systems using EIS. Part I: Intact coatings.* Corrosion Science, 2003. 45: p. 123-138.

102. J.Li, C.S. Jeffcoate, G.P. Bierwagen, D.J. Mill, D.E. Tallman, *Thermal transition effects on corrosion protective organic coating :Part 1- Initial studies on corrosion protective organic coatings.* Corrosion, 1998. 54(10): p. 763-771.

103. R.J. Li, W.P. Hsu, T.K. Kwei, A.S. Myerson, *Transport of gases in miscible polymer blends above and below the glass transition region.* AIChE Journal, 1993. 39(9): p. 1509-1518.

104. G. Santarini, *Activation energy in the modeling of complex and poorly known physicochemical processes in corrosion.* Corrosion, 1995. 51(9): p. 698 - 710.

105. M. Cappadonia, J.W. Erning, U. Stimming, *Proton conduction of Nafion® 117 membrane between 140 K and room temperature.* Journal of Electroanalytical Chemistry, 1994. 376(1-2): p. 189-193.

106. D.J. Mills, J.E.O. Mayne, *The inhomogeneous nature of polymer films and its effect on resistance inhibition in corrosion control by organic coating.* H. Leidheiser, editor(s) p 12, NACE, Houston, TX, 1981.

107. J.E.O. Mayne, D.J. Mills, *Structural changes in polymers films. Part 1: The influence of the transition temperature on the electrolytic resistance and water uptake.* Journal of the Oil and Colour Chemists' Association, 1982. 65: p. 138-142.

108. J.E.O. Mayne, *The mechanism of the protective action of an unpigmented film of polystyrene.* Journal of the Oil and Colour Chemists' Association, 1949. 32(352): p. 481.

109. H. Leidheiser, *Electrical and electrochemical measurements as predictors of corrosion at the metal - Organic coating interface.* Progress in Organic Coatings, 1979. 7(1): p. 79-104.

110. F. Mansfeld, M.W. Kendig, S.Tsai, *Evaluation of corrosion behaviour of coated metals with AC impedance measurements.* Corrosion 1982. 38(9): p. 478-485.

111. J.N. Murray, *Electrochemical test methods for evaluating organic coatings on metals: An update - Part I : Introduction and generalities regarding electrochemical testing of organic coatings.* Progress in Organic Coatings, 1997. 30(4): p. 225-233.

112. J.N. Murray, *Electrochemical test methods for evaluating organic coatings on metals: An update - Part III: Multiple test parameter measurements.* Progress in Organic Coatings, 1997. 31(4): p. 375-391.

113. *Gamry instrument - Application notes.*

114. F. Bellucci, L. Nicodemo, *Water transport in organic coatings.* Corrosion 1993. 49(3): p. 235.

115. D.M. Brasher, A.H. Kingsbury, *Electrical measurements in the study of immersed paint coating on metal: I Comparison between capacitance and gravimetric methods of estimating water-uptake.* Journal of Applied Chemistry, 1954. 4: p. 62.

116. F. Mansfeld, *Use of electrochemical impedance spectroscopy for the study of corrosion protection by polymer coatings.* Journal of Applied Electrochemistry, 1995. 25(3): p. 187-202.

117. F. Deflorian, L. Fedrizzi, S. Rossi, P.L. Bonora, *Organic coating capacitance measurement by EIS: Ideal and actual trends.* Electrochimica Acta, 1999. 44(24): p. 4243-4249.

118. J.-T. Zhang, J.-M. Hu, J.-Q. Zhang, C.-N. Cao, *Studies of water transport behavior and impedance models of epoxy-coated metals in NaCl solution by EIS.* Progress in Organic Coatings, 2004. 51(2): p. 145-151.

119. A.S.L. Castela, A.M. Simões, M.G.S. Ferreira, *EIS evaluation of attached and free polymer films.* Progress in Organic Coatings, 2000. 38(1): p. 1-7.

120. G.W. Walter, *A comparison of single frequency and wide frequency range impedance tests for painted metals.* Corrosion Science, 1990. 30(6-7): p. 617-629.

121. M. Stern, A.L. Geary, *Electrochemical Polarization.* Journal of The Electrochemical Society, 1957. 104(1): p. 56-63.

122. F.M. Geenen, J.H.W. De Wit, E.P.M. Van Westing, *An impedance spectroscopy study of the degradation mechanism for a model epoxy coating on mild steel.* Progress in Organic Coatings, 1990. 18(3): p. 299-312.

123. J.B. Jorcin, M. Orazemb, N.Pebere, B.Tribollet, *CPE analysis by local electrochemical impedance spectroscopy.* Electrochimica Acta, 2006. 51: p. 1473-1479.

124. F. Mansfeld, L.T. Han, C.C. Lee, G. Zhang, *Evaluation of corrosion protection by polymer coatings using electrochemical impedance spectroscopy and noise analysis.* Electrochimica Acta, 1998. 43(19-20): p. 2933-2945.

125. W.J. Lorenz, F. Mansfeld, *Determination of corrosion rates by electrochemical DC and AC methods.* Corrosion Science, 1981. 21(9-10): p. 647-672.

126. F. Mansfeld, C.H.Tsai, *Determination of coating deterioration with electrochemical impedance spectroscopy - Basic relationships.* Corrosion 1991. 47(12): p. 958-963.

127. R. Hirayama, S. Haruyama, *Electrochemical impedance for degraded coated steel having pores.* Corrosion, 1991. 42(12): p. 952.

128. J.R. Scully, *Electrochemical impedance of organic-coated steel: Correlation of impedance parameters with long-term coating deterioration.* Journal of The Electrochemical Society, 1989. 136(4): p. 979-990.

129. G.W. Walter, *The application of impedance methods to study the effects of water uptake and chloride ion concentration on the degradation of paint films - I. Attached films.* Corrosion Science, 1991. 32(10): p. 1059-1084.

130. M. Mahdavian, M.M. Attar, *OCP measurement: A method to determine CPVC.* Scientia Iranica, 2007. 14(4): p. 369 - 372.

131. J.R. Vilche, E.C. Bucharsky, C.A. Giúdice, *Application of EIS and SEM to evaluate the influence of pigment shape and content in ZRP formulations on the corrosion prevention of naval steel.* Corrosion Science, 2002. 44(6): p. 1287-1309.

132. J.E.O. Mayne, *Electrochemical behaviour of paint films in sea-water.* Chemistry and Industry 1951.

133. J.E.O. Mayne, *Electrochemical behaviour of paint films in sea water.* Transactions of the Institute of Metal Finishing, 1964. 41: p. 121.

134. M.C. Deyá, G. Blustein, R. Romagnoli, B. del Amo, *The influence of the anion type on the anticorrosive behaviour of inorganic phosphates.* Surface and Coatings Technology, 2002. 150(2-3): p. 133-142.

135. H. Marchebois, S. Joiret, C. Savall, J. Bernard, S. Touzain, *Characterization of zinc-rich powder coatings by EIS and Raman spectroscopy.* Surface and Coatings Technology, 2002. 157(2-3): p. 151-161.

136. H.E.M. Smith, *The protection of poorly prepared steel surfaces using water borne coatings.* Oxford Thesis, 1988.

137. M. Rohwerder, M. Stratmann, P. Leblanc, G.S. Frankel, *Application of scanning Kelvin probe in corrosion science* in Analytical Methods in Corrosion Science and Engineering, P. Marcus and F. Mansfeld (editor) , Taylor & Francis, 2006.

138. I.D. Baikie, P.J.Estrup, *Low cost PC based scanning Kelvin probe.* Review of scientific instruments, 1998. 69(11): p. 3902-3907.

139. W. Furbeth, M. Stratmann, *The delamination of polymeric coatings from electrogalvanised steel - A mechanistic approach - Part 1: Delamination from a defect with intact zinc layer.* Corrosion Science, 2001. 43(2): p. 207-227.

140. W. Furbeth, M. Stratmann, *The delamination of polymeric coatings from electrogalvanized steel - A mechanistic approach - Part 3: Delamination kinetics and influence of CO_2.* Corrosion Science, 2001. 43(2): p. 243-254.

141. W. Furbeth, M. Stratmann, *The delamination of polymeric coatings from electrogalvanized steel - A mechanistic approach - Part 2: Delamination from a defect down to steel.* Corrosion Science, 2001. 43(2): p. 229-241.

142. G. Grundmeier, C. Reinartz, M. Rohwerder, M. Stratmann, *Corrosion properties of chemically modified metal surfaces.* Electrochimica Acta, 1998. 43(1-2): p. 165-174.

143. A. Leng, H. Streckel, K. Hofmann, M. Stratmann, *The delamination of polymeric coatings from steel - Part 3: Effect of the oxygen partial pressure on the delamination reaction and current distribution at the metal/polymer interface.* Corrosion Science, 1998. 41(3): p. 599-620.

144. A. Leng, H. Streckel, M. Stratmann, *The delamination of polymeric coatings from steel - Part 2: First stage of delamination, effect of type and concentration of cations on delamination, chemical analysis of the interface.* Corrosion Science, 1998. 41(3): p. 579-597.

145. A. Leng, H. Streckel, M. Stratmann, *The delamination of polymeric coatings from steel - Part 1: Calibration of the Kelvin probe and basic delamination mechanism.* Corrosion Science, 1998. 41(3): p. 547-578.

146. M. Stratmann, A. Leng, W. Furbeth, H. Streckel, H. Gehmecker, K.H. Groe-Brinkhaus, *The scanning Kelvin probe: A new technique for the in situ analysis of the delamination of organic coatings.* Progress in Organic Coatings, 1996. 27(1-4): p. 261-267.

147. K. Wapner, B. Schoenberger, M. Stratmann, G. Grundmeier, *Height-regulating scanning Kelvin probe for simultaneous measurement of surface topology and electrode potentials at buried polymer/metal interfaces.* Journal of The Electrochemical Society, 2005. 152(3): p. E114-E122.

148. K. Ogle, S. Morel, N. Meddahi, *An electrochemical study of the delamination of polymer coatings on galvanized steel.* Corrosion Science, 2005. 47(8): p. 2034-2052.

149. B. Reddy, M.J. Doherty, J.M. Sykes, *Breakdown of organic coatings in corrosive environments examined by scanning Kelvin probe and scanning acoustic microscopy.* Electrochimica Acta, 2004. 49(17-18): p. 2965-2972.

150. B. Reddy, J.M. Sykes, *Degradation of organic coatings in a corrosive environment: A study by scanning Kelvin probe and scanning acoustic microscope.* Progress in Organic Coatings, 2005. 52(4): p. 280-287.

151. S.G. Tan, W.S. Chow, *Thermal properties, fracture toughness and water absorption of epoxy-palm oil blends.* Polymer - Plastics Technology and Engineering. 49(9): p. 900-907.

152. S. Ma, W. Liu, Z. Wei, H. Li, *Mechanical and thermal properties and morphology of epoxy resins modified by a silicon compound.* Journal of Macromolecular Science, Part A: Pure and Applied Chemistry, 2010. 47(11): p. 1084-1090.

153. P. Cañamero-Martínez, J.L. de la Fuente, M. Fernández-García, *Master curve and time–temperature–transformation cure diagram of a polyfunctional epoxy acrylic resin.* Journal of Applied Polymer Science. 120(4): p. 2166-2172.

154. H. Liu, A. Uhlherr, M.K. Bannister, *Quantitative structure-property relationships for composites: prediction of glass transition temperatures for epoxy resins.* Polymer, 2004. 45: p. 2051-2060.

155. H. Leidheiser, W. Wang, *Rate controlling steps in the cathodic delamination of 10 to 40 um thick polybutadiene and epoxy-polyamide coatings from metallic substrate in corrosion control by organic coating.* H. Leidheiser, editor(s) p 70, NACE, Houston, TX, 1981, p70-77

156. H. Leidheiser, J. Catino, *The activation energy for cathodic delamination of polybutadiene from steel in chloride solutions.* Proceeding of the Symposium on Corrosion Protection by Organic Coatings, 1987. 87-2: p. 60 - 67.

157. J.D. Kellner, *Temperature dependence of cathodic disbondment of tape pipeline coatings.* Proceeding of the Symposium on Corrosion Protection by Organic Coatings, M.W. Kendig; H.Leidheiser (eds), Pennington, USA, Electrochemical Soc. Inc, 1987. 87-2: p. 48 - 59.

158. J. H. Leidheiser, D.J. Mills, W. Bilder, *The permeability of a polybutadiene coating to ions, water and oxygen.* Proceedings - Electrochemical Society 1987. 87-2: p. 23 - 36.

159. U. Steinsmo, J.I. Skar, E. Bardal, *The effect of the dry film thickness, temperature, and electrolyte on the cathodic current of painted steel.* Journal of The Electrochemical Society, 1989. 136(12): p. 3583-3588.

160. H. Ochs, J. Vogelsang, *Effect of temperature cycles on impedance spectra of barrier coatings under immersion conditions.* Electrochimica Acta, 2004. 49(17-18): p. 2973-2980.

161. J.I. Skar, *Cathodic disbonding of and transport of charge through paint films.* DPhil Thesis, University of Delft, 1990.

162. J.M. Sykes, X. Yan, *Investigation of electrochemical reactions beneath paint using a combination of methods.* ECS Transactions, 2009. 21.

163. L. Valentinelli, J. Vogelsang, H. Ochs, L. Fedrizzi, *Evaluation of barrier coatings by cycling testing.* Progress in Organic Coatings, 2002. 45(4): p. 405-413.

164. A. Miszczyk, K. Darowicki, *Effect of environmental temperature variations on protective properties of organic coatings.* Progress in Organic Coatings, 2003. 46(1): p. 49-54.

165. H. Leidheiser, W. Wang, L. Igetoft, *The mechanism for the cathodic delamination of organic coatings from a metal surface.* Progress in Organic Coatings, 1983. 11(1): p. 19-40.

166. F. Deflorian, S. Rossi, *An EIS study of ion diffusion through organic coatings.* Electrochimica Acta, 2006. 51(8-9): p. 1736-1744.

167. K. McLeod, *Blistering of paint films.* DPhil Thesis, University of Oxford, 1984.

168. F.A. Cotton, G. Wilkinson, *Advanced inorganic chemistry*. 4th edition ed. 1980: Wiley-Interscience.

169. M. Doherty, J.M. Sykes, *Micro-cells beneath organic lacquers: A study using scanning Kelvin probe and scanning acoustic microscopy.* Corrosion Science, 2004. 46(5): p. 1265-1289.

170. D. Pereira, J.D. Scantlebury, M.G.S. Ferreira, M.E. Almeida, *The application of electrochemical measurements to the study and behaviour of zinc-rich coatings.* Corrosion Science, 1990. 30(11): p. 1135-1147.

171. S.E. Faidi, J.D. Scantlebury, P. Bullivant, N.T. Whittle, R. Savin, *An electrochemical study of zinc-containing epoxy coatings on mild steel.* Corrosion Science, 1993. 35(5-8): p. 1319-1328.

172. X.R. Novoa, M. IZquierdo, P. Merino, L. Espada, *Electrical impedance spectroscopy and zero resistance ammeter (ZRA) as tools for studying the behaviour of zinc-rich inorganic coatings.* Materials Science Forum, 1989. 44 & 45: p. 223 - 234.

173. B.J. Hepburn, K.R. Gowers, J.D. Scantlebury, *Interpretation of low frequency AC impedance data for organic coatings on mild steel.* British Corrosion Journal, 1986. 21: p. 105-108.

174. *Metals Handbook, Volume 13 - Corrosion*: ASM International, 9th edition.

175. A.S. Castela, A.M. Simões, *Water sorption in freestanding PVC films by capacitance measurements.* Progress in Organic Coatings, 2003. 46(2): p. 130-134.

176. C.V.D'Alkaine, C. Garcia, H. Corti, D. Gomez, *Epoxy-chromate coatings: Electric and membrane results.* Journal of the Oil and Colour Chemists' Association, 1980. 63: p. 23-27.

177. M. Kendig, F. Mansfeld, S. Tsai, *Determination of the long term corrosion behavior of coated steel with A.C. impedance measurements.* Corrosion Science, 1983. 23(4): p. 317-329.

178. J. Kittel, N. Celati, M. Keddam, H. Takenouti, *New methods for the study of organic coatings by EIS: New insights into attached and free films.* Progress in Organic Coatings, 2001. 41(1-3): p. 93-98.

179. J.D.B. Sharman, *Breakdown processes in paint coatings on steel.* DPhil Thesis, University of Oxford, 1991.

180. D.D. Macdonald, *Transient techniques in electrochemistry*. 1977: New York : Plenum Press.